78-??T

LEVEL II

ADA058475

(6) CONTROL ASPECTS OF
HIGHLY CONSTRAINED GUIDANCE TECHNIQUES.

by

(10) LOUIS RUSSELL RECORDS, JR

B.S., Aeronautical Engineering, USAF Academy
(1971)

AD No.
DDC FILE COPY

(9) master's thesis,

DDC
SEP 11

SUBMITTED IN PARTIAL FULFILLMENT
OF THE REQUIREMENTS FOR THE
DEGREE OF

MASTER OF SCIENCE

at the
Charles Stark Draper Lab.
MASSACHUSETTS INSTITUTE OF TECHNOLOGY

(11) Feb[redacted]78 (12) 200p.

This document has been approved for public release and sale; its distribution is unlimited.

(14) AFIT-CI-79-70

Signature of Author...
Department of Aeronautics and Astronautics

Approved by...
Technical Advisor, CSDL

Certified by..
Thesis Supervisor

Accepted by...
Chairman, Departmental Graduate Committee

012 200

CONTROL ASPECTS OF
HIGHLY CONSTRAINED GUIDANCE TECHNIQUES

by

LOUIS RUSSELL RECORDS, JR.

Submitted to the Department of Aeronautics and Astronautics on 20 January 1978, in partial fulfillment of the requirements for the Degree of Master of Science

ABSTRACT

This thesis examines the design of the guidance, steering, control, and attitude measurement systems for the third stage of a space vehicle in exoatmospheric powered flight. The guidance methods used in this study include position offset guidance and energy management (fuel depletion) guidance. ~~developed by The Charles Stark Draper Laboratory.~~ A generalized flight control system design method is developed which allows the autopilot filter gains and coefficients to be readily determined for any desired crossover frequency. Several steering modes for velocity-to-be-gained and fuel depletion guidance are then discussed. The effect of terminal steering on the end-of-burn stability and velocity-to-be-gained residuals is discussed for abrupt thrust termination and thrust tailoff conditions. An empirical approach to the determination of sensitivities to thrust direction errors for fuel depletion and simultaneous control of reentry angle and time-on-target guidance is discussed and compared to analytical predictions. Finally, an attitude measurement study is presented which compares several methods of processing the IMU attitude measurements with regard to reducing computational requirements and minimizing worst-case error.

UNCLASSIFIED

SECURITY CLASSIFICATION OF THIS PAGE (When Data Entered)

REPORT DOCUMENTATION PAGE

READ INSTRUCTIONS BEFORE COMPLETING FORM

1. REPORT NUMBER CI 79-70	2. GOVT ACCESSION NO.	3. RECIPIENT'S CATALOG NUMBER
4. TITLE (and Subtitle) Control Aspects of Highly Constrained Guidance Techniques		5. TYPE OF REPORT & PERIOD COVERED Thesis 6. PERFORMING ORG. REPORT NUMBER
7. AUTHOR(s) Captain Louis Russell Records, Jr.		8. CONTRACT OR GRANT NUMBER(s)
9. PERFORMING ORGANIZATION NAME AND ADDRESS AFIT Student at the Massachusetts Institute of Technology, Cambridge MA		10. PROGRAM ELEMENT, PROJECT, TASK AREA & WORK UNIT NUMBERS
11. CONTROLLING OFFICE NAME AND ADDRESS AFIT/CI WPAFB OH 45433		12. REPORT DATE 1978 13. NUMBER OF PAGES 199 Pages
14. MONITORING AGENCY NAME & ADDRESS(if different from Controlling Office)		15. SECURITY CLASS. (of this report) Unclassified 15a. DECLASSIFICATION/DOWNGRADING SCHEDULE

16. DISTRIBUTION STATEMENT (of this Report)

Approved for Public Release; Distribution Unlimited

17. DISTRIBUTION STATEMENT (of the abstract entered in Block 20, if different from Report)

18. SUPPLEMENTARY NOTES

JOSEPH P. HIPPS, Major, USAF AUG 15 1978
Director of Information, AFIT

19. KEY WORDS (Continue on reverse side if necessary and identify by block number)

20. ABSTRACT (Continue on reverse side if necessary and identify by block number)

DD FORM 1 JAN 73 1473 EDITION OF 1 NOV 65 IS OBSOLETE

UNCLASSIFIED

SECURITY CLASSIFICATION OF THIS PAGE (When Data Entered)

SECURITY CLASSIFICATION OF THIS PAGE(When Data Entered)

SECURITY CLASSIFICATION OF THIS PAGE(When Data Entered)

ACKNOWLEDGMENTS

I would like to thank Mr. Gilbert S. Stubbs for his constant flow of ideas and suggestions and for giving me an invaluable opportunity to learn from him. Also, I would like to thank Sean Collins for his help in implementing the guidance methods used in this thesis. Finally, I thank my wife, Loretta, for her constant encouragement and devotion and her help in keeping my sense of humor and perspective.

This report was prepared at The Charles Stark Draper Laboratory, Inc., under Contract F04701-73-C-0277 with the Space and Missile Systems Organization of the Air Force Systems Command.

Publication of this report does not constitute approval by the Draper Laboratory or the U.S. Air Force of the findings or conclusions contained herein. It is published for the exchange and stimulation of ideas.

ACCESSION for
NTIS White Section
DDC Buff Section
UNANNOUNCED
JUSTIFICATION
BY
DISTRIBUTION/AVAILABILITY CODES
CIAL
A

TABLE OF CONTENTS

Section		Page
	SUMMARY	12
1	SYSTEM DESCRIPTION	14
	1.1 The Vehicle	14
	1.2 Guidance and Flight Control Systems	16
	1.3 The Inertial Measurement Unit	21
2	STEERING AND AUTOPILOT ANALYSIS	22
	2.1 Steering and Autopilot Design Parameters	22
	2.2 Steering Modes	22
	2.3 Steering Stability Analysis	25
	2.4 Normalized Compensation Design	33
	2.5 Frequency Response	40
	2.6 Gain Scheduling	59
	2.7 Terminal Steering	60
3	GUIDANCE METHODS	61
	3.1 Position Offset Guidance	61
	3.2 Reentry Angle (γ) and Time-On-Target (TOT) Control	67
	3.3 Perturbation Sensitivity of Fuel Depletion Guidance	67
4	ATTITUDE MEASUREMENT	76
	4.1 Attitude Measurement System	76
	4.2 Attitude Data Processing	79
	4.3 Idealized AIRS Error Study	84
	4.4 Autopilot Simulation Study Based on the STAR Program	86

Table of contents (Cont.)

Section		Page
5	SIMULATION RESULTS	107
	5.1 Overview	107
	5.2 OFFSETT Simulation Runs	108
	5.3 STEER Simulation Runs	117
6	CONCLUSIONS	166
	6.1 Overview	166
	6.2 Attitude Measurement Studies	167
	6.3 STEER Simulation Studies	167

Appendix		
A1	VEHICLE ROTATIONAL TRANSFER FUNCTION	171
A2	ACTUATOR TRANSFER FUNCTION	172
A3	DERIVATION OF $\lambda(s)/\theta(s)$	173
A4	RELATIONSHIP BETWEEN λ, $\lambda_{\Delta V}$, AND λ_{V_g}	175
A5	DERIVATIONS FOR FUEL DEPLETION STEERING	178
A6	CALCULATION OF SPECIFIC FLIGHT CONTROL SYSTEM PARAMETERS	179
B	COORDINATE TRANSFORMATIONS	181
C	SIMULATION DESCRIPTION	183
D	THRUST TAILOFF MODEL	191
E	EFFECT OF IMU POSITION ON ACCELERATION AND RATE VECTORS SENSED	197

LIST OF REFERENCES 199

LIST OF FIGURES

Figure		Page
1	The vehicle model	14
2	System block diagram	17
3	Inertial coordinate frame and nominal trajectory	18
4	Geometry of fuel depletion arc	24
5	Autopilot and steering loop analytical model	26
6	Analytical steering model - case STEER01	29
7	Analytical steering model - case STEER02	30
8	Simplified analytical model - STEER02	31
9	Minimum values of M_p for $\omega_1' = 0.0$	35
10	Minimum values of M_p for $\omega_1' = 0.1$	37
11	Gain vs frequency - uncompensated system	41
12	Phase vs frequency - uncompensated system	41
13	Gain vs phase - uncompensated system	42
14	Gain vs frequency - ω_{xo} = 2 rad/sec.	42
15	Phase vs frequency - ω_{xo} = 2 rad/sec.	43
16	Gain vs phase - ω_{xo} = 2 rad/sec.	43
17	Gain vs frequency - ω_{xo} = 5 rad/sec.	44
18	Phase vs frequency - ω_{xo} = 5 rad/sec.	44
19	Gain vs phase - ω_{xo} = 5 rad/sec.	45
20	Gain vs frequency - ω_{xo} = 8 rad/sec.	45
21	Phase vs frequency - ω_{xo} = 8 rad/sec.	46
22	Gain vs phase - ω_{xo} = 8 rad/sec.	46
23	Effect of steering, normalized design	48
24	Effect of K_{int}, gain vs frequency	49
25	Effect of K_{int}, phase vs frequency	50
26	Effect of T_{go}, gain vs frequency	51
27	Effect of T_{go}, phase vs frequency	52
28	Effect of T_s, gain vs frequency	53
29	Effect of T_s, phase vs frequency	54
30	Effect of steering, optimized design	55
31	Effect of T_{go}, STEER01	56

List of Figures (Cont.)

Figure		Page
32	Effect of T_{go}, STEER02	57
33	Geometrical relationships of perturbation analysis	62
34	Geometrical relationships of perturbation analysis	68
35	The AIRS platform	77
36	Definition of the AIRS band angles and body-angle increment relationship	78
37	Incremental updating of attitude errors	79
38	Pictorial representation of AIRSBAE	81
39	Pictorial representation of AIRSME4	83
40	Ideal attitude feedback, AIRS indicated rate	91
41	Ideal attitude feedback, AIRSX indicated rate	92
42	AIRS attitude feedback, UMAX = 2	93
43	AIRS attitude feedback, UMAX = 15	94
44	AIRS attitude feedback UMAX = 30	95
45	AIRS attitude feedback, UMAX = 45	96
46	AIRS attitude feedback, with random noise, UMAX = 15	97
47	AIRS attitude feedback, with deterministic errors, UMAX = 15	98
48	AIRSX attitude feedback, UMAX = 2	99
49	AIRSX attitude feedback, UMAX = 15	100
50	AIRSX attitude feedback, UMAX = 30	101
51	AIRSX attitude feedback, UMAX = 45	102
52	AIRSX attitude feedback with random noise, UMAX = 15	103
53	AIRSX attitude feedback with deterministic errors, UMAX = 15	104
54	AIRS attitude feedback with random noise and deterministic errors, UMAX = 15	105
55	AIRSX attitude feedback with random noise and deterministic errors, UMAX = 15	106
56	OFFSETT, V_g steering	109
57	OFFSETT, fuel depletion steering	110
58-1	OFFSETT, fuel depletion steering with Gamma/TOT Control	111
58-2	OFFSETT, fuel depletion steering with Gamma/TOT control	112

List of Figures (Cont.)

Figure		Page
59-1	OFFSETT, fuel depletion steering, perturbation analysis	113
59-2	OFFSETT, fuel depletion steering, perturbation analysis	114
60-1	OFFSETT, fuel depletion steering with Gamma/TOT control, perturbation analysis	115
60-2	OFFSETT, fuel depletion steering with Gamma/TOT control, perturbation analysis	116
61-1	STEER, V_g steering	118
61-2	STEER, V_g steering	119
62-1	STEER, V_g steering with AIRSX	120
62-2	STEER, V_g steering with AIRSX	121
63-1	STEER, V_g steering with AIRSX and thrust tailoff	122
63-2	STEER, V_g steering with AIRSX and thrust tailoff	123
64-1	STEER, V_g steering with AIRSX, and thrust tailoff, $T_{FR} = 5$	124
64-2	STEER, V_g steering with AIRSX, and thrust tailoff, $T_{FR} = 5$	125
65-1	STEER, fuel depletion steering	126
65-2	STEER, fuel depletion steering	127
66-1	STEER, fuel depletion steering, integral feedback	128
66-2	STEER, fuel depletion steering, integral feedback	129
67-1	STEER, fuel depletion steering, integral feedback, $T_{FR} = 2$	130
67-2	STEER, fuel depletion steering, integral feedback, $T_{FR} = 2$	131
68-1	STEER, fuel depletion steering, integral feedback, $T_{FR} = 2$, AIRSX	132
68-2	STEER, fuel depletion steering, integral feedback, $T_{FR} = 2$, AIRSX	133
69-1	STEER, fuel depletion steering, integral feedback, $T_{FR} = 2$ AIRSX, thrust tailoff	134
69-2	STEER, fuel depletion steering, integral feedback, $T_{FR} = 2$, AIRSX, thrust tailoff	135

List of Figures (Cont.)

Figure		Page
70-1	STEER, fuel depletion steering, T_{FR} = 2, simplified θ calculation	136
70-2	STEER, fuel depletion steering, T_{FR} = 2, simplified θ calculation	137
71-1	STEER, fuel depletion steering, Gamma/TOT control, T_{FR} = 2	138
71-2	STEER, fuel depletion steering, Gamma/TOT control, T_{FR} = 2	139
72-1	STEER, fuel depletion steering, Gamma/TOT control, integral feedback, T_{FR} = 2	140
72-2	STEER, fuel depletion steering, Gamma/TOT control, integral feedback, T_{FR} = 2	141
73-1	STEER, fuel depletion steering, 2 rad/sec autopilot, T_{FR} = 2	142
73-2	STEER, fuel depletion steering, 2 rad/sec autopilot, T_{FR} = 2	143
74-1	STEER, fuel depletion steering, 2 rad/sec autopilot, integral feedback, T_{FR} = 2	144
74-2	STEER, fuel depletion steering, 2 rad/sec autopilot, integral feedback, T_{FR} = 2	145
75-1	STEER, fuel depletion steering, 8 rad/sec autopilot, T_{FR} = 2	146
75-2	STEER, fuel depletion steering, 8 rad/sec autopilot, T_{FR} = 2	147
76-1	STEER, fuel depletion steering, 8 rad/sec autopilot, integral feedback, T_{FR} = 2	148
76-2	STEER, fuel depletion steering, 8 rad/sec autopilot, integral feedback, T_{FR} = 2	149
77-1	STEER, fuel depletion steering, optimized design, T_{FR} = 2	150
77-2	STEER, fuel depletion steering, optimized design, T_{FR} = 2	151
78-1	STEER, fuel depletion steering, optimized design, integral feedback, T_{FR} = 2	152
78-2	STEER, fuel depletion steering, optimized design, integral feedback, T_{FR} = 2	153

List of Figures (Cont.)

Figure		Page
79-1	STEER, fuel depletion steering, optimized design, integral feedback, AIRSX, T_{FR} = 2	154
79-2	STEER, fuel depletion steering, optimized design, integral feedback, AIRSX, T_{FR} = 2	155
80-1	STEER, fuel depletion steering, optimized design, integral feedback, AIRSX, thrust tailoff, T_{FR} = 2	156
80-2	STEER, fuel depletion steering, optimized design, integral feedback, AIRSX, thrust tailoff, T_{FR} = 2	157
81-1	STEER, fuel depletion steering, 8 rad/sec autopilot, AIRS, T_{FR} = 2	158
81-2	STEER, fuel depletion steering, 8 rad/sec autopilot, AIRS, T_{FR} = 2	159
82-1	STEER, fuel depletion steering, 8 rad/sec autopilot, AIRSX, T_{FR} = 2	160
82-2	STEER, fuel depletion steering, 8 rad/sec autopilot, AIRSX, T_{FR} = 2	161
83-1	STEER, fuel depletion steering, optimized design, AIRSX, thrust tailoff, T_{FR} = 2	162
83-2	STEER, fuel depletion steering, optimized design, AIRSX, thrust tailoff, T_{FR} = 2	163
A2-1	Actuator model	172
A4-1	Definition of angles in inertial frame	175
A4-2	Relation between $\lambda(s)$ and $\lambda_{\Delta V}(s)$	176
A4-3	Relationship between $\lambda V_g(s)$ and $\lambda(s)$	177
A5-1	Geometry of the fuel depletion arc	178
B-1	Body frame to inertial frame transformation	181
B-2	Engine frame to body frame transformation	182
C-1	Simplified flow chart-STEER program	188
D-1	Thrust vs time	193
D-2	Thrust acceleration vs time	194
D-3	Mass vs time	195
D-4	Mass flow rate vs time	196
E-1	Effect of IMU position on sensed acceleration	197

LIST OF TABLES

Table		Page
1	Vehicle parameters	15
2	Nominal cycle times	20
3	Design parameters	22
4	Sensitivity of fuel depletion angle θ to small changes in the ratio V_g/V_{cap}	25
5	Minimum values of M_p (peak closed-loop gain) for $\omega_1' = 0$	35
6	Minimum values of M_p (peak closed-loop gain) for $\omega_1' = 0.1$	37
7	K_o' vs ω'	38
8	Autopilot parameters	39
9	Z-domain filter coefficients	39
10	Comparison of design results	40
11	Nominal steering loop parameters	40
12	Gain scheduling autopilot coefficients	59
13	Comparison of analytical and computed sensitivities of fuel depletion angle to variations in the velocity-to-be-gained (no reentry control)	74
14	Comparison of analytical and computed sensitivities of fuel depletion angle to variations in the velocity-to-be-gained (Gamma/Time-On-Target Control)	75
15	Comparison of computational requirements of AIRSBAE and AIRSME4 based on the Honeywell 701P Computer	85
16	Maximum errors at the end of T_s (T_s = 0.45 sec)	87
17	STAR simulation runs	90
18	OFFSETT and STEER simulation initial conditions	107
19	OFFSETT simulation runs	108
20	STEER simulation runs	164
21	Comparison of STEER and OFFSETT Terminal Conditions	170
C-1	Sample OFFSETT/PERT output	185
C-2	Sample STAR output	187
C-3	Sample STEER output	190

SUMMARY

In the design of space vehicle flight control systems for highly constrained guidance methods, the system elements must be carefully analyzed in terms of the required vehicle response to guidance commands. These guidance commands, particularly in the case of highly constrained methods, may require at the same time a high degree of steering accuracy and a well-behaved response to large transients.

In the case of fuel depletion steering, for example, if we assume that the vehicle is initially thrusting along the velocity-to-be-gained vector, there will be a large instantaneous attitude error (50 degrees might be a typical value) as the vehicle maneuvers to "waste" excess fuel. This large input command can result in extremely high turning rates, which, even neglecting the structural aspects, can severely tax the capability of the flight control system. This is a particularly severe problem for flight control systems which are designed to precisely null the velocity-to-be-gained.

The transient may also cause saturation of the engine actuator, forcing the actuator into position and rate limits. Also, since the attitude data is sampled at discrete times and extrapolated over an interval, the high turning rates can cause significant attitude (and hence derived rate) errors. The high rotation rates may also cause significant errors in the sensed acceleration due to the location of the IMU away from the vehicle center of gravity.

In spite of these problems, the overall goal of the flight control system is to cause the vehicle to precisely achieve the velocity required to coast to the impact point at thrust termination. This requirement drives the design to be highly sensitive to small steering errors which is at odds with the requirement to be well-behaved in the presence of large transient signals.

In this thesis, these problems are examined in terms of their impact on the design of a flight control system for a Stage III vehicle. The system design is evolved to minimize residual velocity-to-be-gained errors and maintain vehicle stability despite the highly constrained nature of the guidance techniques.

SECTION 1

SYSTEM DESCRIPTION

1.1 The Vehicle

The vehicle used in this study is the third stage booster and payload of a ballistic missile. The missile is assumed to be a rigid body, symmetric about the longitudinal (X) axis. The vehicle is powered by a solid fuel rocket engine with constant thrust (unless otherwise specified) and the vehicle mass, moments of inertia, and center of gravity are assumed to vary linearly with time. The vehicle is assumed to be operating outside the atmosphere. The vehicle parameters are illustrated in Figure 1 and listed in Table 1.

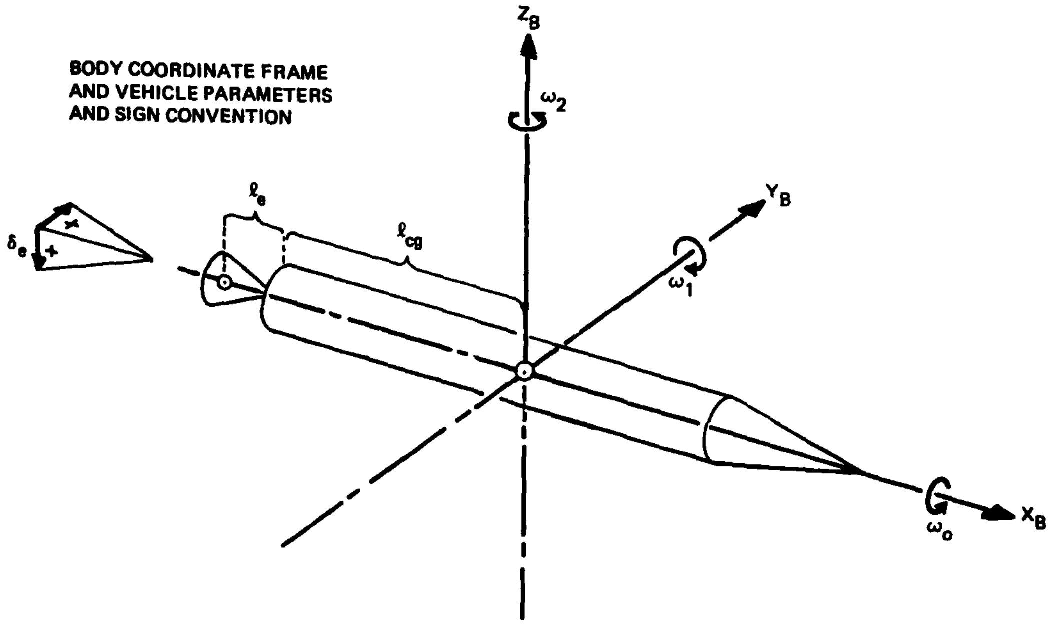

Figure 1. The vehicle model.

Table 1. Vehicle parameters.

PARAMETER	SYMBOL	UNITS	IGNITION VALUE	BURNOUT VALUE	RATE OF CHANGE
Thrust	T	lbs	100,000	0	Zero
Mass	M	slugs	1060	430	*10.50
Pitch & Yaw Inertia	I_{PY}	slug-ft^2	25,000	12,500	208.33
Roll Inertia	I_R	slug-ft^2	5,000	3,750	20.8
Exhaust Vel	V_{ex}	ft/sec	9,524	9,524	Zero
ΔV Capability	V_{cap}	ft/sec	8,400	0	-
Length from Nozzle Hinge Point to Nozzle cg	ℓ_e	ft	2	2	Zero
Length From CG to Nozzle Hinge Point	ℓ_{cg}	ft	5	10	0.0833
Nominal Burn Time	T_{BURN}	seconds	60	-	*-

*See Thrust Model - Appendix D

Control of the vehicle is accomplished by deflecting the rocket nozzle in pitch and yaw. The pitch and yaw autopilot channels are identical. Motion about the roll axis is assumed constrained to zero. It is further assumed that there are no inertial coupling effects.

The derivations of the vehicle, actuator, and steering loop transfer functions are given in Appendix A. Although the digital autopilot operates by sampling inputs and performing calculations at discrete intervals of time, we will assume the autopilot-actuator-vehicle combination to be approximately continuous, since the sampling frequency of the autopilot is high (33.33 cycles/sec) relative to the expected crossover frequency (<8 rad/sec).

The open-loop transfer function for the actuator and vehicle from Appendix A is given below. "Tail-Wags-Dog" and IMU location effects have been analyzed and will be neglected. A second-order actuator model will be used. System lags, such as sampling delays (T/2) and computational lags, are combined into the delay term

$$G_{OL}(s) = \underbrace{\left\{\frac{K_v}{s^2}\right\}}_{\text{Vehicle}} \underbrace{\left\{\frac{K_s^2}{s^2 + K_s s + K_s^2}\right\}}_{\text{Actuator}} \underbrace{\left\{e^{-T_o s}\right\}}_{\text{Lags}}$$

with

K_v = Vehicle DC gain = $T\ell_{cg}/I$

K_s = Actuator ω_n

T_o = Σ delay terms (sampling and computational)

The frequency response of the uncompensated vehicle and actuator is given in Section 2.5, along with the response curves for several autopilot filter configurations and steering loop designs.

1.2 Guidance and Flight Control Systems

The guidance and flight control systems are diagrammed in Figure 2. The guidance system receives accelerometer-sensed velocity increments from the IMU, which is the Advanced Inertial Reference System (AIRS) developed by CSDL. This information is used with other inputs to compute predicted orbital parameters at the guidance cycle

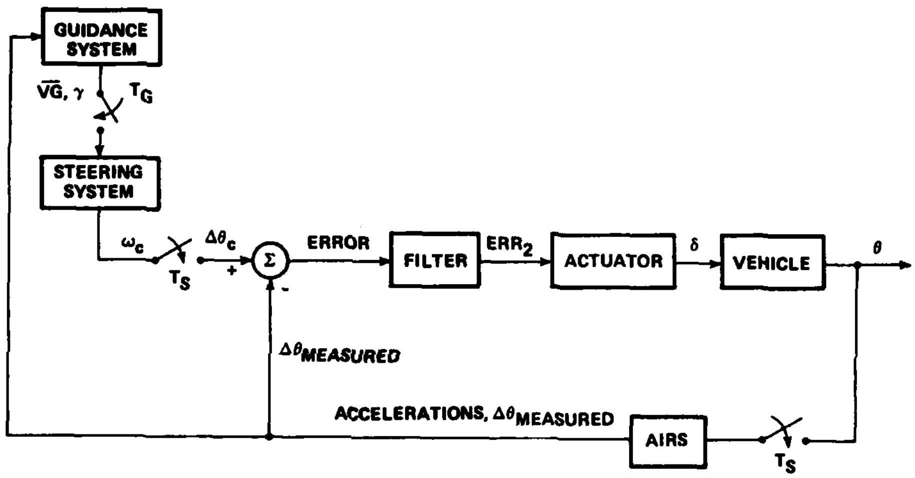

Figure 2. System block diagram.

rate, in particular, the required velocity and the reentry angle. The required velocity, $\bar{V}_{req}$, is the velocity needed to coast from the current position to the desired impact point. The velocity-to-be-gained, $\bar{V}_g$, is defined as the vector difference between the required velocity and the current vehicle velocity

$$\bar{V}_g = \bar{V}_{req} - \bar{V} \tag{1}$$

The reentry angle is the predicted flight path angle at 300,000 feet and may be controlled by selecting the appropriate guidance mode (see Section 3).

The guidance parameters are computed by specifying the present and final position vectors, $\bar{r}$, and $\bar{r}_2$, and the desired time of flight and solving the "Lambert Problem." The inertial reference frame and the nominal trajectory used in this study are illustrated in Figure 3.

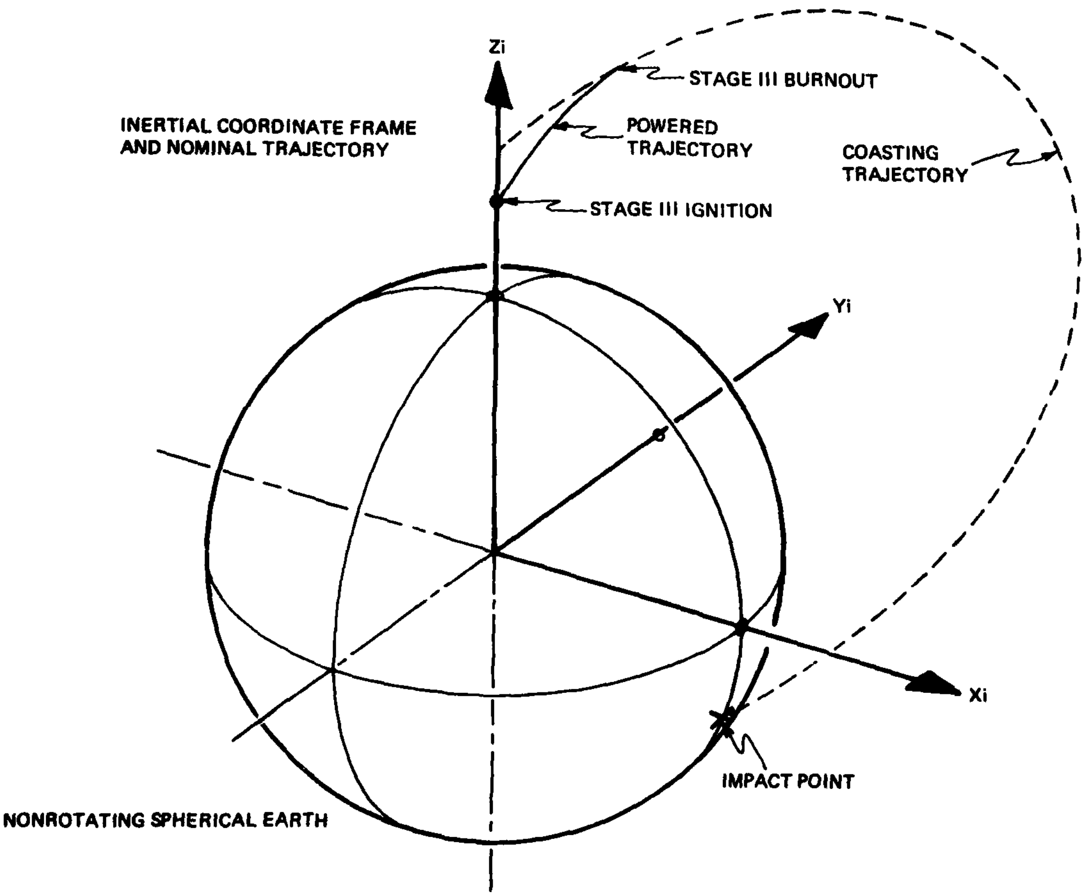

Figure 3. Inertial coordinate frame and nominal trajectory.

The flight control system consists of the digital autopilot, steering loop and engine actuator. Steering is accomplished at the steering cycle rate by computing a desired thrust vector in platform coordinates, $U\bar{S}F$, and by taking the vector cross-product between the incremental sensed velocity vector, $\Delta\bar{V}$, and $U\bar{S}F$. This steering method, popularly known as cross-product steering, results in an inertially-referred steering vector, $ALP\bar{H}ASTEER$, where

$$ALPHA\bar{S}TEER = \Delta\bar{V} \times U\bar{S}F \qquad (2)$$

For simple cross-product steering (no integral term in the feedback) the rate command vector in the body axis, $\bar{\omega}_c$, is obtained by the expression

$$\bar{\omega}_c = \overset{*}{PB}\left[K_{steer}\ ALPHA\bar{S}TEER\right] \qquad (3)$$

where $\overset{*}{PB}$ is the platform-to-body transformation matrix and K_{steer} is the steering gain.

When integral feedback is added, the body rate command vector is obtained by the operation

$$\bar{\omega}_c = \overset{*}{PB}\left[K_{steer}\ ALPH\bar{A}STEER + K_{int}\ ALPH\bar{A}INT\right] \qquad (4)$$

where K_{int} is the integral steering gain and $ALPH\bar{A}INT$ is computed each steering cycle from

$$ALPH\bar{A}INT(nT_s) = ALPH\bar{A}INT(n-1)T_s + ALPH\bar{A}STEER\ T_s \qquad (5)$$

where T_s is the sampling time of the steering loop.

The incremental attitude command vector to the autopilot, $THCM\bar{D}INC$, is computed by

$$THCM\bar{D}INC = \bar{\omega}_c T_{DAP} \qquad (6)$$

where T_{DAP} is the sampling time of the digital autopilot.

The nominal cycle times for the guidance, steering, and autopilot times are given below in Table 2.

Table 2. Nominal cycle times.

System	Element	Cycle Time	No. of DAP Cycles
Guidance	(T_G)	1.35 sec	45
Steering	(T_S)	0.45 sec	15
Autopilot	(T_{DAP})	0.03 sec	1

The autopilot computes an error signal by comparing measured attitude increments with the commanded attitude increments. The compensation filter provides gain and phase stabilization to this conditionally stable system by modifying the open-loop gain and adding phase lead to meet the design requirements given in Section 2.1. The transfer function of the compensator is given below

$$D(w) = K_w \left[\frac{w + w_2}{w + w_3} \right] \quad \text{w Domain}$$

With the substitution $w = \frac{z - 1}{z + 1}$, the function becomes

$$D(z) = K_z \left[\frac{1 - A_2 z^{-1}}{1 - B_2 z^{-1}} \right] \quad \text{z Domain}$$

where

$$K_z = \left[\frac{w_3}{w_2} \; \frac{1 + w_2}{1 + w_3} \right] K_w$$

$$A_2 = \frac{1 - w_2}{1 + w_2}; \quad B_2 = \frac{1 - w_3}{1 + w_3}$$

The autopilot DC gain is continually modified as a function of the magnitude of the thrust acceleration in order to maintain the open loop gain at a constant value as described in Section 2.6.

1.3 The Inertial Measurement Unit

The Inertial Measurement Unit (IMU) used in this study, is the Advanced Inertial Reference System (AIRS) described in detail in Section 4. This system provides measured body-angle increments as a feedback signal to the autopilot loop and accelerometer (assumed ideal) sensed velocity increments as a feedback signal to the guidance and steering systems. The attitude feedback approach is to initialize the attitude errors at the beginning of the burn and then to update the attitude errors approximately by adding to the attitude error for each body axis the difference between the commanded body-angle increment and the AIRS measured body-angle increment for that axis every autopilot cycle. The advantages of this approach are (1) it requires only one time-consuming computation of the platform-to-body transformation matrix from measured band angles for error initialization at the beginning of the burn, and (2) it also minimizes the computation time by precisely undating the band-angle-increment-to body-angle-increment matrix only every steering cycle.

After initialization, computation time is minimized by using feedback body-angle increments determined by multiplying the measured band angle increments over autopilot cycle by a band-angle-to-body-angle transformation matrix. This incremental transformation matrix requires less computation time than computing the platform-to-body transformation matrix, and does not have to be updated precisely every autopilot cycle.

SECTION 2

STEERING AND AUTOPILOT ANALYSIS

2.1 Steering and Autopilot Design Parameters

The overall function of the steering and autopilot combination is to minimize steering errors without exceeding actuator position or rate limits. The steering errors are generally reflected by velocity-to-be-gained errors at thrust termination. Another requirement is that the vehicle response be stable throughout the burn and particularly near the end, when the steering methods used in this study are inherently unstable. As we shall see, the steering mode must be switched to a "terminal" mode near the end of the burn, and it may also be advantageous to vary the autopilot parameters at this time.

In terms of specific autopilot design goals, we shall specify the phase margin, gain margin, and peak closed-loop gain. In addition we shall also specify residual V_g "goals". These design paramters are given in Table 3 below.

Table 3. Design parameters.

Parameter	Design Value
Open-Loop Gain Margin	6 dB
Open-Loop Phase Margin	30 degrees
Peak Closed-Loop Gain	6 dB
Residual Velocity to be Gained	<10 fps

2.2 Steering Modes

The vehicle may be operated in either of two distinct steering modes; V_g (velocity-to-be-gained) steering, or fuel depletion steering. In V_g steering, the vehicle thrust vector is pointed in the direction of the velocity-to-be-gained vector, which is computed by the guidance

computer as the difference between the required velocity, $\bar{V}_{req}$, and the present velocity, $\bar{V}$. In vector notation, this is again

$$\bar{V}_g = \bar{V}_{req} - \bar{V} \tag{1}$$

(Repeated)

The required velocity at a given point on the trajectory is calculated by solving the Lambert problem, given the present and desired final radius vectors, and the desired time of flight. The vehicle radius vector is offset to account for the nonimpulsive nature of the thrust. This guidance scheme is discussed in detail in Section 3. V_g steering assumes that the vehicle has thrust cut-off capability or that the thrust may be modulated so that the ΔV capability of the vehicle is exactly equal to the magnitude of the velocity-to-be-gained. In V_g steering, then, the vehicle is steered such that the thrust vector is pointed along the velocity-to-be-gained vector and the engine is shut off when the magnitude of the velocity-to-be-gained goes to zero. Since all three components of the $\bar{V}_g$ vector do not normally go to zero at exactly the same time, the engine is usually shut down when the component of $\bar{V}_g$ along the vehicle x-axis goes to zero.

If the vehicle has a ΔV capability which is greater than the magnitude of the velocity-to-be-gained for a given burn, and the engine cannot be shut off, then fuel depletion steering must be used. In this steering mode, the thrust vector is rotated at an angle to the $\bar{V}_g$ vector to "waste" the excess fuel. As the magnitude of the ΔV capability is reduced, the angle between the thrust vector and the velocity-to-be-gained vector goes to zero in such a way that when the fuel depletion angle is zero, the remaining ΔV capability and the velocity-to-be-gained are also zero. The geometrical relationships of fuel depletion steering are shown in Figure 4. After the vehicle rotates to the initial fuel depletion angle, the rate of change of the fuel depletion angle is almost constant. As shown in Figure 4, the vehicle thrust vector rotates through an angle 2θ during the burn, so this rate is approximately $2\theta/T_{BURN}$.

When fuel depletion steering is initiated, a plane containing the radius vector $\bar{r}$, the $\bar{V}_g$ vector, and the normal to the $\bar{V}_g$ vector, the unit vector $\hat{B}$, is defined in velocity space. The fuel depletion angle θ is computed from Equation (7) which is derived in Appendix 4

$$\frac{\sin\theta}{\theta} = \frac{V_g}{V_{cap}} \tag{7}$$

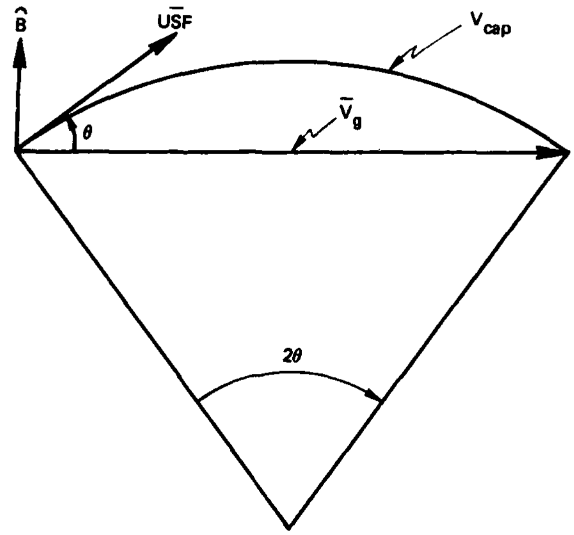

Figure 4. Geometry of the fuel depletion arc.

This relationship is obtained from the geometry of the arc of a circle where 2θ is the interior angle subtended by a chord line, represented by V_g, and the arc length is equal to the magnitude of the ΔV capability.

The desired thrust vector, $U\bar{S}F$, is computed from θ, $\bar{V}_g$, and $\hat{B}$ using the equation

$$U\bar{S}F = \cos\theta \text{ Unit } (\bar{V}_g) + \sin\theta\ (\hat{B}) \tag{8}$$

The USF vector is always tangent to the circular arc and forms the angle θ with the $\bar{V}_g$ vector.

The computation of the fuel depletion angle θ may be simplified by expanding $(\sin\theta)/\theta$ in a power series and neglecting terms of order θ^4. This gives the simpler expression given in Equation (9)

$$\theta \cong \sqrt{6(1 - V_g/V_{cap})} \tag{9}$$

A comparison of the resulting θ using this method and the exact method and the sensitivity of the fuel depletion angle to small V_{cap} changes are given in Table 4. Note that the angle computed by Equation (9) is always less than the exact method.

Table 4. Sensitivity of the fuel depletion angle θ to a small change in the ratio of V_g/V_{cap}.

	V_g/V_{cap}	θ (deg) exact	Δθ (deg)	% Change	θ (deg) simplified
+2%	0.816	61.99	-2.82	-4.35	-
Nominal	0.800	64.81	-	-	62.76
-2%	0.784	67.54	2.73	4.21	-
+2%	0.918	40.70	-4.37	-9.70	-
Nominal	0.900	45.07	-	-	44.38
-2%	0.882	49.10	4.03	8.94	-
+2%	0.969	24.83	-6.79	-21.47	-
Nominal	0.950	31.62	-	-	31.38
-2%	0.9310	37.26	5.64	17.84	-
+2%	0.997	2.81	-17.10	-85.89	-
Nominal	0.980	19.91	-	-	19.85
-2%	0.960	28.10	8.19	41.14	-

2.3 Steering Stability Analysis

The stability characteristics of the steering modes presented in this study are conveniently analysed in terms of the frequency response characteristics of the pitch (or yaw) autopilot channel and steering loops. As previously stated, we assume that the roll orientation is constant, and translational motion occurs in the pitch (or yaw) plane.

The single plane analytical model to be used in this analysis is presented in Figure 5. This model represents the steering effects in terms of two sampled-data transfer functions $F_1^*(s)$ and $F_2^*(s)$ which are based on the steering sample period T_s. The key definitions, assumptions, and approximations of this model are:

(1) The autopilot and steering systems are approximated by linear perturbation equations where the vehicle rotation, θ, the engine deflection δ, and the inertial rotation of the thrust vector, λ_V, have zero steady-state values. The steady-state position of the vehicle center of mass is assumed to be on the vehicle x-axis, and the steady-state directions of the commanded and actual thrust vectors are assumed to be along the steady-state inertial orientation of the vehicle x-axis.

AUTOPILOT LOOP APPROXIMATE CONTINUOUS MODEL

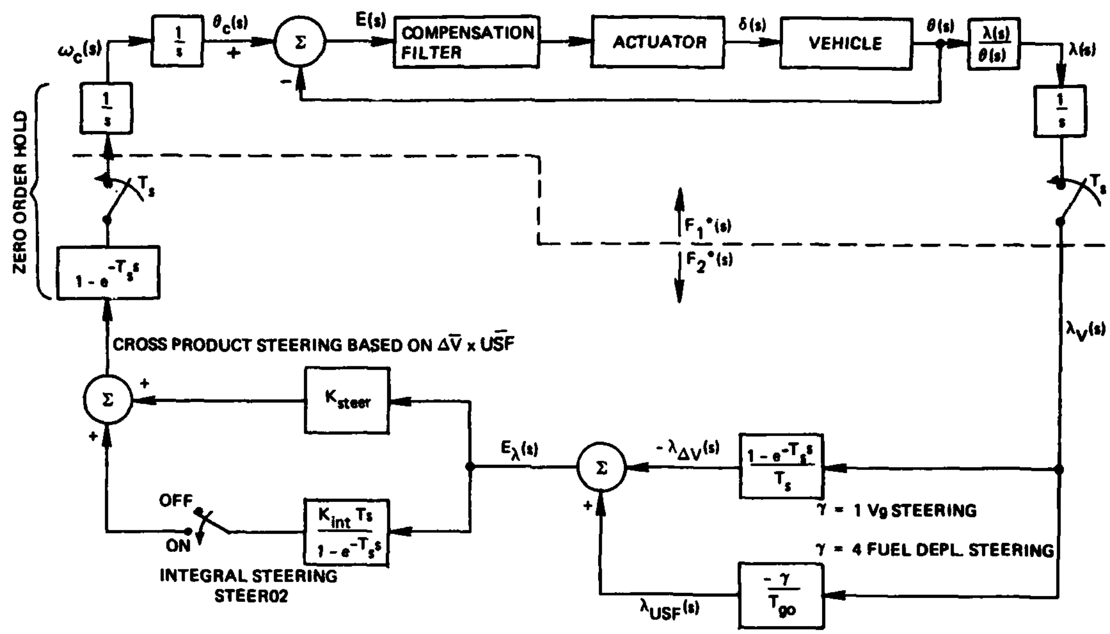

Figure 5. Autopilot and steering loop analytical model.

(2) Since the autopilot sampling period T_{DAP} is much shorter than the steering period T_s, it is possible to treat the autopilot as continuous and to combine the autopilot function $\theta(s)/\theta_c(s)$ with other factors to obtain

$$F_1(s) = \frac{1}{s^3}\left(\frac{\theta(s)}{\theta_c(s)}\right)\left(\frac{\lambda(s)}{\theta(s)}\right)$$

(3) It can be shown that the sampled function $F_1^*(s)$ which is expressed as

$$F_1^*(s) = \frac{1}{T_s}\sum_{n=-\infty}^{\infty} F_1(s + jn\omega_s)$$

can be approximated by the n=0 term

$$F_1^*(s) \cong \frac{1}{T_s} F_1(s)$$

and so

$$F_1^*(s) \cong \left(\frac{1}{T_s}\right)\left(\frac{1}{s^3}\right)\left(\frac{\theta(s)}{\theta_c(s)}\right)\left(\frac{\lambda(s)}{\theta(s)}\right)$$

This approximation can be justified on the basis that the $1/s^3$ term in $F_1(s)$ causes the $|n|>0$ terms in $F_1^*(j\omega)$ to be small compared to the n=0 term in the frequency range less than half the steering sampling frequency.

(4) Starting with the approximation that $F_1^*(s) = 1/T_s\, F_1(s)$ and noting that the resulting steering loop transfer function is given by

$$F_1^*(s)\; F_2^*(s) = \left[\left(\frac{1}{T_s}\right)\left(\frac{1}{s^3}\right)\left(\frac{\theta(s)}{\theta_c(s)}\right)\left(\frac{\lambda(s)}{\theta(s)}\right)\right] F_2^*(s)$$

it can be reasoned that the effect of this transfer function can be equivalently represented by treating the steering as merely an addition to the unity-gain attitude feedback of the autopilot. This yields a modified "total" open-loop function of the autopilot which is expressed as

$$G_{TOT}(s) = \left[\frac{\theta(s)}{E(s)}\right]\left[1 - \left(\frac{1}{T_s}\right)\left(\frac{1}{s^3}\right)\left(\frac{\lambda(s)}{\theta(s)}\right) F_2^*(s)\right] \qquad (9)$$

(5) The sampled-data transfer function $F_2^*(s)$ is expressed, as shown in Figure 5, in terms of the sampled integral λ_V of the thrust angle λ and in terms of the sensed-velocity angle $\lambda_{\Delta V}$ and commanded thrust angle λ_{USF}.

(6) The sensitivity of the angle λ_{USF} of the commanded thrust direction to the sampled angle λ_V of the integral of the thrust angle λ is approximately expressed as the ratio γ/T_{go}, where γ=1 for V_g steering and γ=4 for fuel depletion steering, and where T_{go} is the time-to-go. The derivation of these sensitivities is presented in Appendix A4 and Section 3.3.

(7) An approximate expression for $\lambda(s)/\theta(s)$ is given in Eq. (A-12) of Appendix A3. It can be shown that for the vehicle parameters used in this study that $\lambda(s)/\theta(s) \cong 1$, and this assumption will be made for the purposes of the following analysis.

We now consider two steering models, STEERθ1 (shown in Figure 6) in which the gain of the integral path of the steering law is set to zero and STEERθ2 (shown in Figure 7) which includes the integral path. In case STEERθ1, the function $F_2^*(s)$ is given by

$$F_2^*(s) = -K_{steer}\left(1 - e^{-T_s s}\right)\left\{\frac{1 - e^{-T_s s}}{T_s} + \frac{\gamma}{T_{go}}\right\}$$

Assume for this case that T_{go} is sufficiently large such that γ/T_{go} can be neglected

then

$$F_2^*(s) \cong -K_{steer}\frac{\left(1 - e^{-T_s s}\right)^2}{T_s}$$

Now, $\left(1 - e^{-T_s s}\right)$ can be transformed first to the z-domain-and then to the w-domain by the substitutions

$$e^{-T_s s} = z^{-1}$$

and

$$z^{-1} = \frac{1 - w}{1 + w}$$

Therefore

$$F_2^*(s) = -K_{steer}\frac{4}{T_s}\left(\frac{w}{1 + w}\right)^2$$

w is related to real frequency, ω, by the relationship

$$w = j\tan\left(\frac{\omega T_s}{2}\right)$$

Assume that the steering loop crossover frequency is much smaller than the half-steering loop sampling frequency. *Then for the region of* frequencies of interest

$$w \simeq j\omega\frac{T_s}{2} = \frac{T_s s}{2}$$

Then, $F_2^*(s)$ can be approximated as

$$F_2^*(s) \approx -K_{steer} \, T_s \frac{s^2}{(1 + T_s s)}$$

The modified total open-loop function then becomes

$$G_{TOT} = \left[\frac{\theta(s)}{E(s)}\right]\left[1 + \frac{\lambda(s)}{\theta(s)} K_{steer} \frac{1}{s(1 + T_s s)}\right]$$

If we make the further approximations that $T_s s << 1$ and $\frac{\lambda(s)}{\theta(s)} \approx 1$

then

$$G_{TOT} \approx \left[\frac{\theta(s)}{E(s)}\right]\left[1 + \frac{K_{steer}}{s}\right] = \frac{\theta(s)}{E(s)} \frac{s + K_{steer}}{s} \qquad (10)$$

This simplified steering loop model is used in Section 2.4 to select the autopilot parameters in the normalized design process. The selection of the value of K_{steer} is dependent on the design of the autopilot and its desired crossover frequency, since we desire the frequency of the steering loop to be significantly lower than the autopilot crossover frequency.

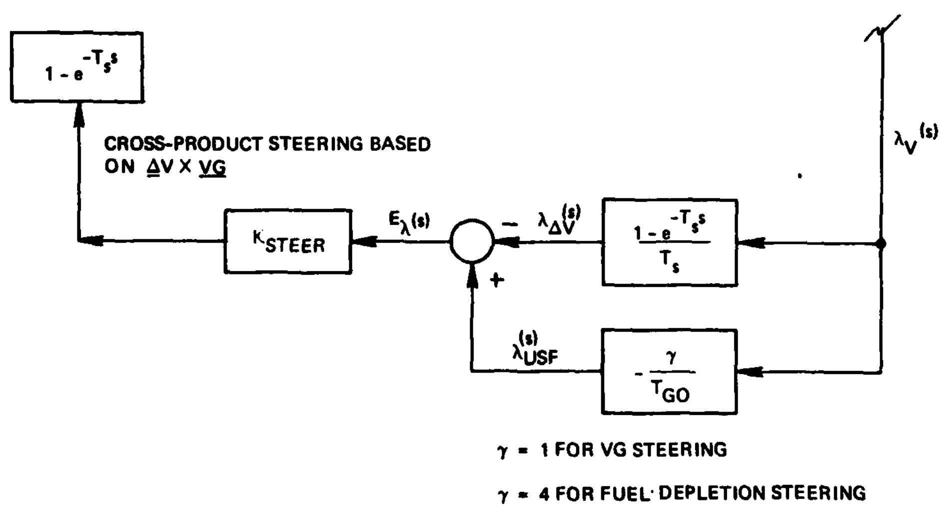

Figure 6. Analytical steering model - case STEER01.

In the second steering model, (STEER02) to be considered, the effect of adding integral feedback to the proportional loop will be considered. The integral feedback is added to reduce the steady-state errors due to the approximately constant rate command during fuel depletion steering. It will be shown how the integral gain, K_{int}, can be selected based on K_{steer}. The STEER02 model is described in Figure 7. For this case the function $F_2^*(s)$ is given by

$$F_2^*(s) = -\left[K_{steer} + \frac{K_{int}\,T_s}{\left(1 - e^{-T_s s}\right)}\right]\left(1 - e^{-T_s s}\right)\left[\frac{1 - e^{-T_s s}}{T_s} + \frac{\gamma}{T_{go}}\right]$$

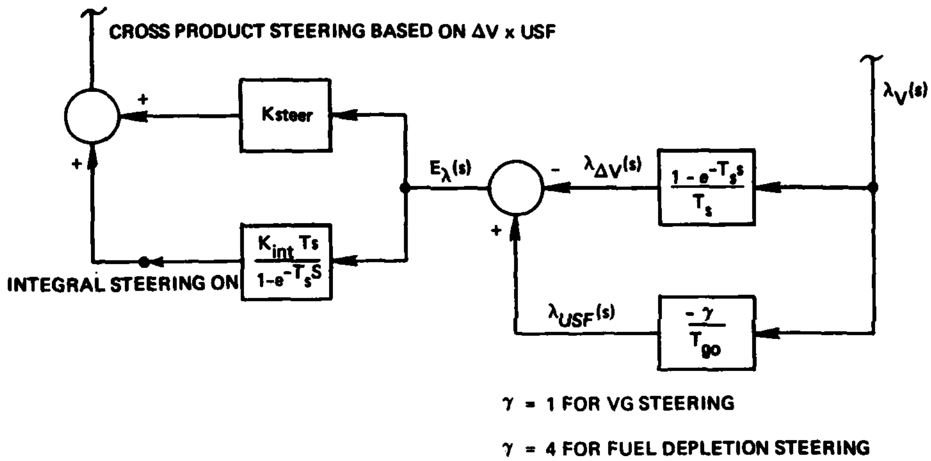

Figure 7. Analytical steering model - Case STEER02.

If the same assumptions are made as in the case of STEER01, then $\left(1 - e^{-T_s s}\right)$ is again replaced by sT_s and γ/T_{go} is assumed negligible. THE STEER02 steering model of Figure 7 reduces to that shown in Figure 8 and $F_2^*(s)$ is given by

$$F_2^*(s) = -sT_s\left(K_{steer}\,s + K_{int}\right)$$

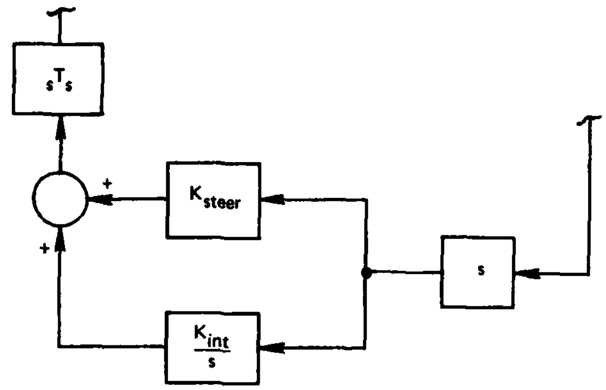

Figure 8. Simplified analytical model STEER02.

For the assumption that $\lambda(s)/\theta(s) \approx 1$, the modified total open-loop function (for which the unity-gain attitude feedback is added to the steering loop feedback) then becomes

$$G_{TOT}(s) = \left[\frac{\theta(s)}{E(s)}\right]\left[1 + \frac{K_{steer}\ s + K_{int}}{s^2}\right]$$

$$= \left[\frac{\theta(s)}{E(s)}\right]\left[\frac{s^2 + K_{steer}\ s + K_{int}}{s^2}\right] \quad (11)$$

If the second order numerator is expressed in the "standard" second order form

then

$$s^2 + K_{steer}\ s + K_{int} \equiv s^2 + 2\zeta\omega_n s + \omega_n^2$$

Therefore

$$K_{steer}^2 = 4\zeta^2\omega_n^2 = 4\zeta^2\ K_{int}$$

Select a damping ratio for the steering loop of $\zeta = 0.5$.

Then

$$K_{int} = K_{steer}^2$$

This relationship will be used to determine K_{int} after K_{steer} has been determined from the normalized compensation design.

Finally, STEER02 can be modified to include the case near the end of the burn when T_{go} becomes small. In this case, the function $F_2{}^*(s)$ is approximated by

$$F_2{}^*(s) \approx -T_s \left[K_{steer}\, s + K_{int}\right]\left[s + \frac{\gamma}{T_{go}}\right]$$

Therefore

$$G_{TOT}(s) \approx \left[\frac{\theta(s)}{E(s)}\right]\left[1 + \frac{K_{steer}\, s^2 + \left(\frac{K_{steer}\,\gamma}{T_{go}} + K_{int}\right) s + \frac{\gamma\, K_{int}}{T_{go}}}{s^3}\right]$$

$$= \left[\frac{\theta(s)}{E(s)}\right]\left[\frac{s^3 + K_{steer}\, s^2 + \left[\frac{K_{steer}\,\gamma}{T_{go}} + K_{int}\right] s + \frac{\gamma\, K_{int}}{T_{go}}}{s^3}\right] \tag{12}$$

Approximations for the modified total open-loop steering and control transfer function have been derived for three different sets of assumptions for the steering loop. These are summarized as follows:

<u>Assumptions for all 3 cases</u>:

(1) For frequency range below steering loop crossover frequency, the expression $\left(1 - e^{-T_s s}\right)$ can be approximated by $T_s s$

(2) $\frac{\lambda(s)}{\theta(s)} \approx 1$

Case I: Steering Model STEER01—No integral path in steering law.

Assumption: T_{go} large $\left(\frac{\gamma}{T_{go}} \text{ negligible}\right)$

$$G_{TOT}(s) = \frac{\theta(s)}{E(s)} \cdot \frac{\left(s + K_{steer}\right)}{s}$$

Case II: Steering Model STEER02—Proportional and integral paths in steering law.

Assumption: T_{go} large $\left(\frac{\gamma}{T_{go}} \text{ negligible}\right)$

$$G_{TOT}(s) = \left[\frac{\theta(s)}{E(s)}\right]\left[\frac{s^2 + K_{steer}\, s + K_{int}}{s^2}\right]$$

(K_{int} is chosen to be equal to K^2_{steer} corresponding to a damping ratio of 0.5)

Case III: Steering Model STEER02—Proportional and integral paths in steering law.

Assumption: T_{go} small $\left(\frac{\gamma}{T_{go}} \text{ term cannot be neglected}\right)$

$$G_{TOT}(s) = \left[\frac{\theta(s)}{E(s)}\right]\left[\frac{s^3 + K_{steer}\, s^2 + \left[\frac{K_{steer}\,\gamma}{T_{go}} + K_{int}\right] s + \frac{\gamma\, K_{int}}{T_{go}}}{s^3}\right]$$

2.4 Normalized Compensation Design

In this section, we develop a design approach that is based on normalizing the system parameters such that the characteristics of the autopilot and steering loop become independent of the autopilot crossover frequency. The result is a general expression for the simplified open-loop transfer function that is used to select values of normalized gain and system delays that provide the desired response. After these values are selected, the system parameters are readily determined for any desired value of autopilot crossover frequency.

To develop this expression, we write the open-loop transfer function of the combined compensator, actuator and vehicle derived in Section 1.1 as

$$G(s) = \frac{((s/\omega_2) + 1)K_c K_v e^{-T_o' s}}{s^2} \tag{13}$$

Equation (13) is obtained by treating the pole of the rigid body compensator, ω_3, and the actuator transfer function as pure delays since they

occur at high frequencies relative to the desired range of crossover frequencies. These lags are lumped into T_o' along with the sampling and computational delays. If we then let

$$s' = s/\omega_2; \; K_o' = \frac{K_c K_v}{(\omega_2)^2}$$

and

$$\phi_o' = \omega_2 T_o'$$

we can rewrite (13) as

$$G'(s) = \frac{(s'+1)\, K_o' e^{-\phi_o' s'}}{s'^2} \tag{14}$$

We then obtain the open and closed-loop frequency response of (14) and then plot the locus of maximum values of the closed-loop gain M, M_p against K_o' and ϕ_o'. This data is tabulated in Table 5 and plotted in Figure 9 for autopilot loop (without steering). Figure 9 indicates that, in order to keep M_p less than 6 dB, for $\phi_o' = 0.30$, the allowable range of K_o' is approximately $1.2 \leq K_o' \leq 1.75$. For $\phi_o' = 0.25$, K_o' has an allowable range of $0.8 \leq K_o'$. If we select a nominal $K_o' = 1.4$, for $\phi_o' = 0.30$, the closed-loop gain margin is 0.12 dB and for $\phi_o' = 0.25$, the closed-loop gain margin is 1.03 dB.

We now turn to the design of the system including steering effects. For the purpose of this design process, we will use the simple cross-product steering transfer function developed in Section 2.3. The incorporation of this simplified model gives an open-loop transfer function shown in Equation (15).

$$G(s) = \left[\frac{s+\omega_1}{s}\right]\left[\frac{(s/\omega_2 + 1) K_c K_v e^{-T_o' s}}{s^2}\right] \tag{15}$$

Again, we normalize this function to the frequency of the rigid body compensator zero, ω_2, and the result is

$$G'(s) = \left[\frac{s' + \omega_1'}{s'}\right]\left[\frac{(s'+1) K_o' e^{-\phi_o' s'}}{s'^2}\right] \tag{16}$$

Table 5. Minimum values of M_p (peak closed-loop gain) for $\omega_1' = 0$.

ϕ_0' Delay \ K_0' Gain	0.8	1.0	1.2	1.4	1.6	1.8	2.0
0.20	5.39	4.91	4.56	4.21	4.08	3.90	3.81
0.25	6.00	5.50	5.20	4.97	4.84	4.79	4.82
0.30	6.62	6.27	6.00	5.88	5.89	6.06	6.35
0.35	7.49	7.11	7.02	7.09	7.39	7.90	8.70

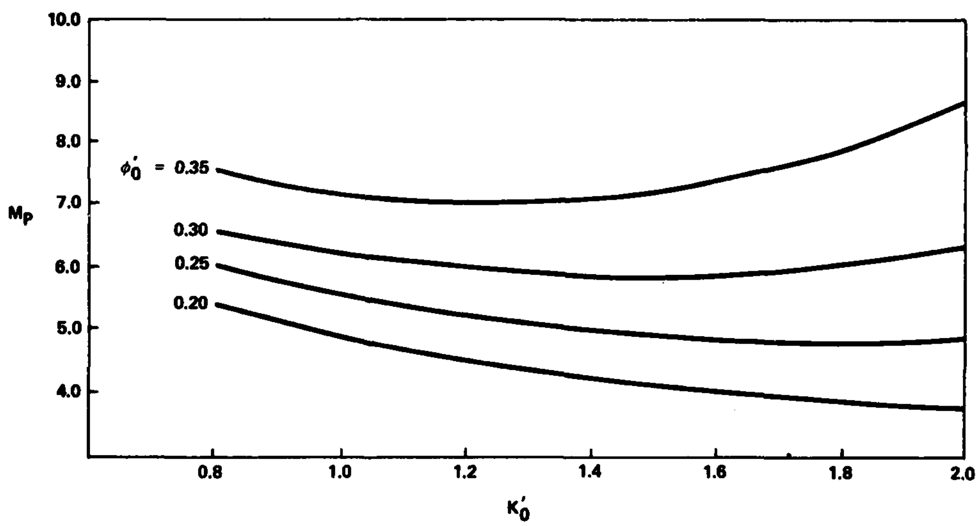

Figure 9. Minimum values of M_p for $\omega_1' = 0.0$.

where

$$s' = s/\omega_2 \qquad \omega_1' = \omega_1/\omega_2$$

$$K_o' = \frac{K_c K_v}{\omega_2^2} \qquad \phi_o' = \omega_2 T_o'$$

As in the case without steering, this design will result in a 0 dB crossover frequency which is proportional to ω_2. Again, we obtain the open and closed-loop frequency response of (16) and plot the locus of peak closed-loop gain, M_p versus K_o' and ϕ_o'. These results are tabulated in Table 6 and graphed in Figure 10, and show that, with steering included, the maximum value of ϕ_o' that gives $M_p \leq 6$ dB is now 0.25. For $K_o' = 1.4$, the closed-loop gain margin is 0.10 dB for $\phi_o' = 0.25$ and 0.91 dB for $\phi_o' = 0.20$.

If we now select a ratio of the steering frequency to the frequency of the compensator zero, ω_1/ω_2, of 0.10, for example, we can determine the approximate crossover frequency of the "real" transfer function as a function of the normalizing frequency ω_2.

Equation (16) is written as

$$G'(s) = \frac{K_o'(s' + \omega_1/\omega_2)(s' + 1)e^{-\phi_o' s'}}{s'^3} \tag{17}$$

With $\omega_1/\omega_2 = 0.1$, we can safely neglect the gain contribution of the steering loop at the expected 0 dB crossover frequency of the autopilot loop and set $|G'(j\omega)| = 1$.

$$G_o(s) \cong \frac{K_o'(s' + 1)e^{-\phi_o' s'}}{s'^2}$$

and squaring the magnitude of $G_o(j\omega)$

$$(G_o(j\omega))^2 = \frac{K_o'^2(\omega'^2 + 1)}{\omega'^4} = 1$$

$$\omega'^4 = K_o'^2(\omega'^2 + 1) = K_o'^2\omega'^2 + K_o'^2 \tag{18}$$

Table 6. Minimum values of M_p (peak closed loop gain for $\omega_1' = 0.1$.

K_0' Gain

ϕ_0' Delay	K \ ϕ_0'	1.0	1.2	1.4	1.6	1.8	2.0	2.2
	0.20	6.06	5.50	5.09	4.78	4.57	4.41	4.31
	0.25	6.75	6.25	5.90	5.66	5.54	5.51	5.60
	0.30	7.67	7.19	6.96	6.87	6.96	7.22	7.70
	0.35	8.76	8.40	8.35	8.57	9.02	9.80	>10

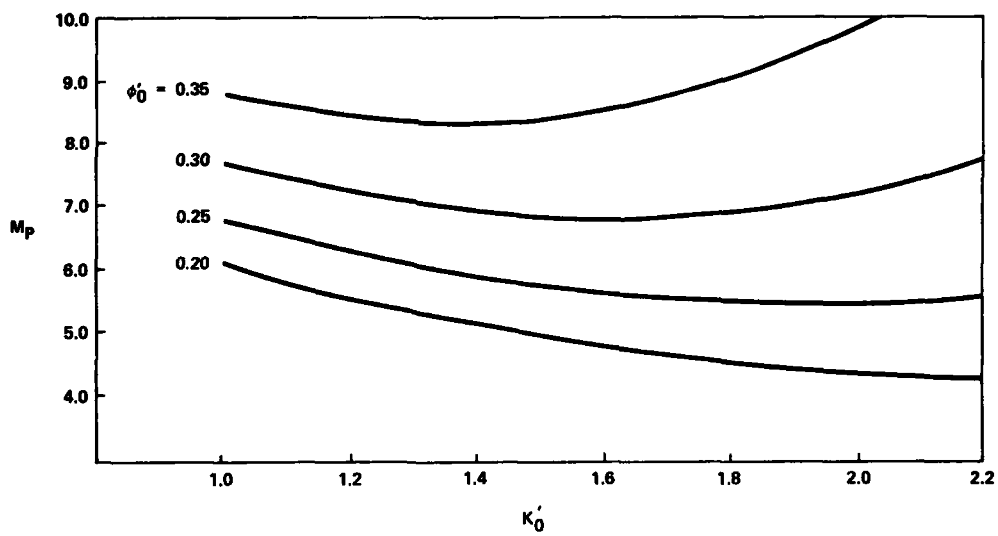

Figure 10. Minimum values of M_p for $\omega_1' = 0.1$.

and

$$-\frac{1}{K_o'^2}\omega'^4 + \omega'^2 + 1 = 0$$

which is written as

$$-\frac{1}{K_o'^2}(\omega'^2)^2 + (\omega'^2) + 1 = 0$$

The positive solution for ω' is

$$\omega' = \left[\frac{K_o'^2}{2} + \left(\frac{K_o'^4}{4} + K_o'^2\right)^{1/2}\right]^{1/2} \tag{19}$$

Now ω' can be solved for in terms of K_o'. These results are shown in Table 7.

Table 7. K_o' vs ω'.

K_o'	0.80	1.0	1.2	1.4	1.6	1.8	2.0
ω'	1.09	1.27	1.46	1.64	1.82	2.01	2.20

The crossover frequency, ω_{xo}, is given by

$$\omega_{xo} = \omega'\omega_2 \tag{20}$$

If we use the previously selected value of $K_o' = 1.4$, this gives $\omega' = 1.64$, and hence, ω_2 is determined for any desired crossover frequency (approximate). Once ω_2 is determined, all other system parameters are determined from Equation (16).

The determination of these specific parameters for autopilot crossover frequencies of 2, 5, and 8 rad/sec is given in Appendix A5. The results of these calculations are summarized in Tables 8, 9, and 10. From Table 8, we see that, if we restrict the lead ratio, ω_3/ω_2 to values less than 15, then a crossover frequency of 10 rad/sec is not attainable.

Table 8. Autopilot parameters.

Desired Crossover Frequency	s-Plane			w-Plane			w-Plane Filter Gain
ω_{x0}	ω_1	ω_2	ω_3	w_1	w_2	w_3	**K_c
2	0.12195	1.2195	5.9113	0.001829	0.01829	0.08867	0.10410
5	0.30488	3.0488	21.6606	0.004573	0.04573	0.3249	0.65066
5‡	0.60000	3.0488	15.000	0.09000	0.04573	0.22500	0.65066
8	0.48781	4.87805	64.8635	0.007317	0.073171	0.97295	1.66568
* 10	0.60976	6.09756	193.548	0.009146	0.091463	2.9032	>4

*For $\omega_{x0} = 10$; $\frac{\omega_3}{\omega_2} = 31.74 > 15$ (We assume that this lead ratio is too large to be obtained with a simple compensator.)

**For $K_v = 20$

‡Optimized design

Table 9. Z-domain filter coefficients.

DESIRED ω_{x0}	A_2	B_2	K_z
2.0	0.964072	0.837104	0.471993
5.0	0.912540	0.509548	3.6485
5.0‡	0.912540	0.632651	2.732
8.0	0.866636	0.013710	12.0475

‡Optimized design

Table 10. Comparison of design results.

Desired ω_{xo} (rad/sec)	Actual ω_{xo} (rad/sec)	Gain Margin (dB)	Phase Margin (deg)	Freq. at Phase Crossover (rad/sec)
2.0	1.9	20.12	34.6	9.4
5.0	4.9	12.59	32.5	15.6
5.0‡	4.8	12.70	27.0	13.3
8.0	7.3	9.2	30.6	20.9

‡Optimized design

For the specific point design to be used in this study, an autopilot crossover frequency of 5 rad/sec will be selected and evaluated. If this design can be shown to satisfy the responsiveness required by the steering techniques used, it will also have the additional benefit of reduced sensitivity to noise from the IMU relative to the 8 rad/sec autopilot.

2.5 Frequency Response

This section contains the frequency response plots of the uncompensated system, (Figures 11-13) the compensated system resulting from the normalized compensator design, (Figures 14-22) and various steering parameter effects. Also, the frequency response of the compensated system for the 5 rad/sec autopilot is "optimized" to obtain a desired closed loop gain over the maximum possible range of frequencies. Unless otherwise stated in these analyses, the nominal value of the steering loop parameters K_{steer} (steering gain), K_{int} (integral gain), T_{go} (time to go until the end of the burn), and T_s (sample period of the steering loop) are used. These are given in Table 11.

Table 11. Nominal steering loop parameters.

	K_{steer}	K_{int}	T_{go}	T_s
Normalized Design	0.30488	0.0930	60 sec	0.45 sec
Optimized Design	0.6000	0.3600	60 sec	0.45 sec

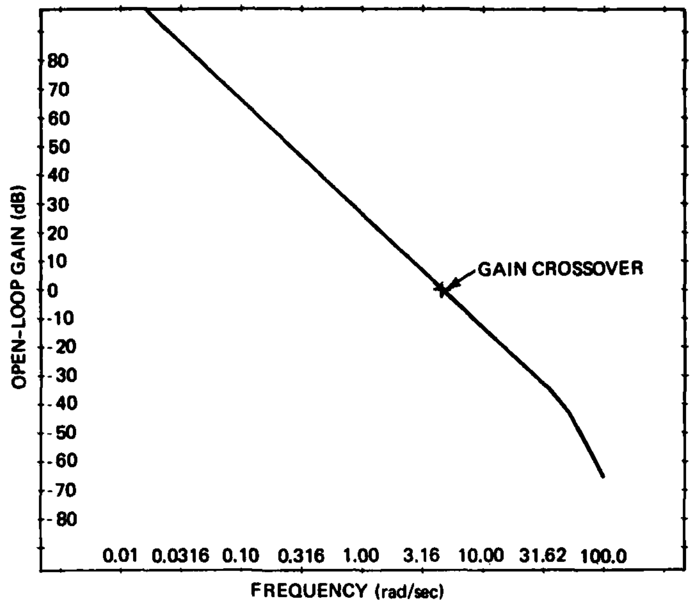

Figure 11. Gain vs frequency - uncompensated system.

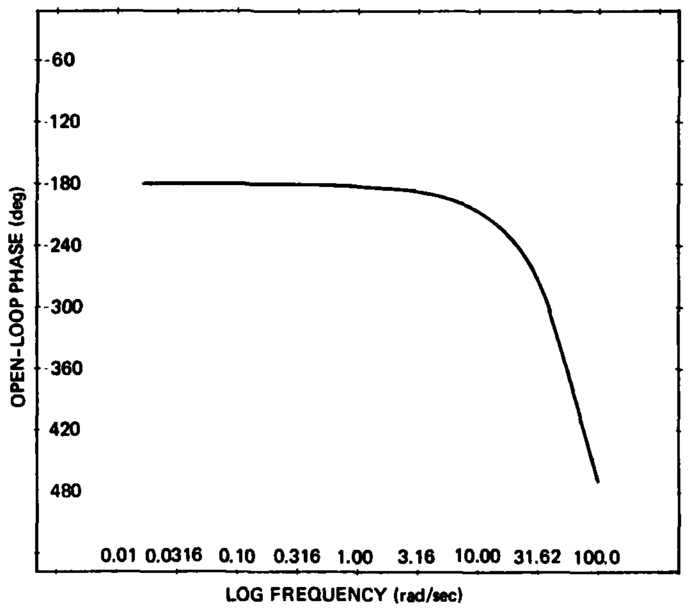

Figure 12. Phase vs frequency - uncompensated system.

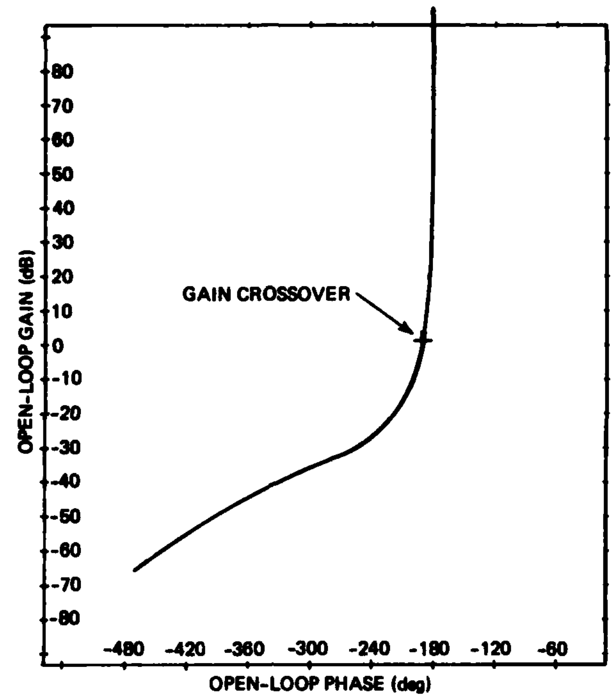

Figure 13. Gain vs phase - uncompensated system.

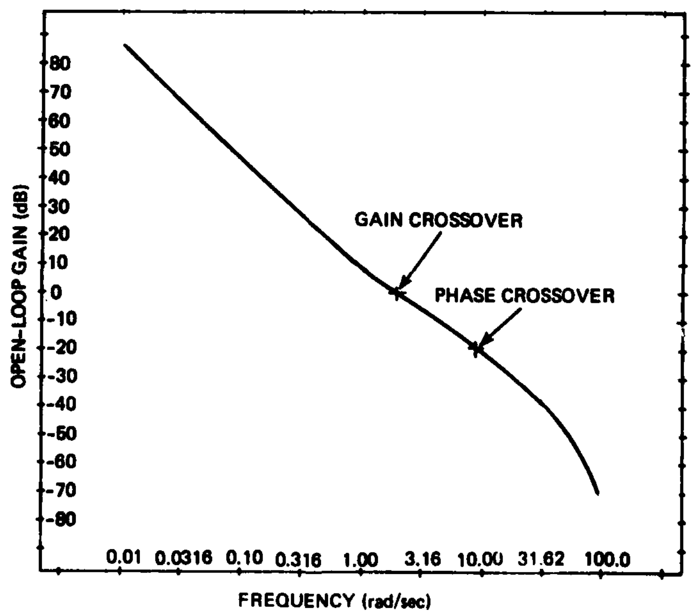

Figure 14. Gain vs frequency - ω_{xo} = 2 rad/sec.

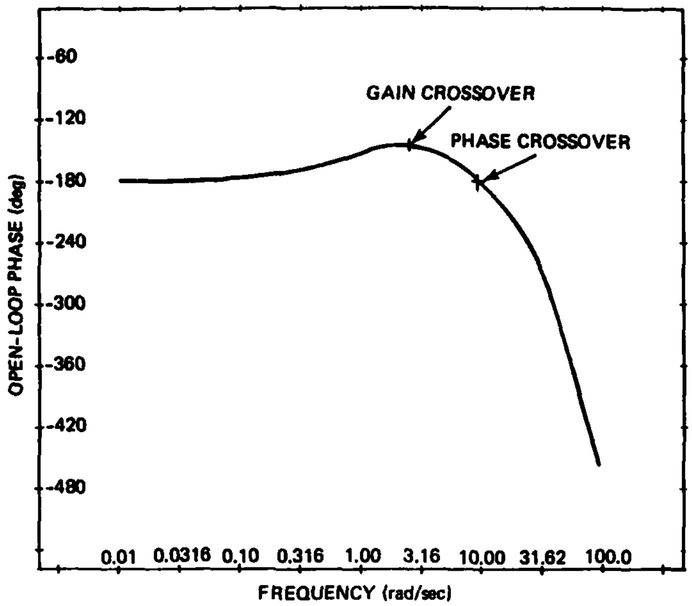

Figure 15. Phase vs frequency - ω_{xo} = 2 rad/sec.

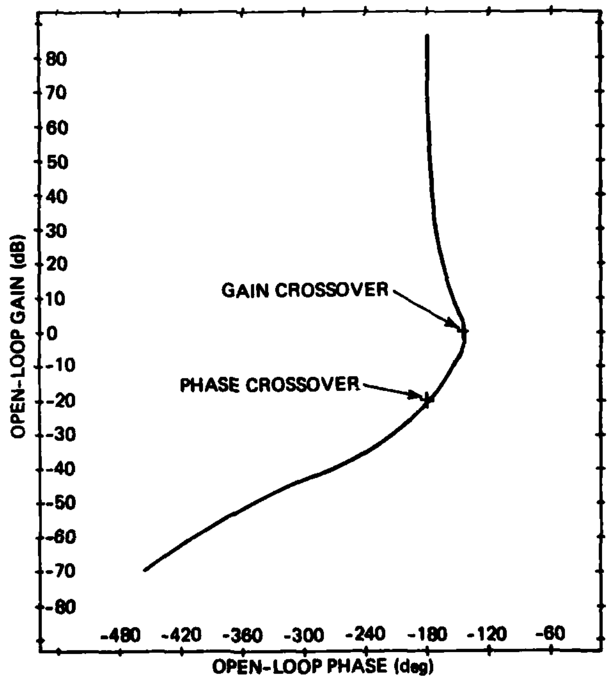

Figure 16. Gain vs phase - ω_{xo} = 2 rad/sec.

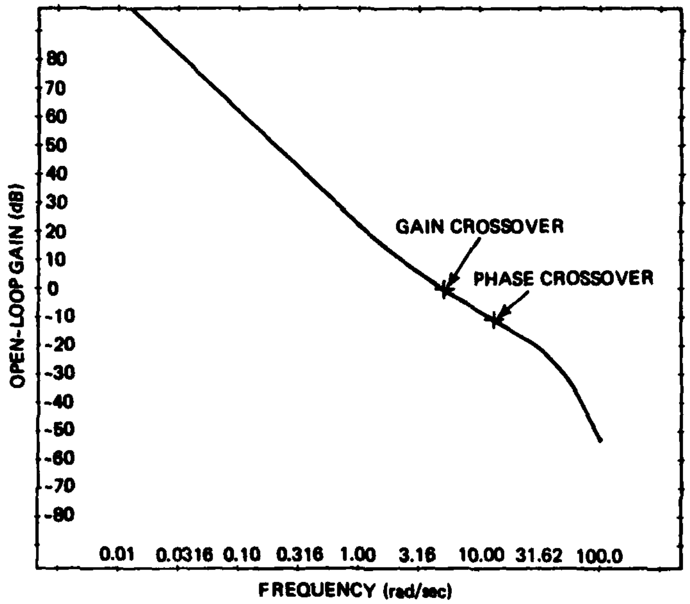

Figure 17. Gain vs frequency - ω_{XO} = 5 rad/sec.

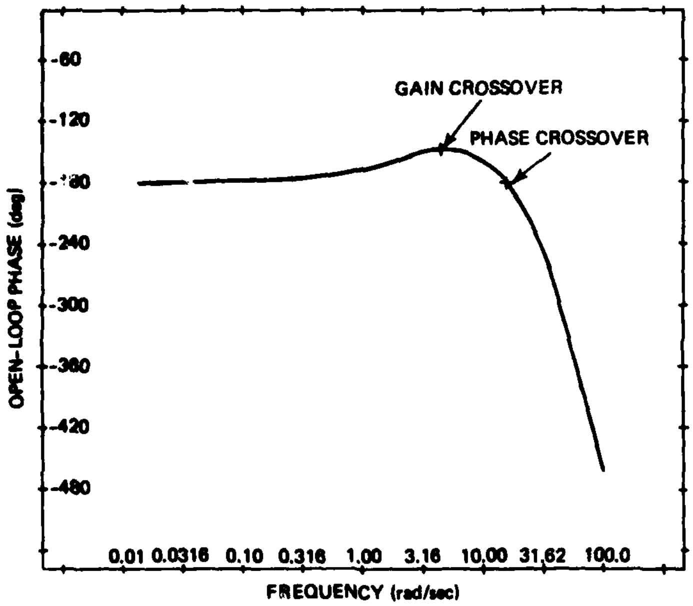

Figure 18. Phase vs frequency - ω_{XO} = 5 rad/sec.

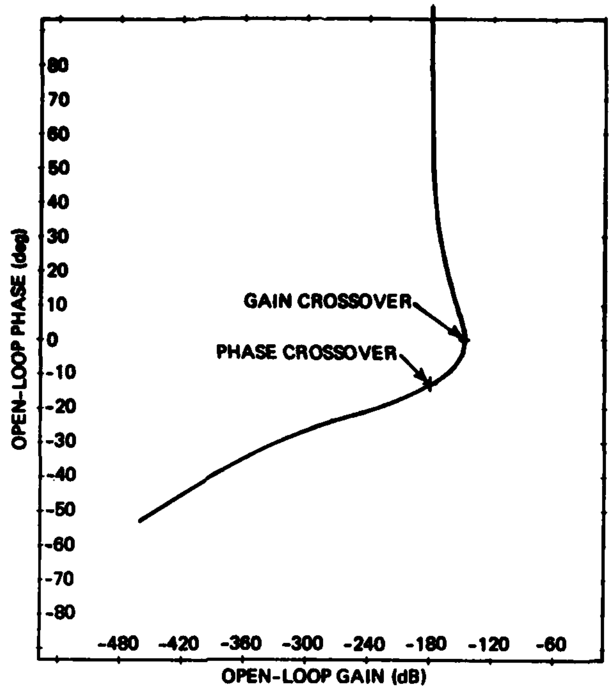

Figure 19. Gain vs phase - ω_{xo} = 5 rad/sec.

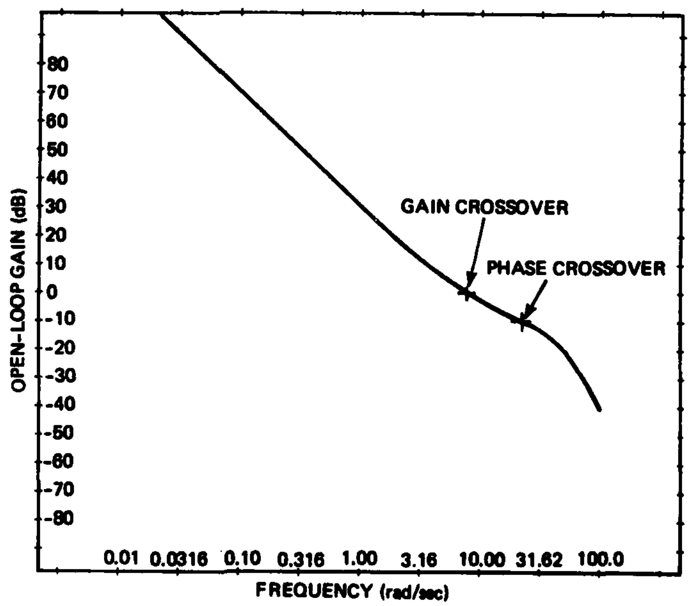

Figure 20. Gain vs frequency - ω_{xo} = 8 rad/sec.

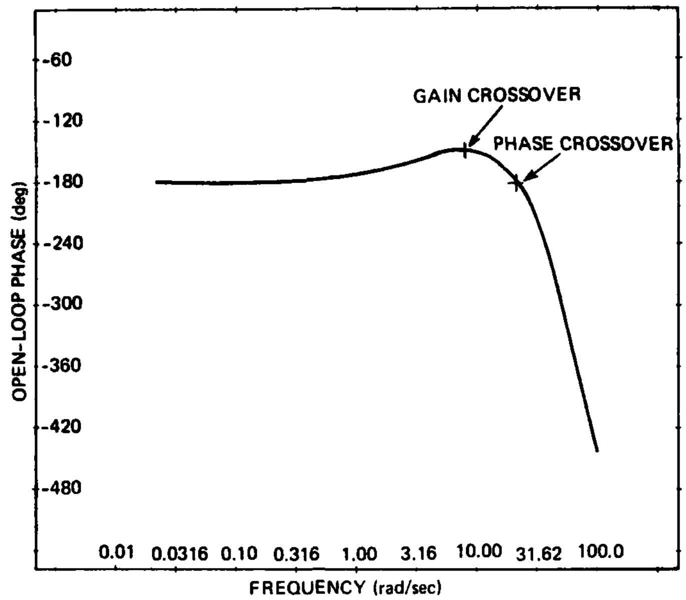

Figure 21. Phase vs frequency - ω_{xo} 8 rad/sec.

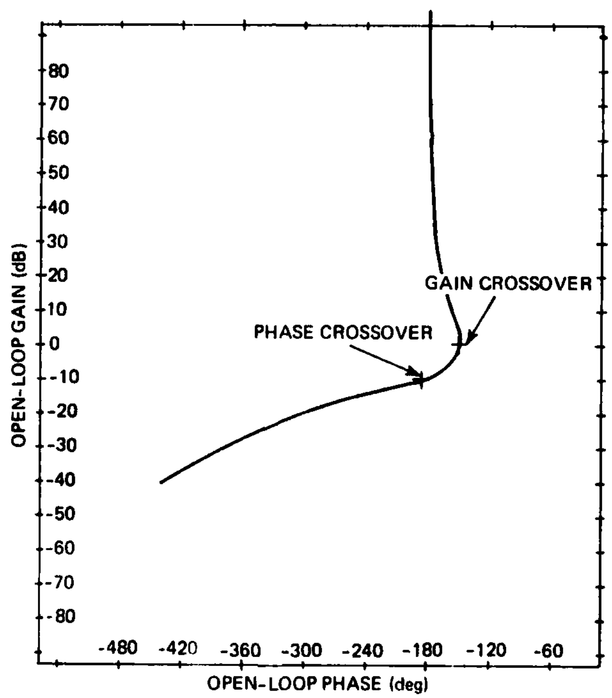

Figure 22. Gain vs phase - ω_{xo} = 8 rad/sec.

The frequency response of the steering models is obtained by using the exact steering representation from Figure 5 and substituting

$$1 - e^{-T_s s}\big|_{s = j\omega} = 1 - [\cos \omega T_s - j \sin \omega T_s]$$

If we now say

$$C_\omega = 1 - \cos \omega T_s$$

and

$$s_\omega = \sin \omega T_s$$

The total steering loop can be represented as

$$F_{steer}(s)\big|_{s = j\omega} = j\left(\frac{K_{steer}}{T_s^2\omega^3}\right)\left[s_\omega^2 + T_s C_\omega\left(\frac{K_{int}}{K_{steer}} + \frac{\gamma}{T_{go}}\right) - s_\omega\right]$$
$$+ \left[1 - \left(\frac{K_{steer}}{T_s^2\omega^3}\right)\left(2C_\omega s_\omega + \left(\frac{K_{int}}{K_{steer}} + \frac{\gamma}{T_{go}}\right)T_s s_\omega\right)\right] \qquad (21)$$

Equation (21) is used in determining the frequency responses given in Figures 23 through 32.

Figure 23 shows the frequency response of the combined system with no steering and with V_g steering with and without integral compensation. The other steering loop parameters are set to their nominal values. Note that in this frequency range there is very little difference in the two steering modes and both modes contribute phase lead at the autopilot crossover frequency. Figures 24 through 29 show the effects of changing the steering loop parameters (K_{int}, T_{go}, T_s) on the frequency response of the steering loop alone. Figure 24 shows that increasing K_{int} gives increased gain at very low frequencies, but more attenuation at about 1 rad/sec. Figure 25 shows that increasing K_{int} gives more phase lag at very low frequency, and slightly more phase lead near the autopilot crossover. The effects of decreasing the time-to-go are shown in Figures 26 and 27. The low frequency gain and phase lag from steering are increased significantly as $T_{go} \to 0$. Figures 28 and 29 show the effects of sampling period T_s for both steering modes. At low frequency, the effect of changing the sample period is almost negligible, and at the higher frequencies where it would become important, the effect of the other steering parameters causes the total effect of the steering to disappear.

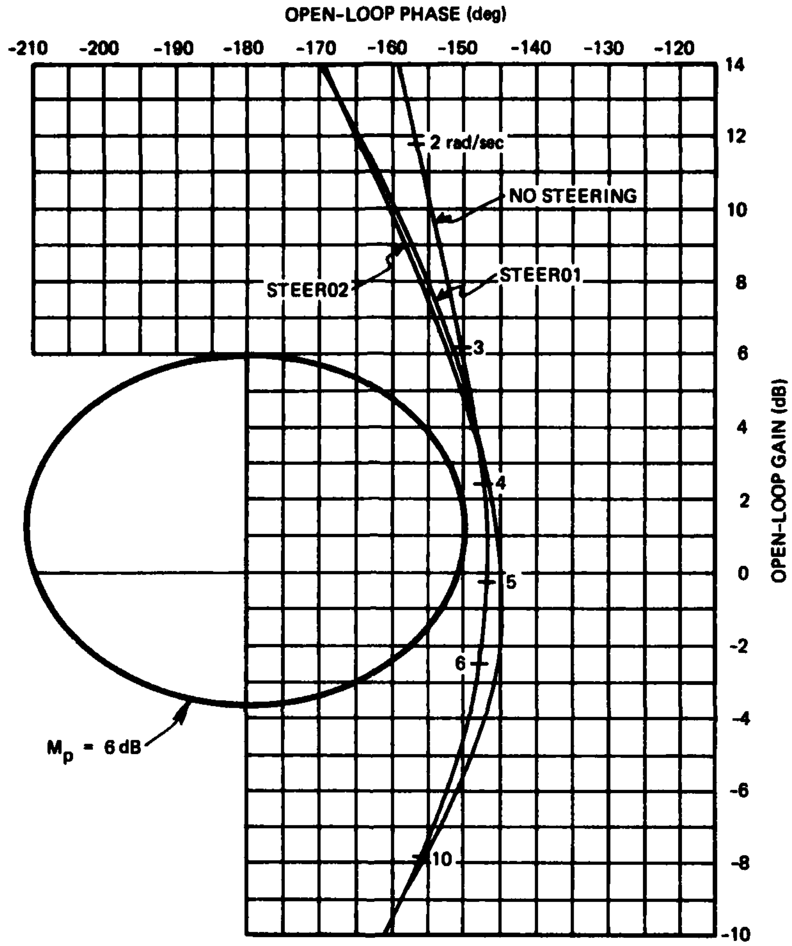

CONDITIONS – NORMALIZED DESIGN

V_g STEERING K_{steer} = 0.3048
T_s = 0.45 K_{int} = 0, 0.093
T_{go} = 60 sec

Figure 23. Effect of steering, normalized design.

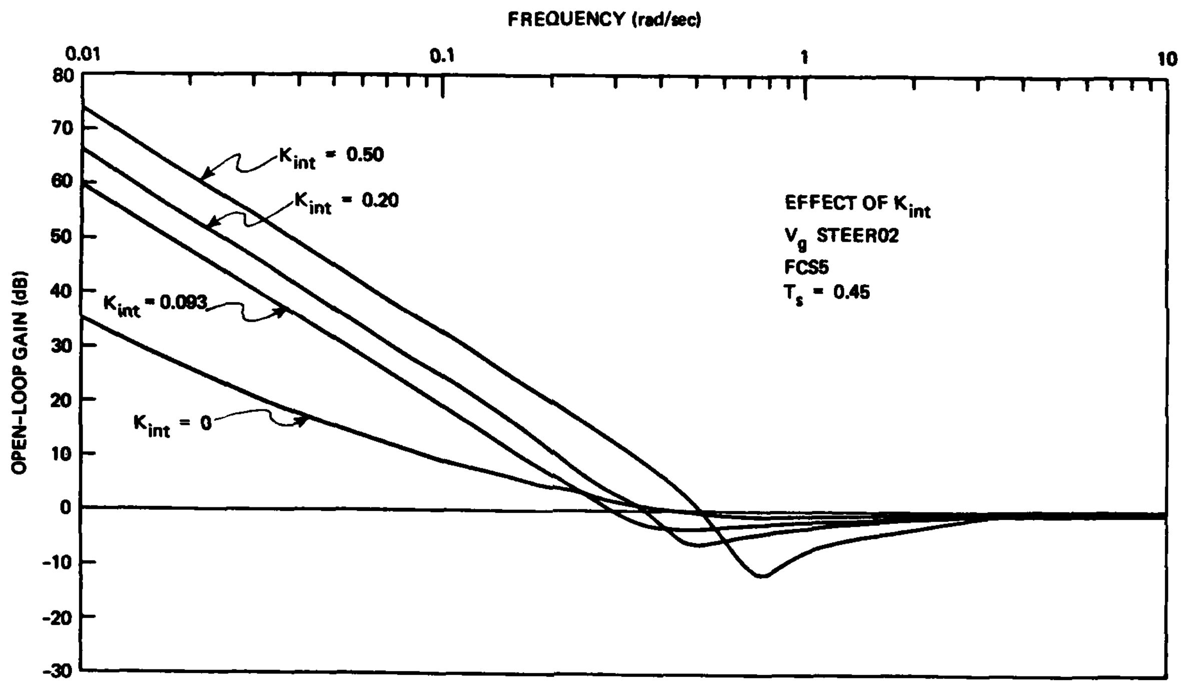

Figure 24. Effect of K_{int}, gain vs frequency.

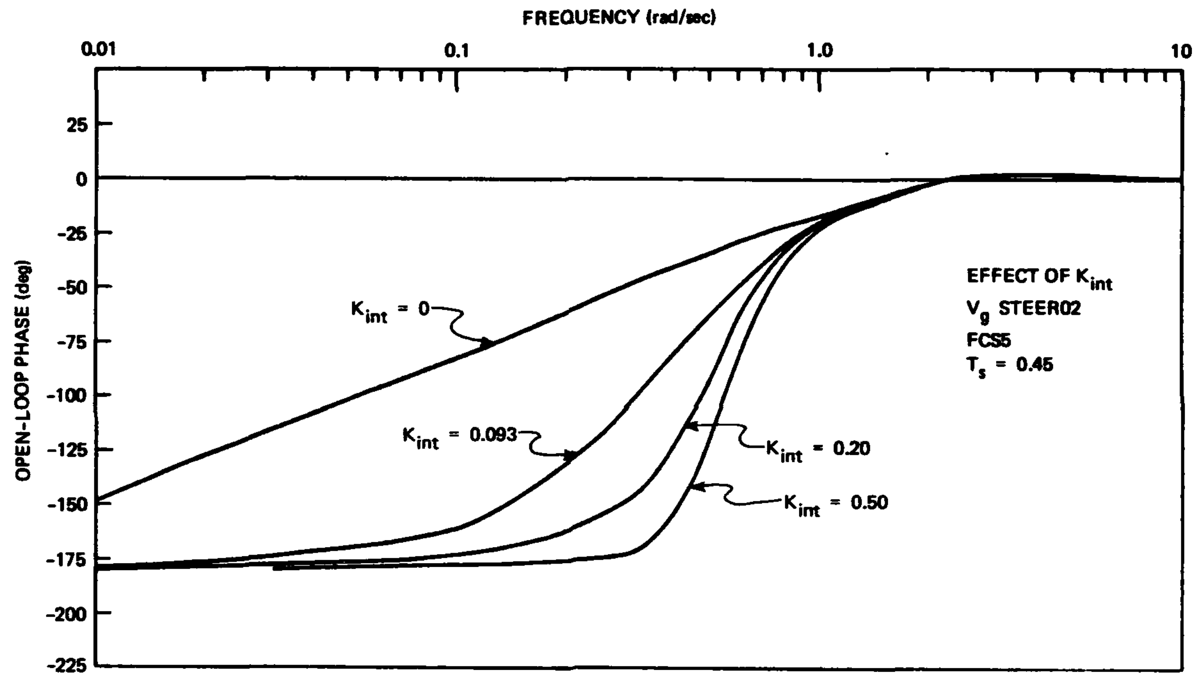

Figure 25. Effect of K_{int}, phase vs frequency.

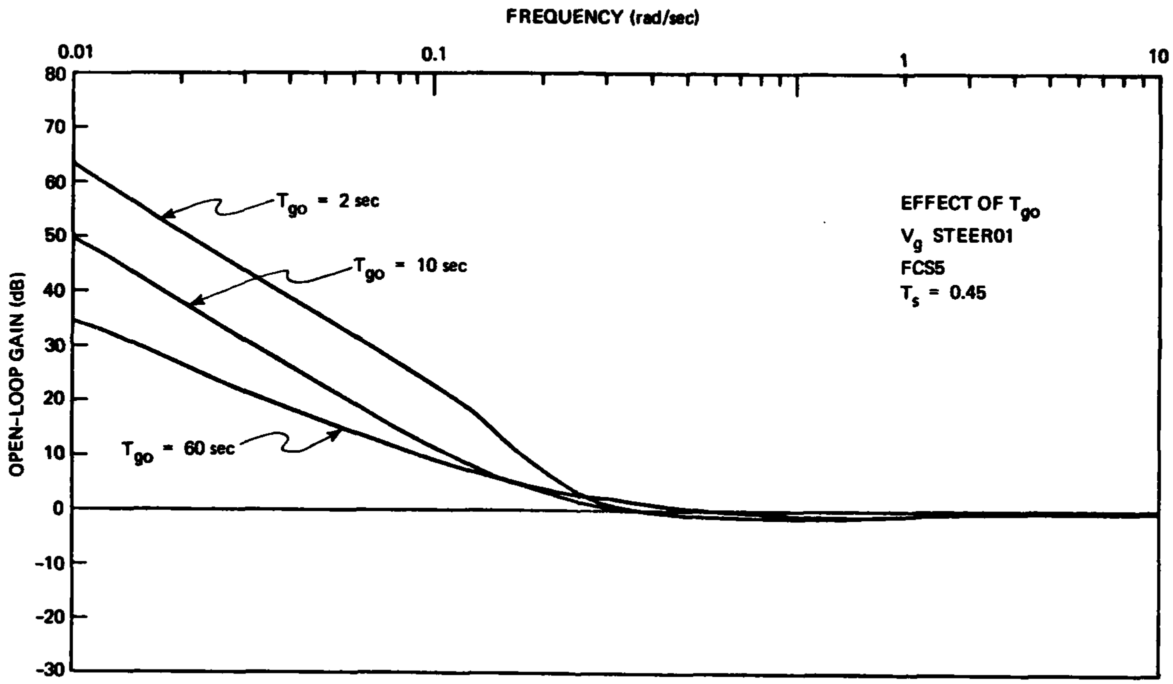

Figure 26. Effect of T_{go}, gain vs frequency.

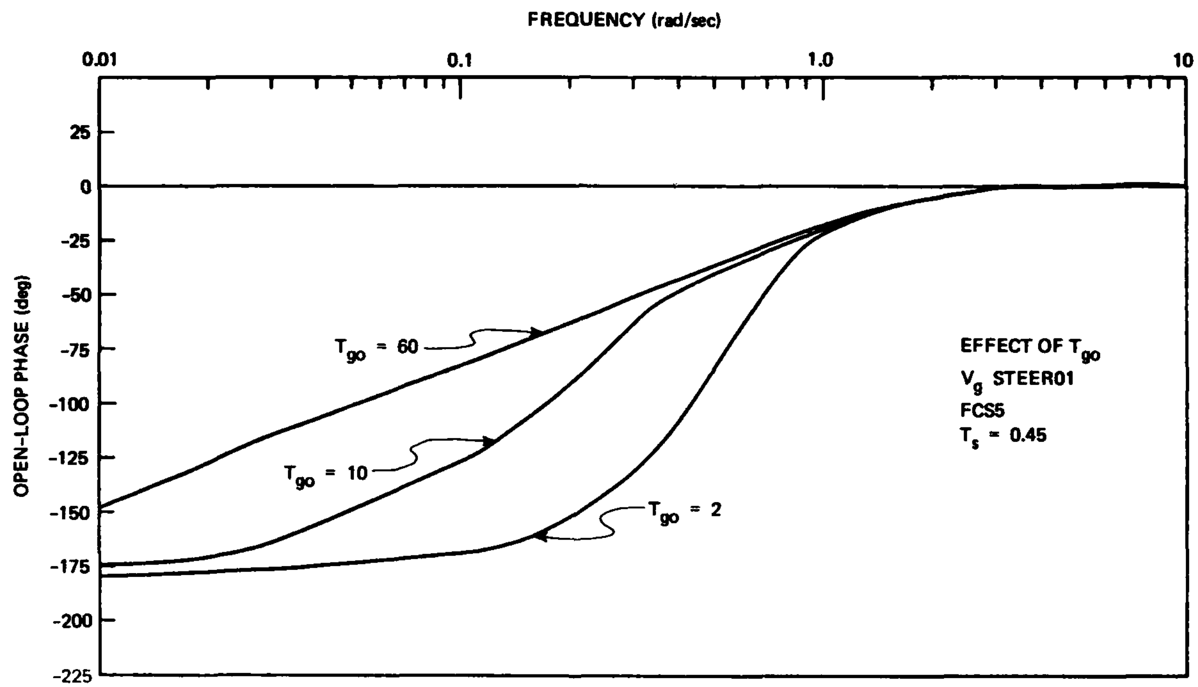

Figure 27. Effect of T_{go}, phase vs frequency.

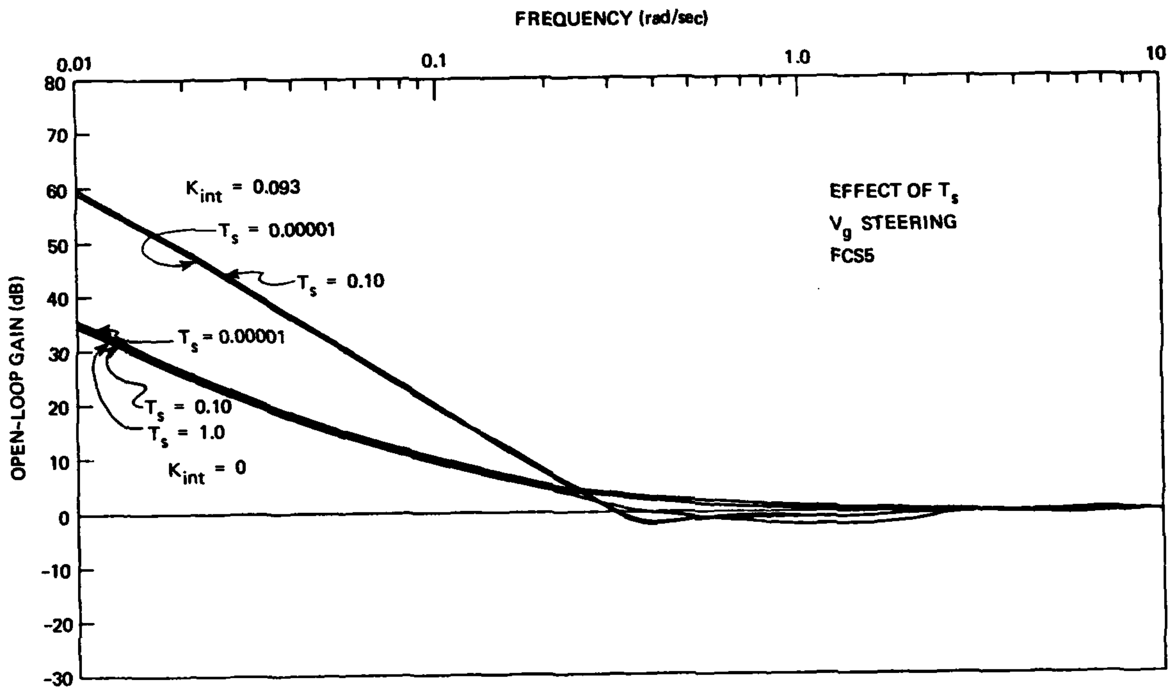

Figure 28. Effect of T_s, gain vs frequency.

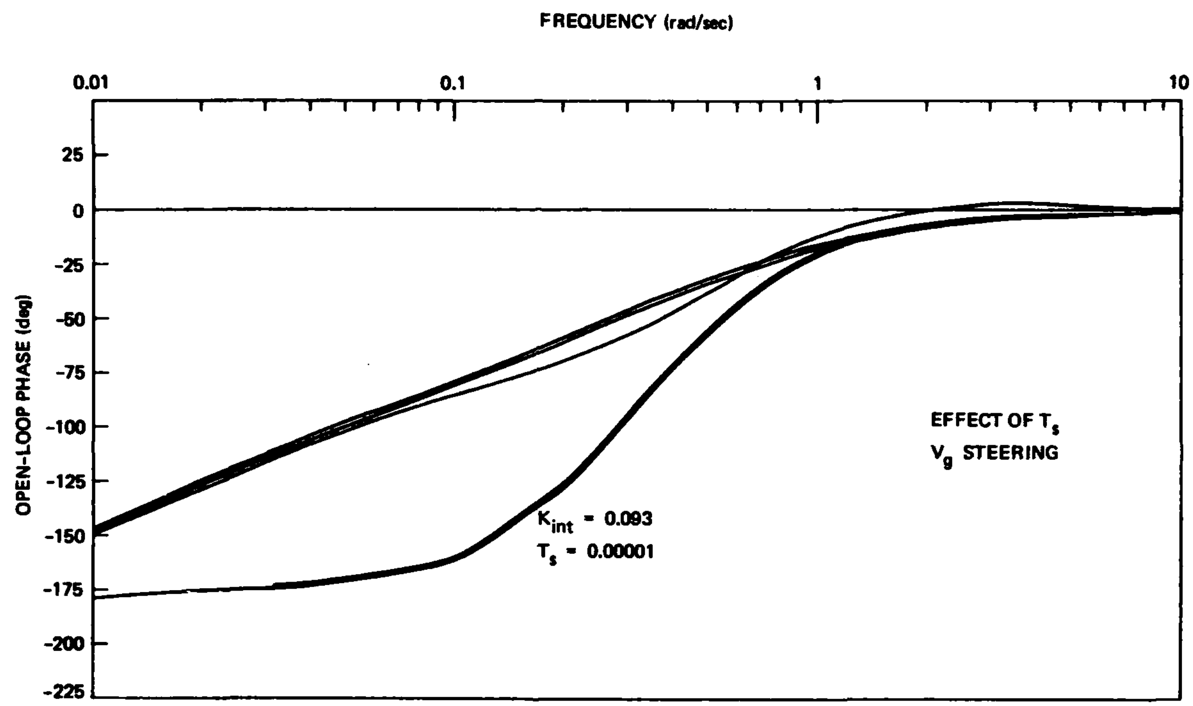

Figure 29. Effect of T_s, phase vs frequency.

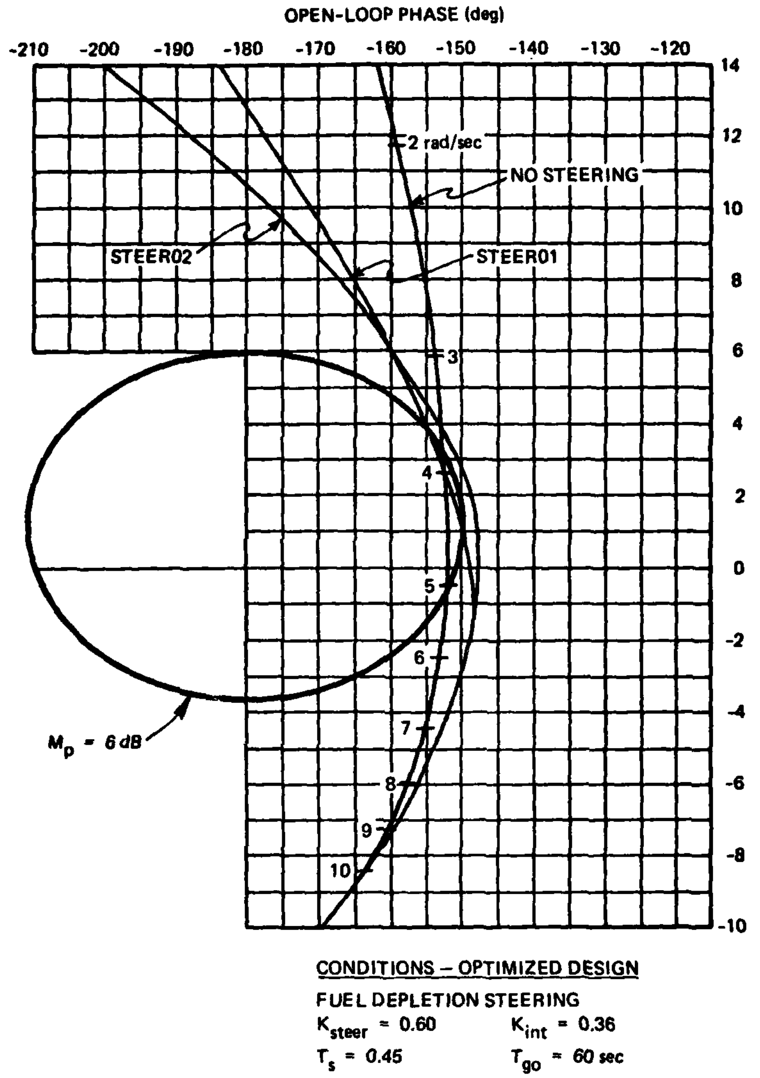

Figure 30. Effect of steering, optimized design.

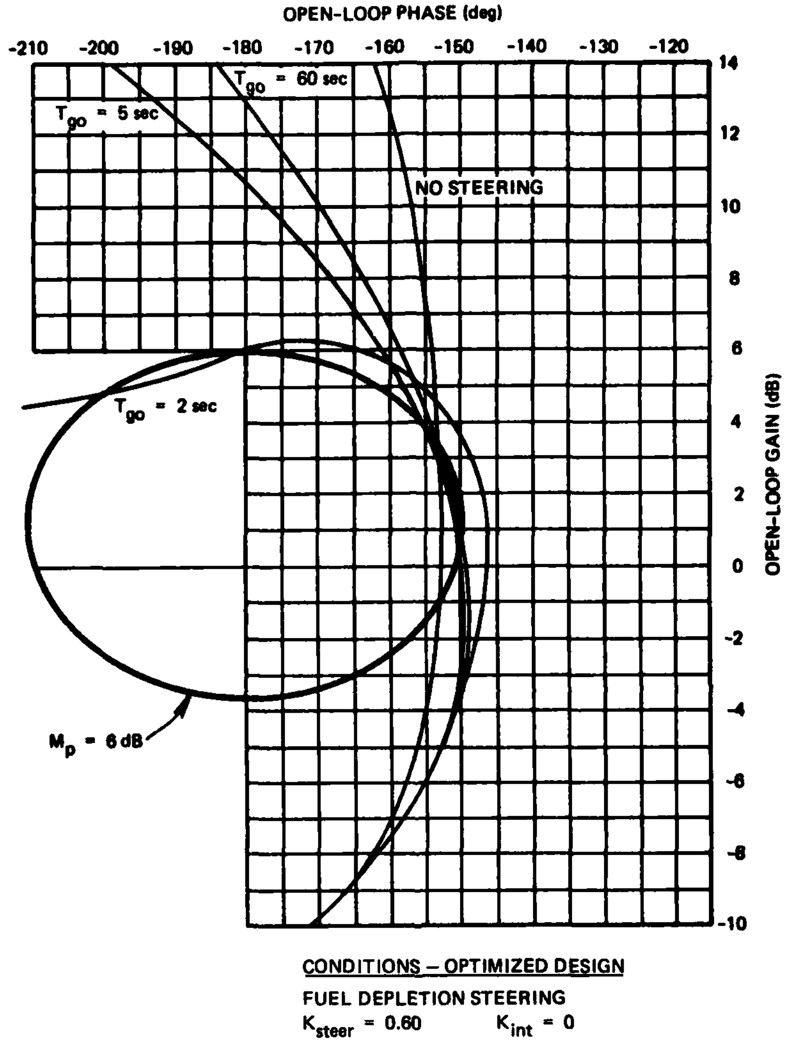

Figure 31. Effect of T_{go}, STEER01.

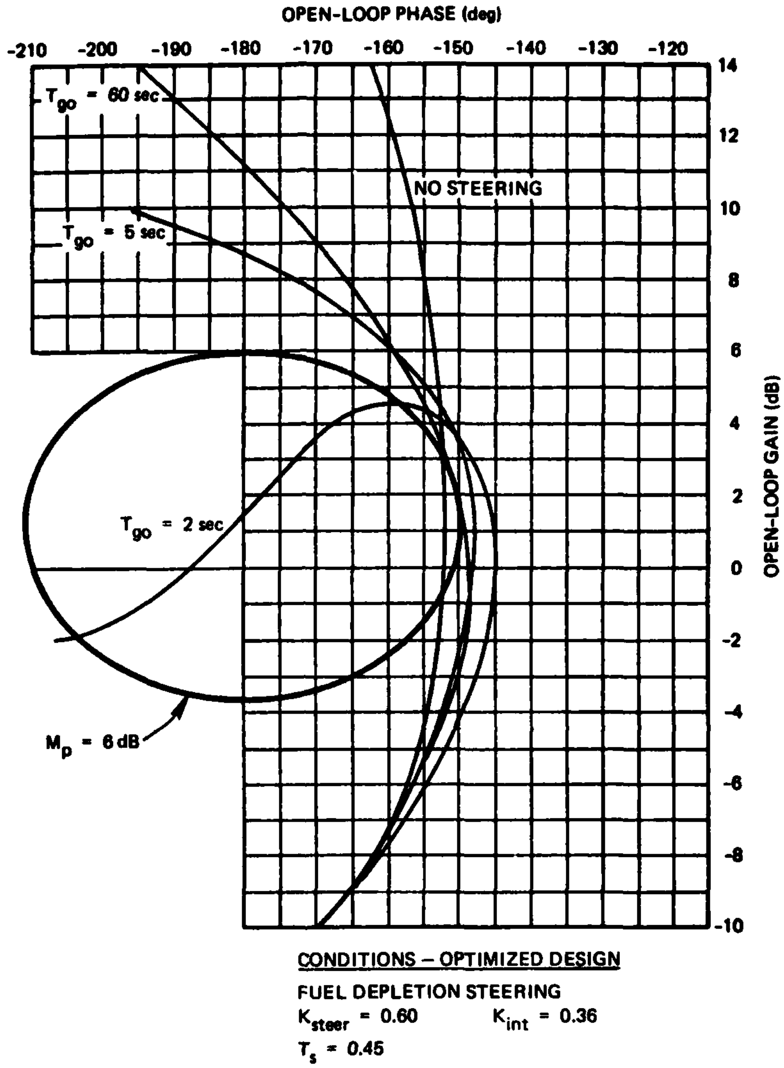

Figure 32. Effect of T_{go}, STEER02.

This series of plots show that for $\omega_1/\omega_2 = 0.10$, the steering effects have little impact on the autopilot in the vicinity of crossover. We would like to use the response characteristics of the steering to modify the overall system characteristics to shape the gain-phase curve to the M = 6 dB contour to give an "optimum" closed-loop gain over a wider range of frequencies. To do this, we increase the frequency of the steering loop by changing the steering gain from $K_{steer} = 0.3048$ to $K_{steer} = 0.60$. This corresponds to a ratio of $\omega_1/\omega_2 = 0.20$. We also wish to shape the gain-phase curve at frequencies at and above the crossover point. We do this by decreasing the frequency of the compensator pole from $\omega_3 = 21.66$ rad/sec to $\omega_3 = 15.0$ rad/sec. This will reduce the overall phase lead of the compensator and bend the high frequency part of the gain-phase plot around the 6 dB contour. The effect of the steering parameters on the steering loop response will remain the same except for the frequency shift, but the steering loop response now will have more effect on the total system response.

In this optimization process, we use the time-to-go sensitivity of the fuel depletion steering as a worst case, since we have seen how the time-to-go contributes significant phase lag, and the time-to-go sensitivity of the fuel depletion steering is 4 times as great as V_g steering. The effect of steering on the "optimized" autopilot is shown in Figure 30. Since the autopilot is optimized around the effect of the steering loop, in particular the phase lead contribution, without steering the gain-phase curve crosses the 6 dB contour. The integral term in STEER02 gives more phase lag at low frequency, but more phase lead near crossover. The gain-phase curve for steering mode STEER01 crosses the 6 dB contour between 3 and 5 rad/sec, but with a small increase in open-loop gain, this curve could be adjusted to be tangent to the 6 dB contour.

Figure 31 shows the effect of decreasing time-to-go for STEER01. Note the dramatic change in the gain-phase curve for $T_{go} = 2$ sec. Here, the curve crosses the 6 dB contour between 1.4 and [illegible].6 rad/sec, but this can easily be prevented by a slight change in open-loop gain.

Figure 32 shows the effect of decreasing time-to-go for STEER02. Here, the phase lag contributions from the integral term and from time-to-go cause a significant invasion of the 6 dB contour which can only be prevented by "freezing" the steering command at T_{go} values greater than 2 seconds. In this case, the dependance of the steering loop on time-to-go disappears entirely.

2.6 Gain Scheduling

The analysis and parametric design of the autopilot and steering loops assume that the open loop gain, $K_c K_v$ of the compensator and vehicle combination is constant. Since the vehicle gain, K_v, is defined as $K_v = Tl_{cg}/I$ and these parameters vary as the burn progresses, the vehicle gain increases from $K_v = 20$ at ignition to $K_v = 80$ at burnout (assuming constant thrust). When the thrust tailoff model is used, the vehicle gain changes from a maximum value of $K_v = 61.4$ to $K_v = 0$. In order to present the dynamics of the system from drastically changing due to these gain shifts, it is desirable to schedule the generalized compensator gain K_c as an inverse function of the vehicle gain to preserve the desired value of open-loop gain. This is accomplished by computing the digital filter gain K_z as follows

$$K_z = KV/K_v$$

KV is given as a function of the autopilot configuration of the initial values of K_w (w-plane equivalent gain) and K_z (digital filter equivalent gain) in Table 12. When the thrust tailoff model is used, the compensator gain is increased as the vehicle gain is reduced. In order to prevent the compensator gain from becoming infinite, it is frozen when it reaches its initial value. This occurs at approximately 2 seconds to go.

Table 12. Gain scheduling autopilot coefficients.

Desired W_{xo}	Initial K_w	Initial K_z	KV
2	0.104103	0.47199	9.4398
5	0.650663	3.6485	72.9700
8	1.665679	12.04788	240.9576

In a similar manner, the steering gain, K_{steer}, is decreased as a function of thrust acceleration during tailoff in order to prevent the decreasing torque capability of the engine from forcing the actuator into rate or position limits. After the thrust acceleration reaches its peak value, K_{steer} is computed from

$$K_{steer} = K_{steer_{init}} - K_{change} (A_{T_{max}} - A_T)$$

K_{change} is defined as

$$K_{change} = \frac{K_{steer_{init}} - K_{steer_{final}}}{A_{T_{max}}}$$

Nominally, $K_{steer_{final}}$ is set to 0.01. For the different values of steering gain corresponding to the three autopilot configurations, K_{change} is

FCS	K_{change}
2	0.0006
5	0.00158
8	0.00256

2.7 Terminal Steering

As previously discussed, the steering modes used in this study are unstable at the end of the burn, the perturbation sensitivities being $1/T_{go}$ for V_g steering, and $4/T_{go}$ for fuel depletion steering. To avoid this problem, the steering signal must be modified as the time-to-go approaches zero. Two approaches were considered for this study:

(1) Zero the rate command vector, $\overline{W}_{CMD}$.

(2) Freeze the commanded thrust vector, $U\overline{S}F$.

The latter method has the slight advantage of having the final commanded thrust direction oriented in the direction of the last computed thrust vector command. Since V_g steering results in an almost constant attitude maneuver near the end of the burn, the advantage of either mode is probably negligible for this mode. For fuel depletion steering, zeroing the commanded rate may contribute to the terminal stability, but if the fuel depletion maneuver continues to very near the end of the burn, this increase in stability may be at the expense of slight increases in the V_g residuals. The guidance commands are not used in the last second of the burn, but the $\Delta\overline{V}$ vector and the rate command vector are continually computed, and this results in a slightly more accurate steering signal than simply commanding a zero rate. Therefore, the approach we will use in the study will be to freeze the commanded thrust vector, $U\overline{S}F$.

SECTION 3

GUIDANCE METHODS

3.1 Position Offset Guidance

As mentioned in Section 1.2, position offset guidance can be used during the powered flight portion of the trajectory to correct for inaccuracies in the calculation of velocity-to-be-gained caused by assuming that the velocity change is made impulsively. The development of the position offset guidance method in this section is taken from "A New Approach to Lambert Guidance," by Timothy J. Brand of CSDL. (Reference 1).

The traditional guidance method involves the pre-maneuver calculation of a target offset. This calculation requires accurate prediction of the initial state and the path to be taken by the vehicle to the target. In the traditional method, an impulsive velocity change is used to approximate the thrust phase, then the velocity required to coast from the initial position to the terminal position in a specified time is determined using Lamberts' routine. Direct numerical integration of the equations of motion, accounting for gravity perturbations, is then used to extrapolate this required velocity and initial position along the trajectory. The first estimate of the target offset is taken as the negative of the resultant miss. Further iterations using the offset target derived from the previous iteration as the desired final radius vector for the Lambert routine are generally required to accurately determine the offset target.

Unless the thrust maneuver is very short, the offset target determined by assuming an impulsive velocity change can cause significant terminal errors when used with the Lambert routine. This is due to the fact that the compensation for gravity perturbations is based on prediction of those effects over both the thrust and the subsequent coasting periods. Due to the nonzero length of the thrust phase, the actual trajectory does not follow the path predicted by the impulsive velocity change assumption, but rather a neighboring path.

The difference in the perturbing gravitational acceleration between the two paths accumulates over the entire trajectory, causing a miss at the target.

An improvement, then, to the traditional method would be to determine a coasting trajectory that is coincident with the actual trajectory at thrust cutoff. In this case, the difference in gravitational accelerations only affects the trajectory during the thrust phase, and as shown by Brand in Reference 1, can usually be neglected.

This improvement is the position offset method, where the initial position is offset to lie on a coasting trajectory such that at thrust cutoff, the thrusting path and the coasting path are coincident as shown in Figure 33. This pseudo-initial position is then used in the Lambert

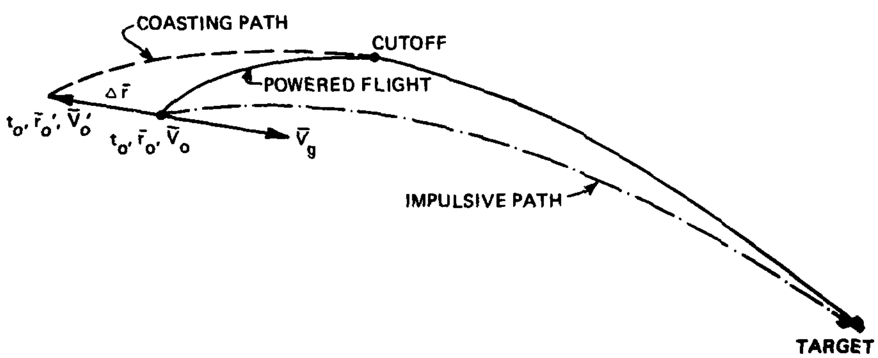

Figure 33. Geometrical relationships of perturbation analysis.

routine to accurately determine the velocity-to-be-gained. An important advantage of this method is that it simplifies the computation of $\bar{V}_g$ between guidance cycles. On a coasting trajectory we define

$$\bar{V}_g' = \bar{V}_{req}' - \bar{V} \tag{22}$$

Since $\dot{\bar{V}}_{req}' = \bar{g}(\bar{r}')$, we can write

$$\dot{\bar{V}}_g' = \dot{\bar{V}}_{req}' - \dot{\bar{V}}$$

$$\dot{\bar{V}}_g' = \bar{g}(\bar{r}') - \bar{g}(r) - \bar{A}_T$$

$$\dot{\bar{V}}_g = \Delta\bar{g} - \bar{A}_T$$

where $\Delta\bar{g}$ is the difference in the gravitational acceleration between the coasting trajectories, powered trajectories, and $\bar{A}_T$ is the thrust acceleration. Brand gives numerical justification for neglecting this term in Reference (1), so we have that

$$\dot{\bar{V}}_g \cong -A_T \tag{23}$$

This equation indicates that $\bar{V}_g$ may be accurately updated between computations of V_{req}' by decrementing V_g at the steering cycle rate by the accelerometer-sensed ΔV over the steering period T_s. Since $\Delta\bar{g} \rightarrow 0$ as the coasting and powered trajectories become coincident at thrust cutoff, this computation becomes more accurate near the end of the burn when it is important to have an accurate $\bar{V}_g$ for thrust cutoff calculation. The position and velocity at thrust cutoff, $\bar{r}_{co}$ and $\bar{V}_{co}$, can be expressed in terms of the initial state $\bar{r}_o$ and $\bar{V}_o$ by the following equations

$$\bar{V}_{co} = \bar{V}_o + \int_o^{t_{co}} [\bar{A}_T + \bar{g}(\bar{r})]dt \tag{24}$$

$$\bar{r}_{co} = \bar{r}_o + \int_o^{t_{co}} \bar{V}\, dt \tag{25}$$

where $\bar{A}_T$ is the thrust acceleration and $\bar{g}(\bar{r})$ is the gravitational acceleration.

The state at thrust termination can also be expressed in terms of the coasting trajectory initial conditions, $\bar{r}_o'$ and $\bar{V}_o'$, as

$$\bar{V}_{co} = \bar{V}_o' + \int_o^{t_{co}} \bar{g}(\bar{r}')dt \tag{26}$$

$$\bar{r}_{co} = \bar{r}_o' + \int_o^{t_{co}} \bar{V}'dt \tag{27}$$

where $\bar{g}'(\bar{r})$ is the gravitational acceleration along the coasting path. Then, the difference in initial velocity on the coasting and thrusting trajectories is

$$\Delta\bar{V}_o = \bar{V}_o' - \bar{V}_o = \int_o^{t_{co}} [\bar{A}_T + \bar{g}(\bar{r}) - \bar{g}(\bar{r})]dt \qquad (28)$$

The expression for the thrust acceleration of a vehicle with constant thrust T and mass flow rate in is

$$\bar{A}_T = \frac{T}{M_o - \dot{m}t} \hat{i}_\lambda$$

where $\hat{i}_\lambda$ is a unit vector in the direction of the thrust vector and M_o is the initial mass. From Equations 24 and 26, the velocity difference ΔV between the velocity on the coasting trajectory $\bar{V}'$ and the powered trajectory $\bar{V}$ can be written

$$\Delta\bar{V} = \bar{V}' - \bar{V} = \Delta\bar{V}_o - \int_o^t \frac{T \hat{i}_\lambda}{M_o - \dot{m}t} dt \qquad (29)$$

where $\Delta\bar{V}_o$ is the initial velocity difference and the gravity difference is ignored.

Evaluating this integral gives

$$\Delta\bar{V} = \Delta\bar{V}_o - V_{ex} \hat{i}_\lambda \log \left[1 - \frac{t}{\tau} \right]$$

where $\tau = M_o/\dot{m}$ and the exhaust velocity

$$V_{ex} = T/\dot{m}$$

Since $\Delta\bar{V} = 0$ at the cutoff time

$$\Delta\bar{V}_o = V_{ex}\hat{i}_\lambda \log (1 - \frac{t_{co}}{\tau})$$

We can solve this equation for the cutoff time and derive

$$t_{co} = \tau(1 - e^{-\Delta V_o/V_{ex}}) \tag{30}$$

From Equations 25 and 27, the expression for the initial position offset is

$$\Delta\bar{r}_o = -\int_0^{t_{co}} (\bar{V}' - \bar{V})dt = -\int_0^{t_{co}} \Delta\bar{V}\, dt$$

Substituting for $\Delta\bar{V}$, we obtain

$$\Delta\bar{r}_o = -\int_0^{t_{co}} \left[\Delta\bar{V}_o - V_{ex}\, \hat{i}_\lambda \log\,(1 - \frac{t}{\tau})\right]dt$$

Integrating this expression

$$\Delta\bar{r}_o = -\Delta\bar{V}_o t_{co} - \tau\, V_{ex}\, \hat{i}_\lambda \left[\left(1 - \frac{t_{co}}{\tau}\right) \log \left(1 - \frac{t_{co}}{\tau}\right) + \frac{t_{co}}{\tau}\right] \tag{31}$$

Replacing $V_{ex}\hat{i}_\lambda \log\,(1 - \frac{t_{co}}{\tau})$ by $\Delta\bar{V}_o$, Equation 31 reduces to

$$\Delta\bar{r}_o = -\tau\, \Delta\bar{V}_o - t_{co}\, V_{ex}\, \hat{i}_\lambda \tag{32}$$

which can be used to determine the initial position offset after the cutoff time, t_{co}, is computed from Equation 30.

For fuel depletion steering, the vehicle thrust acceleration is not pointed in the direction of $\bar{V}_g$, but instead is rotated from the $\bar{V}_g$ vector by the amount of the fuel depletion angle. For this case with constant thrust and linear mass loss, it is shown in Reference 3 that the position offset equation is

$$\Delta\bar{r} = -K_{po}\left[V_{cap}\, \bar{V}_g + V_{cap}{}^2\left[\cos\,\theta - V_g/V_{cap}\right]\hat{B}/\theta\right] \tag{33}$$

where $\hat{B}$ is a unit vector normal to $\bar{V}_g$ and V_{cap} and K_{po} are functions of the elapsed time, t (measured from the time of the initial state conditions) defined by the expressions

$$\left\{\begin{aligned} V_{cap} &\equiv \int_{\mu=t}^{t_{co}} \frac{T}{(M_o - \dot{m}\mu)}\, d\mu \\ K_{po} &\equiv \frac{\displaystyle\int_{\mu=t}^{t_{co}} (\mu - t)\, \frac{T}{(M_o - \dot{m}\mu)}\, d\mu}{V_{cap}^2} \end{aligned}\right. \tag{34}$$

Since the fuel depletion angle $\theta=0$ for V_g steering, the position offset equation can be written as

$$\Delta\bar{r} = -K_{po}\, V_{cap}\, \bar{V}_g \tag{35}$$

Equations 33 and 35 are implemented in the guidance routines of the simulation programs OFFSETT and STEER. For assumed constant thrust, T, and constant mass flow rate of fuel, $\dot{m}$, the integrals in equation 34 can be solved to yield the following solution for K_{po}

$$K_{po} = \frac{(\tau - t)\log\left[\dfrac{M_o - \dot{m}t}{M_o - \dot{m}t_{co}}\right] + (t - t_{co})}{V_{ex}\left[\log\left(\dfrac{M_o - \dot{m}t}{M_o - \dot{m}t_{co}}\right)\right]^2} \tag{36}$$

where, as previously defined, $V_{ex} \equiv \dfrac{T}{\dot{m}}$ and $\tau \equiv \dfrac{M_o}{\dot{m}}$

For in-flight mechanization (as represented by the STEER program), the guidance computer solves for the required velocity and the position offset using these equations at each guidance cycle time (every 1.35 seconds), and the velocity-to-be-gained is updated every steering cycle (0.45 second) by subtracting from the previous $\bar{V}_g$ the change in velocity over the steering period. The velocity is updated every autopilot cycle by accumulating the accelerometer sensed velocity increments.

3.2 Reentry Angle (γ) and Time-On-Target (TOT) Control

The fuel depletion steering method coupled with position offset guidance provides a convenient technique for simultaneously controlling the reentry angle, γ, and the Time-On-Target (TOT). By modifying the ratio V_g/V_{cap}, the fuel depletion angle may be modulated to introduce a pitch profile that modifies the trajectory of the missile such that γ and TOT are controlled simultaneously.

Time-On-Target is readily controlled since time of flight is a specification to the Lambert guidance routine, i.e., the routine computes a trajectory that satisfies the time of flight and hence the Time-On-Target constraint.

For reentry angle control, the guidance system first computes the reentry angle as the flight path angle at an altitude of 300,000 feet on a trajectory that satisfies the Time-On-Target constraint. If this angle differs from the desired reentry angle, the guidance program incrementally changes V_{cap} to modify the ratio V_g/V_{cap} and thence the fuel depletion angle. This resulting change in the pitch profile modifies the orbit. A new position offset is then computed since the offset is a function of both V_{cap} and the depletion angle, and the Lambert routine computes a trajectory that satisfies the time of flight constraint. A new reentry angle is then computed. This process continues iteratively until the reentry angle error is within a desired tolerance.

3.3 Perturbation Sensitivity of Fuel Depletion Guidance

We are interested in determing the sensitivity of the fuel depletion angle to small deviations in the velocity-to-be-gained caused by guidance inaccuracies and autopilot/steering errors. Obviously, if the computation of $\overline{V}_g$ is exact and the vehicle is steered precisely along the fuel depletion arc, there will be no stability problems. However, since there will be steering errors, we need to determine how this sensitivity varies as a function of the maneuver parameters. We have seen that in velocity-to-be-gained steering, the sensitivity of the steering loop to steering errors increases as $1/T_{go}$ and the commanded thrust vector $U\overline{S}F$ must be "frozen" near the end of the burn to prevent instability. We expect to find a similar problem in fuel depletion steering; as we shall demonstrate, the sensitivity of the steering loop in this mode is actually $4/T_{go}$.

This indicates that steering instability occurs in fuel depletion steering at a value of T_{go} four times as great as in velocity-to-be-gained

steering. This variable sensitivity is represented in Figure 5 in Section 2.3 as the γ/T_{go} term in the steering loop model.

To analytically determine this sensitivity, we introduce a small perturbation, $\bar{V}_{err}$, in the velocity-to-be-gained in a direction normal to the fuel depletion arc and the unperturbed thrust vector command $U\bar{S}F_1$. Referring to Figure 34, we call the perturbed $\bar{V}_g$ vector $\bar{V}_{g1}$,

$$\Delta\theta_T = \theta_2 - \theta_1 - \theta_g$$

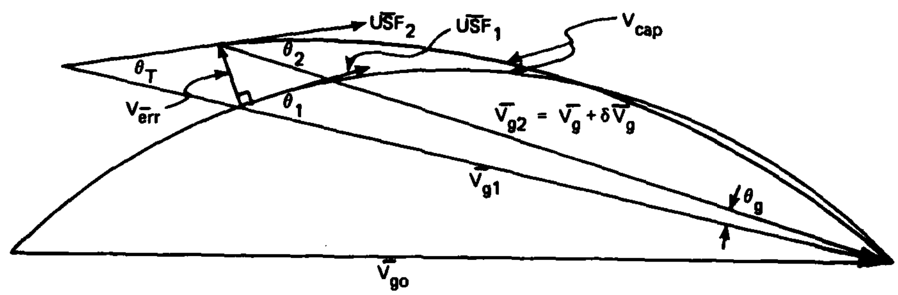

Figure 34. Geometrical relationships of perturbation analysis.

and the vector sum of $\bar{V}_{err}$ and $\bar{V}_{g1}$ is designated $\bar{V}_{g2}$. We assume that this velocity error is the result of accumulated steering errors such that its magnitude, V_{err}, is given by the integral

$$V_{err} = \int A_T \lambda dt \tag{37}$$

where λ is the agnle between $\Delta\bar{V}$ and the commanded thrust vector as defined in Appendix A3. If we assume that the thrust acceleration, A_T, is constant, we can write

$$V_{err} = T/M \int \lambda dt$$

We can write the remaining impulse, V_{cap} at this point again assuming constant acceleration as

$$V_{cap} \cong A_T\, T_{go} \cong T/M\, T_{go}$$

So the ratio of V_{err}/V_{cap} is now

$$V_{err}/V_{cap} = \frac{1}{T_{go}} \int \lambda dt$$

From the geometry of Figure 34, we see that

$$V_{g2} = V_{err}^2 + V_{g1}^2 - 2V_{g1} V_{err} \cos (90 + \theta_1)$$

writing $V_{g2}^2 = (V_{g1} + \delta V_g)^2$ and $\cos (90 + \theta_1) = - \sin \theta_1$, we now have

$$\cancel{V_{g1}^2} + 2V_{g1}\delta V_g + \cancel{\delta V_g^2} = V_{err}^2 + \cancel{V_{g1}^2} + 2V_{g1} V_{err} \sin \theta_1$$

or

$$\delta V_g = \frac{1}{2} \frac{V_{err}^2}{V_{g1}} + V_{err} \sin \theta_1 \qquad (38)$$

Also from geometry, we have that

$$\sin \theta_g = \frac{V_{err}}{V_{g2}} \cos \theta_1$$

Assuming for small θ_g that $\sin \theta_g \cong \theta_g$, we obtain

$$\theta_g \cong \frac{V_{err}}{V_{g2}} \cos \theta_1 \qquad (39)$$

The basic relation derived in Appendix A5 is

$$\frac{\sin \theta_1}{\theta_1} = \frac{V_{g1}}{V_{cap}} \qquad (7)$$

Repeated

Taking the variation of both sides: with V_{cap} constant

$$\delta\left(\frac{\sin \theta_1}{\theta_1}\right) = \frac{\delta V_g}{V_{cap}}$$

or

$$\frac{\theta_1 \cos \theta_1 - \sin \theta_1}{\theta_1^2} \; \delta\theta_1 = \frac{\delta V_g}{V_{cap}}$$

$$\frac{\delta\theta_1}{\delta V_g} = \frac{\theta_1^2}{V_{cap}\,(\theta_1 \cos \theta_1 - \sin \theta_1)}$$

Expanding cos θ and sin θ in power series around θ = 0 and subtracting gives

$$\frac{\delta\theta_1}{\delta V_g} = \frac{\theta_1^2}{V_{cap}(-\theta^3_{1/3} + \ldots)}$$

and

$$\delta\theta = -\frac{3\,\delta V_g}{V_{cap}\,\theta_1} \tag{40}$$

Equation 4 gives the change in θ due to a small variation in the magnitude of the velocity-to-be-gained. Substituting for δV_g gives

$$\delta\theta = -\frac{3}{V_{cap}\,\theta_1}\left[\frac{1}{2}\frac{V_{err}^{\;2}}{V_{g1}} + V_{err}\sin\theta_1\right]$$

or

$$\delta\theta = -\left[\frac{3}{2}\frac{V_{err}^{\;2}}{V_{cap}\,V_{g1}\,\theta} + \frac{3\,V_{err}\sin\theta_1}{V_{cap}\,\theta_1}\right]$$

or

$$\delta\theta = -\frac{V_{err}}{V_{cap}}\left[\frac{3}{2}\frac{V_{err}}{V_{g1}\,\theta} + 3\left(\frac{\sin\theta_1}{\theta_1}\right)\right] \tag{41}$$

Examining the two terms inside the bracket discloses that, while both terms have singularities at $\theta_1 = 0$, the first term is much smaller than the second term during a nominal burn. From a typical fuel depletion simulation run (OFFSET), we have that at $T_{go} = 1$ second, $V_{g1} = 250$ ft/sec and $\theta_1 = 0.113$ radian. For these values, we see that for $V_{err} = 5$ ft/sec

$$\frac{3}{2}\frac{V_{err}}{V_{g1}\,\theta_1} = 0.265$$

and

$$3\left(\frac{\sin\theta_1}{\theta_1}\right) = 2.994$$

Therefore, we neglect the contribution of the first term and we write the expression for the change in θ due to a variation in the magnitude of the velocity-to-be gained as

$$\delta\theta = -\frac{V_{err}}{V_{cap}}\left[3\left(\frac{\sin\theta_1}{\theta_1}\right)\right] \tag{42}$$

To determine the total change in the fuel depletion angle relative to the unperturbed V_g vector, we must subtract the angle of rotation θ_g since θ_2 is computed relative to V_{g2} rather than V_{g1}. This gives

$$\delta\theta_{total} = -\frac{V_{err}}{V_{cap}}\left[3\left(\frac{\sin\theta_1}{\theta_1}\right) - \frac{V_{err}}{V_{g2}}\cos\theta_1\right] \tag{43}$$

Near the end of the burn, we can determine an approximate expression by assuming that

$$\frac{\sin\theta_1}{\theta_1} \cong 1 \;;\; \cos\theta_1 \cong 1$$

and

$$V_{g2} \cong V_{cap}$$

We can then write Equation 43 as

$$\delta\theta_{Total} \cong -\frac{4\,V_{err}}{V_{cap}}$$

and

$$\frac{\delta\theta_{Total}}{V_{err}} \cong -\frac{4}{V_{cap}} \tag{44}$$

We have already shown that

$$\frac{V_{err}}{V_{cap}} \cong \frac{1}{T_{go}} \int \lambda dt$$

So now we have

$$\delta\theta_{total} = -\frac{4}{T_{go}} \int \lambda dt \qquad (45)$$

We now wish to compare the sensitivity determined from the approximate analytical expression of Equation 43 with the actual sensitivity. To do this, we introduce a perturbation subroutine, PERT, in the guidance program, OFFSETT. After the nominal parameters (θ, $\overline{V}_{g1}$, V_{cap}, $U\overline{S}F_1$) are computed at a particular time, we perturb the $\overline{V}_{g1}$ vector by adding to $\overline{V}_{g1}$ a small perturbation vector, $\overline{V}_{err}$, and use this new $\overline{V}_{g2}$ to recompute a new fuel depletion angle θ_2 and a new commanded thrust vector, $U\overline{S}F_2$ as shown in Figure 34. Since we are computing these perturbation parameters at the same instant of time as the unperturbed parameters, V_{cap} remains constant. Note that the magnitude of V_{g2} is equal to V_{g1} plus a small increment, δV_g and V_{g2} is rotated from V_{g1} by a small angle θ_g. The actual parameters are computed by the PERT routine as follows

$$\Delta\theta_{total} = \arcsin \left| U\overline{S}F_1 \times U\overline{S}F_2 \right| \qquad (46)$$

$$\frac{\delta\theta}{\delta V_{err}} = \frac{\Delta\theta_{Total}}{V_{err}} \qquad (47)$$

To compare the actual sensitivity to the analytical sensitivity, we first compare the actual rotation of V_{g2} with respect to V_{g1} to the approximation given by Equation 39. The actual rotation is computed by

$$\theta_g = \arcsin \left| \text{Unit}(V_{g1}) \times \text{Unit}(V_{g2}) \right| \qquad (48)$$

and the approximate rotation is again

$$\theta_g \cong \frac{V_{err}}{V_{cap}} \cos \theta_1 \doteq \frac{V_{err}}{V_{cap}} \qquad \begin{array}{c}(39)\\ \text{Repeated}\end{array}$$

The difference (normalized to V_{err}) of these two terms we will call ERR1 and

$$\mathrm{ERR1} = \frac{1}{V_{cap}} - \frac{\theta_g}{V_{err}}$$

The assumptions made in this approximation are that for $\theta_g << 1$, $\sin \theta_g \cong \theta_g$ and that $\cos \theta_1 \cong 1$.

We now look at Equation 42. We have assumed that $\sin \theta_1/\theta_1 \cong 1$ and that $3/2\ (V_{err}/V_{g1}\theta)$ can be neglected. Therefore, the approximate sensitivity contribution of this term is $3\ V_{err}/V_{cap}$. The actual contribution of this term to the sensitivity is computed in PERT as the difference between the fuel depletion angles computed from the perturbed and unperturbed V_g vectors and the constant V_{cap}. ERR3 is then defined as

$$\mathrm{ERR3} = \frac{3}{V_{cap}} - \frac{(\theta_2 - \theta_1)}{V_{err}} \tag{49}$$

The total sensitivity of the fuel depletion angle to V_g perturbations is the sum of ERR1 and ERR3. We therefore write

$$\mathrm{ERR4} = \frac{4}{V_{cap}} - \frac{1}{V_{err}}(\theta_2 - \theta_1 - \theta_g) \tag{50}$$

We can compute the sensitivity partial by normalizing the total change in θ to V_{err} so we have

$$\mathrm{DTH/DV_g} = (\theta_2 - \theta_1 - \theta_g)/V_{err} \tag{51}$$

The values of these four parameters are shown with the unperturbed values of V_g, V_{cap}, and θ for a nominal fuel depletion burn in Table 13 and for a fuel depletion burn with reentry control in Table 14. Note that the sensitivities computed with and without reentry control are essentially the same.

Table 13. Comparison of analytical and computed sensitivities of fuel depletion angle to variations in the velocity-to-be-gained (no reentry control).

Approximate Time-to-Go (sec)	Velocity-to-be-Gained (ft/sec)	ΔV Capability (ft/sec)	Fuel Depletion Angle (deg)	ERR1 (rad/ft/sec)	ERR3 (rad/ft/sec)	ERR4 (rad/ft/sec)	DTH/DV_g (rad/ft/sec)
60	6071	8400	77.34	-	-	-	-
50	5829	7513	68.89	7.13×10^{-5}	3.49×10^{-5}	1.06×10^{-4}	-4.26×10^{-4}
40	5360	6419	58.51	5.84×10^{-5}	3.11×10^{-5}	8.95×10^{-5}	-5.34×10^{-4}
30	4626	5184	46.84	4.51×10^{-5}	2.56×10^{-5}	7.08×10^{-5}	-7.01×10^{-4}
20	3554	3765	33.42	3.10×10^{-5}	1.68×10^{-5}	4.78×10^{-5}	-1.014×10^{-3}
10	2063	2095	17.54	1.53×10^{-5}	-1.10×10^{-5}	4.27×10^{-6}	-1.904×10^{-3}
2	510	511	2.16	3.41×10^{-4}	-1.69×10^{-3}	-1.66×10^{-3}	-9.50×10^{-3}

Table 14. Comparison of analytical and computed sensitivity of fuel depletion angle to variations in the velocity-to-be gained (Gamma/Time-On-Target control).

Approximate Time-to-Go(sec)	Velocity-to-be-Gained (ft/sec)	ΔV Capability (ft/sec)	Fuel Depletion Angle (deg)	ERR1	ERR3	ERR4	DTH/DV_g
60	6082	9688	91.23	9.96×10^{-5}	5.85×10^{-5}	1.58×10^{-4}	-2.55×10^{-4}
50	6031	8739	82.25	9.21×10^{-5}	5.16×10^{-5}	1.43×10^{-4}	-3.14×10^{-4}
40	5749	7589	71.87	7.77×10^{-5}	4.44×10^{-5}	1.22×10^{-4}	-4.05×10^{-4}
30	5195	6286	66.09	6.31×10^{-5}	3.63×10^{-5}	9.95×10^{-5}	-5.46×10^{-4}
20	4145	4573	43.60	4.40×10^{-5}	2.91×10^{-5}	7.32×10^{-5}	-8.01×10^{-4}
10	2480	2548	22.99	2.15×10^{-5}	1.25×10^{-5}	3.40×10^{-5}	-1.55×10^{-3}
2	546	547	1.85	3.71×10^{-4}	-9.85×10^{-4}	-9.84×10^{-4}	-8.30×10^{-3}

SECTION 4

ATTITUDE MEASUREMENT

4.1 Attitude Measurement System

As previously discussed, the vehicle uses the Advanced Inertial Reference System (AIRS) to measure the attitude of the vehicle with respect to an inertial reference. The AIRS platform, shown in Figure 35, consists of a hydraulically floated inner sphere inside an outer spherical case. The inner sphere contains the gyroscopes that are used to maintain the orientation of the inner ball relative to an inertial reference and the accelerometers which measure vehicle inertial accelerations and compute the velocity increments. The inner sphere is maintained at an initial alignment relative to inertial space by a system of hydraulic jets that rotate the inner ball in response to signals from the gyros. The inertial ball has three printed circuit resolver "driver" bands which are mounted as three orthogonal great circles on the outer surface of the ball. The platform attitude is measured in terms of the intersection points of the driver bands with a "receiver" band, also mounted as a great circle on the inner surface of the case. The positions of these intersections are defined in terms of the angles χ_1, χ_2, χ_3 measured along the receiver band and in terms of the angles ϕ_1, ϕ_2, ϕ_3 measured along the driver bands.

As illustrated in Figure 36, the three receiver band angles are all measured from the intersection with the receiver band of the vector $\underline{Q}_1$, in the plane of the receiver band, in a direction that would cause a right-handed screw to advance along the vector $\underline{Q}_3$ (which is perpendicular to the plane of the receiver band). The terminal points of the receiver band angles are defined as follows in terms of the receiver-driver band intersections and the triad of vectors $\underline{P}_2$, $\underline{P}_3$, $\underline{P}_1$, perpendicular to driver bands 1, 2, 3, respectively: the terminal point of χ_i (where i = 1, 2, or 3) occurs where the receiver band crosses driver band i going from the positive to the negative side of band i, as defined by its vector $\underline{P}_i$.

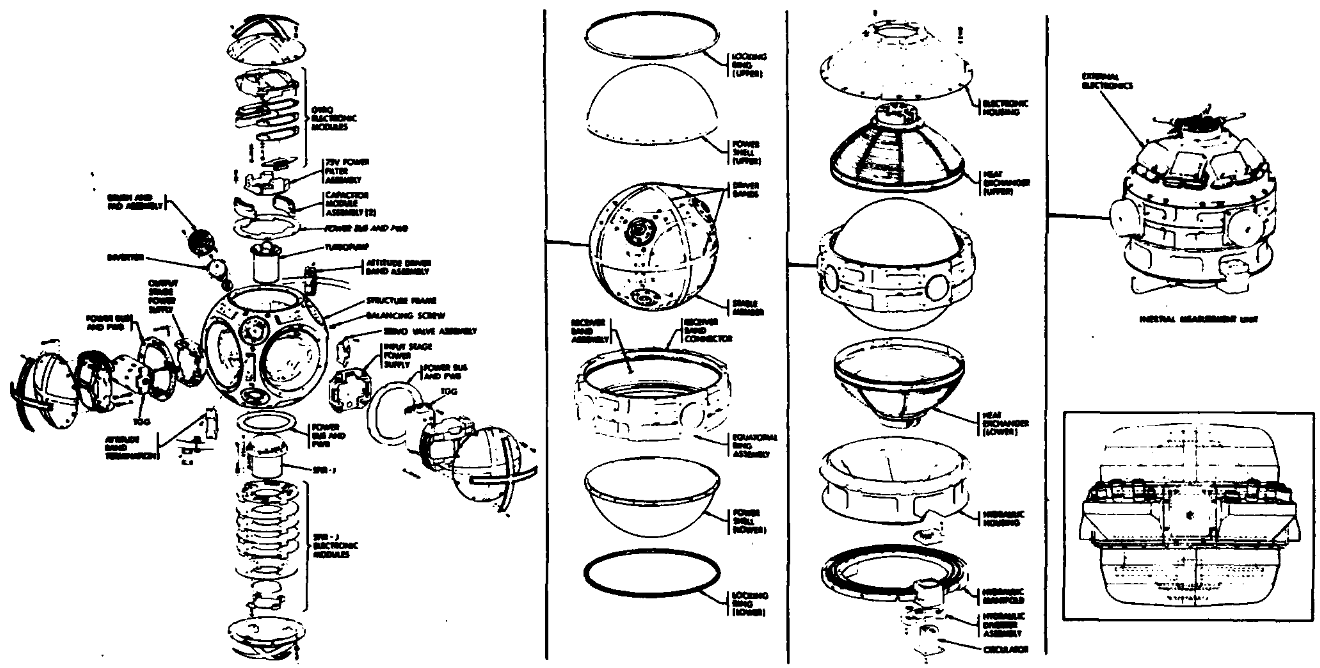

Figure 35. The AIRS platform.

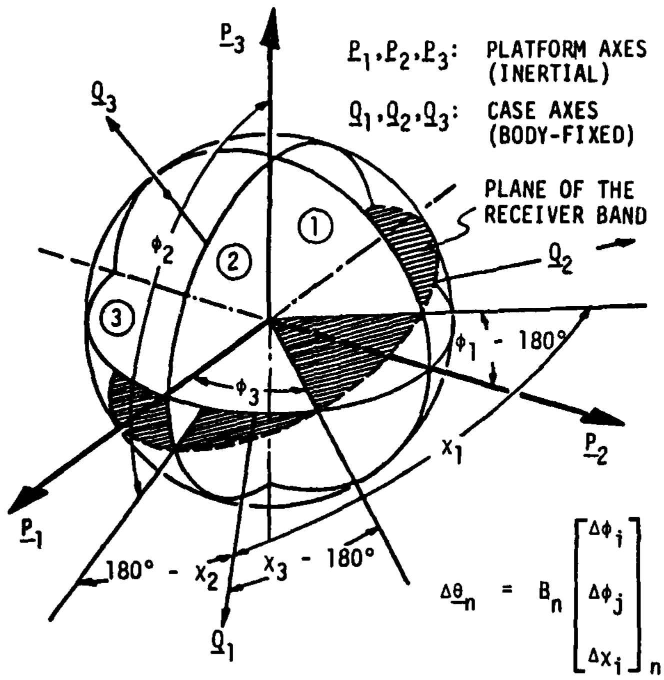

Figure 36. Definition of the AIRS band angles and body-angle increment relationship.

The three driver band angles ϕ_1, ϕ_2, ϕ_3, are measured from the intersections with the ball bands of the vectors $\underline{P}_2$, $\underline{P}_3$, $\underline{P}_1$, respectively, in directions that would advance right-handed screws along $\underline{P}_1$, $\underline{P}_2$, $\underline{P}_3$, respectively. The terminal points of the driver band angles are where the driver bands cross the receiver band from the positive to the negative side as defined by its vector $\underline{Q}_3$.

It is important to note that the point of intersection of any driver band with the receiver band is accurately measurable only if the angle of intersection between these bands is greater than 45 degrees. Fortunately, at least two of the driver bands fulfill this intersection requirement for any ball-case orientation, and only the intersections of these two driver bands with the receiver band need be measured to determine the orientation. The AIRS programs used in this study are capable of selecting those driver bands that have the required ≥45° intersection with the receiver band and are capable of determining the ball-case orientation from any selected pair of driver band angles (e.g., ϕ_i, ϕ_j) in combination with the corresponding receiver band angles (e.g., χ_i, χ_j).

4.2 Attitude Data Processing

The incremental updating of attitude errors following their initialization at the beginning of the Stage 3 burn is simple and convenient for an AIRS based autopilot. This incremental approach, illustrated in Figure 37, requires the computation of an incremental transformation matrix B which transforms a set of two driver band angle increments ($\Delta\phi_i$, $\Delta\phi_j$) and one receiver band angle increment ($\Delta\chi_i$) into the corresponding increments in body angles ($\Delta\theta_1$, $\Delta\theta_2$, $\Delta\theta_3$).

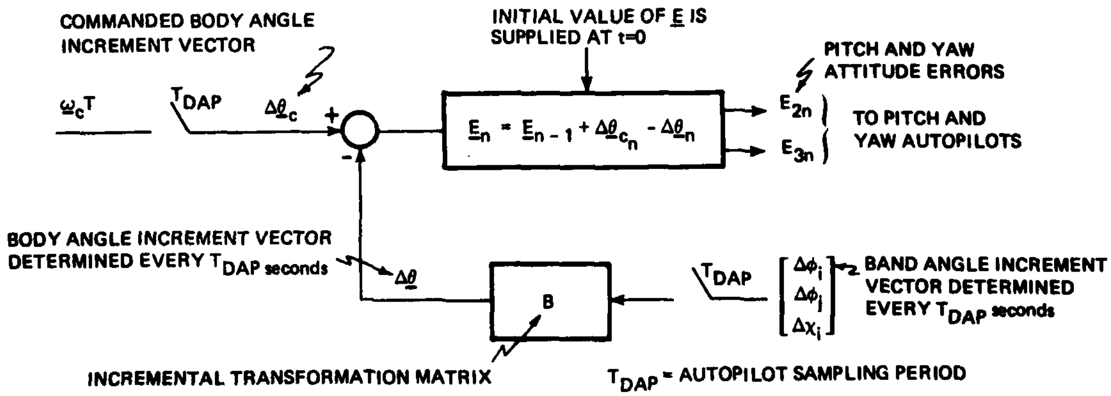

Figure 37. Incremental updating of attitude errors.

The transformation relationship is

$$\begin{bmatrix} \Delta\theta_1 \\ \Delta\theta_2 \\ \Delta\theta_3 \end{bmatrix} = [B] \begin{bmatrix} \Delta\phi_i \\ \Delta\phi_j \\ \Delta\chi_i \end{bmatrix}$$

where

$$[B] = \begin{bmatrix} d_{11} & d_{12} & d_{13} \\ d_{21} & d_{22} & d_{23} \\ d_{31} & d_{32} & d_{33} \end{bmatrix}$$

and

$$d_{11} = -w \cos \phi_i \cos \phi_j$$

$$d_{12} = 0$$

$$d_{13} = -1$$

$$d_{21} = w^2 \sin \phi_j \sin \chi_j$$

$$d_{22} = w^2 \cos \phi_i \sin \chi_i$$

$$d_{23} = 0$$

$$d_{31} = -w^2 \sin \phi_j \cos \chi_j$$

$$d_{32} = w^2 \cos \phi_i \cos \chi_i$$

$$d_{33} = 0$$

$$w = 1/\sin (\chi_i - \chi_j)$$

Ideally, the B-matrix should be updated every autopilot sampling period prior to the computation of each new set of body-angle increments. However, the computation of the trigonometric functions of the band angles which make up the elements of B is such a time-consuming process that it is desirable to consider ways of reducing the computation time by approximating the elements of B and/or updating these elements less often than every autopilot cycle.

AIRSBAE Method

Various schemes for approximating the B-matrix and updating it less frequently were studied at CSDL in 1973 and 1974 as part of the development of the .single-rotation-axis (SRA) autopilot. This autopilot, which was developed for large attitude maneuvers of a space vehicle under the control of reaction jets, takes advantage of a theorem of Euler, according to which the attitude of a body may be changed from one orientation to any other orientation by rotating the body about an axis which is fixed to the vehicle and stationary in inertial space. The SRA autopilot study showed that if the values of the band angles used in the B-matrix updates are extrapolated every 0.45 seconds into the middle of the next 0.45-second time interval, the B-matrix based on these extrapolated angles can be employed over the entire 0.45-second interval, with negligible degradation in SRA autopilot performance compared to updating B precisely every 0.03 seconds. This method of updating the B-matrix has been termed "AIRSBAE" ("AIRS band angle extrapolation").

The AIRSBAE method is illustrated in Figure 38, where the matrix updating interval is designated as T_s. Here, it should be noted that

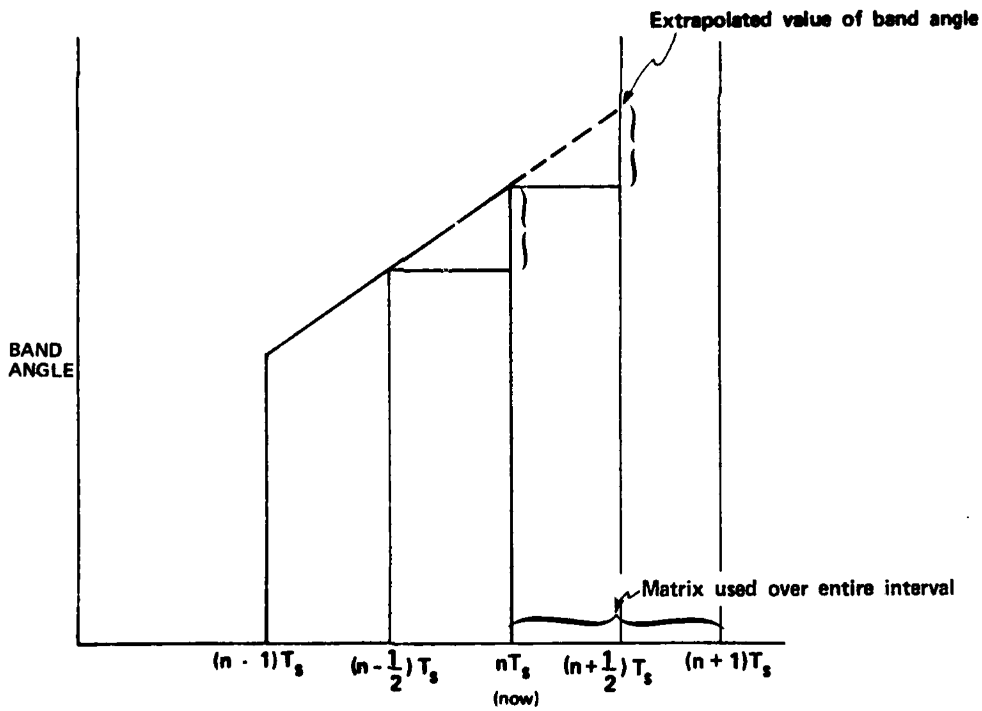

Figure 38. Pictorial representation of AIRSBAE.

the same symbol (T_s) is used for both the steering-loop sampling period and the B-matrix updating interval because the studies carried out in this thesis and in the SRA autopilot investigations have shown that the choice of T_s = 0.45 seconds for both the sampling period and updating interval is reasonable for the dynamic requirements considered. This period amounts to fifteen of the 30 ms autopilot sampling periods which are used in this thesis (as well as in the earlier SRA autopilot studies). However, the investigations of B-matrix updating techniques described below consider also other values of the B-matrix updating interval of 2, 30, and 45 autopilot cycles, which may not be the same as the optimum sampling period for steering-loop computations. Thus, the symbol T_s can represent a different time interval in the case of the B-matrix updating than in the case of steering.

Referring to Figure 38, it is seen that the AIRSBAE method predicts the band angles halfway through the next T_s interval by taking half the difference between the present value of each band angle and the value measured T_s seconds previously, and adding that difference to the present value of the band angle.

The dead zones and allowed terminal errors in both angular velocity and attitude in the SRA autopilot provided some tolerance for the errors resulting from the infrequent updating of the B-matrix in the AIRSBAE approach. However, the dynamic requirements of other autopilots, such as the boost autopilot being considered in this thesis, may not permit the errors in attitude and estimated angular rate which result from the AIRSBAE approach.

One aspect of particular concern in applying the AIRSBAE method to the third stage boost autopilot with fuel depletion and gamma-time-on-target guidance is the relatively large step change in the B-matrix occurring every 0.45 seconds as the result of the large angular rates associated with these guidance methods. This step change in B can produce autopilot transients which might not be considered acceptable in these boost applications.

AIRSME4 Method

The AIRSBAE method was considered along with other B-matrix updating approaches in terms of the Stage 3 boost autopilot and the dynamic requirements imposed by fuel depletion guidance and gamma-time-on-target guidance. The most promising alternative to the AIRSBAE technique has been termed "AIRSME4" ("AIRS matrix extraploation 4").

This alternative, which is illustrated in Figure 39, extrapolates the band angles to the end of the next T_s interval (instead of to the middle,

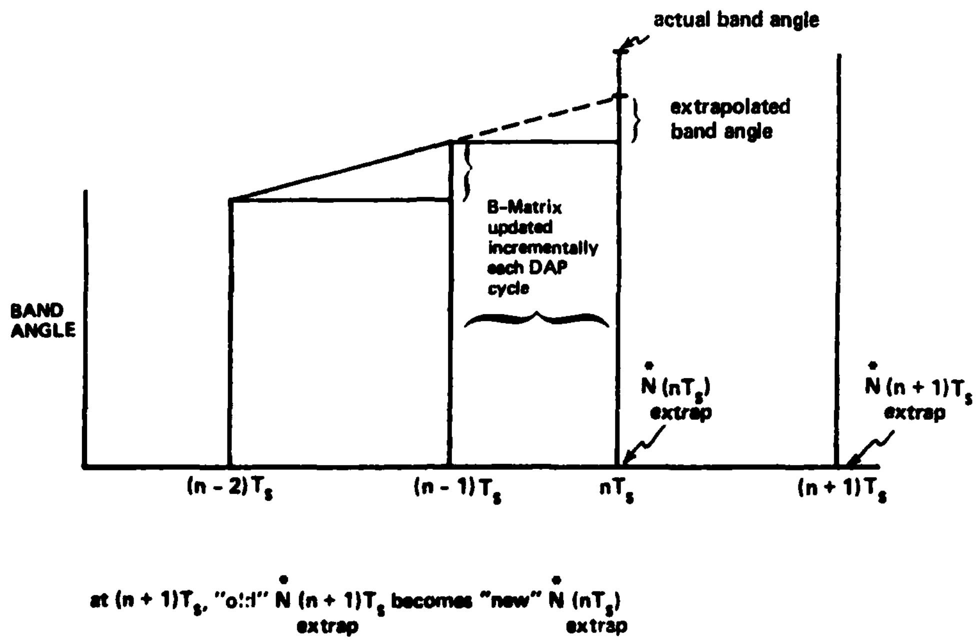

Figure 39. Pictorial representation of AIRSME4.

as in AIRSBAE), and computes a predicted B-matrix from these extrapolated angles. The predicted B-matrix from the previous T_s-interval is then subtracted from the new predicted matrix and the resulting matrix difference divided by the number of autopilot cycles in T_s to obtain an incremental B-matrix, ΔB. The B-matrix is then updated every autopilot cycle within T_s by adding ΔB to the B-matrix determined in the previous cycle, starting with the predicted B-matrix from the previous T_s interval.

The band angle extrapolation approach used in AIRSME4 is based on differencing the band angles over T_s, as is done in AIRSBAE, but in AIRSME4 the entire difference is added (rather than half the difference) to perform the extrapolation.

The incremental updating of the B-matrix every autopilot cycle by the AIRSME4 approach results in a smoother operation of the autopilot

than with AIRSBAE, and accomplishes this improvement with only a small increase in the computational burden.

Band Angle Switchover

The switching of band angles, which can occur of any autopilot cycle, is treated in the following manner as a special case in both AIRSBAE and AIRSME4:

(1) The B-matrix is recomputed in terms of the new set of band angles as soon as the switchover occurs.

(2) The switchover value of the B-matrix is retained for a pre-specified number of autopilot cycles, $U_{switchover}$, which is equal to 5 in all the simulation results presented in this thesis.

(3) When $U_{switchover}$ autopilot cycles, have elapsed, the band angles are again extrapolated (to the middle of T_s in AIRSBAE and to the end of T_s in AIRSME4) and the standard B-matrix updating approach is resumed. In the case of AIRSME4 the value of B needed at the beginning of the new T_s interval is computed from current band angles.

Computation Requirements

A comparison of the computation times required by AIRSBAE and AIRSME4 for an updating time interval of T_s = 0.45 sec is presented in Table 15. Here, it is seen that AIRSBAE requires 4.65 ms per 0.45 sec, while AIRSME4 requires 5.38 ms per 0.45 sec. Thus, the difference in computation times of the two updating methods is an almost negligible value of 0.73 ms per 0.45 sec (which is less than 0.05 ms per 30 ms autopilot cycle). However, it should be pointed out that both B-matrix techniques are very substantial improvements over updating the B-matrix from its trigonometric functions every 30 ms autopilot cycle, which would require about 36 ms per 0.45 sec. The reduction from 36 ms per 0.45 sec to an approximate time of 5 ms for AIRSBAE and AIRSME4 amounts to a reduction from an 8% computation load to a 1.1% computation load for attitude data processing.

4.3 Idealized AIRS Error Study

The first phase of the attitude measurement study evaluated the purely geometric errors resulting from AIRSBAE and AIRSME4 when the

Table 15. Comparison of computational requirements of AIRSBAE and AIRSME4* based on the Honeywell 701P computer.

Operations Common to Both AIRSBAE and AIRSME4		Units	Computation Time (m sec) per T_s
1. Update Incremental Transformation Matrix at Beginning of T_s			
4 sin/cos @ 125 units**	=	500	2.23
14 Mult./Div @ 3 units	=	42	0.19
1 Subtr. @ 1 unit	=	1	0.0045
2. Matrix/Vector Multiplication at Each Autopilot Cycle (T_{DAP})			
9 Mult. @ 3 units × 15	=	405	1.80
6 Add. @ 1 unit × 15	=	90	0.40
Totals		1038	4.62
AIRSBAE			
1. Common Operations	=	1038	4.62
2. Extrapolate Band Angles Over T_s			
6 Add. @ 1 unit	=	6	0.03
(Division by 2 is handled by a SHIFT operation which takes neglible time)			
Totals		1044	4.65
AIRSME4			
1. Common Operations	=	1038	4.62
2. Difference Incremental Matrices at T_s			
9 Subtr. @ 1 unit	=	9	0.04
3. Division of T_s Increments by T_{DAP}			
9 Div. @ 3 units	=	27	0.12
4. Addition of T_{DAP} Increments to Matrix at Each Autopilot Cycle			
9 Add @ 1 unit × 15	=	135	0.60
Totals		1209	5.38

*Neglecting Computer Bookkeeping Operations, assuming T_s = 15 autopilot cycles = 0.45 sec

**1 Unit = 4.45 μsec,

boost vechicle is rotating at constant and equal rates about the pitch and yaw axes, with no motion about the roll axis. Two programs were developed for AIRSBAE and AIRSME4 which determine the errors in computed body-angle increments per degree of separate pitch, yaw and roll rotations which occur when the vehicle rotates at specified rates at various orientations. Vehicle orientations considered were defined in terms of roll Euler angles of 0°, 45°, 90°, 135°, and 180° pitch Euler angles which are incremented by 30° from -180° to +180° and yaw Euler angles which are incremented by 30° from -90° to +90°. These programs also search for the worst-case errors in body-angle increments per degree rotation for each pair of equal pitch and yaw angular rates assumed. Rates were considered which yield pitch and yaw rotations over T_s seconds of 2.5°, 5°, 10°, and 20°. The programs compute the body-angle errors at only those points where there is not a switchover of the attitude bands over the T_s intervals used for computing these errors. A comparison of the worst-case body-angle errors per degree rotation about any body axis is given in Table 16. This comparison. indicates consistently lower errors for AIRSME4.

4.4 Autopilot Simulation Study Based on the STAR Program

The next step in the evaluation of the attitude measurement study was to use AIRSBAE (renamed AIRS) and AIRSME4 (renamed AIRSX) as subroutines in the STAR simulation program. The STAR program is basically a simulation of the Stage III vehicle operating in inertial space with no guidance system. The vehicle is steered by commanding a pitch rate profile that approximates the profile seen in fuel depletion guidance. This profile consists of a parabolically-increasing pitch rate command until the pitch rate reaches 31.25 deg/sec, then a constant 31.25 deg/sec rate is commanded for two seconds. At that time a linearly-decreasing rate signal is commanded for two seconds, followed by a steady state 10 deg/sec rate signal. This commanded pitch profile is shown on channel two of the response curves. The displayed variables are given below.

PITCH RATE - The vehicle pitch rate in deg/sec.

PITCH RATE COMMAND - The commanded pitch profile

INDICATED RATE - The vehicle pitch rate as indicated by the AIRS (AIRSBAE) or AIRSX (AIRSME4) platform. In a NOAIRS run, this measured rate is not used as the feedback signal.

Table 16. Maximum errors at the end of T_s (T_s = 0.45 sec).

Pitch Rate	$2.5°/T_s$		$5.0°/T_s$		$10.0°/T_s$		$20.0°/T_s$	
Initial Platform Roll Angle	BAE	ME4	BAE	ME4	BAE	ME4	BAE	ME4
0	2.67×10^{-2}	3.53×10^{-3}	5.53×10^{-2}	1.16×10^{-2}	1.20×10^{-1}	4.38×10^{-2}	2.44×10^{-1}	*BSW
45	2.58×10^{-2}	2.75×10^{-3}	5.22×10^{-2}	1.32×10^{-2}	1.068×10^{-1}	3.15×10^{-2}	2.22×10^{-1}	1.14×10^{-1}
90	2.67×10^{-2}	3.59×10^{-3}	5.53×10^{-2}	1.61×10^{-2}	1.20×10^{-1}	4.38×10^{-2}	2.44×10^{-1}	*BSW
135	2.67×10^{-2}	2.46×10^{-3}	5.47×10^{-2}	1.02×10^{-2}	1.15×10^{-1}	4.40×10^{-2}	2.22×10^{-1}	1.52×10^{-2}
180	2.67×10^{-2}	3.59×10^{-3}	5.53×10^{-2}	1.61×10^{-2}	1.20×10^{-1}	4.38×10^{-2}	2.44×10^{-1}	*BSW

*The three cases denoted by "BSW" yielded a band switchover at every point investigated. Since the error-computing programs reject all points where switchovers occur, no body-angle errors were computed in these cases.

ENGINE DEFLECTION - The engine actuator pitch deflection in degrees.

PITCH ATTITUDE - The vehicle pitch attitude in degrees.

REJECTED BAND - The driver band that has an intersection with a receiver band of less than 45 degrees. Since only two band intersections are required to completely determine the orientation of the AIRS inner sphere relative to the case, this band is not needed and is rejected.

Plots of the above variables versus time are presented in Figures 40 through 55 for various combinations of the following conditions:

(1) Type of feedback:

(a) Ideal feedback (denoted as "NOAIRS") in which the actual body-angle increments are employed for feedback.

(b) AIRS-based feedback in which the feedback body-angle increments are computed either by an "AIRS" subroutine (based on the AIRSBAE approach) or by an "AIRSX" subroutine (based on the AIRSME4 method).

(2) AIRS errors:

(a) If the types of errors in the AIRS band-angle measurements are not specified in the title of the simulation run, these errors have been assumed zero.

(b) The measured angle of any driver or receiver band contains a deterministic error term which is a function of the angles of both the driver and receiver band angles which define any particular band intersection. The maximum magnitude of this error term is less than ten arc minutes although its rate of change can be as large as 3 degrees per degree of band angle change. A table lookup representation of the deterministic errors based on laboratory measurements is employed when these errors are simulated.

(c) A second source of band angle measurement errors is the random electrical noise. This noise is represented in simulation runs by a random number generator whose standard deviations are pessimistically assumed to be 180 arcseconds for the driver bands and 20 arc seconds for the receiver bands.

(3) Time interval between updates of B based on extrapolated band angles:

The number of 30 ms autopilot cycles, UMAX, between updates of the B-matrix based on extrapolated band angles is considered to have the following values in the simulation runs: 2, 15 (nominal case), 30 and 45.

The simulation runs in Figures 40 through 55 are described in terms of the above conditions in Table 17.

It is seen in the figures of simulation runs that increasing UMAX past 15 cycles gives a significant decrease in the fidelity of the feedback signal for both AIRS and AIRSX runs. For all UMAX values the AIRSX data is of significantly higher quality than the AIRS data. This is because the incremental matrix is updated at each autopilot cycle in AIRSX, rather than at intervals of UMAX autopilot cycles as in AIRS.

Table 17. STAR simulation runs.

Run No.	Mode	Ideal Feedback	UMAX	AIRS Noise	Deterministic Errors
4/00	NOAIRS	yes	15	no	no
4/40	NOAIRS	yes	15	no	no
4/21	AIRS	no	2	no	no
4/22	AIRS	no	15	no	no
4/23	AIRS	no	30	no	no
4/24	AIRS	no	45	no	no
4/25	AIRS	no	15	yes	no
4/26	AIRS	no	15	no	yes
4/27	AIRSX	no	2	no	no
4/28	AIRSX	no	15	no	no
4/29	AIRSX	no	30	no	no
4/30	AIRSX	no	45	no	no
4/31	AIRSX	no	15	yes	no
4/32	AIRSX	no	15	no	yes
4/33	AIRS	no	15	yes	yes
4/34	AIRSX	no	15	yes	yes

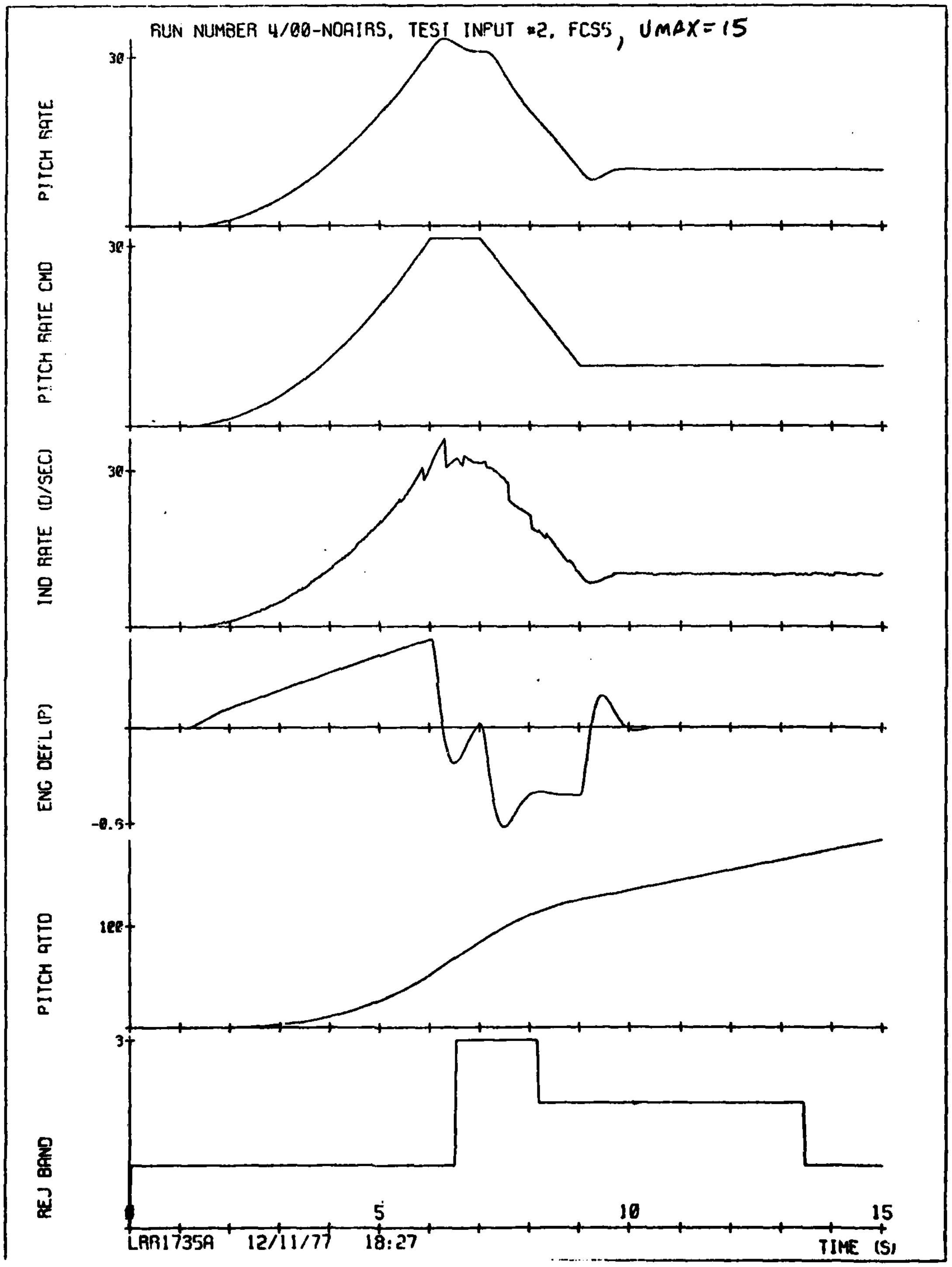

Figure 40. Ideal attitude feedback, AIRS indicated rate.

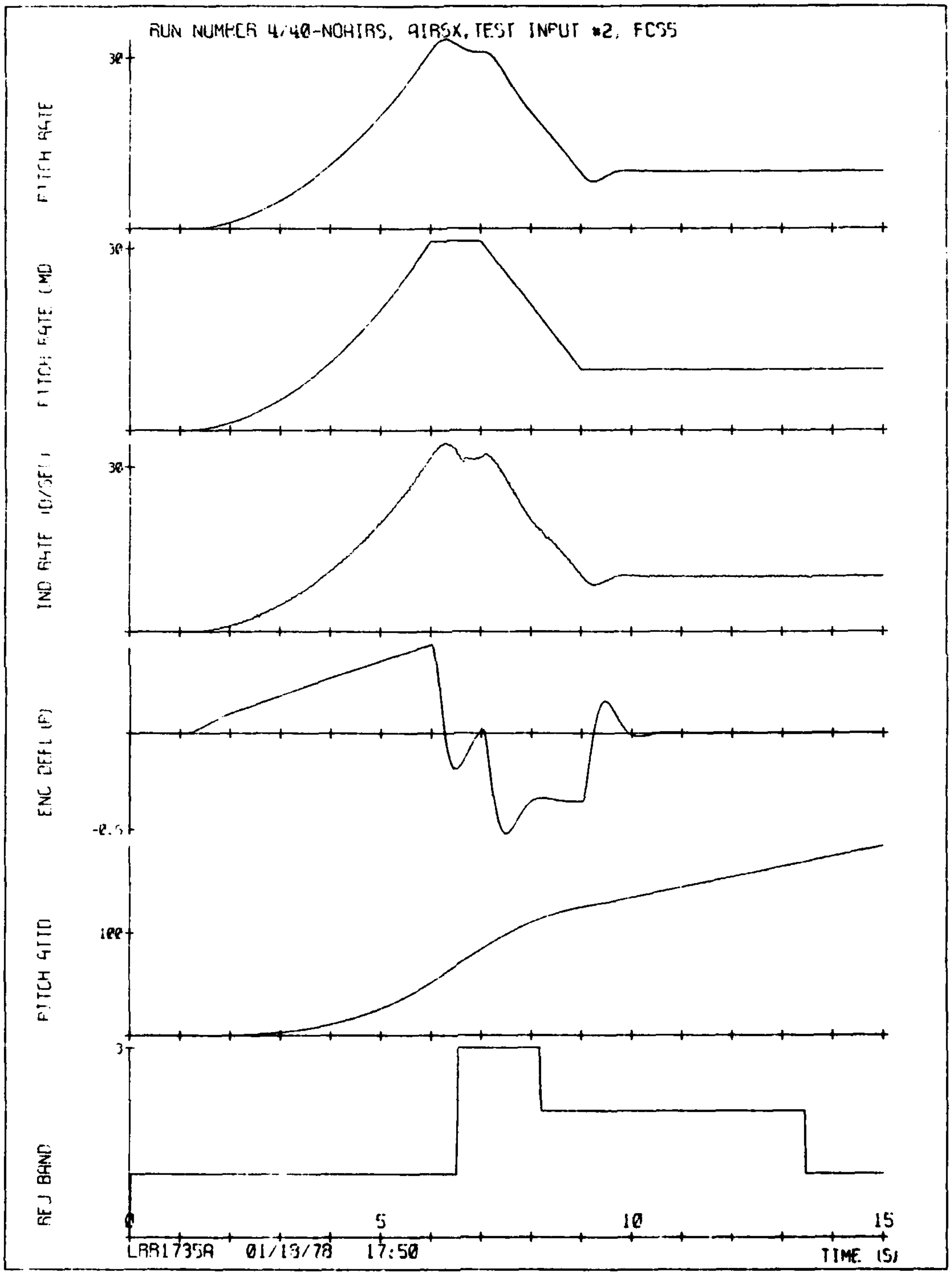

Figure 41. Ideal attitude feedback, AIRSX indicated rate.

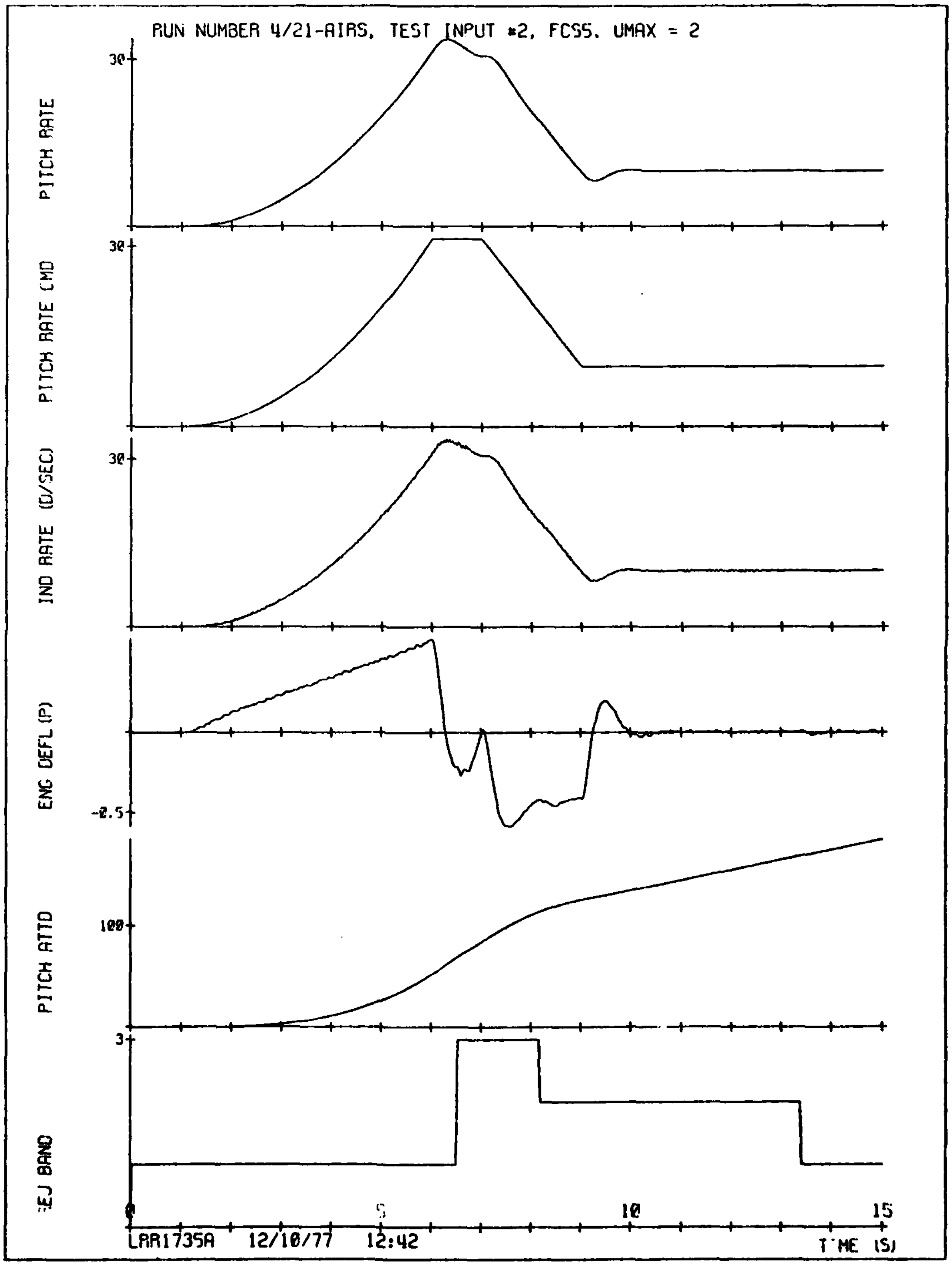

Figure 42. AIRS attitude feedback, UMAX = 2.

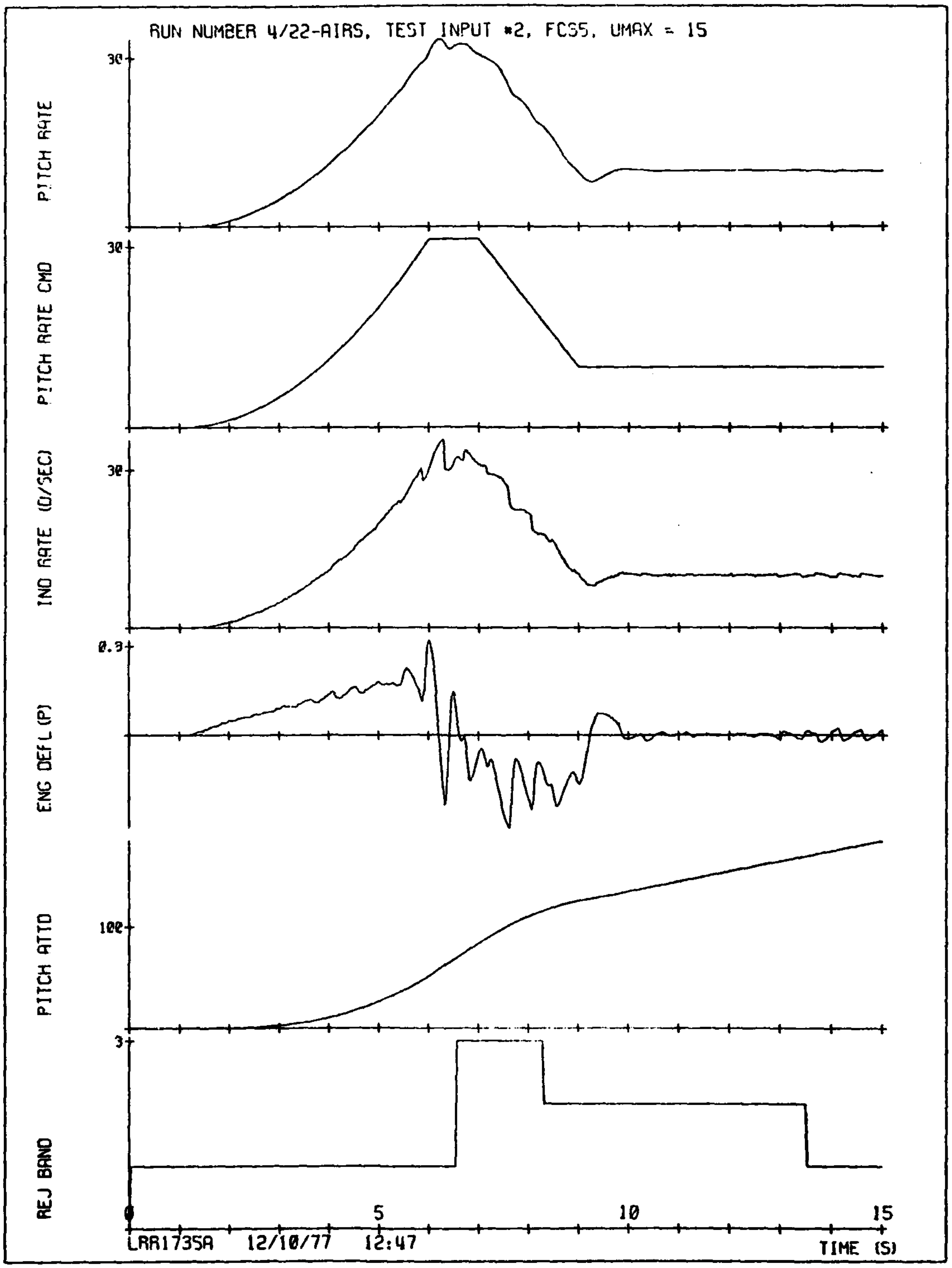

Figure 43. AIRS attitude feedback, UMAX = 15.

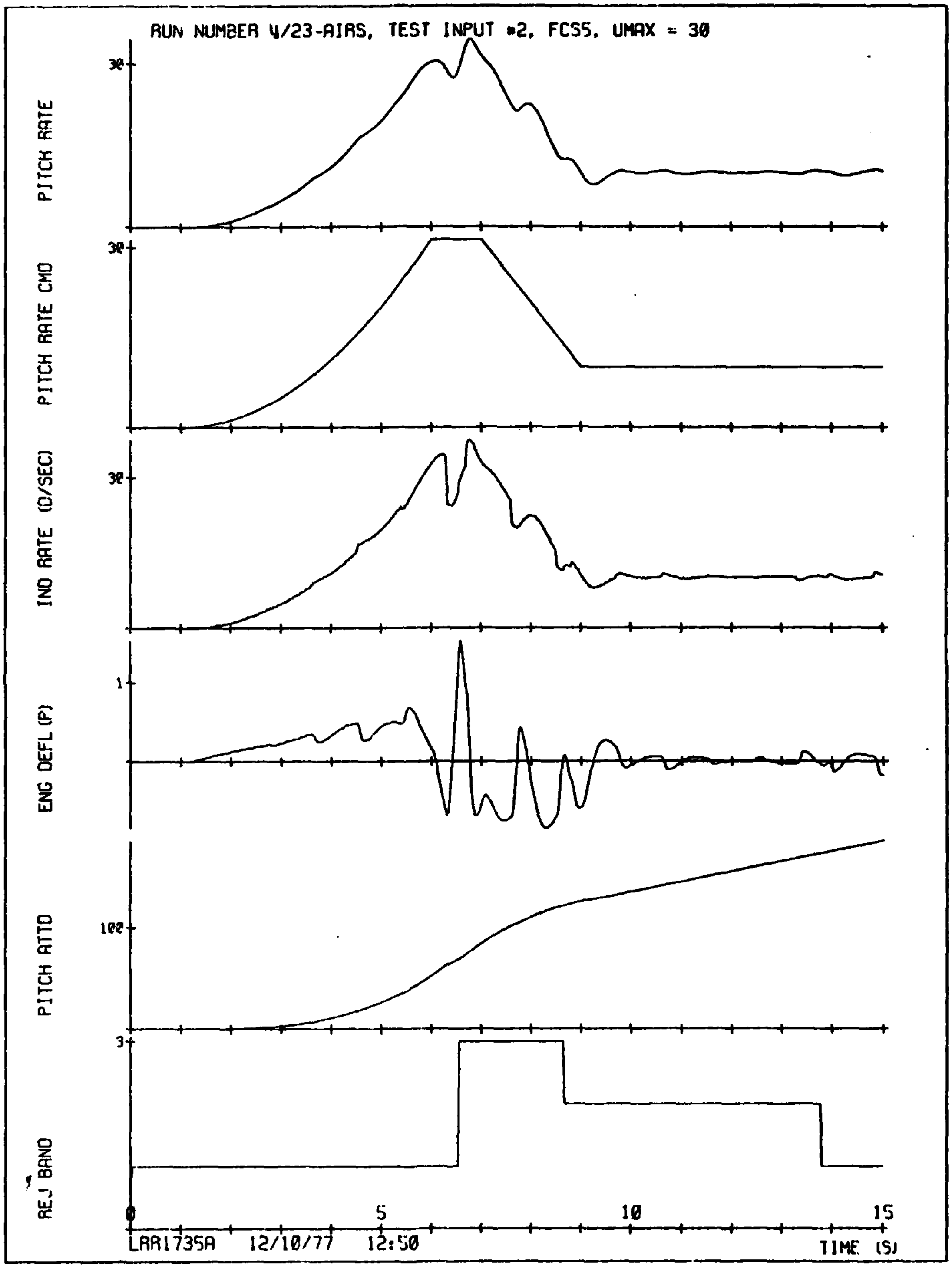

Figure 44. AIRS attitude feedback, UMAX = 30.

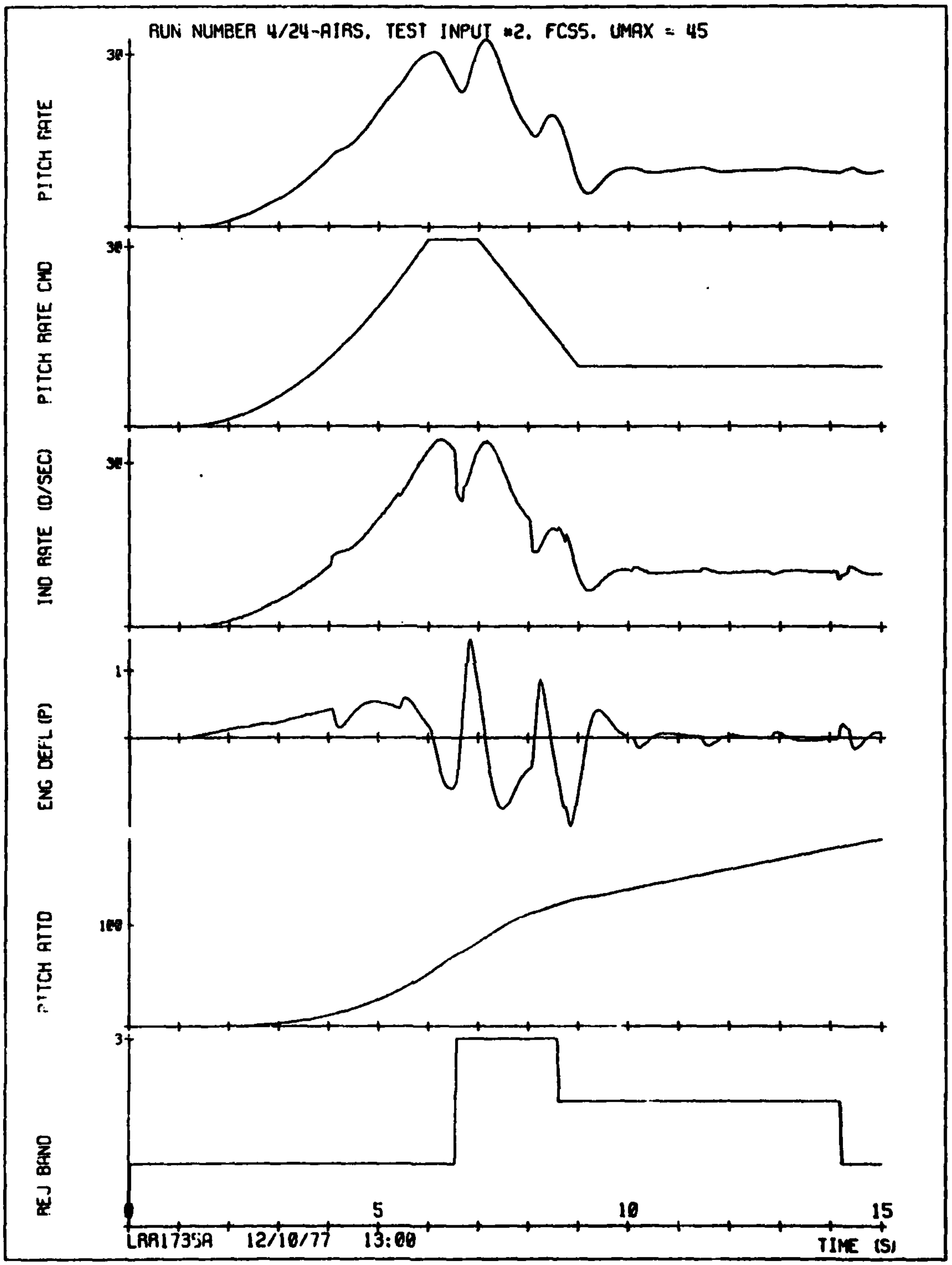

Figure 45. AIRS attitude feedback, UMAX = 45.

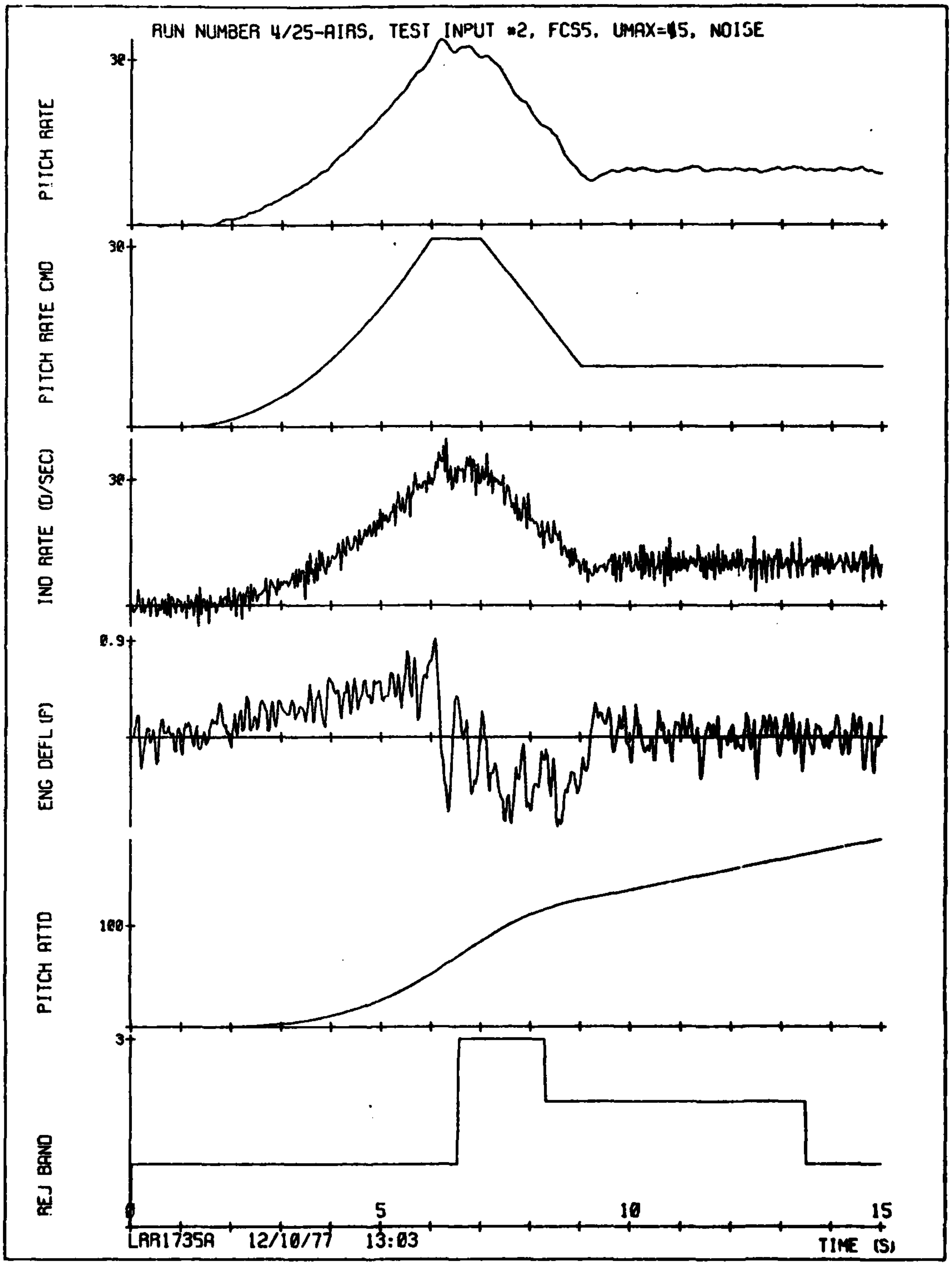

Figure 46. AIRS attitude feedback, with randon noise, UMAX = 15.

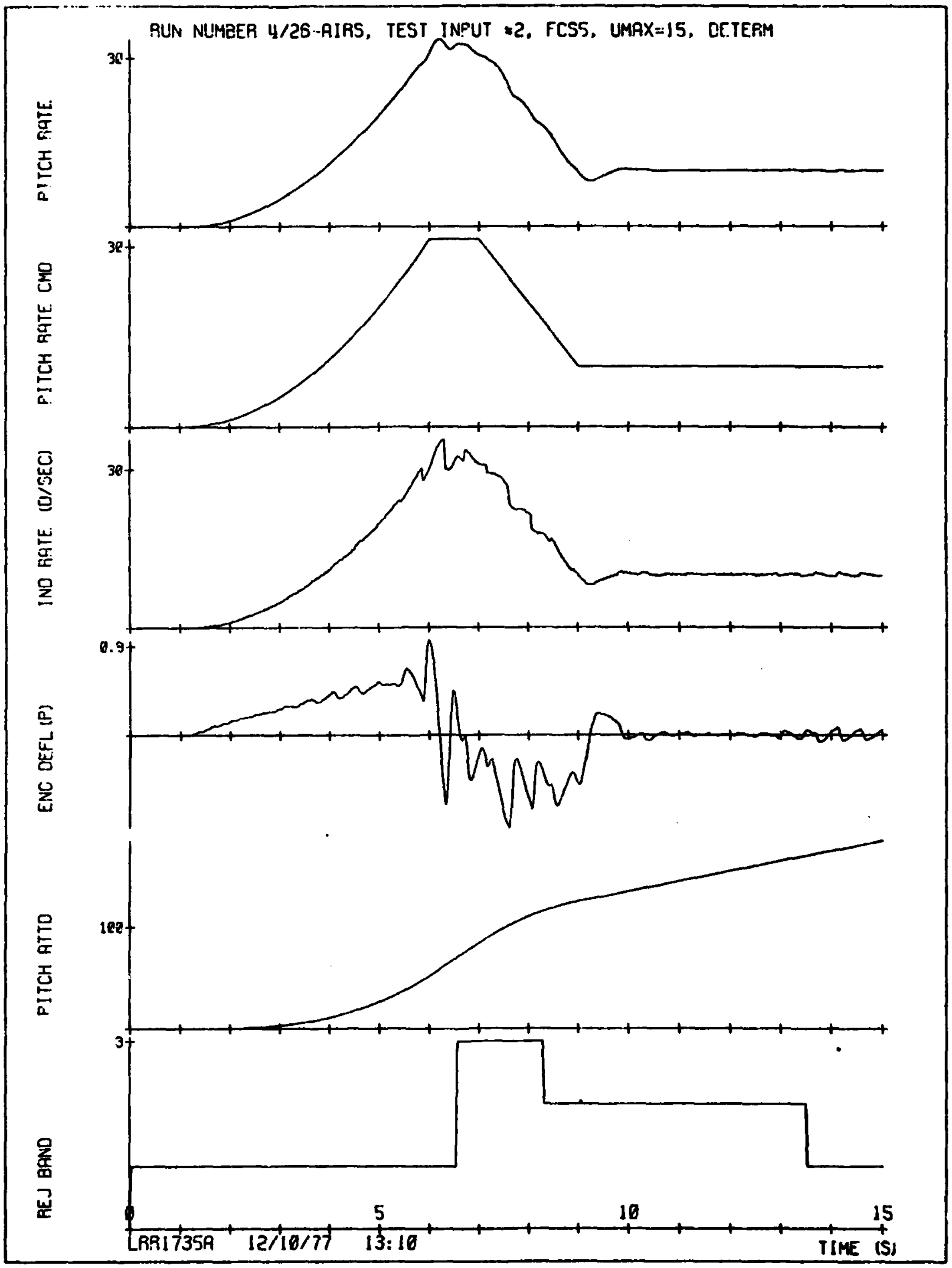

Figure 47. AIRS attitude feedback with deterministic errors, UMAX = 15.

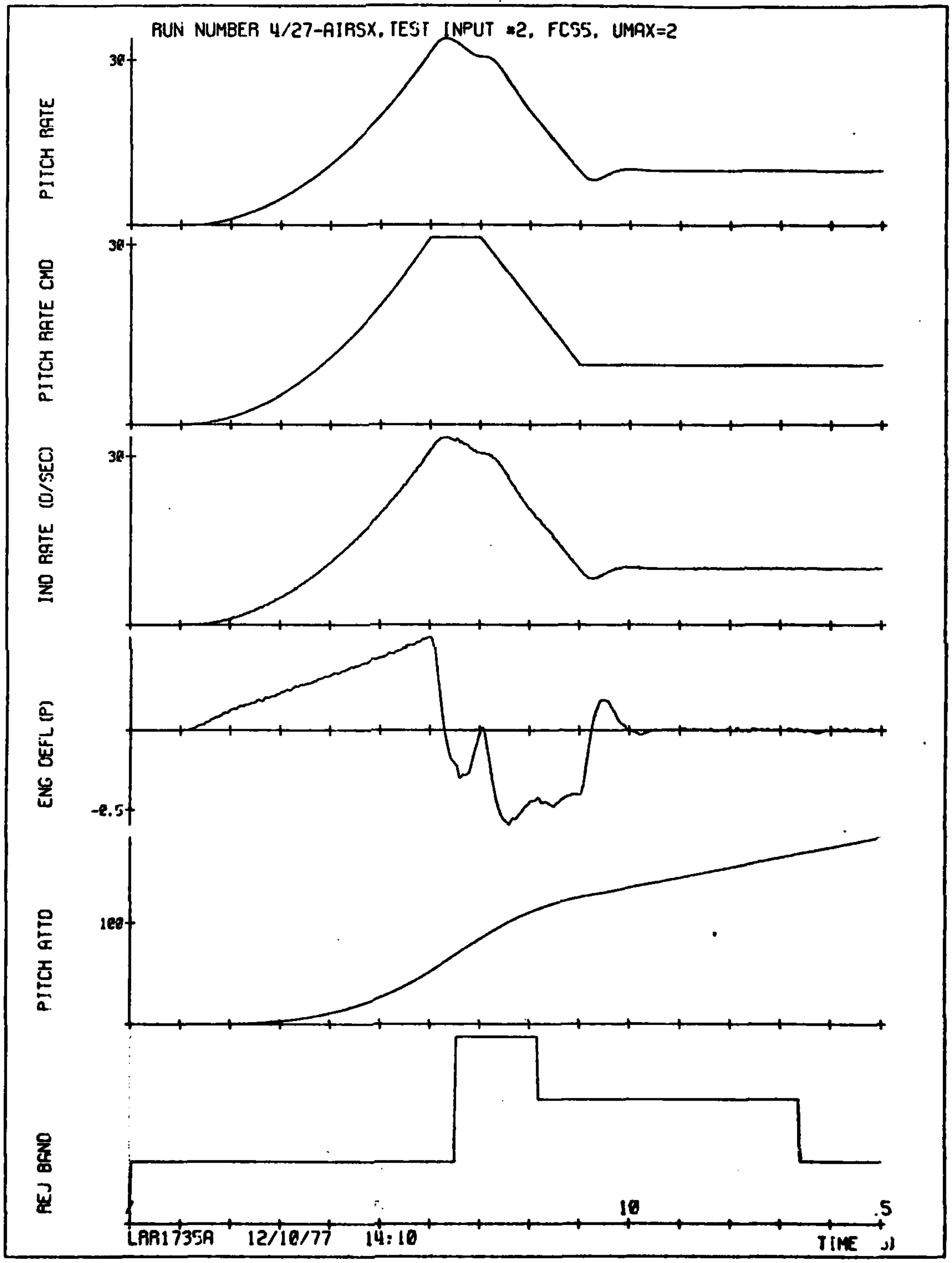

Figure 48. AIRSX attitude Feedback, UMAX = 2.

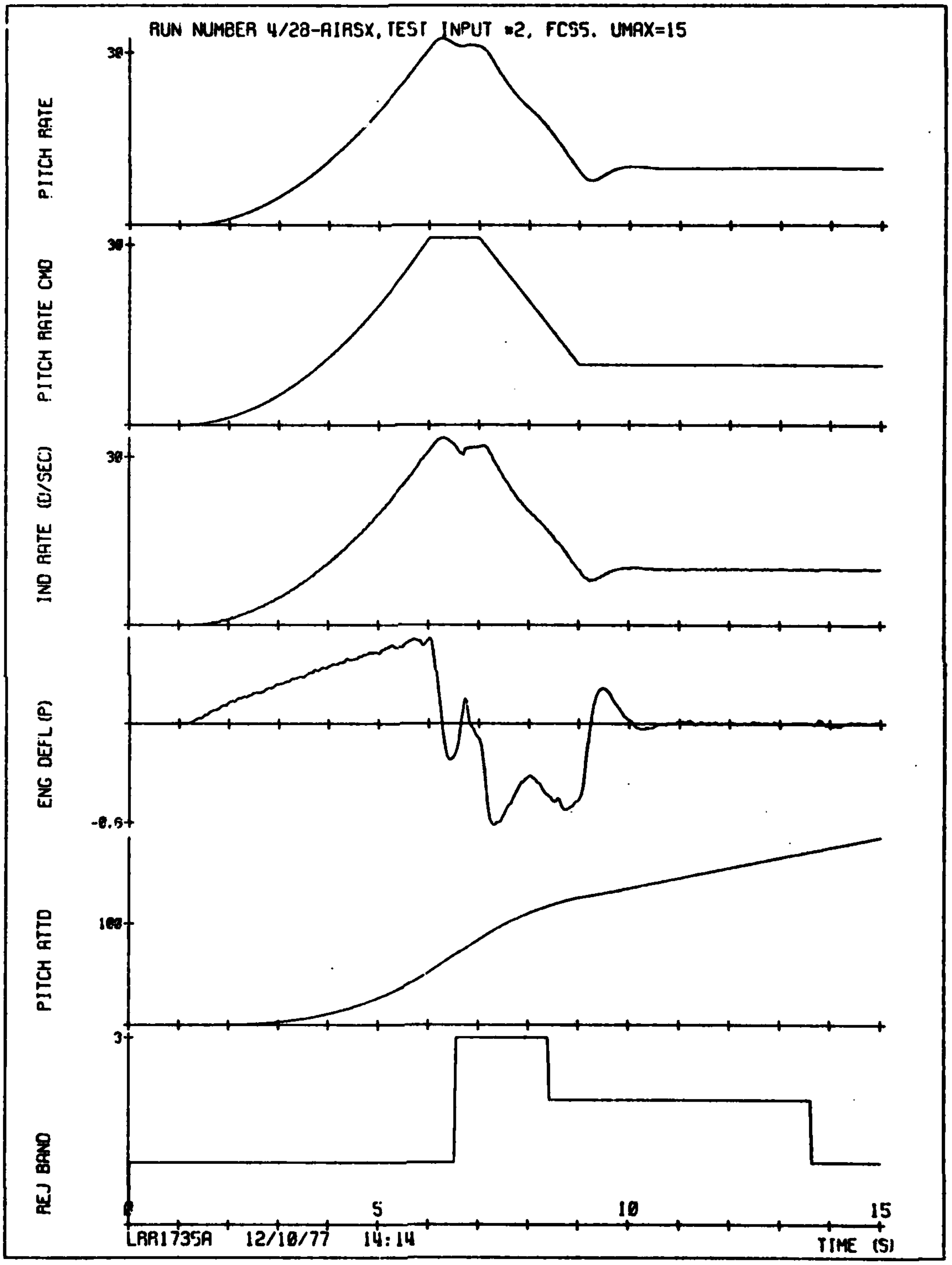

Figure 49. AIRSX attitude feedback, UMAX = 15.

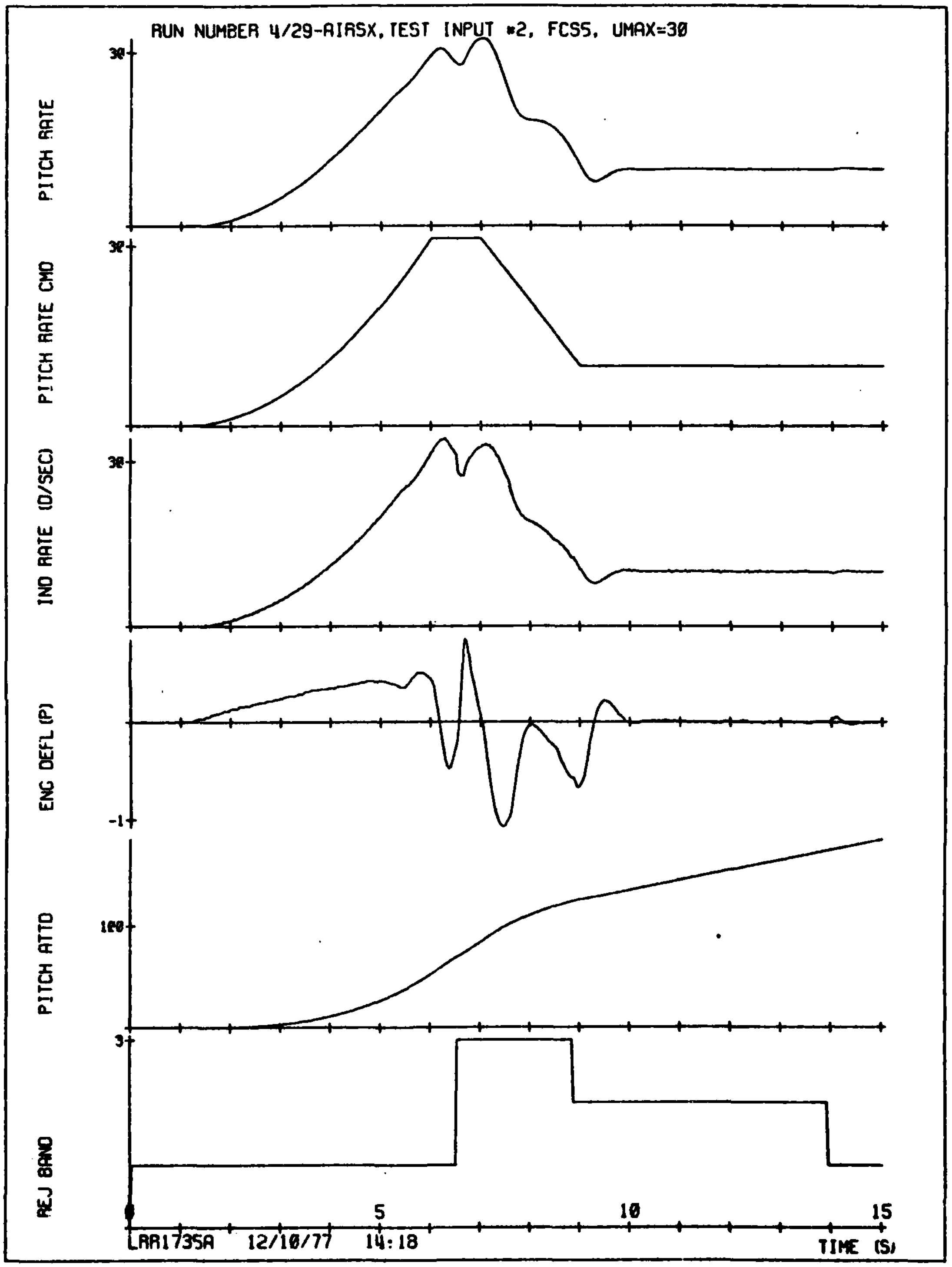

Figure 50. AIRSX attitude feedback, UMAX = 30.

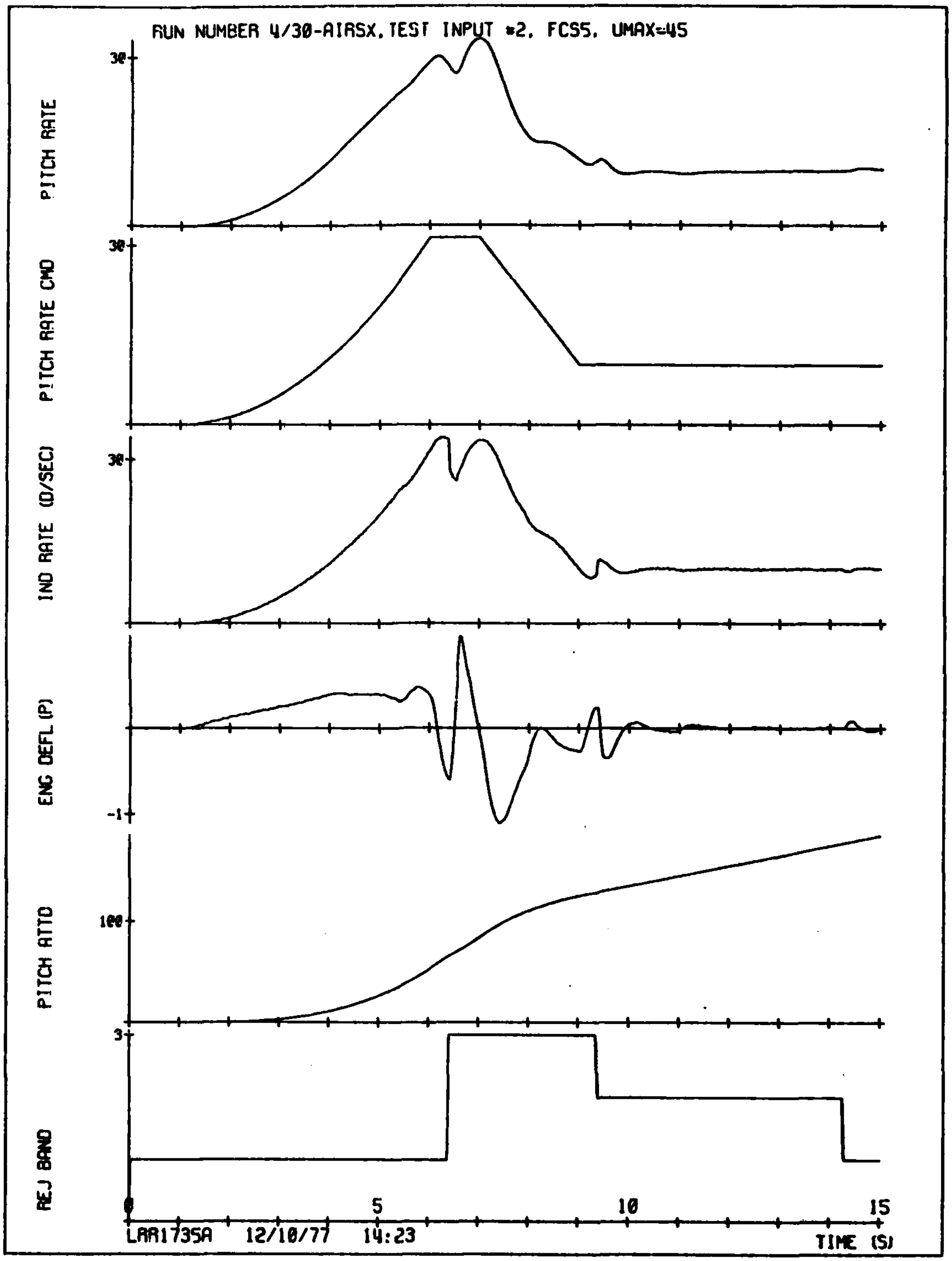

Figure 51. AIRSX attitude feedback, UMAX = 45.

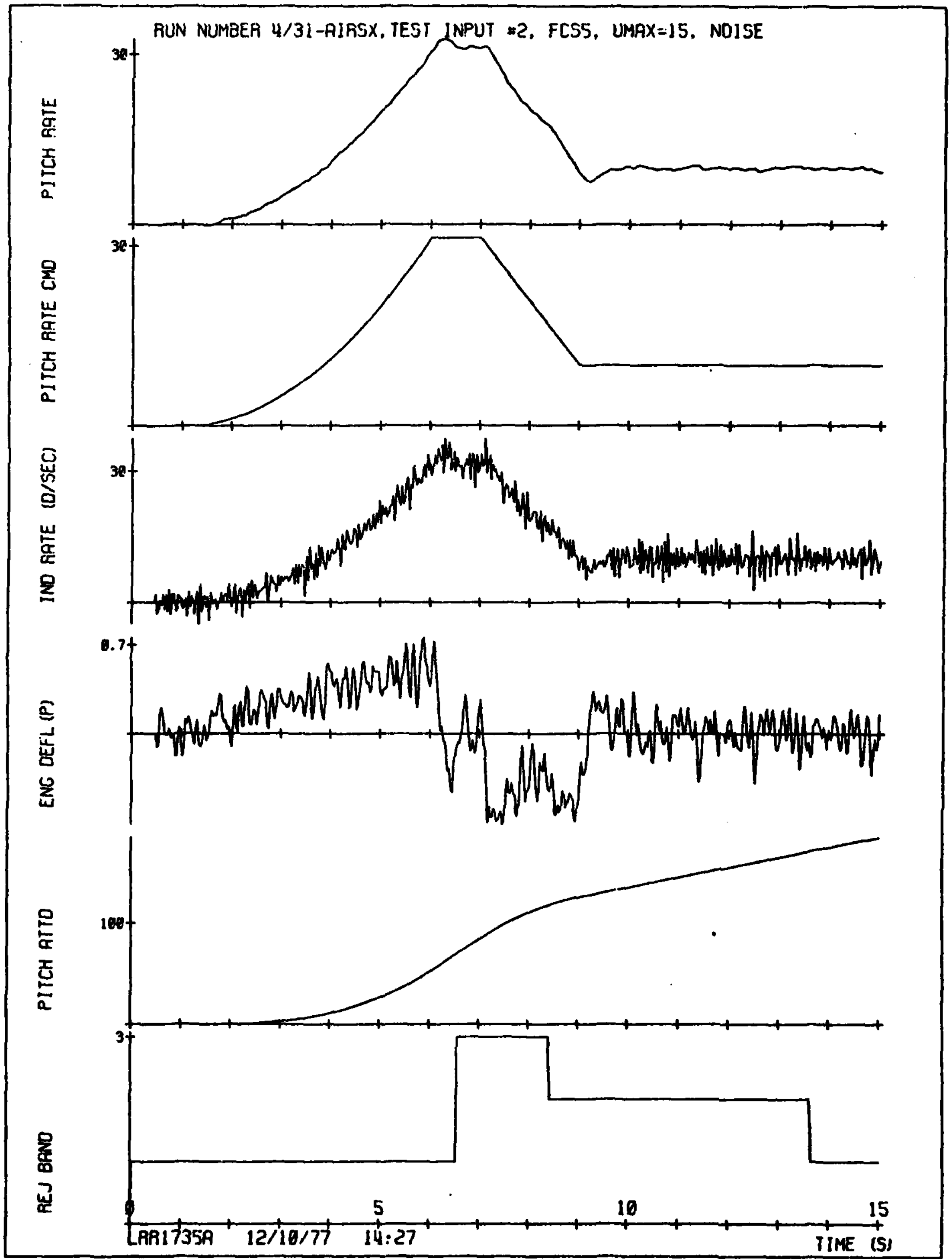

Figure 52. AIRSX attitude feedback with random noise, UMAX = 15.

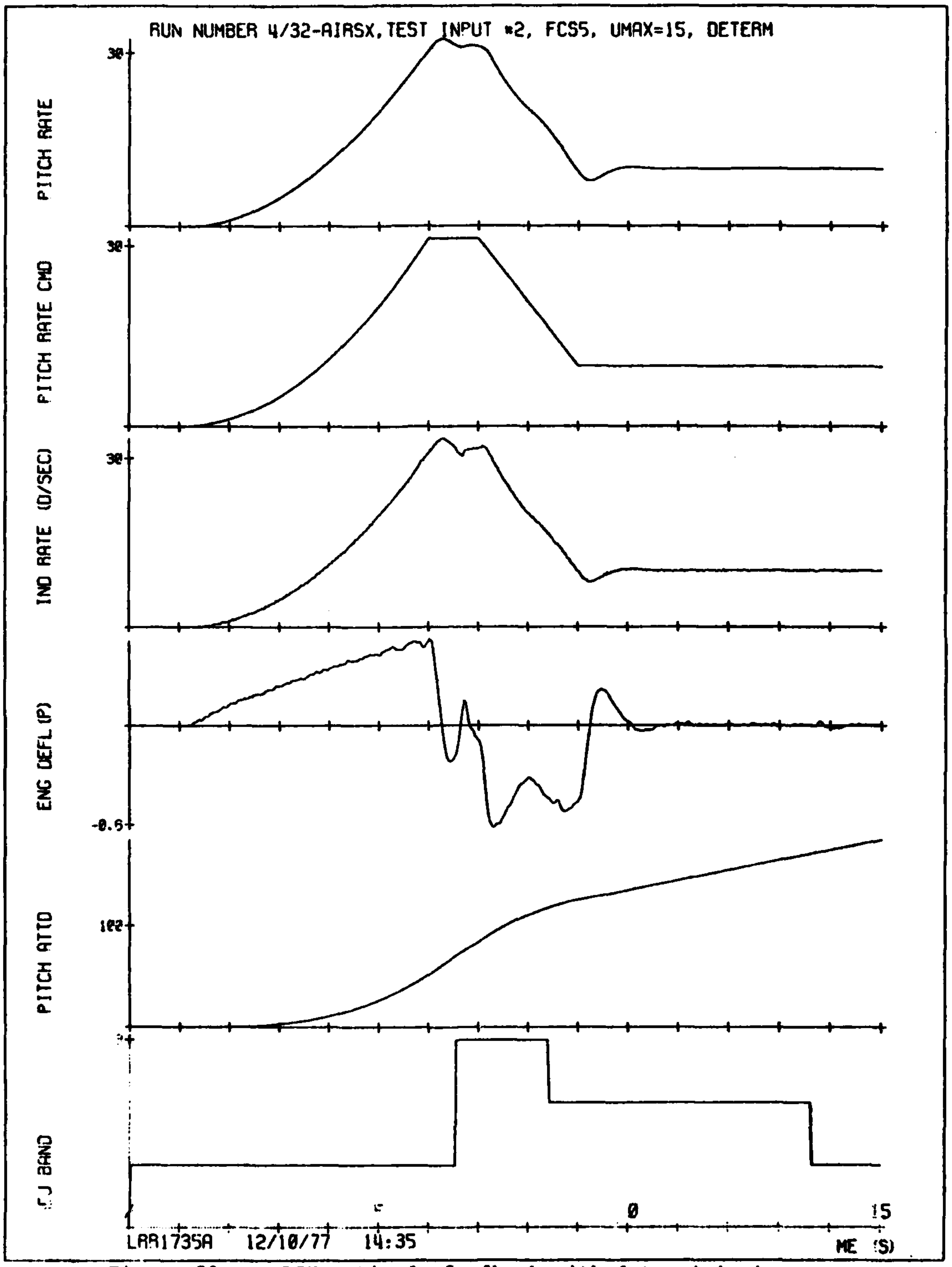

Figure 53. AIRSX attitude feedback with deterministic errors, UMAX = 15.

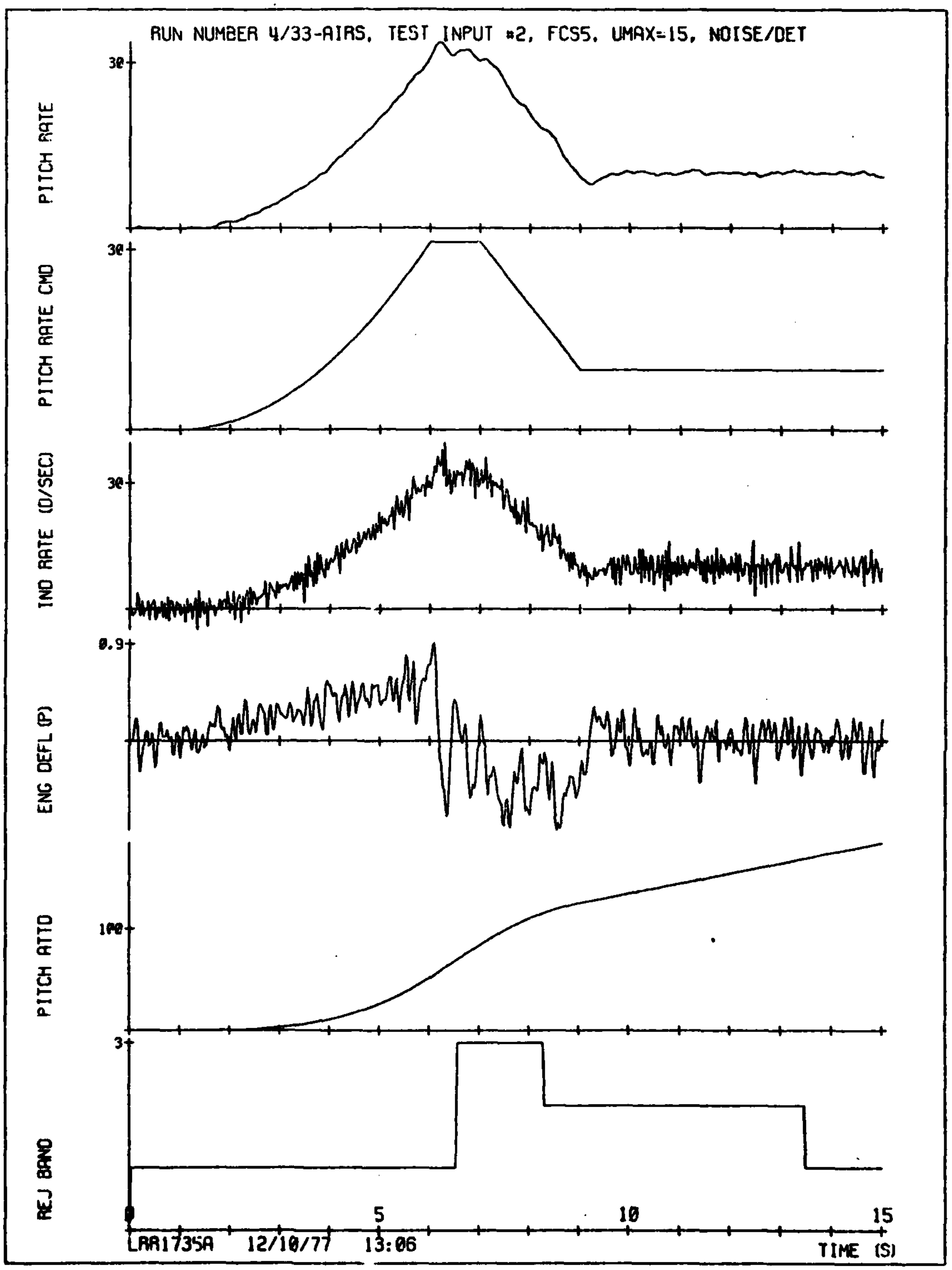

Figure 54. AIRS attitude feedback with random noise and deterministic errors, UMAX = 15.

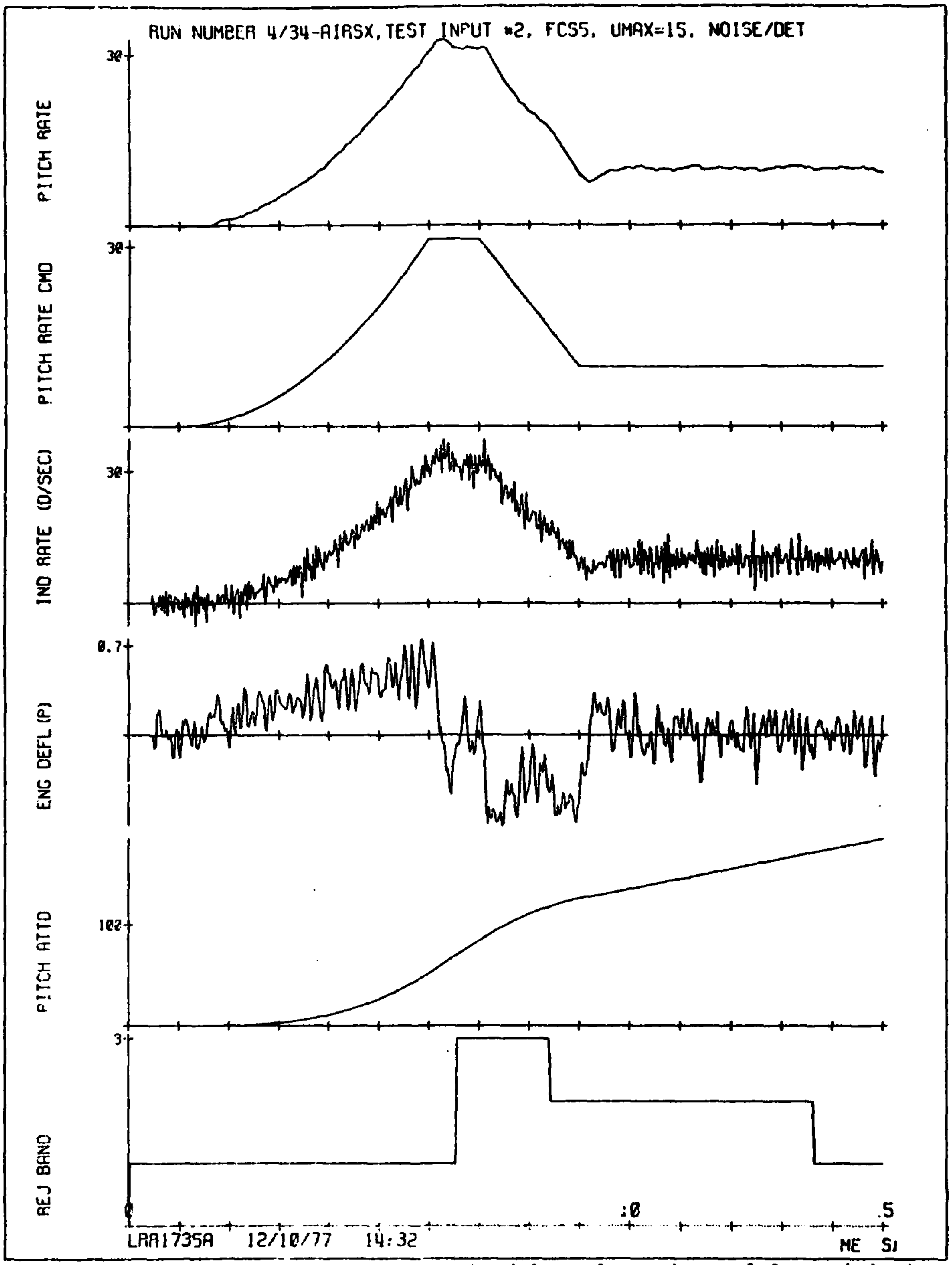

Figure 55. AIRSX attitude feedback with random noise and deterministic errors, UMAX = 15.

SECTION 5

SIMULATION RESULTS

5.1 Overview

This section presents the results of the computer simulations using the OFFSETT and STEER programs. As explained in Appendix C, OFFSETT is the simulation of the guidance system with a point mass vehicle model with no autopilot or steering dynamics. STEER is a complete system simulation that incorporates the guidance equations from the OFFSETT program, the steering, autopilot, and actuator dynamics from the STAR program, and the attitude measurement effects from AIRS.

The simulation initial conditions were the same for both the OFFSETT and STEER simulation runs. These initial conditions are given in Table 18 along with the results of the solution of the Lambert routine, position offset computations, and the fuel depletion guidance equations from the initial guidance cycle.

Table 18. OFFSETT and STEER simulation initial conditions.

Altitude (ft)	Velocity (ft/sec)	Range Angle (deg)	V_{cap} (ft/sec)	Time of Flight (sec)
400,000	18,000	100	8400	2500

The inital solution to the Lambert routine with position offset guidance gives the following results for the given initial conditions and fuel depletion steering:

Required Velocity (ft/sec)	Velocity-to-be-Gained (ft/sec)	Reentry Angle (deg)	Position Offset (ft)
24,070	6,071	-27.54	231,456

Fuel Depletion Angle (deg)
77.3

5.2 OFFSETT Simulation Runs

The results of the OFFSETT simulation are given in Figures 56 through 60, and the parameters of each of the five runs are given in Table 19. Figure 56 is an example of V_g steering, and Figure 57 shows fuel depletion steering. Figures 58-1 and 58-2 show the effect of simultaneous control of Time-On-Target and reentry angle. Figures 59-1 and 59-2 show the effect of velocity perturbations on fuel depletion steering, while Figures 60-1 and 60-2 show the effect of velocity perturbations on fuel depletion steering with reentry control.

Table 19. OFFSETT simulation runs.

Figure	Run	Steering Mode	Reentry Control	Perturbation Analysis
56	2/00	V_g	No	No
57	2/01	Fuel Depletion	No	No
58	2/03	Fuel Depletion	Yes	No
59	2/20	Fuel Depletion	No	Yes
60	2/21	Fuel Depletion	Yes	Yes

The output parameters shown in these figures are explained below:

DEPL ANGLE - The fuel depletion angle, θ

VCAPT - The ΔV capability

VG MAG - The magnitude of the velocity-to-be-gained

RENTRY ANGLE - The reentry angle, γ

RENTRY ERR - The reentry angle error, $\gamma - \gamma_{desired}$

ANGL - The angle between the perturbed and unperturbed $\bar{V}_g$ vectors

THR ACCEL - The thrust acceleration

KPOT - The position offset constant, K_{po}

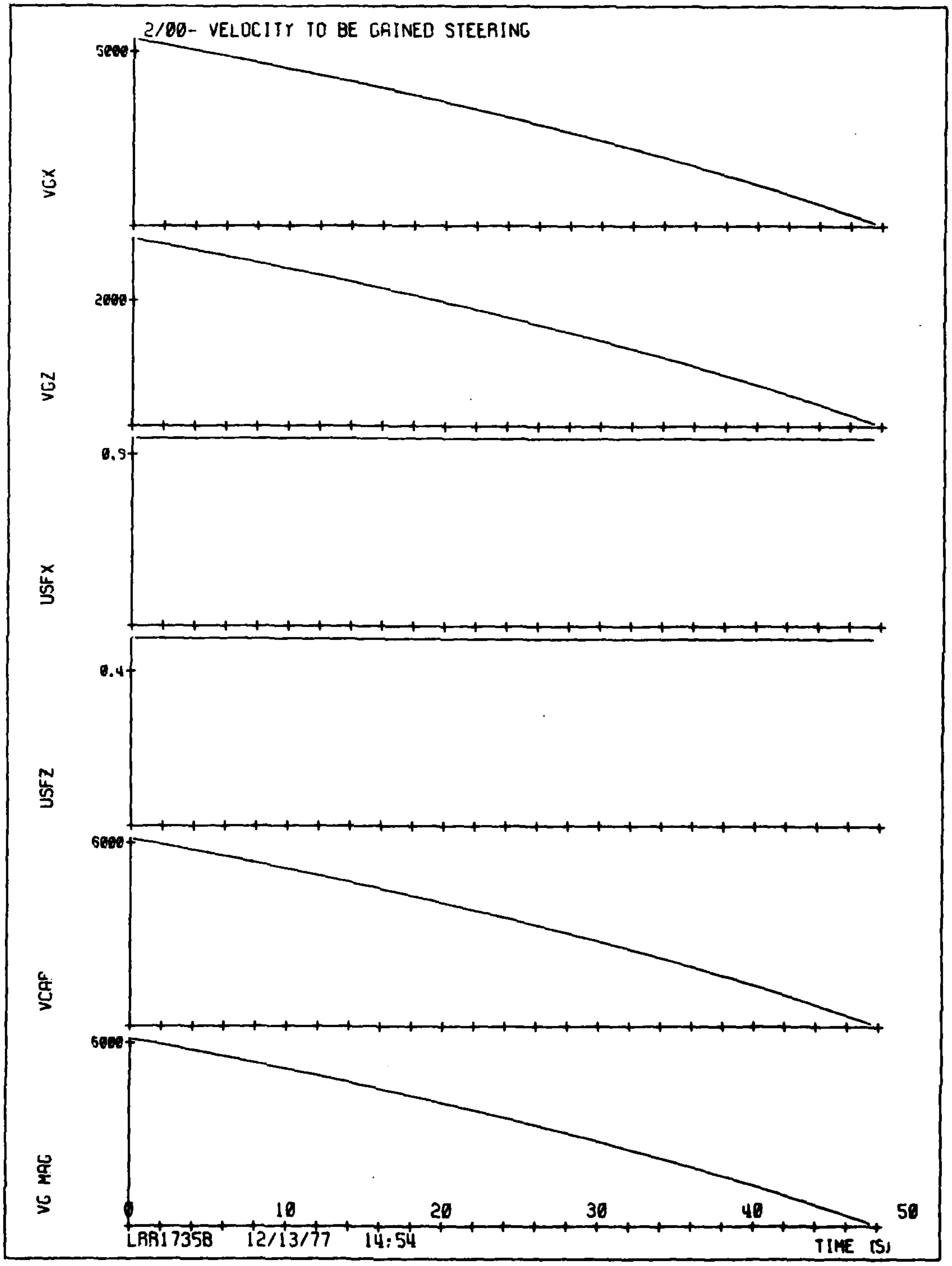

Figure 56. OFFSETT, V_g steering.

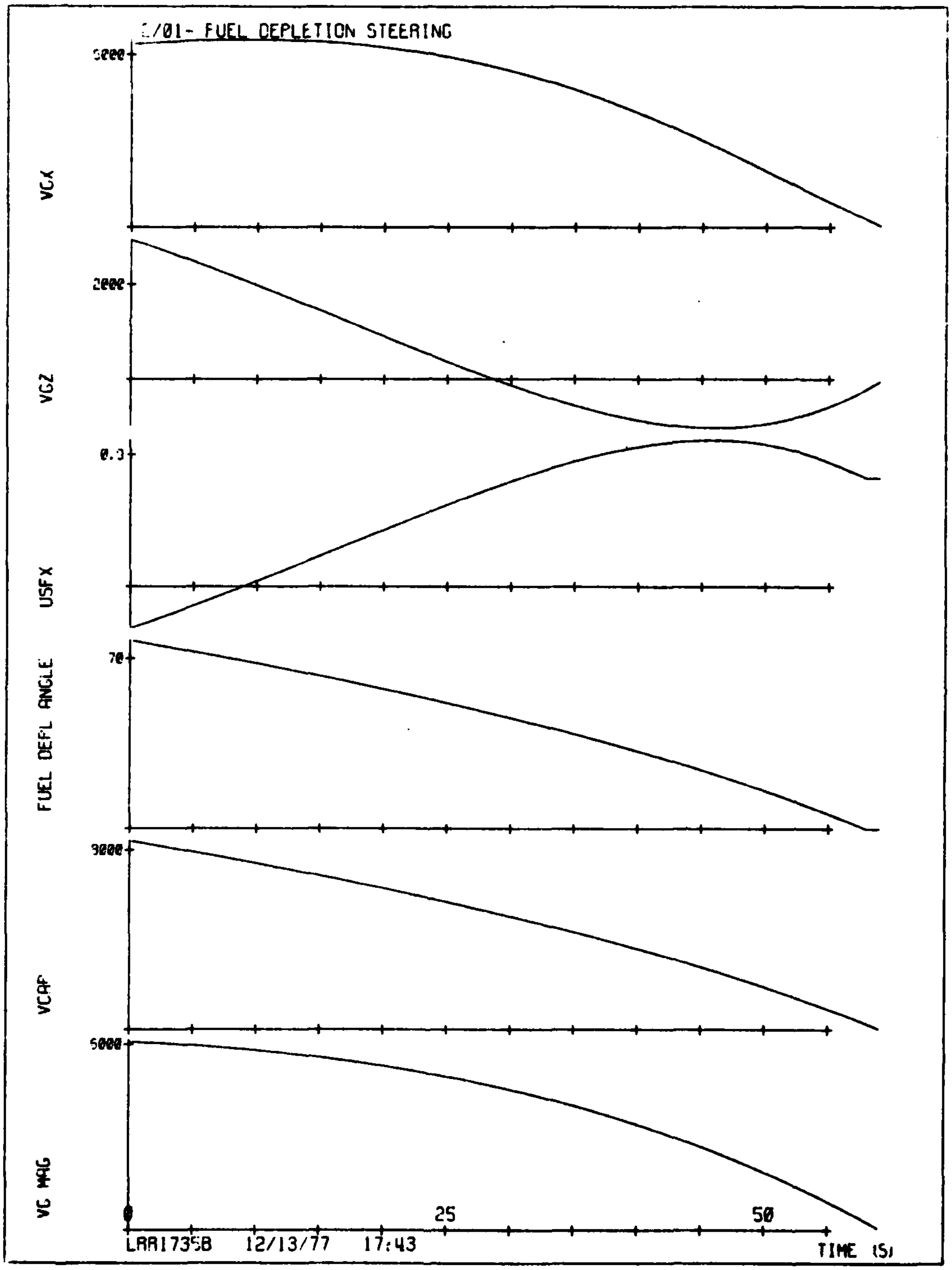

Figure 57. OFFSETT, fuel depletion steering.

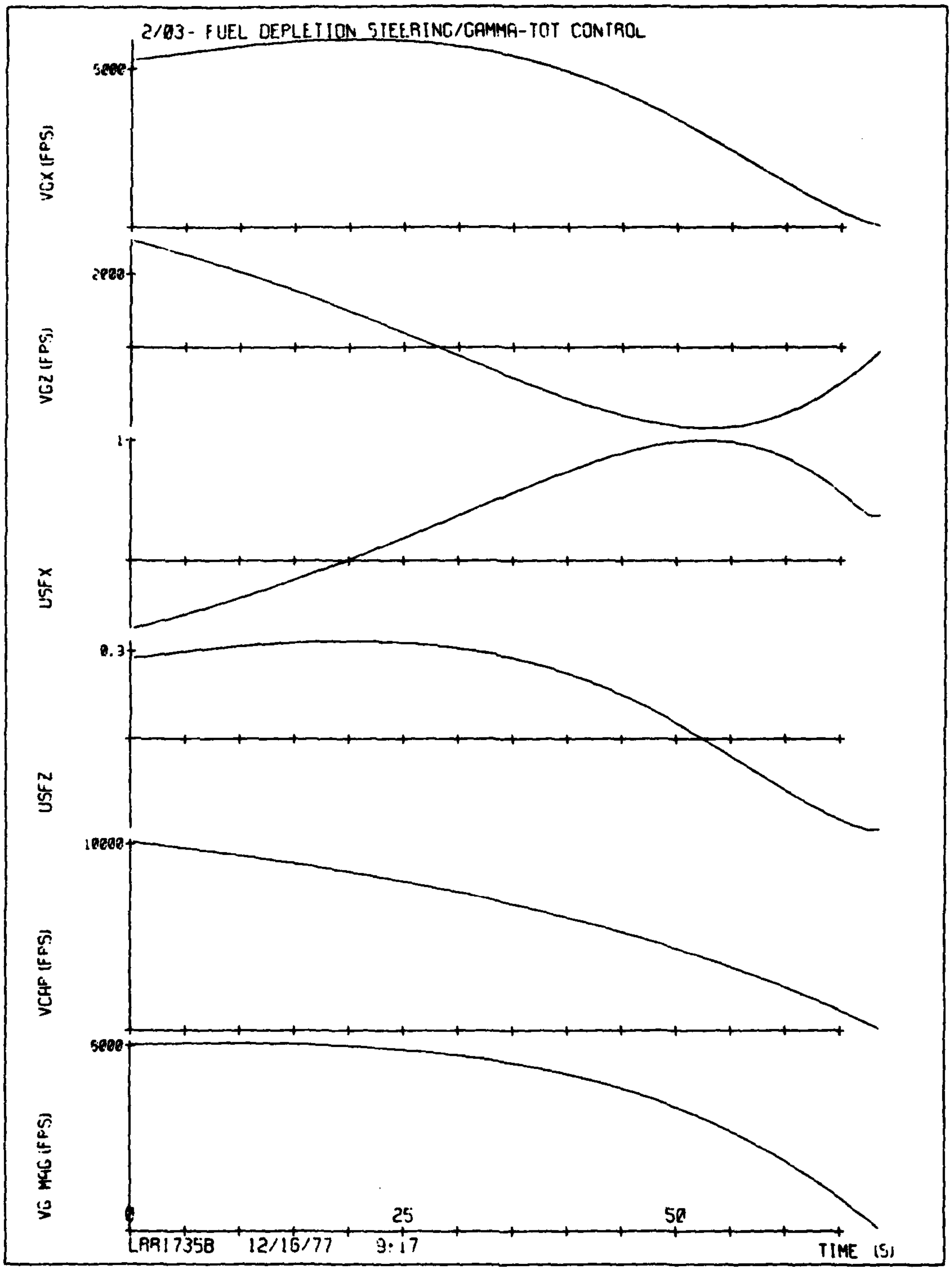

Figure 58-1. OFFSETT, fuel depletion steering with Gamma/TOT control.

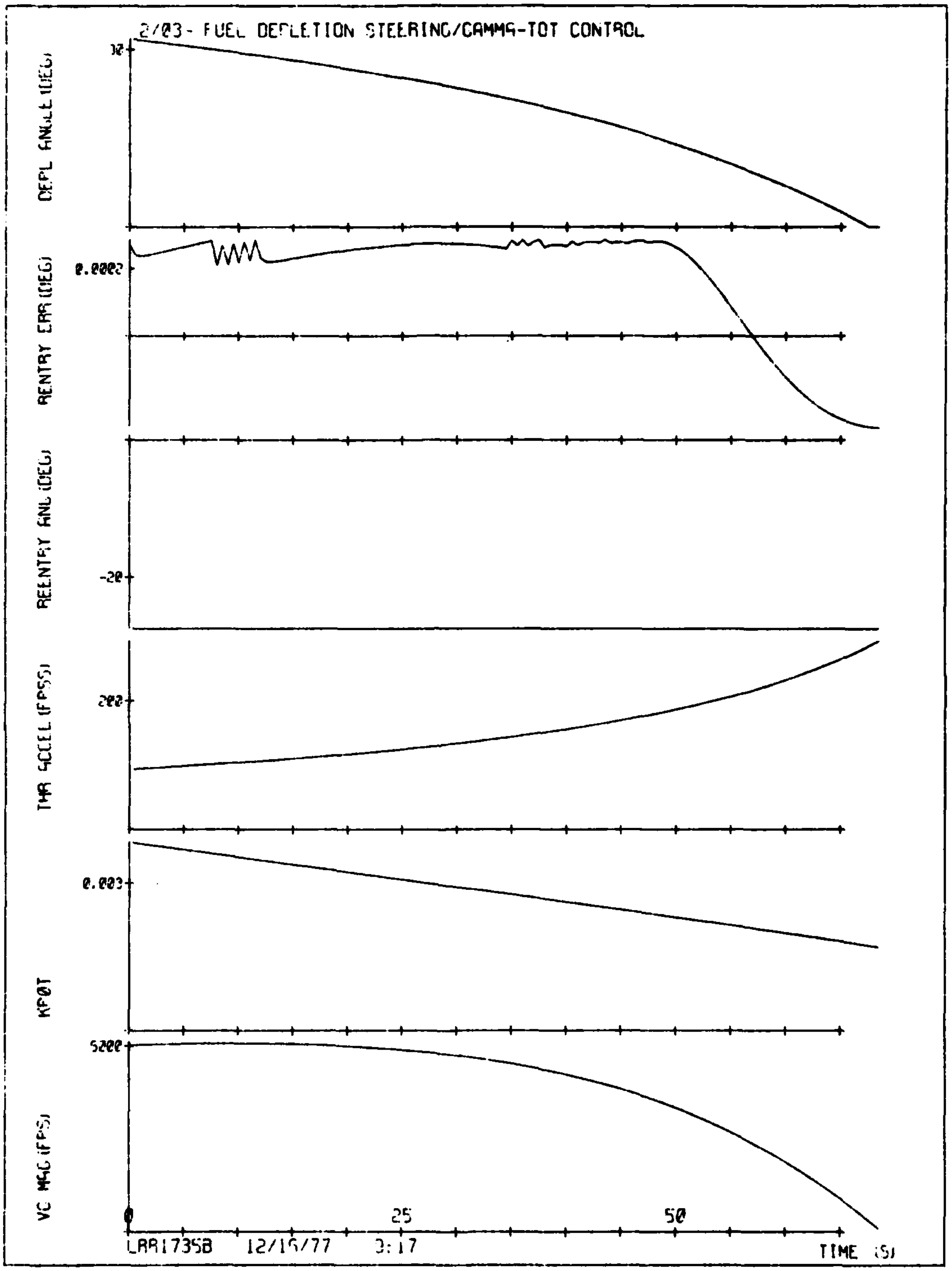

Figure 58-2. OFFSETT, fuel depletion steering with Gamma/TOT control.

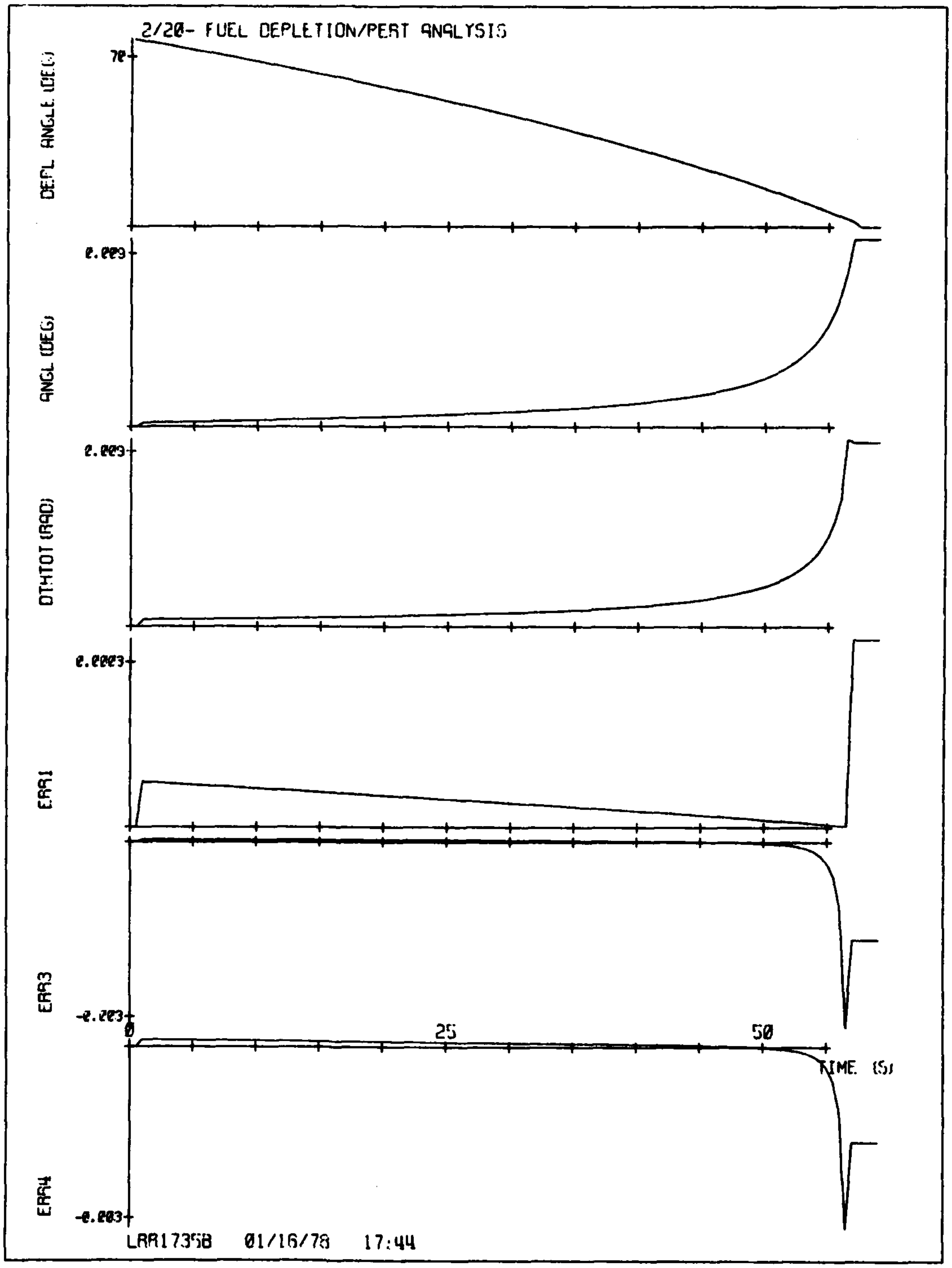

Figure 59-1. OFFSETT, fuel depletion steering, perturbation analysis.

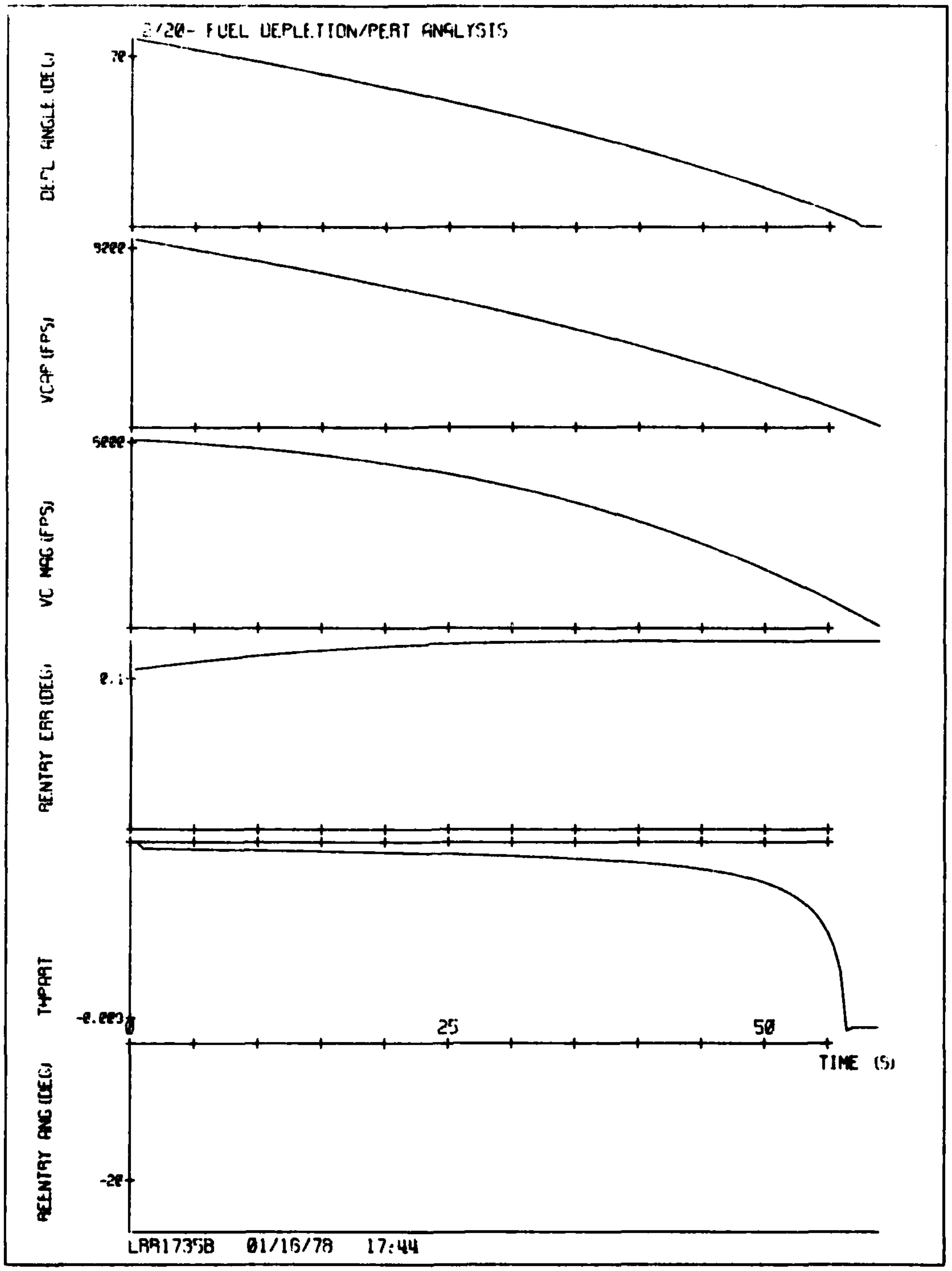

Figure 59-2. OFFSETT, fuel depletion steering, perturbation analysis.

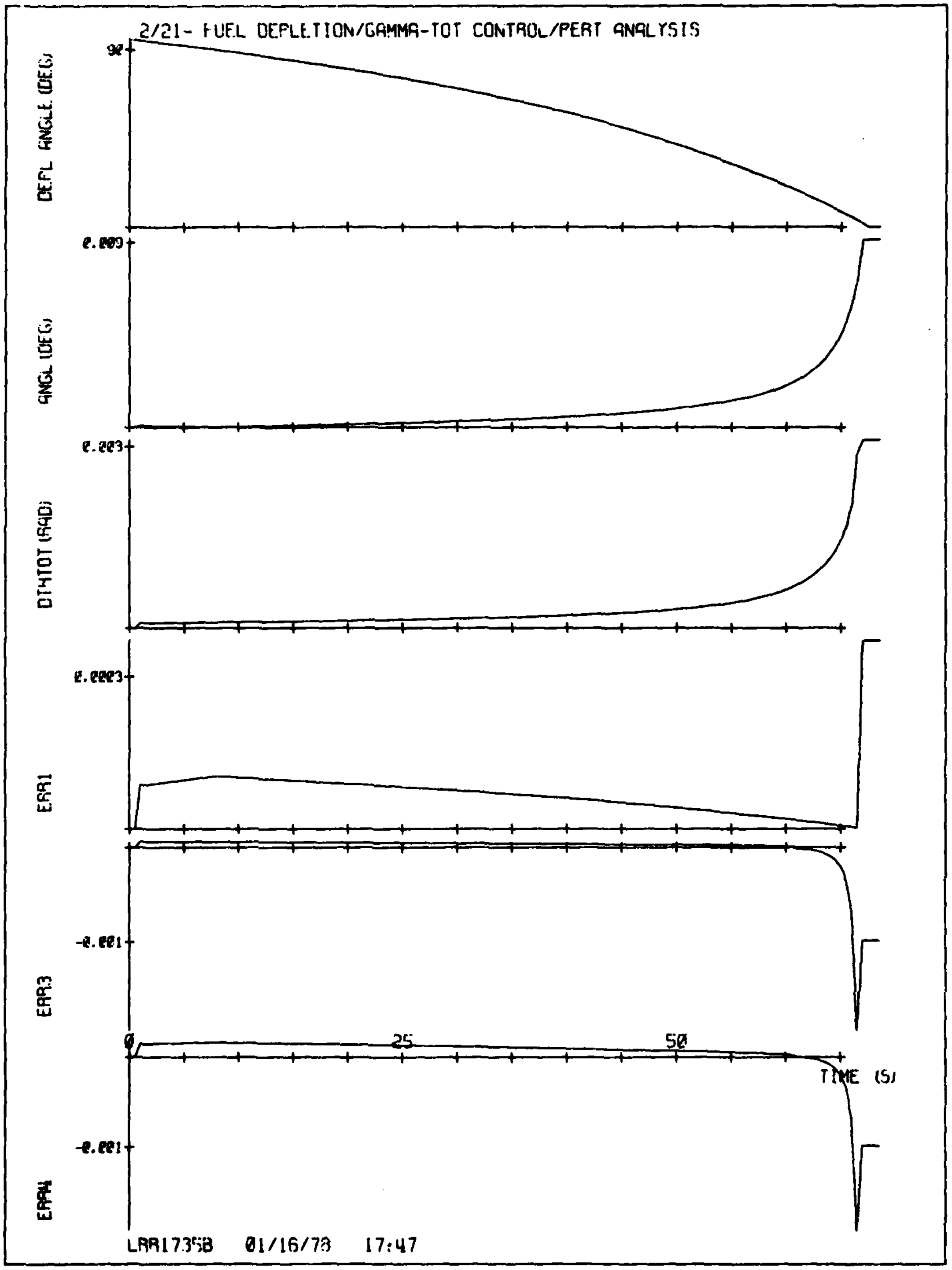

Figure 60-1. OFFSETT, fuel depletion steering with Gamma/TOT control, perturbation analysis.

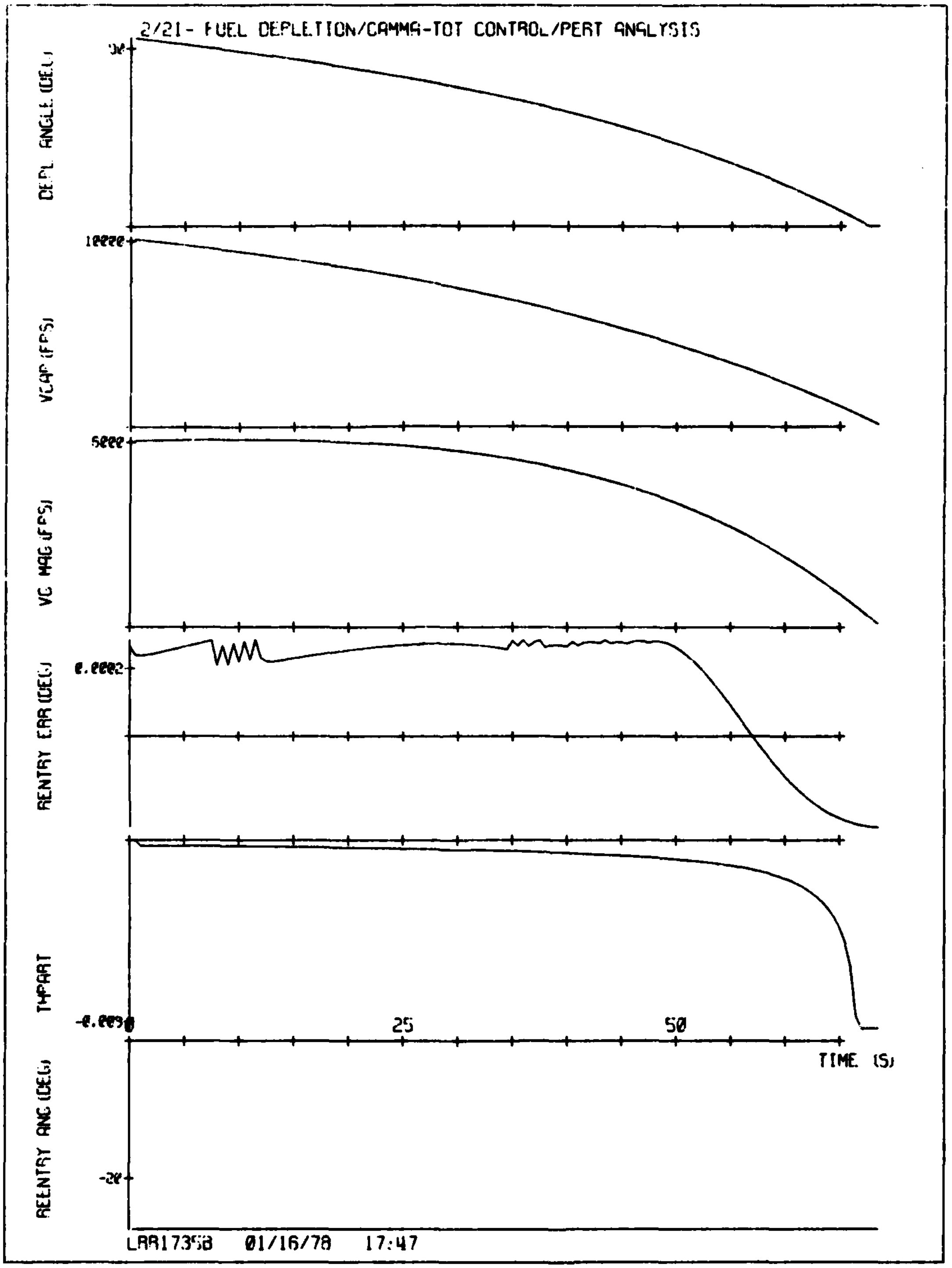

Figure 60-2. OFFSETT, fuel depletion steering with Gamma/TOT control, perturbation analysis.

VGX - The horizontal component of the $\bar{V}_g$ vector relative to inertial axes

VGZ - The vertical component of the $\bar{V}_g$ vector relative to inertial axes

USFX - The horizontal component of the thrust vector command relative to inertial axes

USFZ - The vertical component of the thrust vector command relative to inertial axes

ERR 1, 3, 4, - Differences between theoretical and computed perturbation sensitivities

DTHTOT - The theoretically determined partial, $\partial\theta/\partial V_g$

THPPRT - The actual value of the partial, $\partial\theta/\partial V_g$

5.3 STEER Simulation Runs

The results of the STEER simulation study are given in Figures 61-83. Examples of velocity-to-be-gained steering are given in Figures 61-64, and Figures 65-83 illustrate fuel depletion steering. The initial conditions for the STEER simulations are given in Table 18, and the input parameters for each of the STEER simulation runs are given in Table 20. In Table 20, the autopilot and steering configuration for each run are listed in the second column according to the following code. The first number indicates the autopilot crossover frequency and the number after the slash indicates the steering model, e.g., the 5 rad/sec autopilot (FCS5) and s eering model 01 (no integral feedback) are designated as 5/01. An asterisk after the autopilot frequency means that the "optimized" autopilot and steering combination is used in that run. The fifth column indicates which (if any) AIRS method is used. The code 0 means that ideal measurements are used, the code 1 stands for AIRS, and code 2 stands for AIRSX. The tailoff Column indicates whether or not the thrust tailoff model is used. The comments column are self-explanatory.

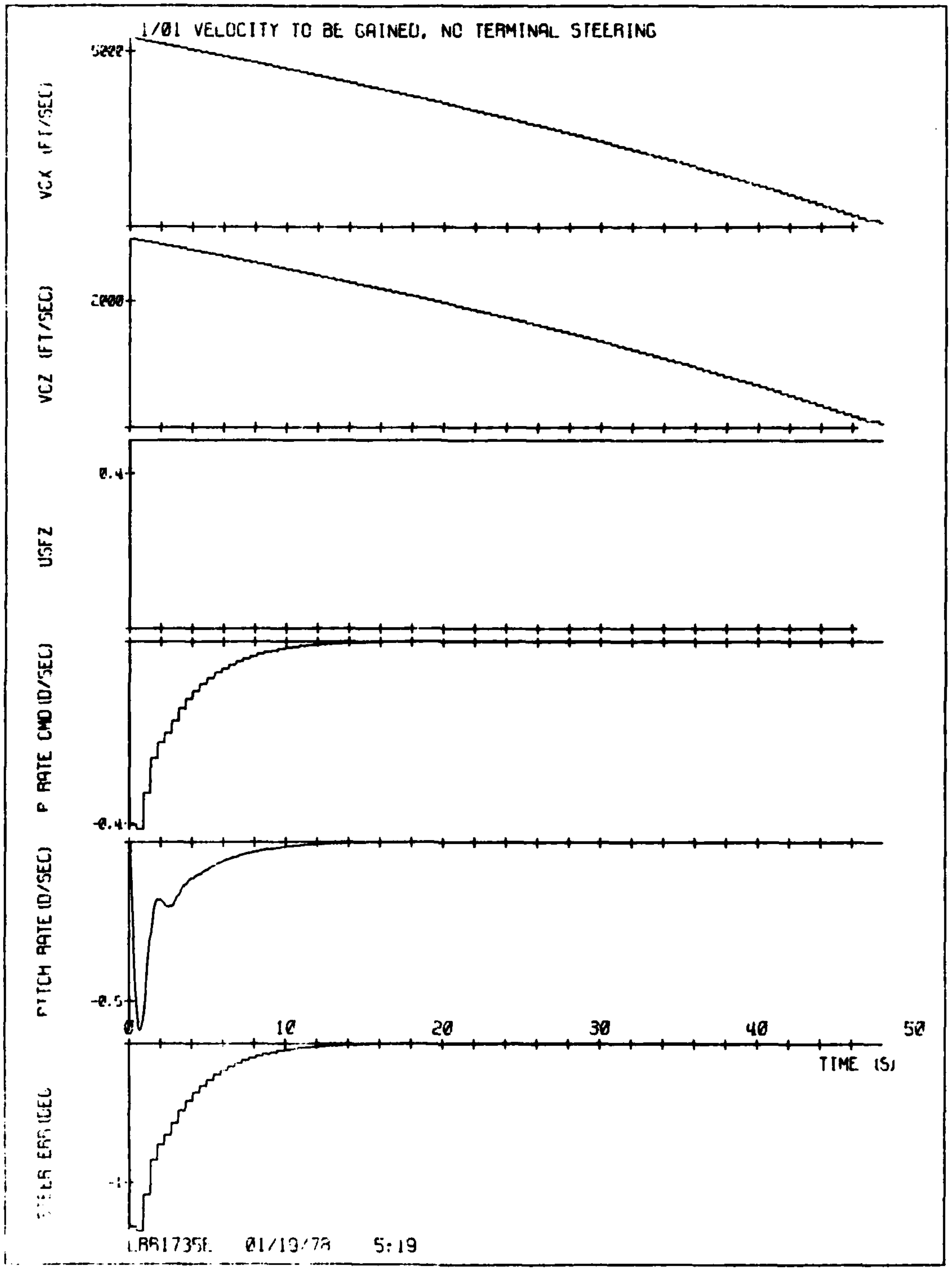

Figure 61-1. STEER, V_g steering.

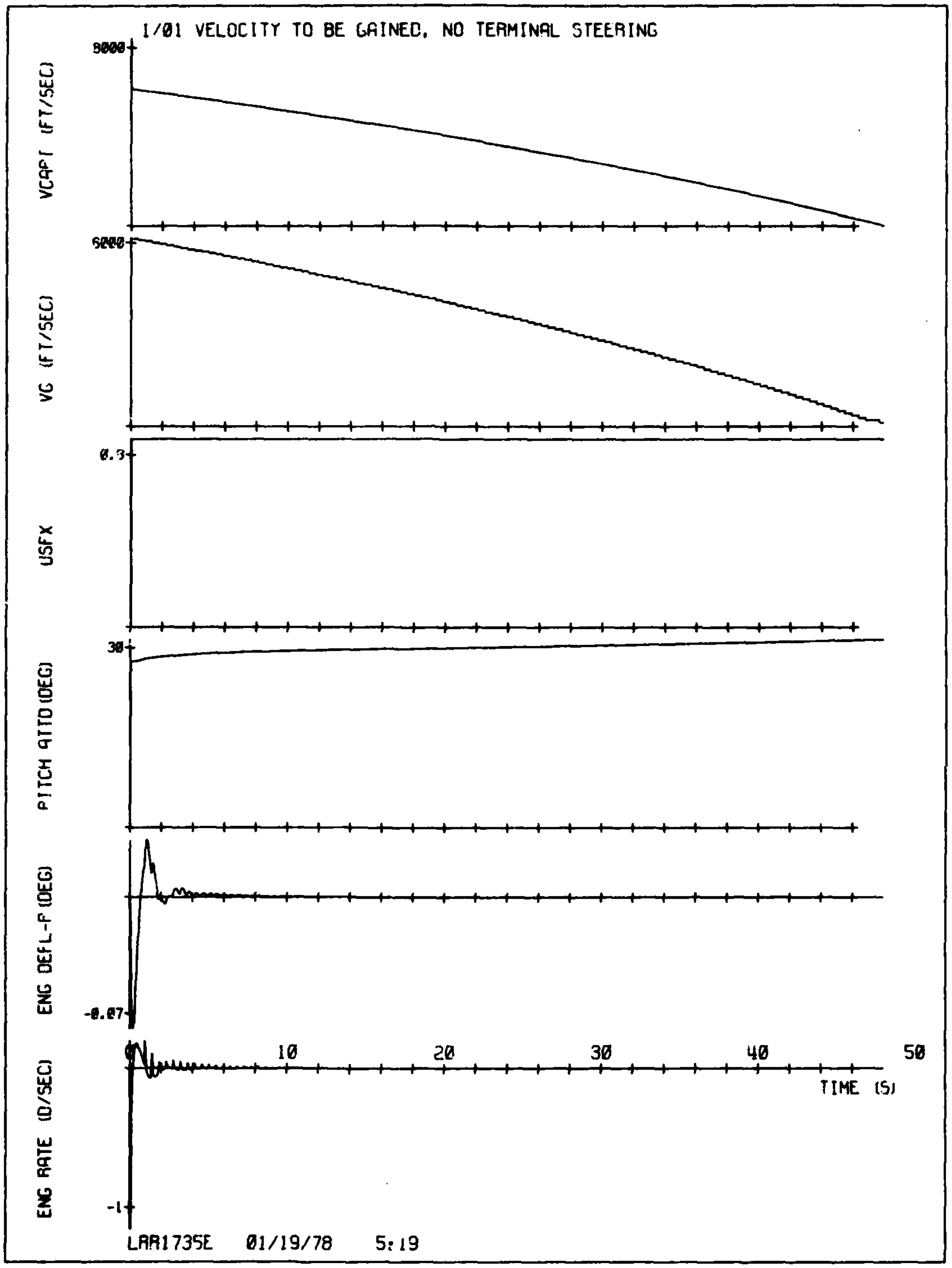

Figure 61-2. STEER, V_g steering.

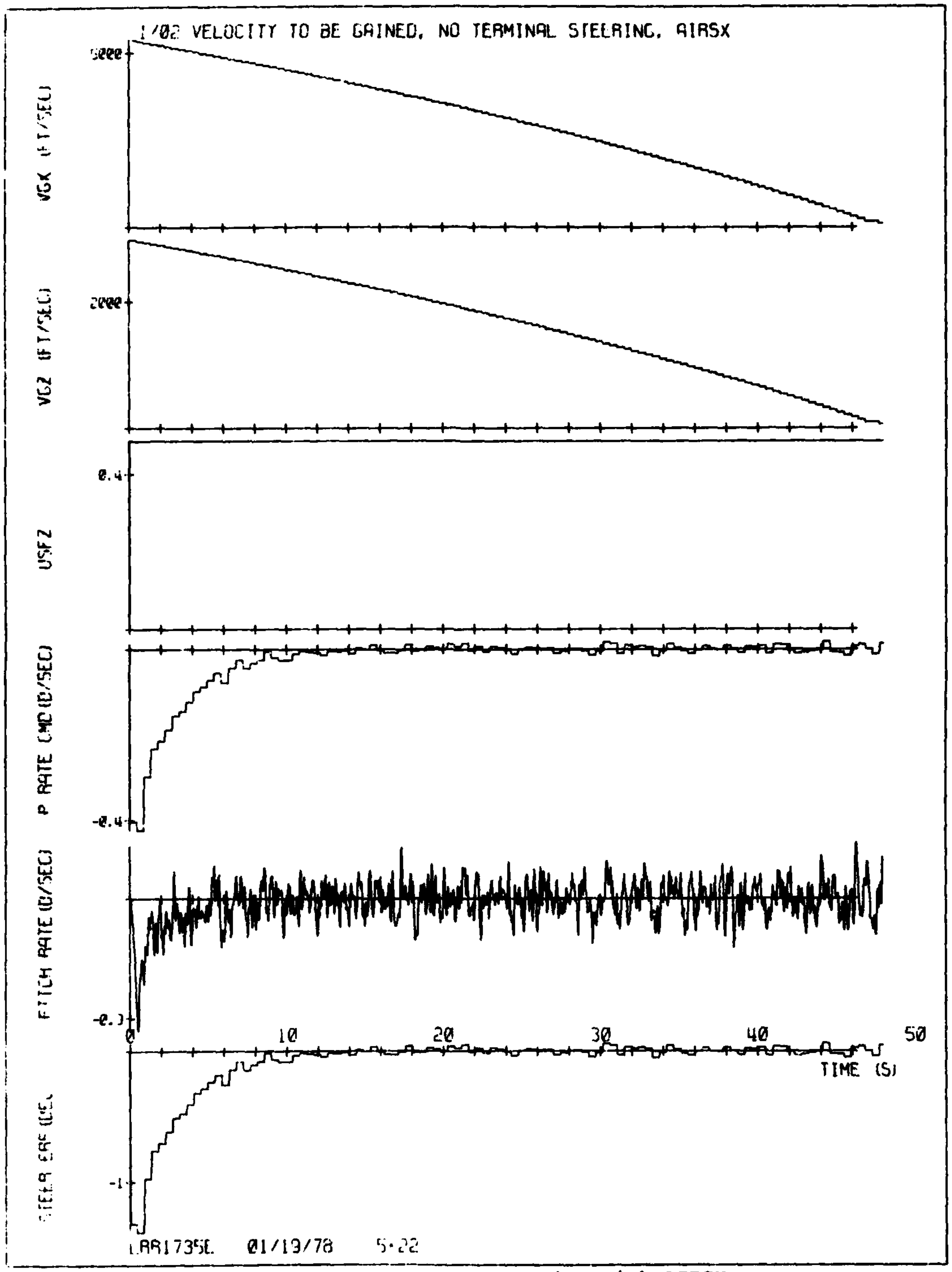

Figure 62-1. STEER, V_g steering with AIRSX.

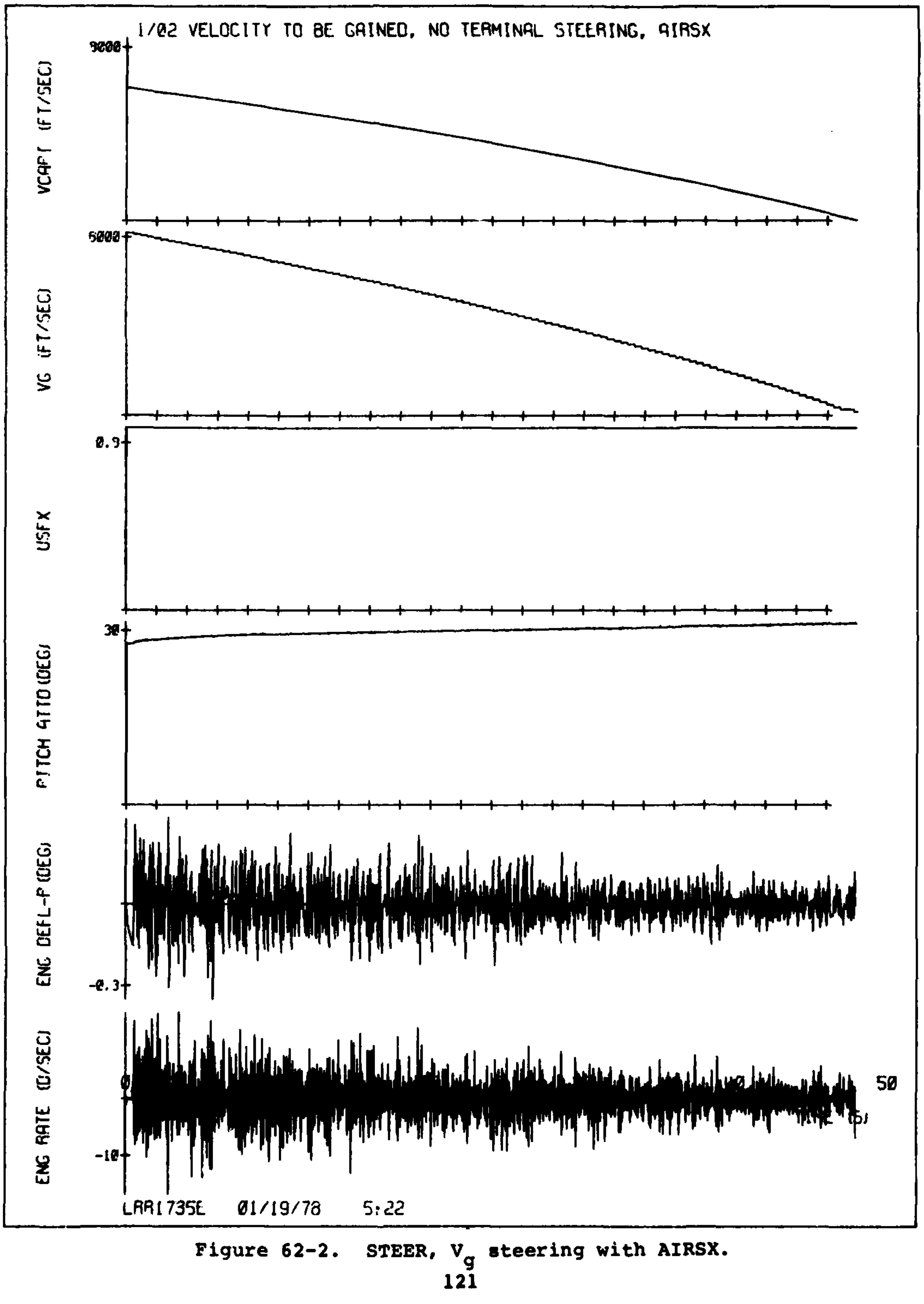

Figure 62-2. STEER, V_g steering with AIRSX.

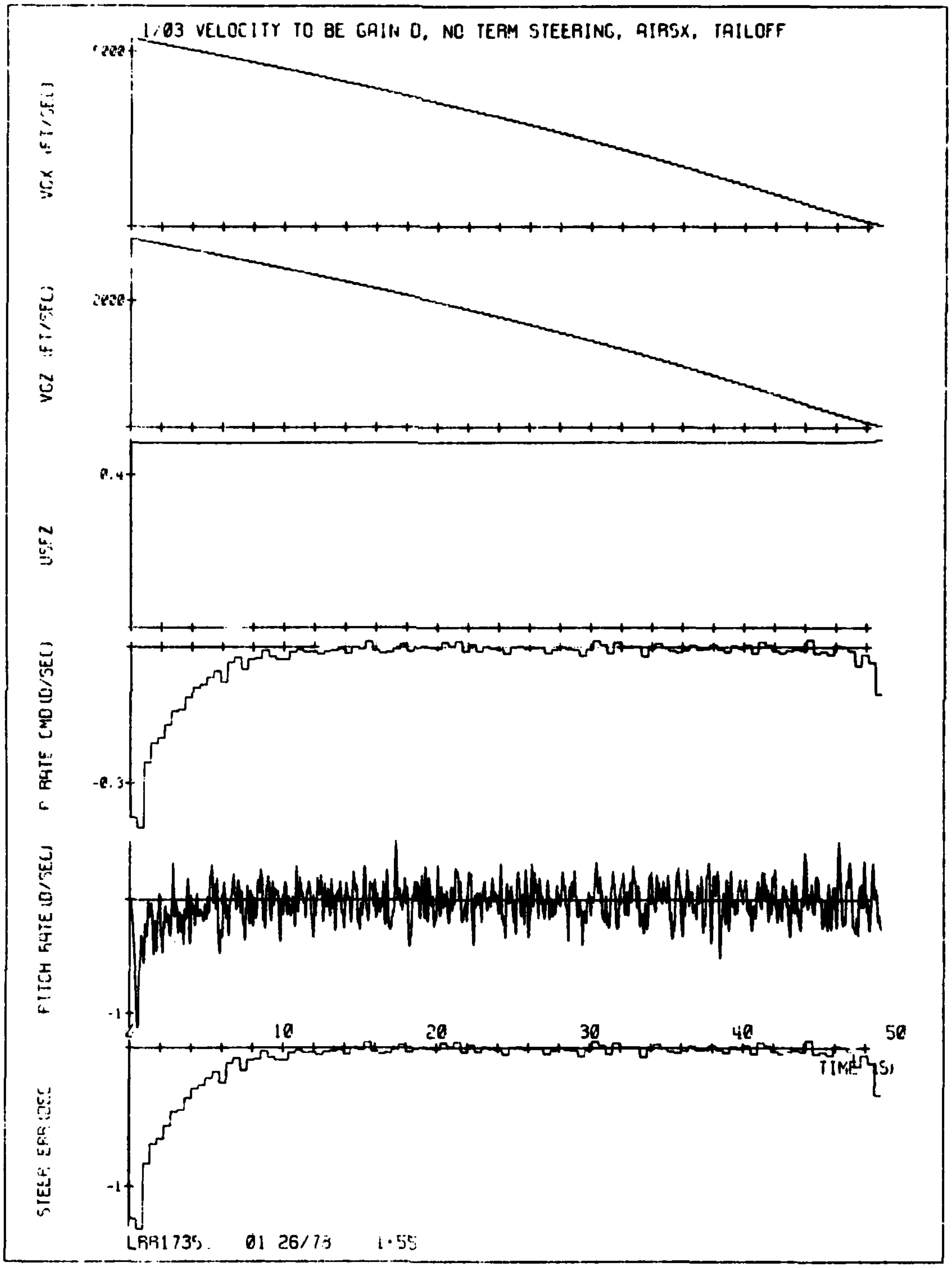

Figure 63-1. STEER, V_g steering with AIRSX and thrust tailoff.

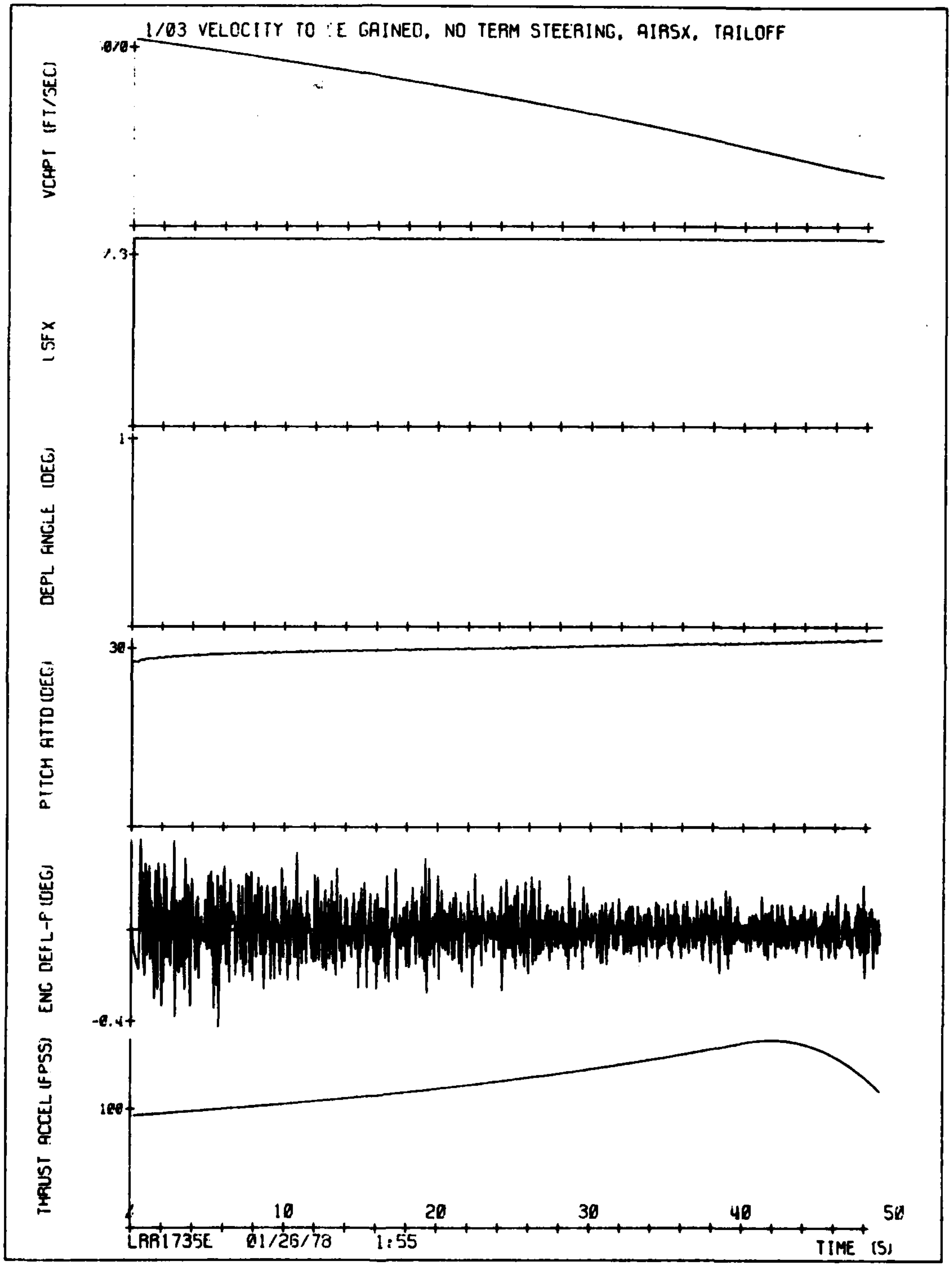

Figure 63-2. STEER, V_g steering with AIRSX and thrust tailoff.

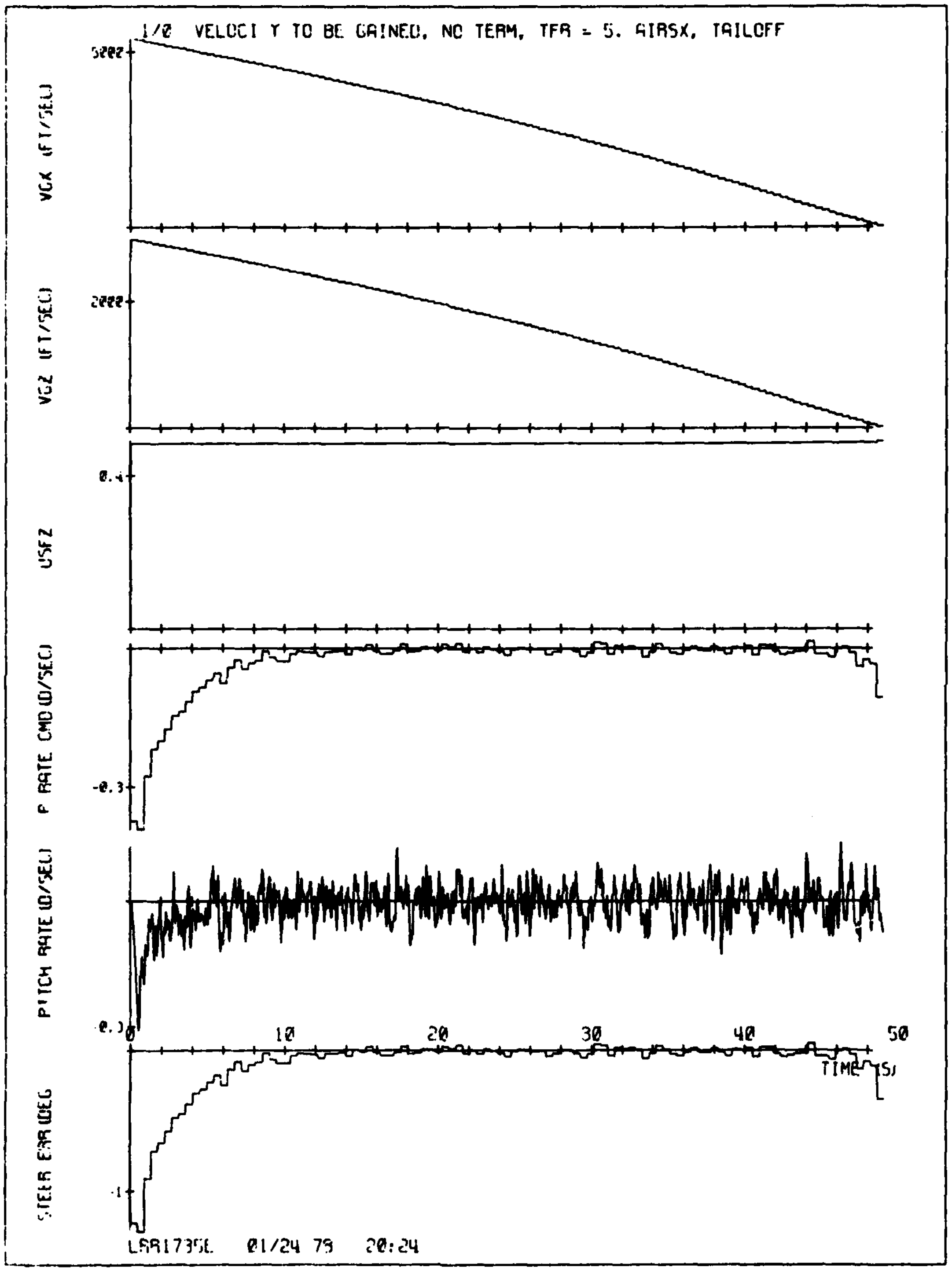

Figure 64-1. STEER, V_g steering with AIRSX, and thrust tailoff, T_{FR} = 5.

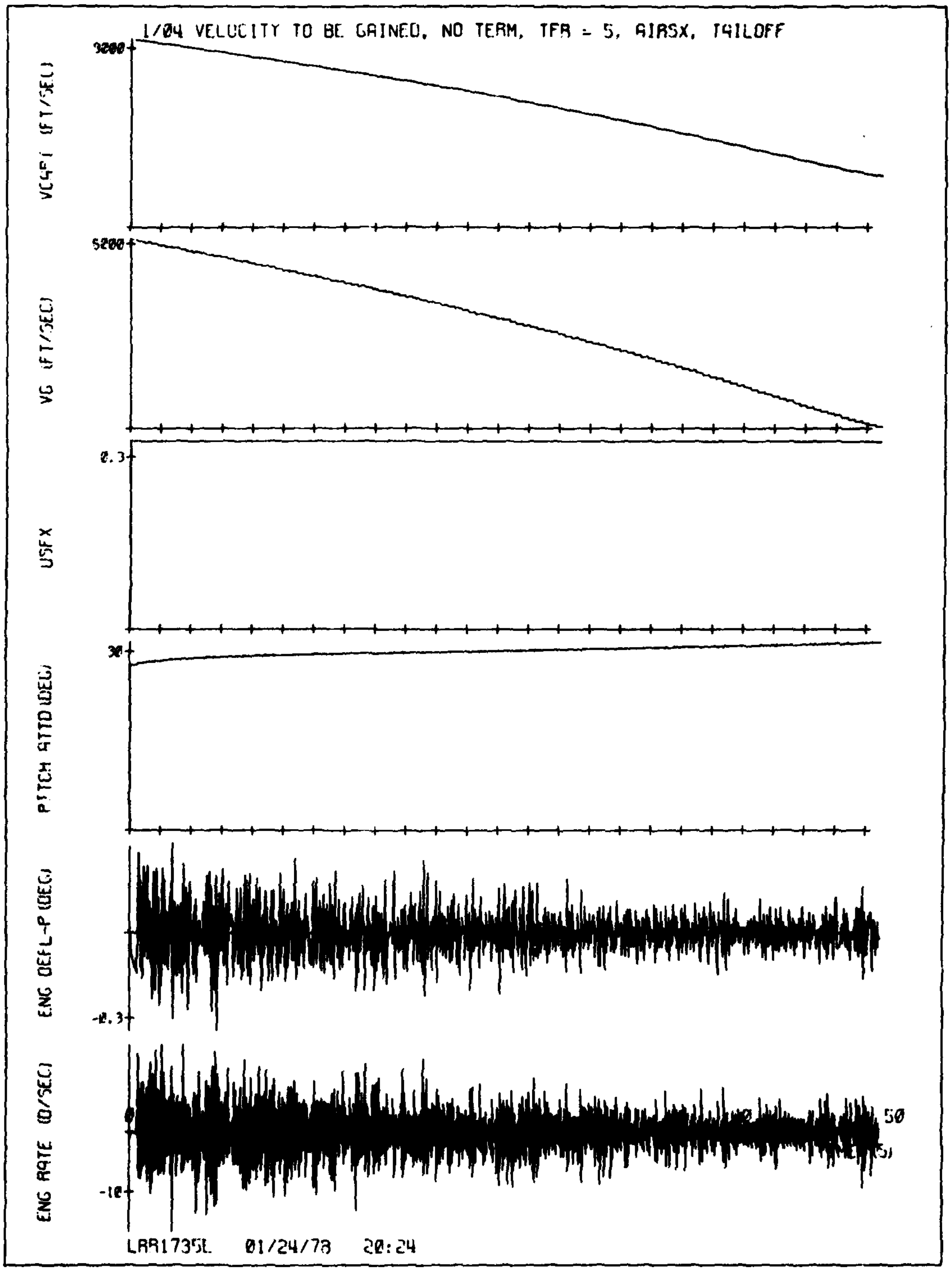

Figure 64-2. STEER, V_g steering with AIRSX, and thrust tailoff, $T_{FR} = 5$.

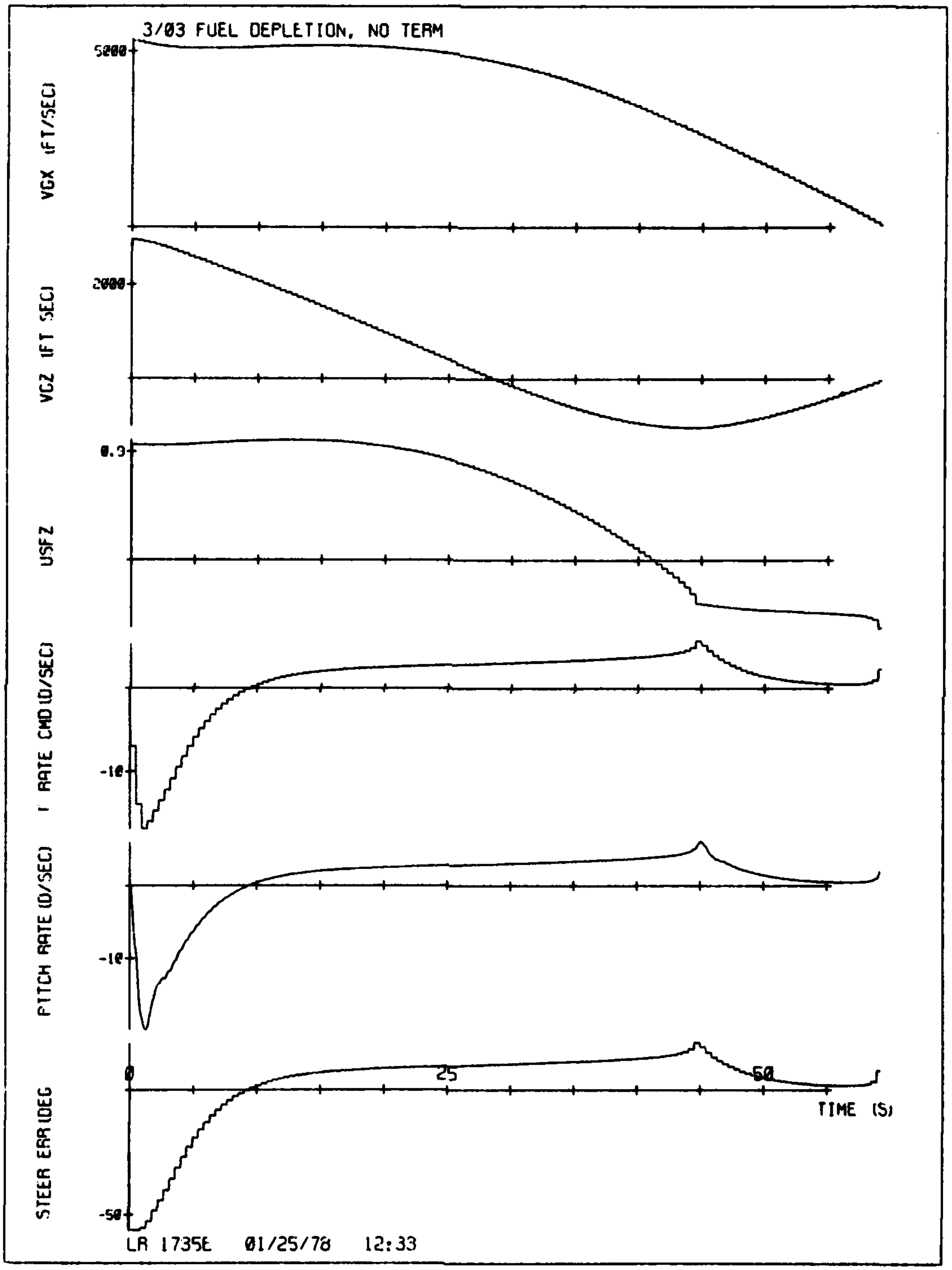

Figure 65-1. STEER, fuel depletion steering.

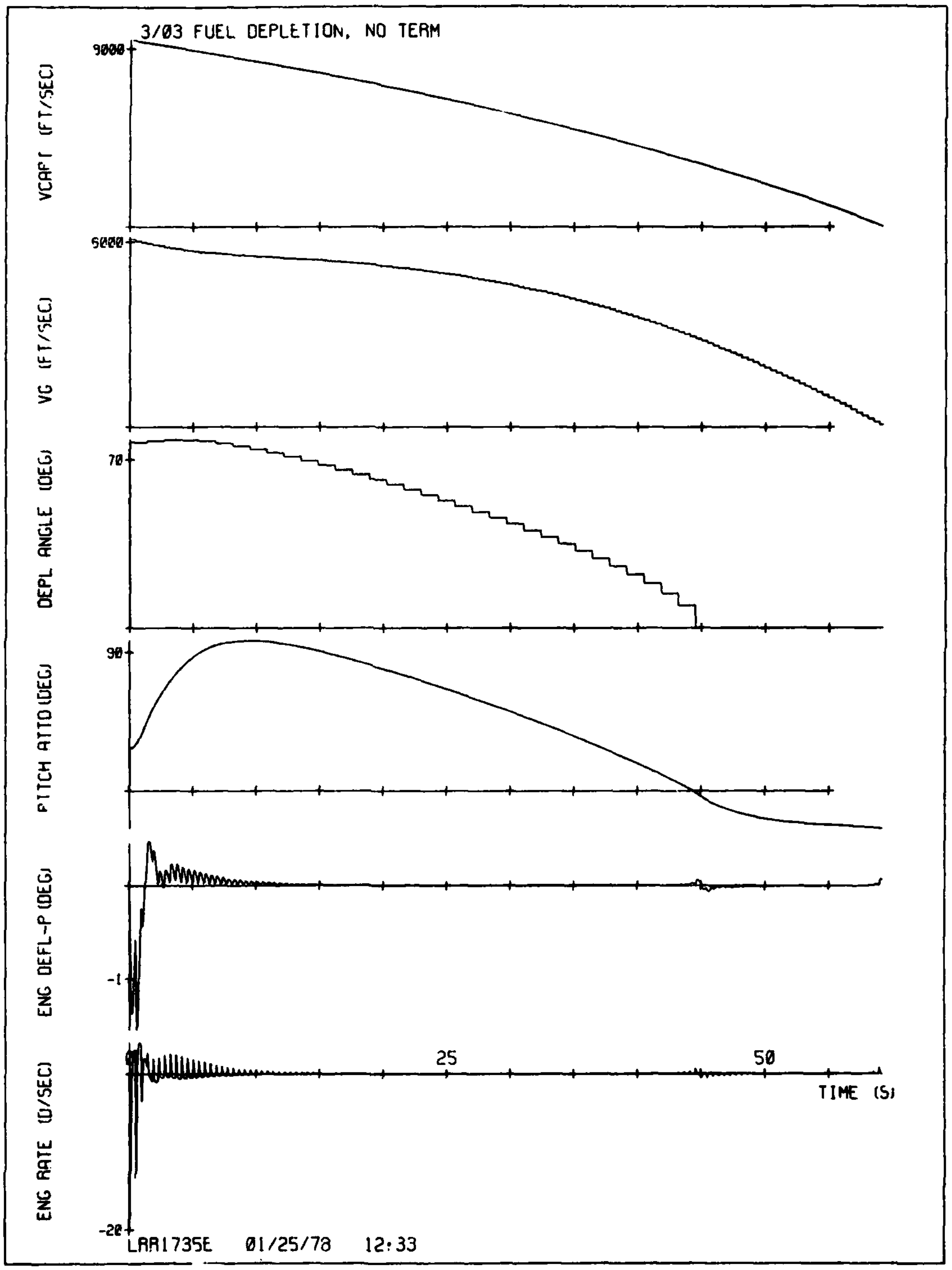

Figure 65-2. STEER, fuel depletion steering.

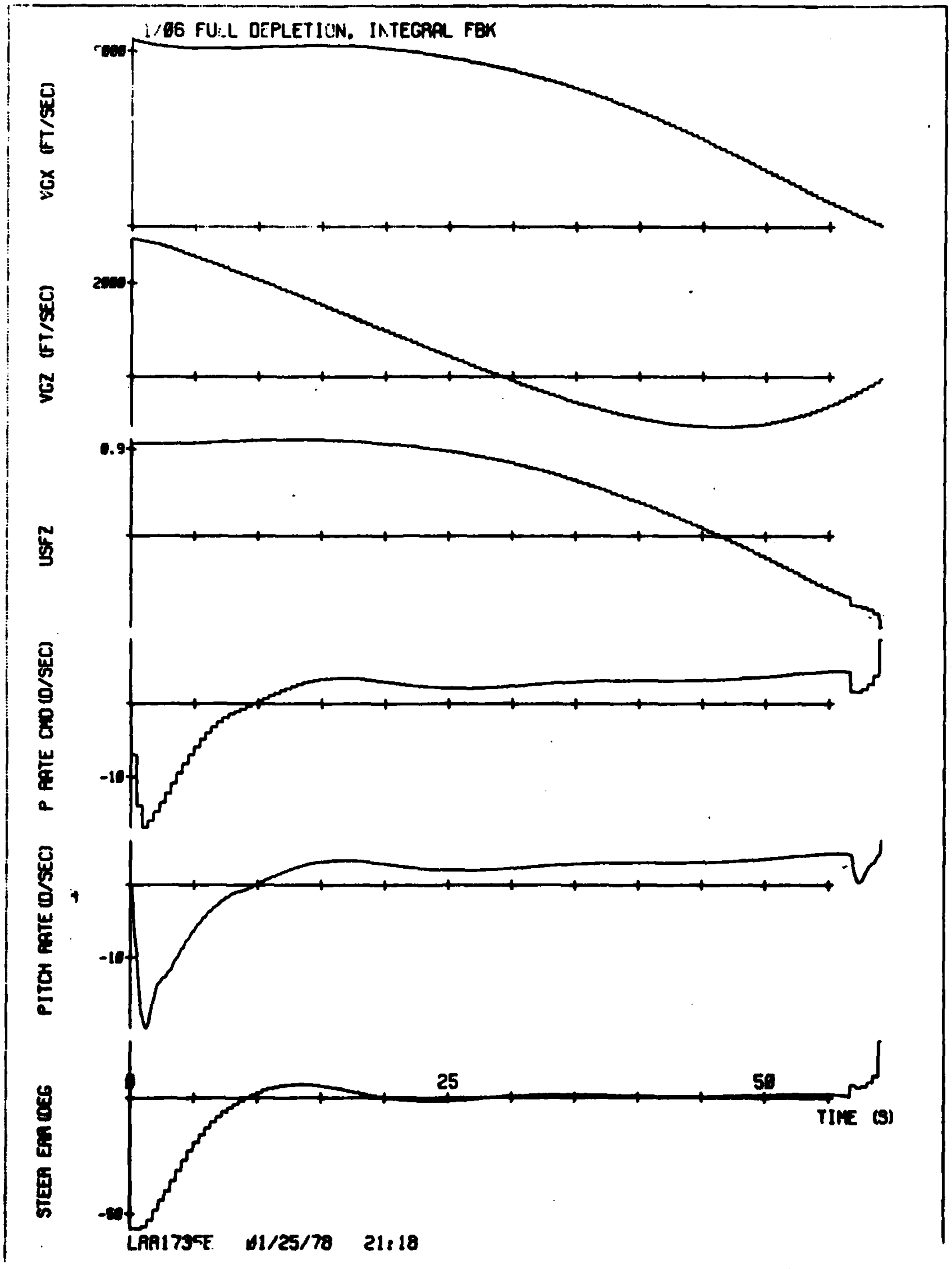

Figure 66-1. STEER, fuel depletion steering, integral feedback.

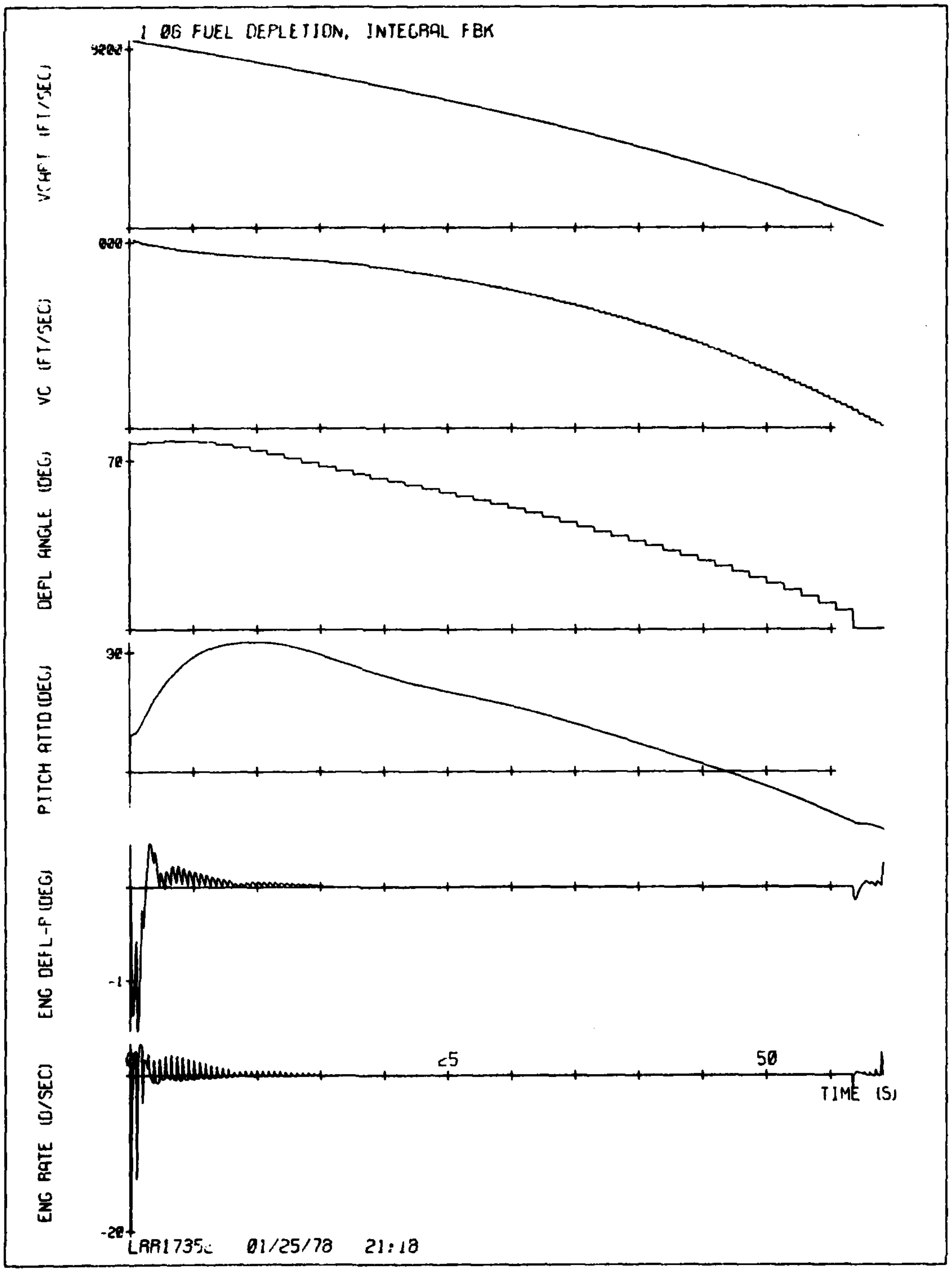

Figure 66-2. STEER, fuel depletion steering, integral feedback.

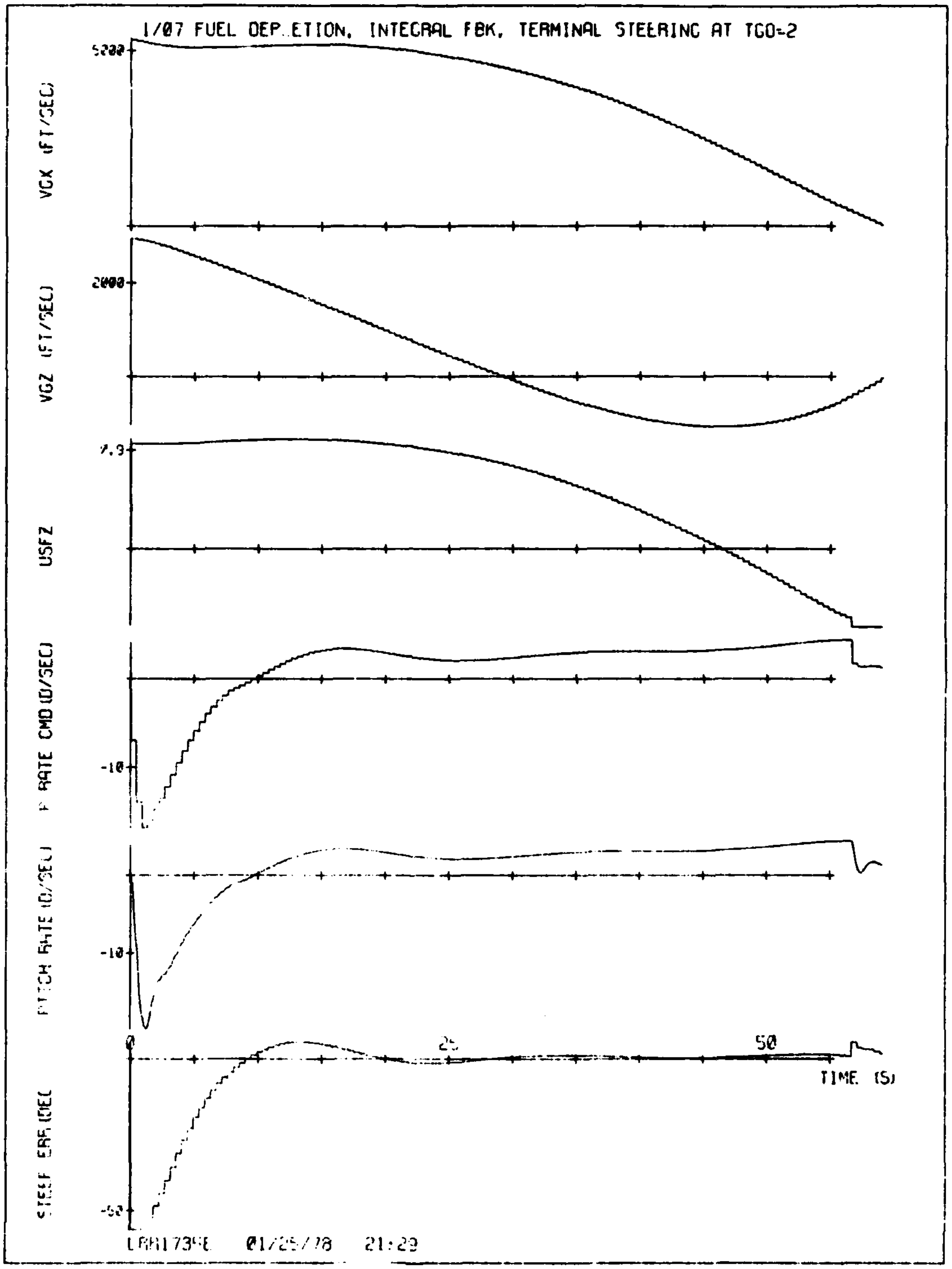

Figure 67-1. STEER, fuel depletion steering, integral feedback, T_{FR} = 2.

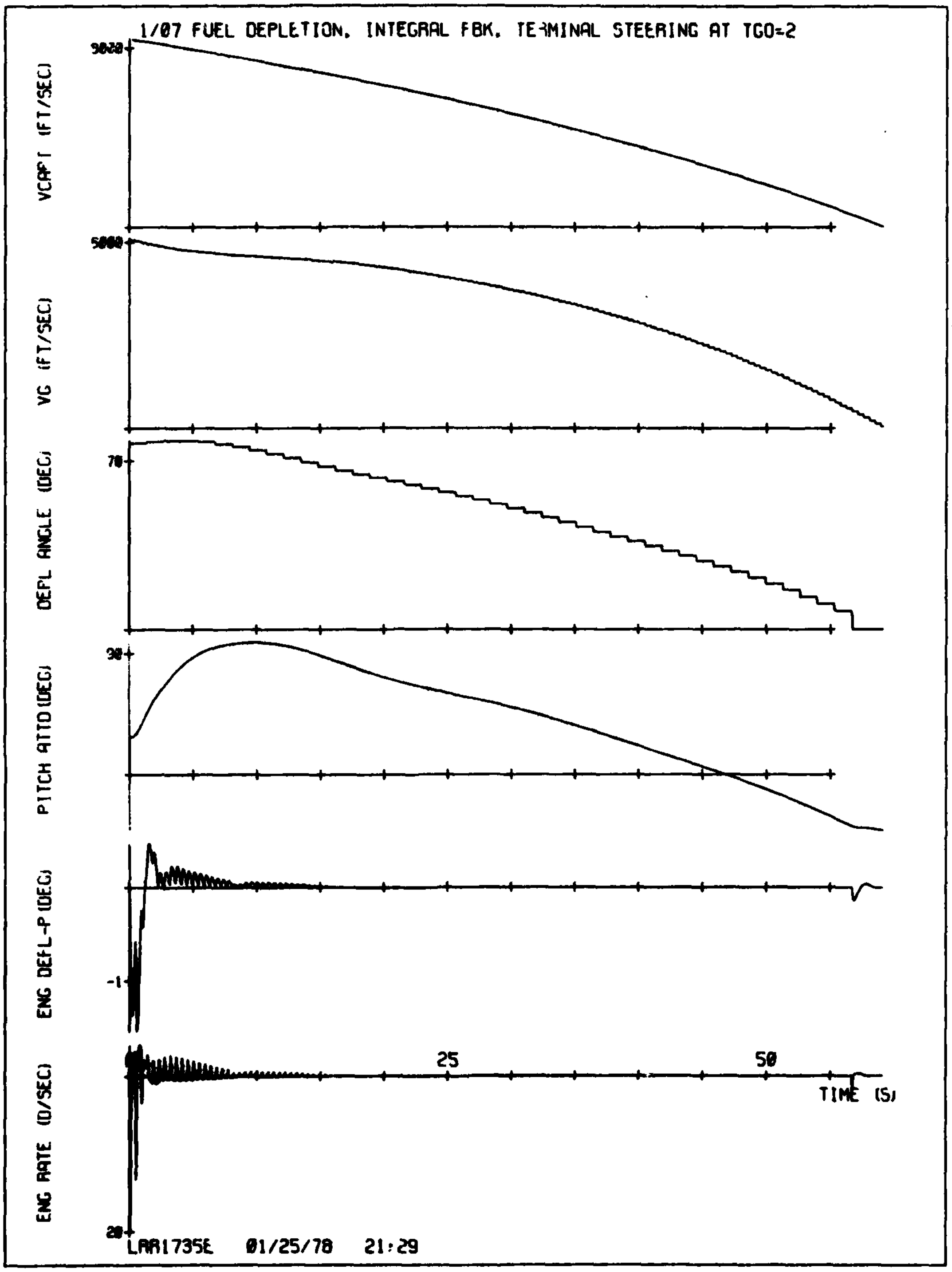

Figure 67-2. STEER, fuel depletion steering, integral feedback, T_{FR} = 2.

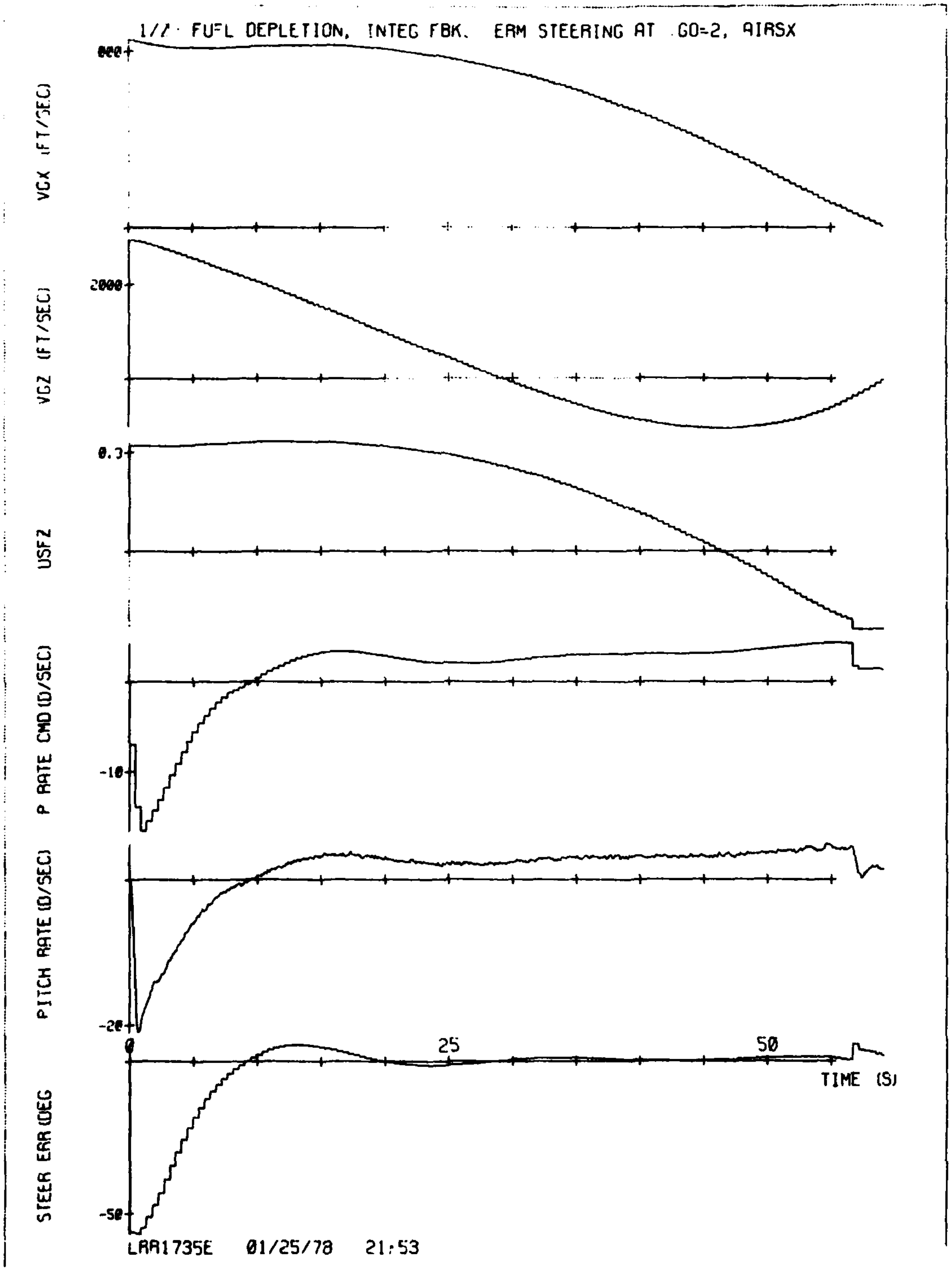

Figure 68-1. STEER, fuel depletion steering, integral feedback, T_{FR} = 2, AIRSX.

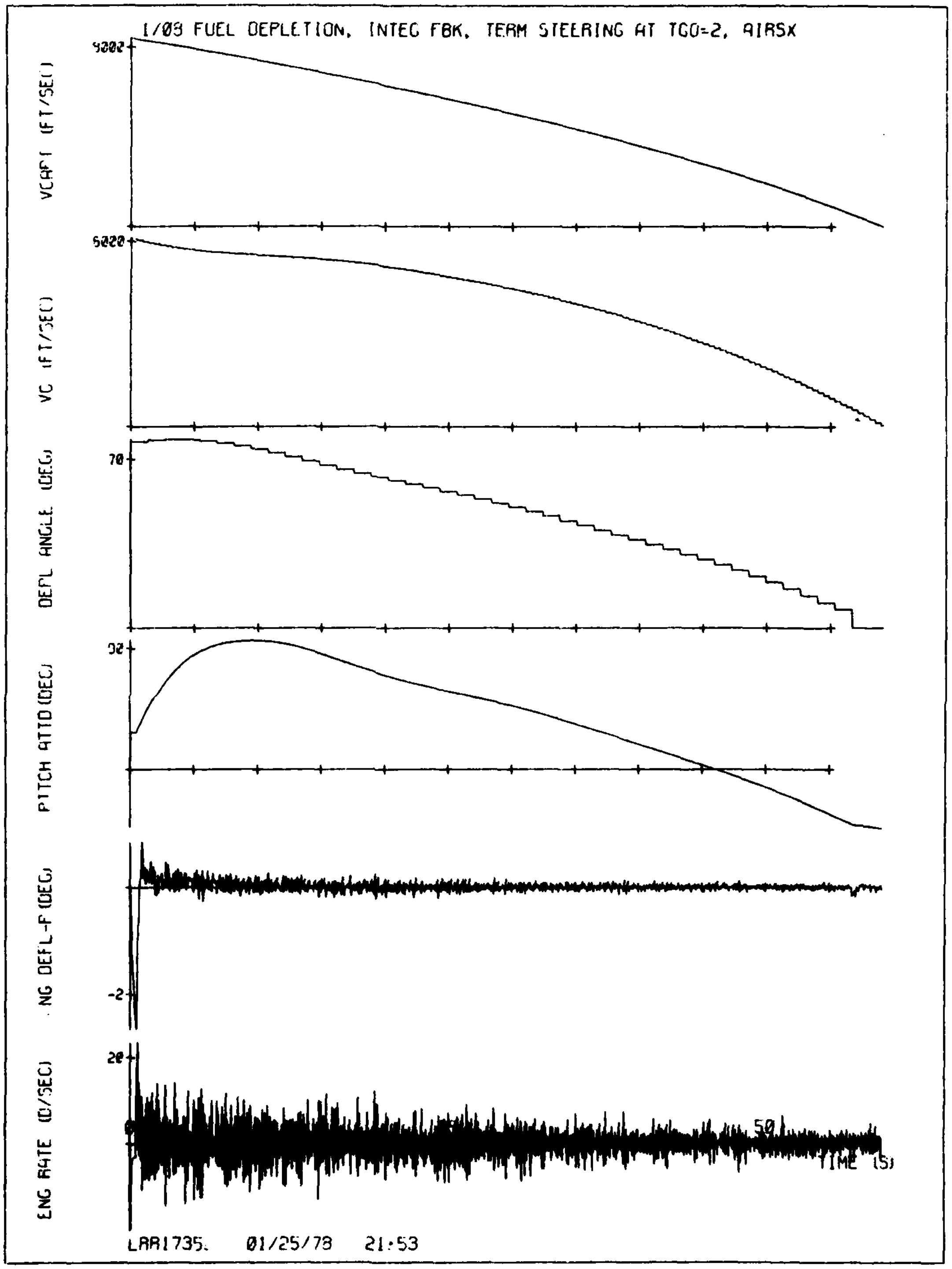

Figure 68-2. STEER, fuel depletion steering, integral feedback, T_{FR} = 2, AIRSX.

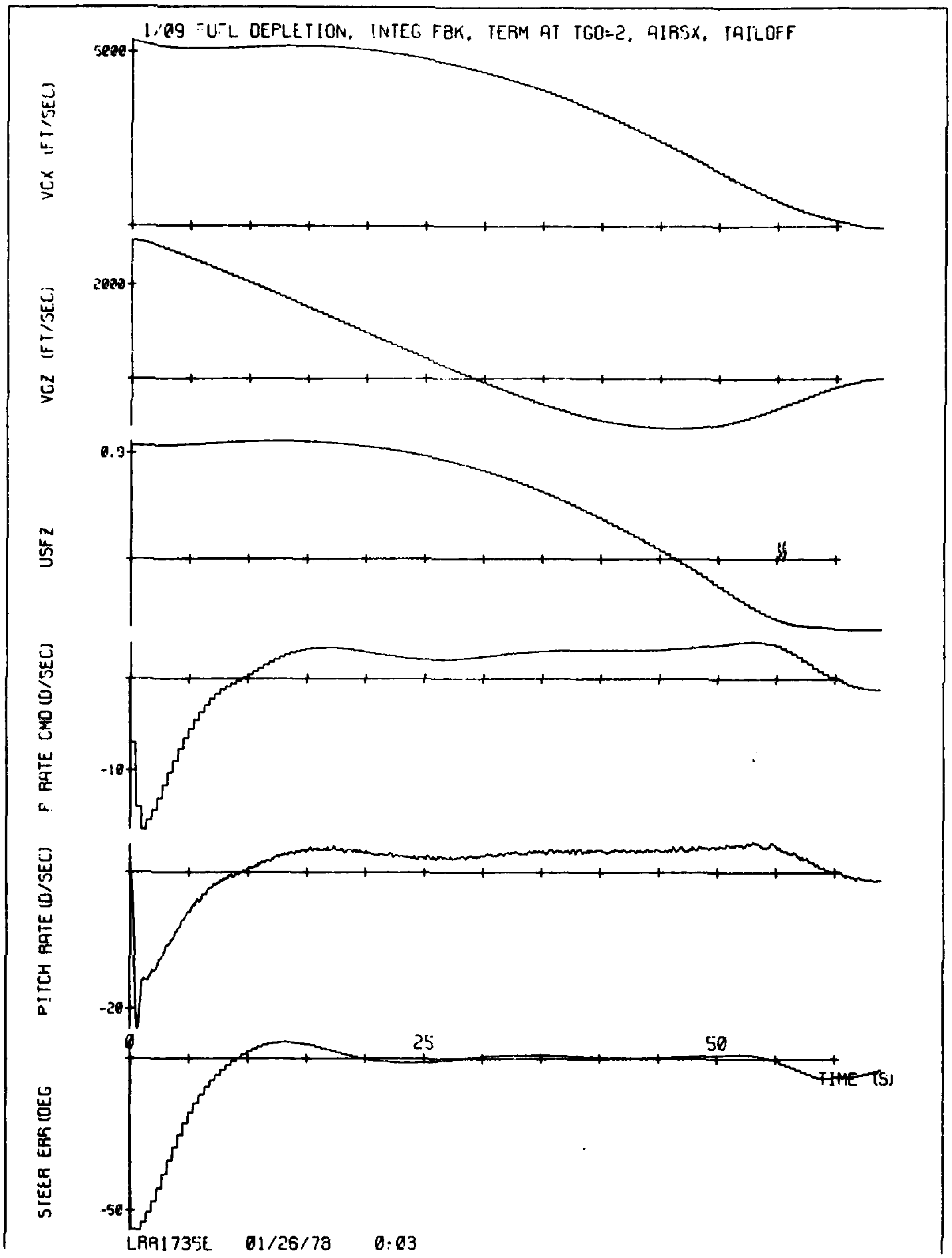

Figure 69-1. STEER, fuel depletion steering, integral feedback, T_{FR} = 2, AIRSX, thrust tailoff.

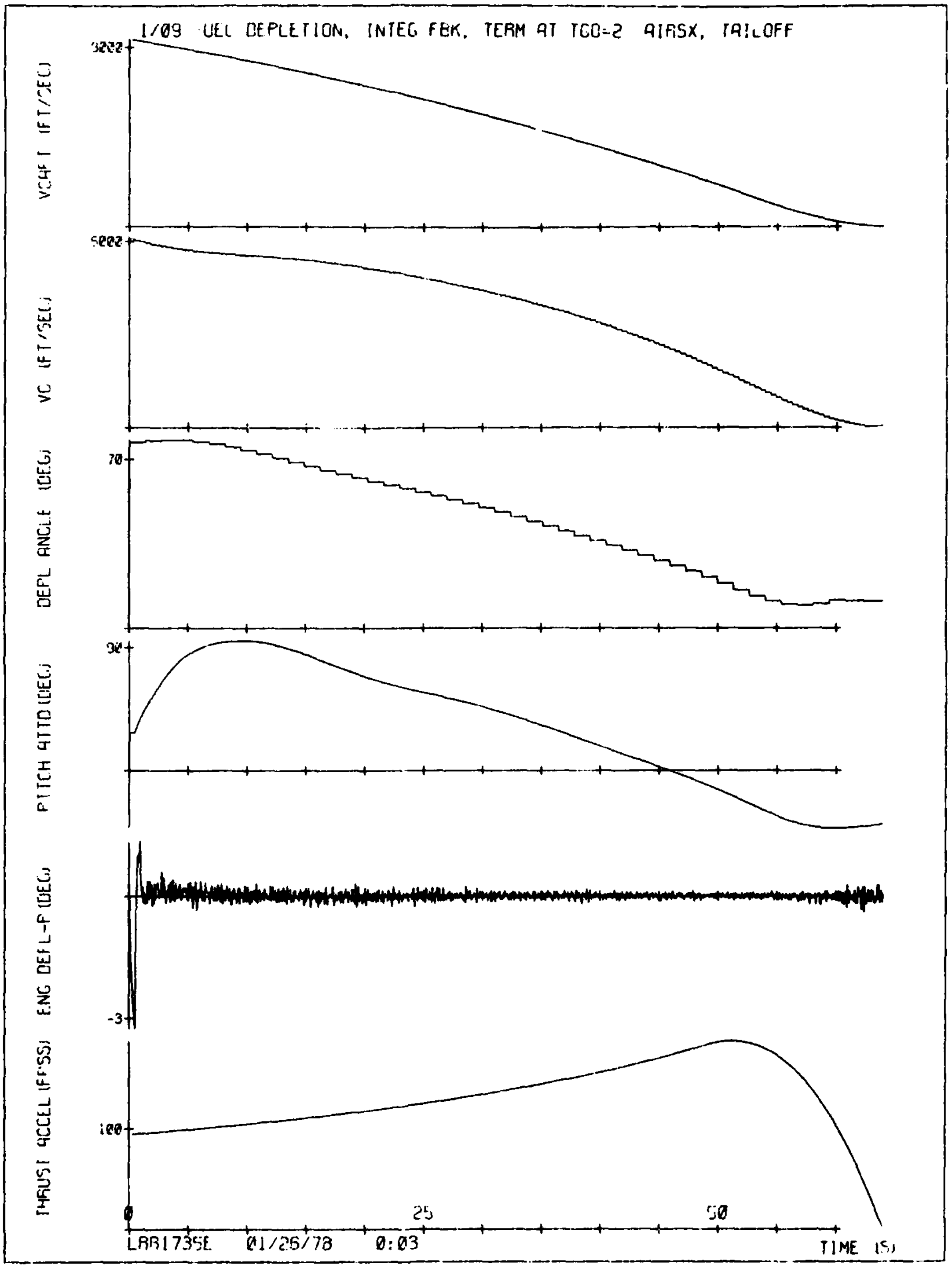

Figure 69-2. STEER, fuel depletion steering, integral feedback, T_{FR} = 2, AIRSX, thrust tailoff.

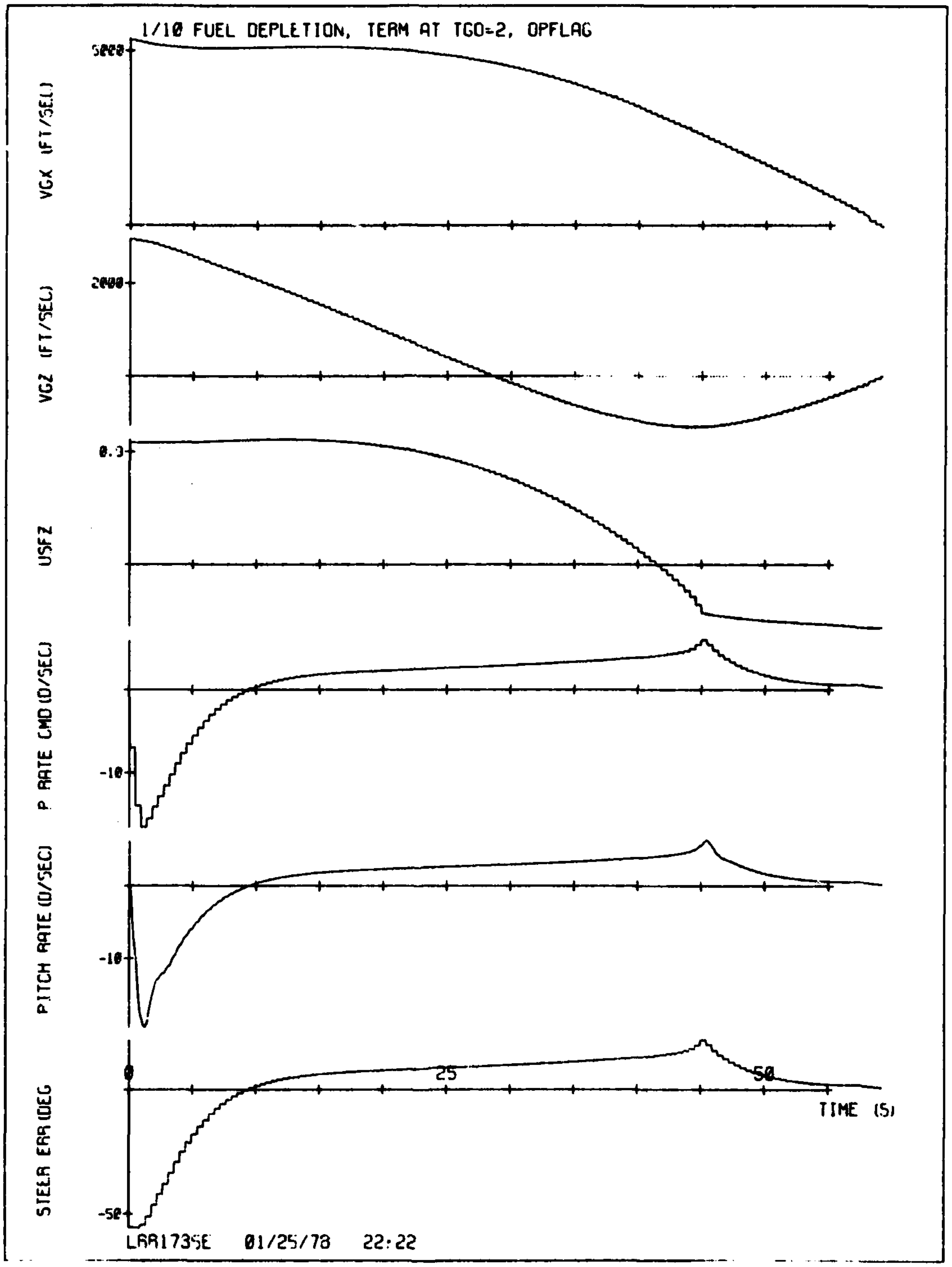

Figure 70-1. STEER, fuel depletion steering, T_{FR} = 2, simplified θ calculation.

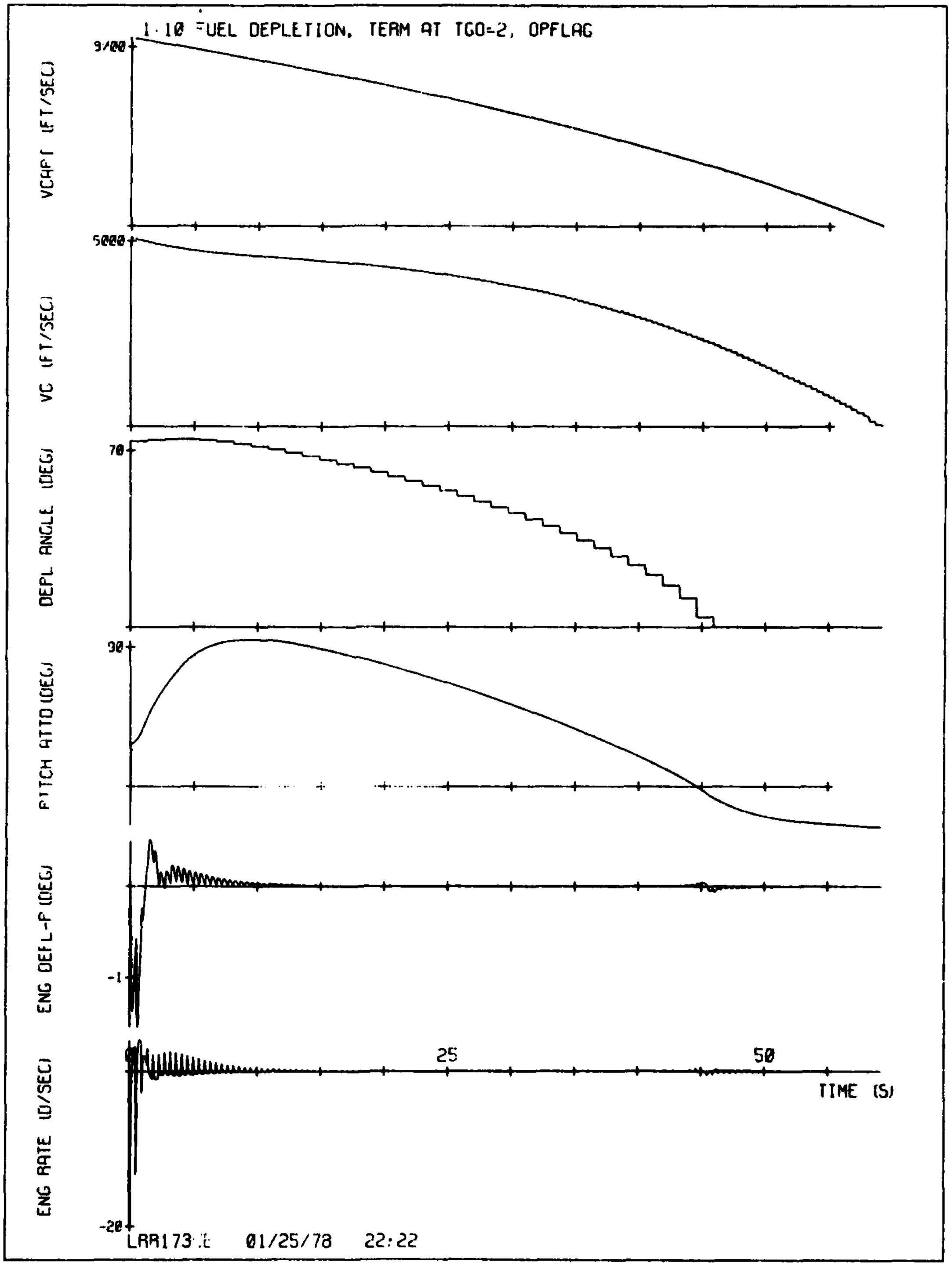

Figure 70-2. STEER, fuel depletion steering, T_{FR} = 2, simplified θ calculation.

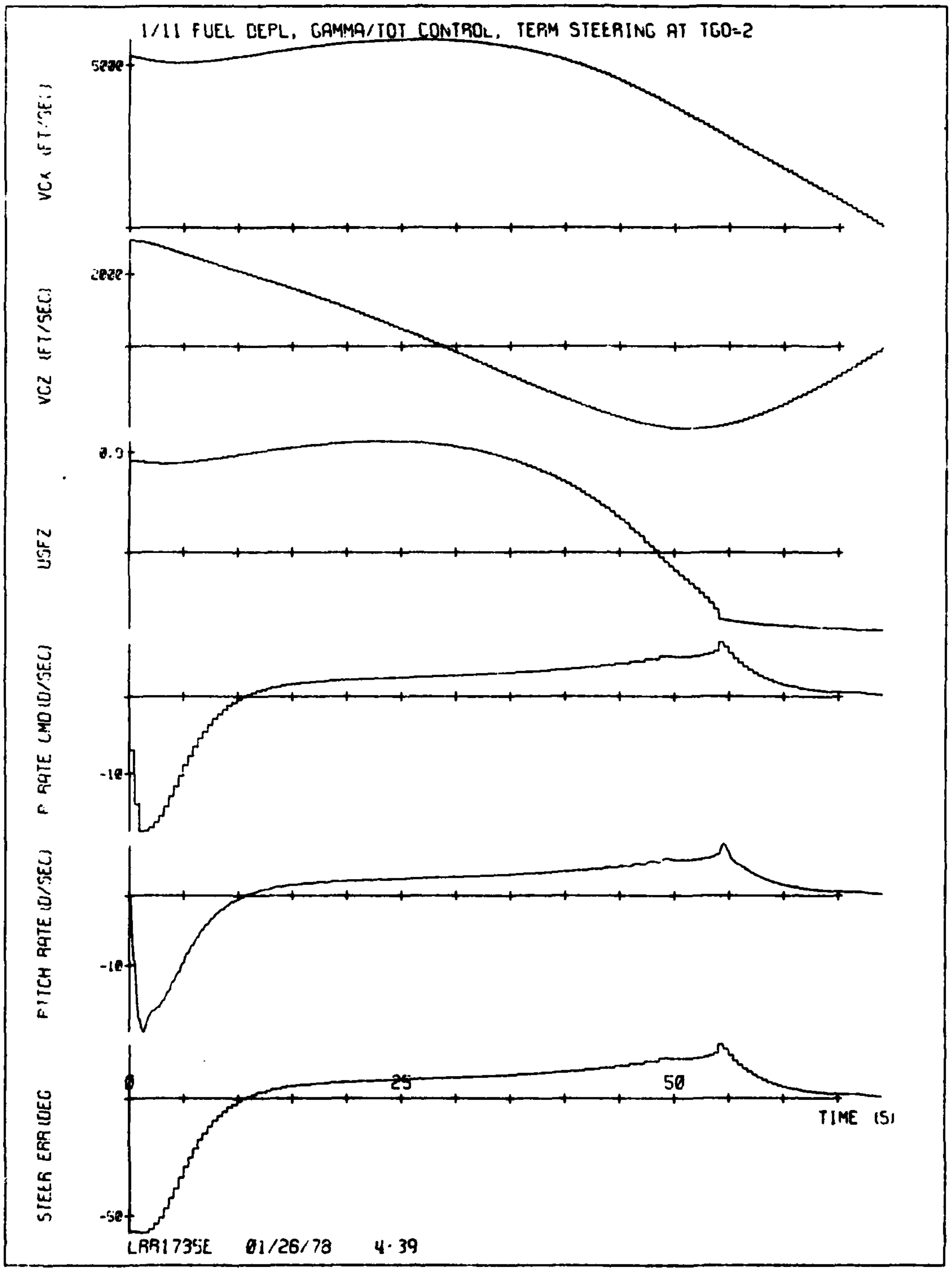

Figure 71-1. STEER, fuel depletion steering, Gamma/TOT control, T_{FR} = 2.

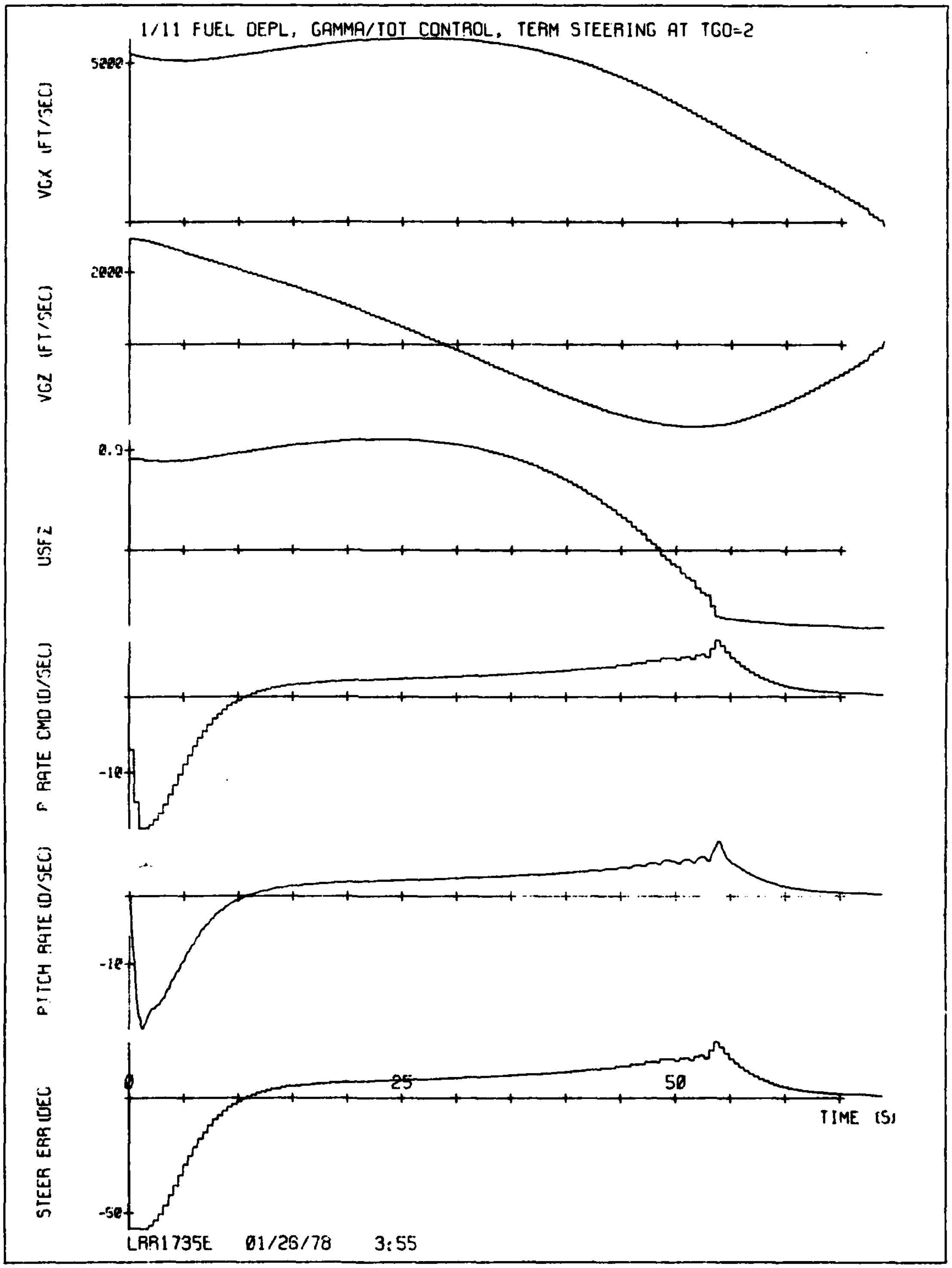

Figure 71-2. STEER, fuel depletion steering, Gamma/TOT control, T_{FR} = 2.

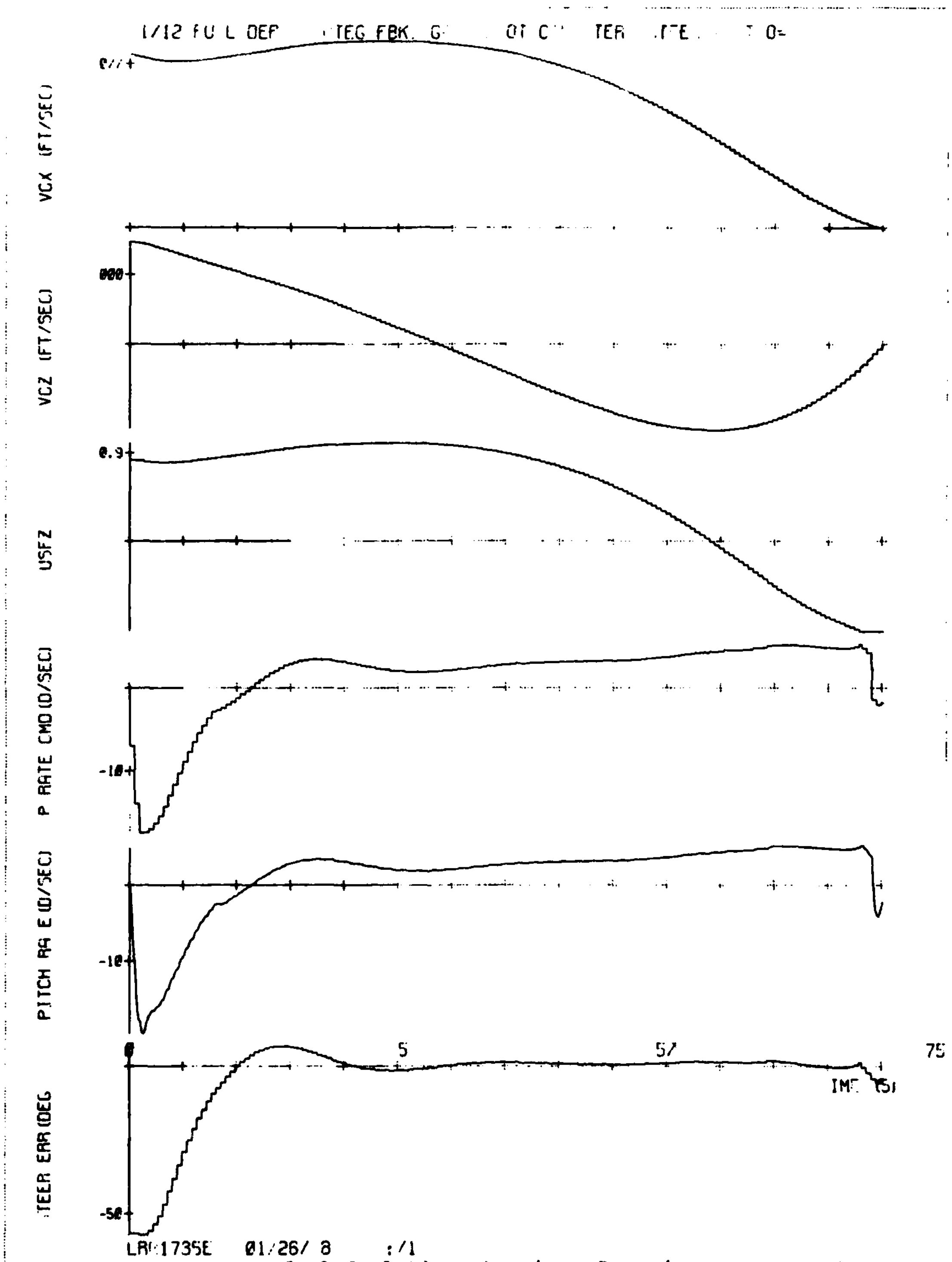

Figure 72-1. STEER, fuel depletion steering, Gamma/TOT control, integral feedback, T_{FR} = 2.

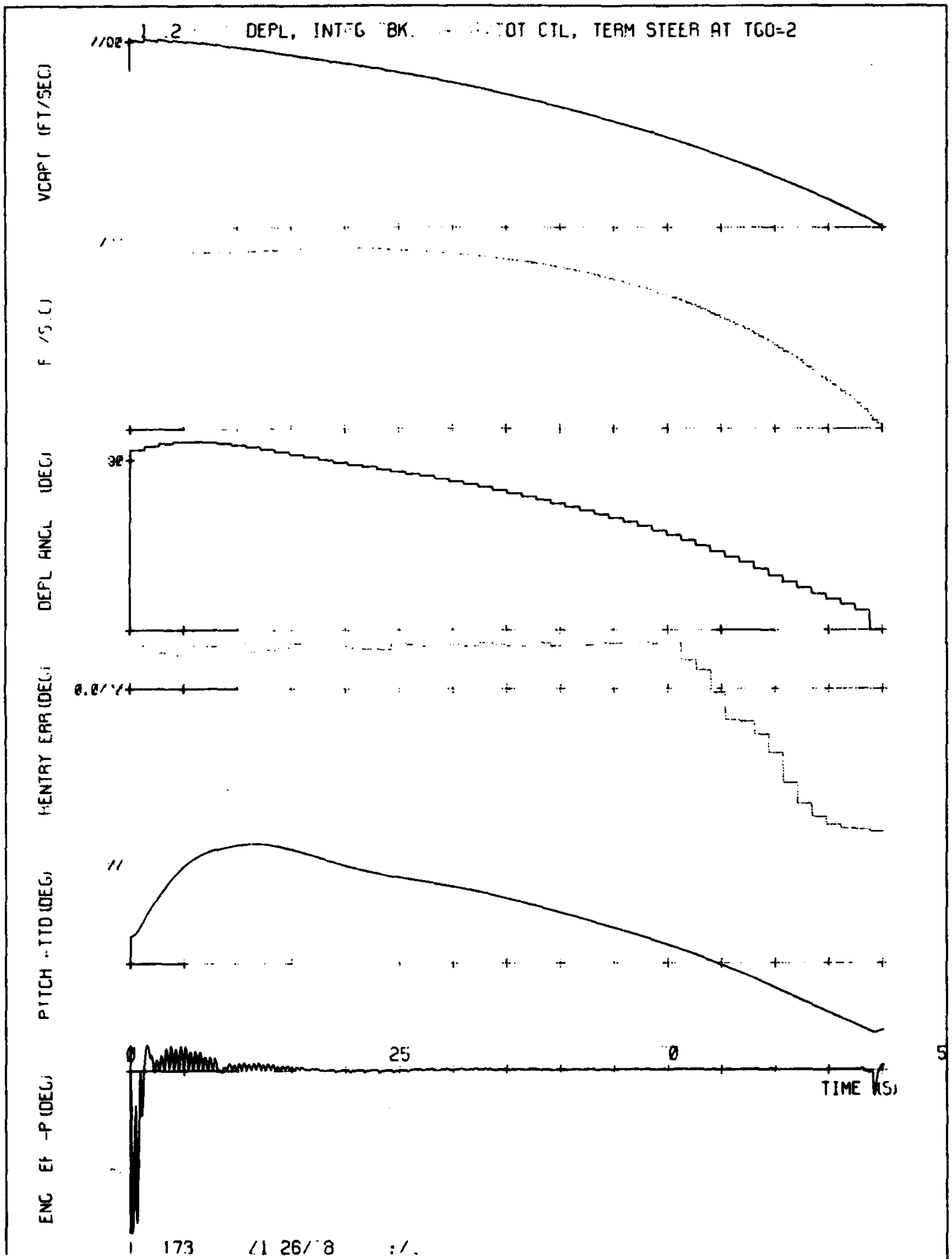

Figure 72-2. STEER, fuel depletion steering, Gamma/TOT control, integral feedback, T_{FR} = 2.

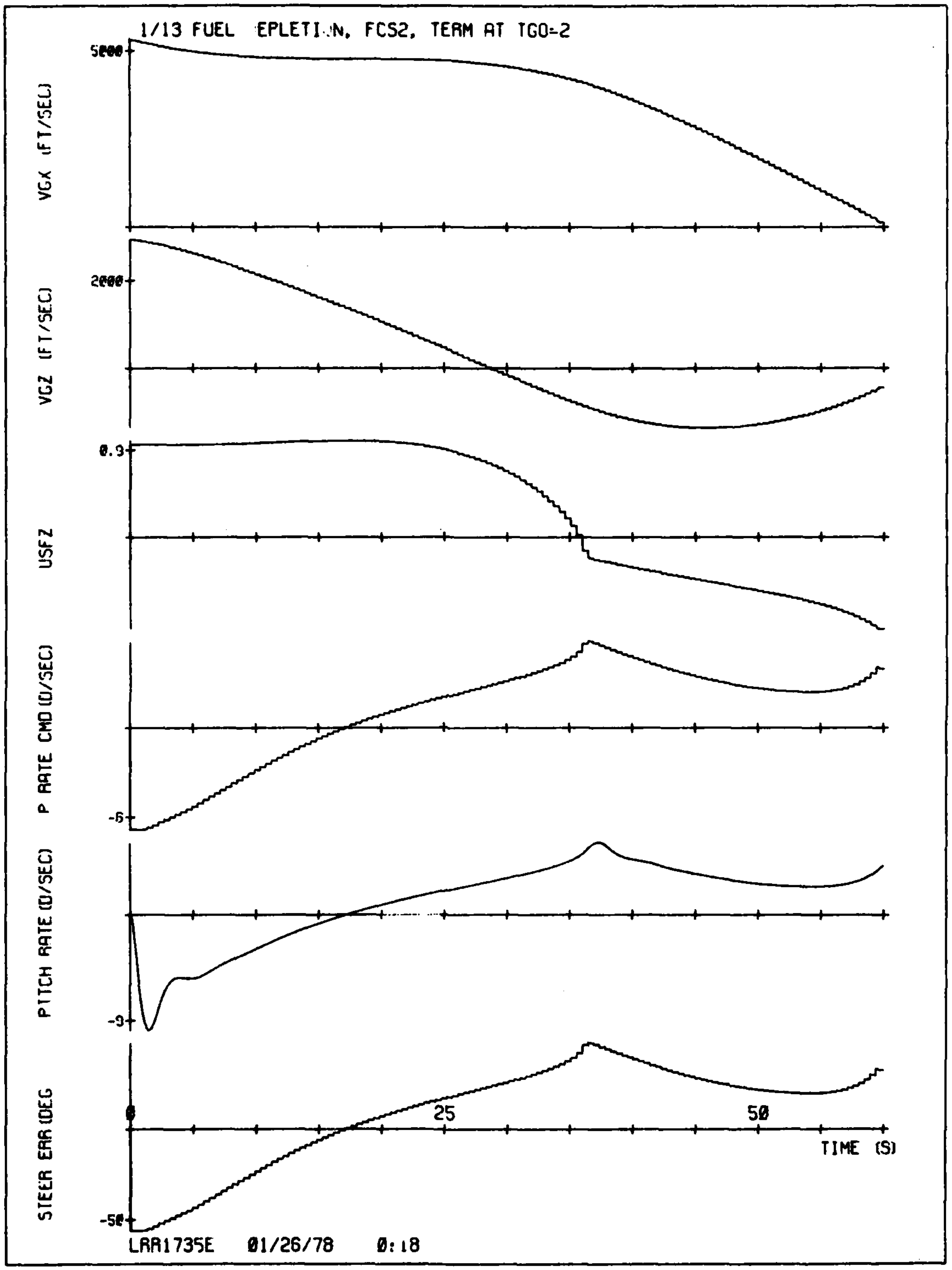

Figure 73-1. STEER, fuel depletion steering, 2 rad/sec autopilot, T_{FR} = 2.

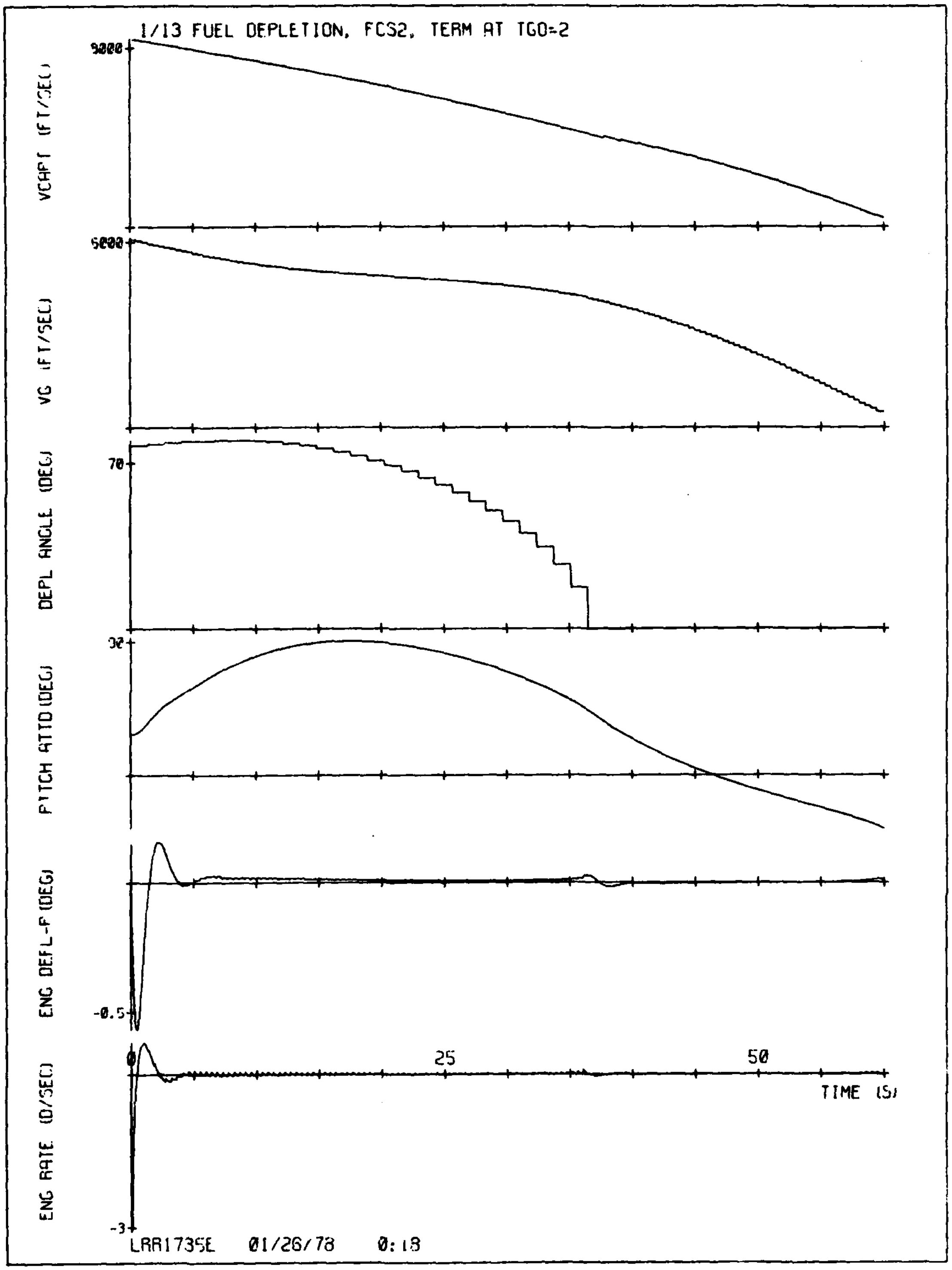

Figure 73-2. STEER, fuel depletion steering, 2 rad/sec autopilot, T_{FR} = 2.

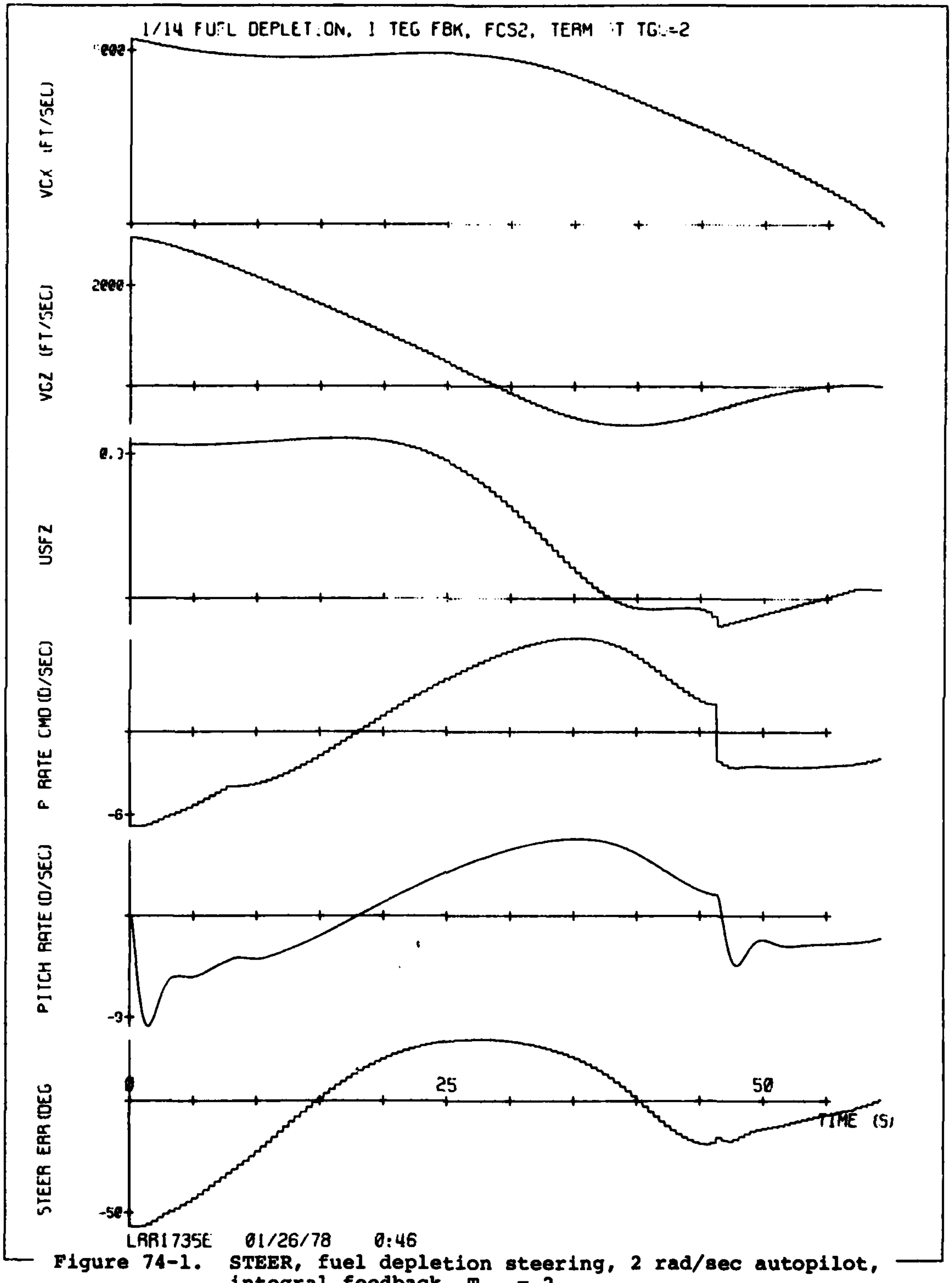

Figure 74-1. STEER, fuel depletion steering, 2 rad/sec autopilot, integral feedback, T_{FR} = 2.

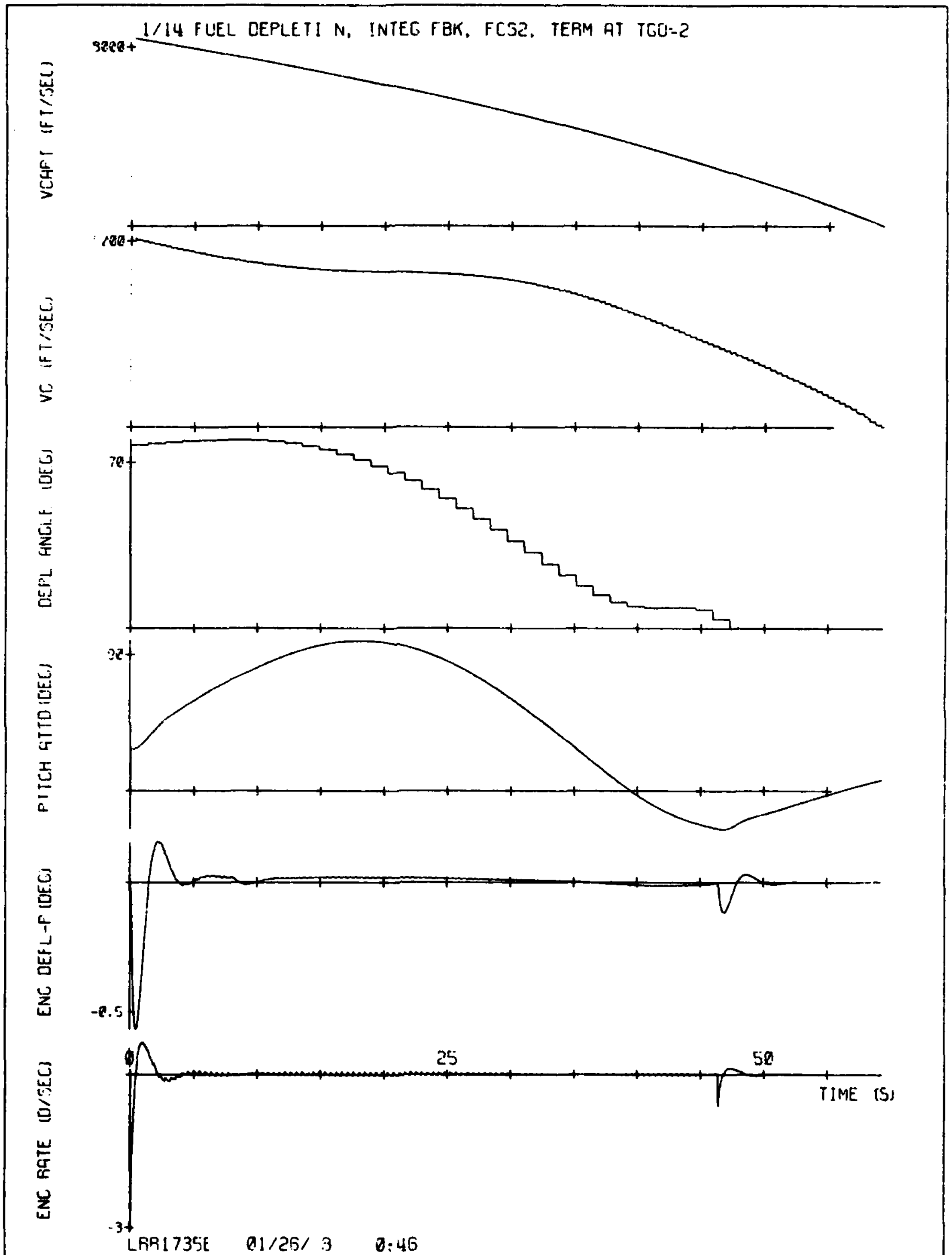

Figure 74-2. STEER, fuel depletion steering, 2 rad/sec autopilot, integral feedback, $T_{FR} = 2$.

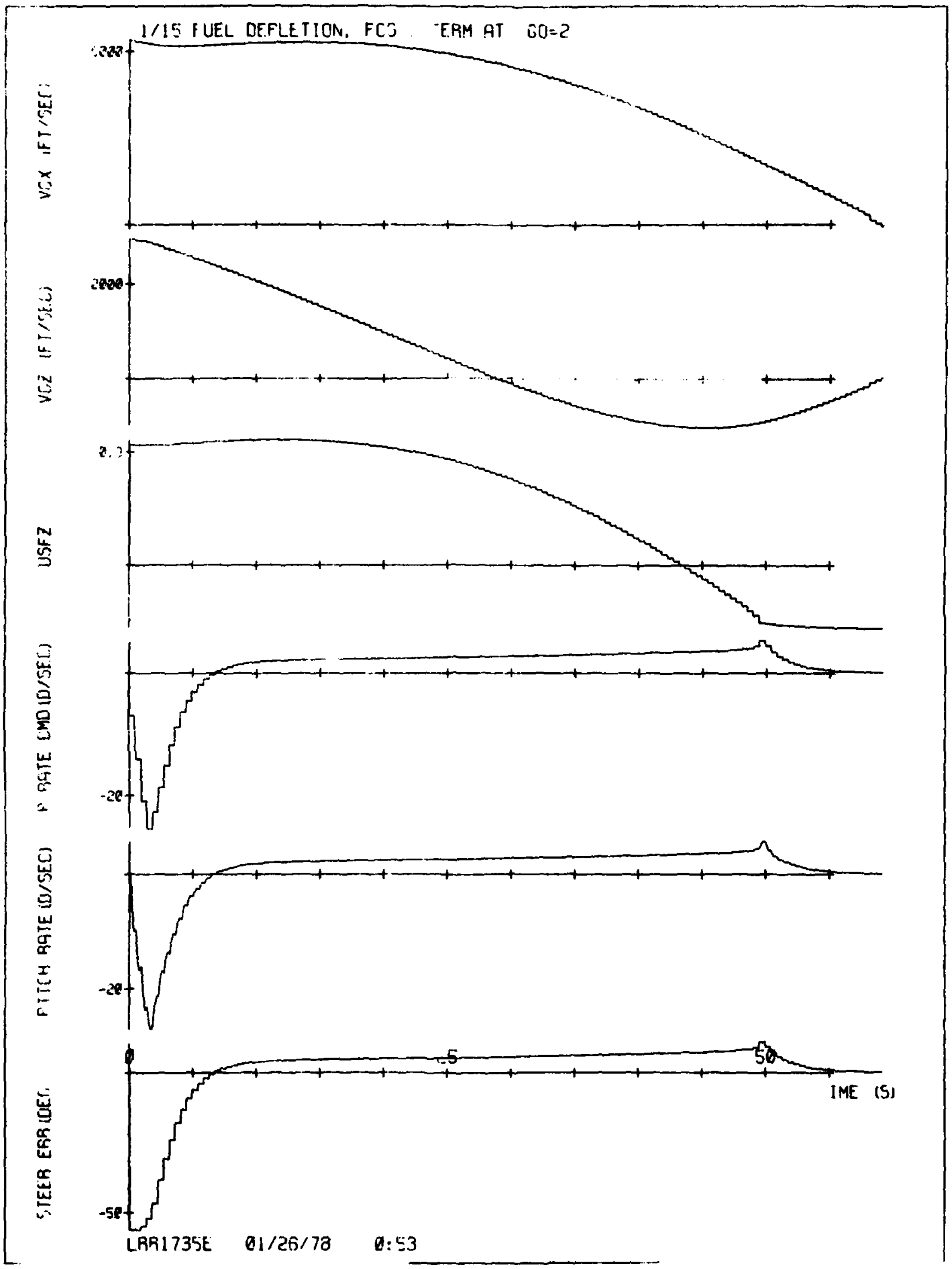

Figure 75-1. STEER, fuel depletion steering, 8 rad/sec autopilot, $T_{FR} = 2$.

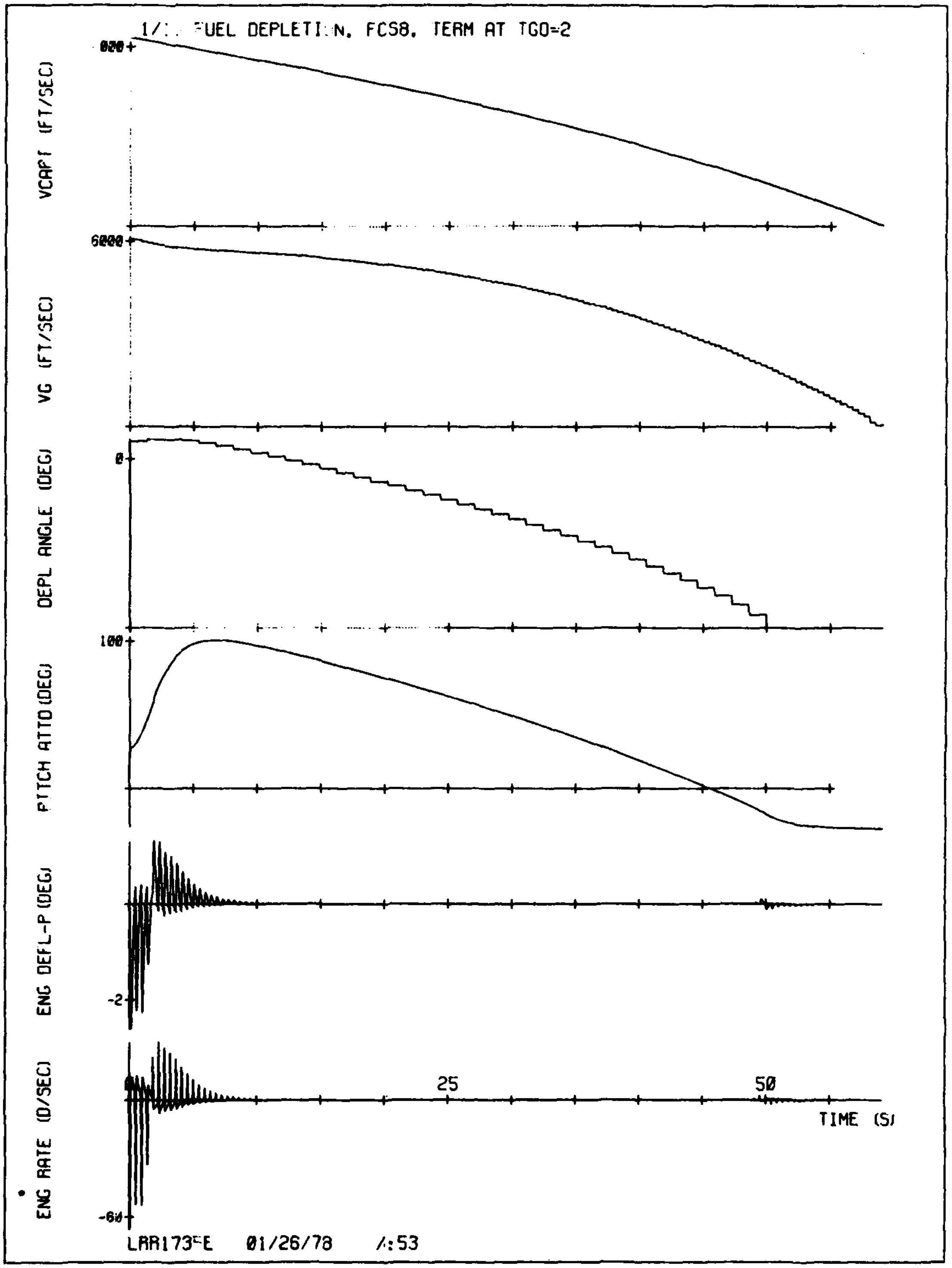

Figure 75-2. STEER, fuel depletion steering, 8 rad/sec autopilot, T_{FR} = 2.

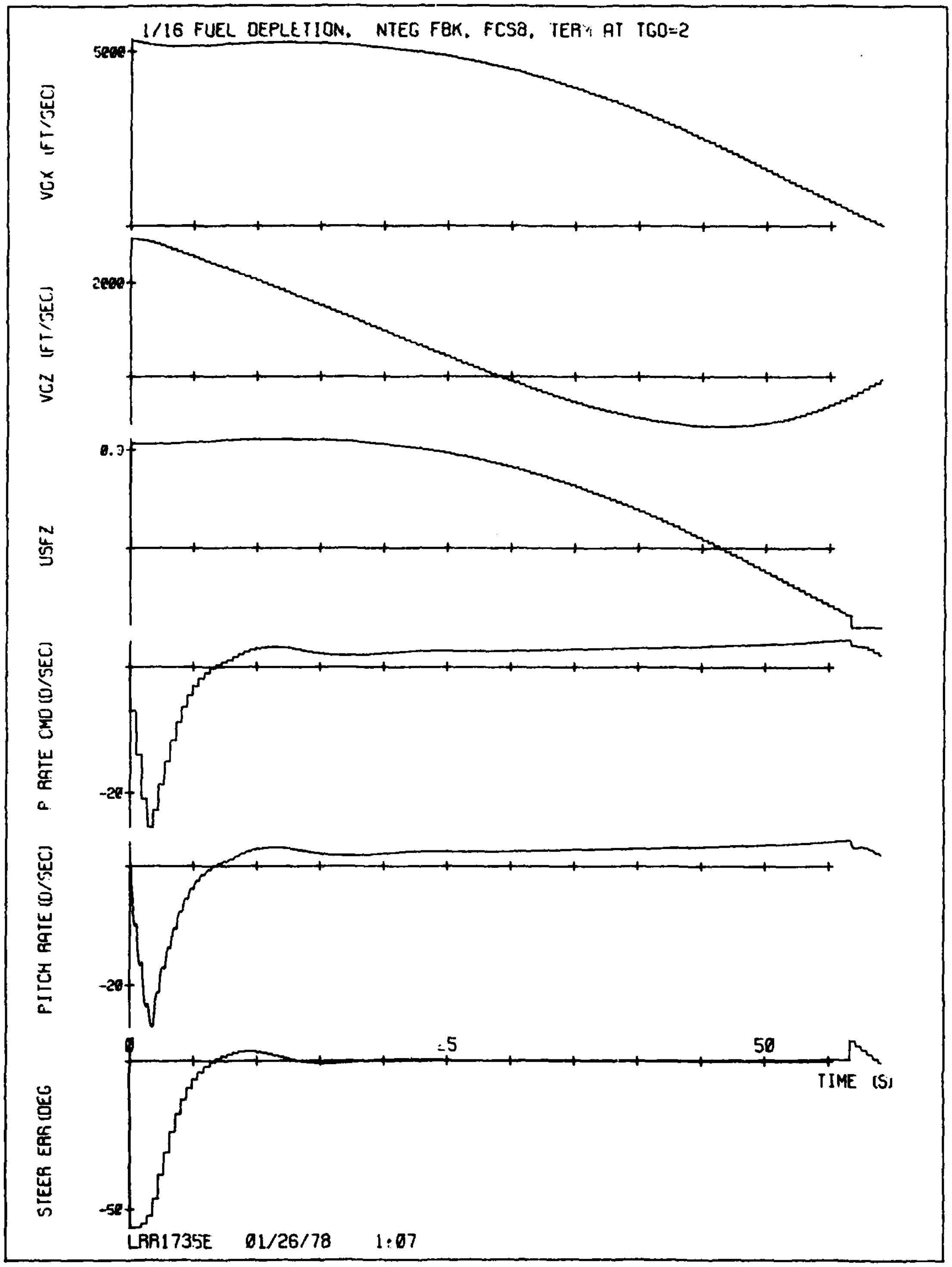

Figure 76-1. STEER, fuel depletion steering, 8 rad/sec autopilot, integral feedback, $T_{FR} = 2$.

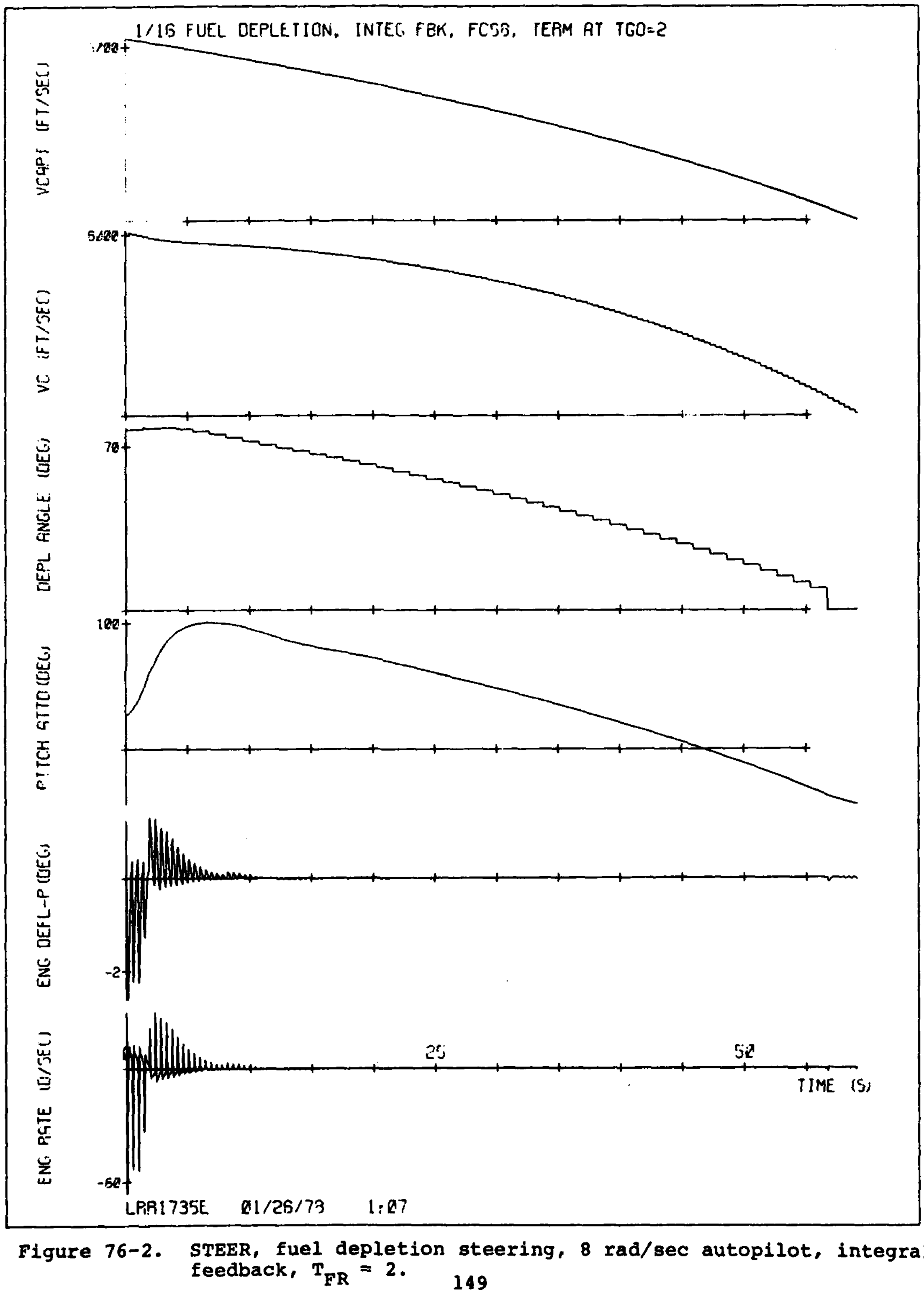

Figure 76-2. STEER, fuel depletion steering, 8 rad/sec autopilot, integral feedback, T_{FR} = 2.

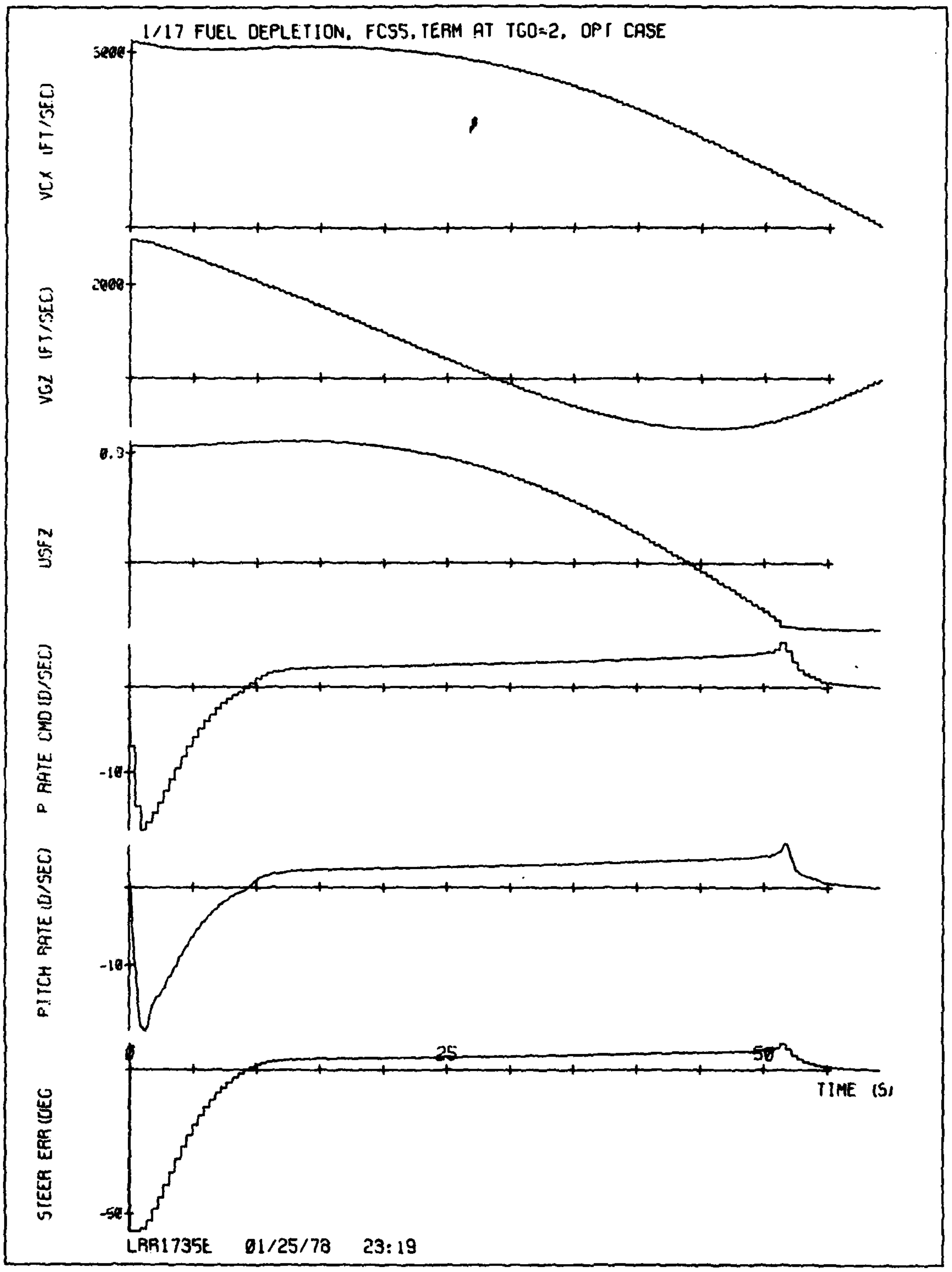

Figure 77-1. STEER, fuel depletion steering, optimized design, $T_{FR} = 2$.

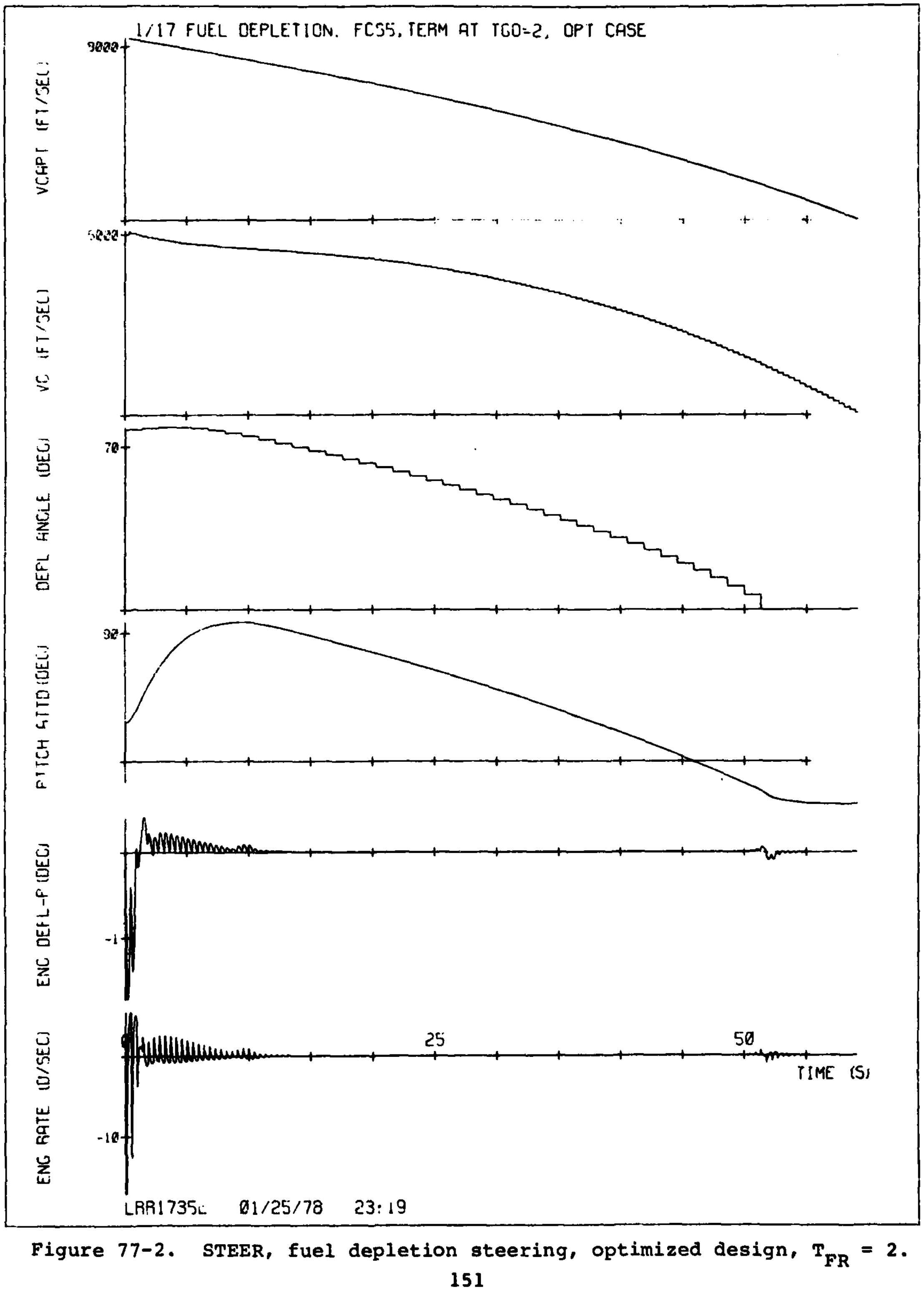

Figure 77-2. STEER, fuel depletion steering, optimized design, T_{FR} = 2.

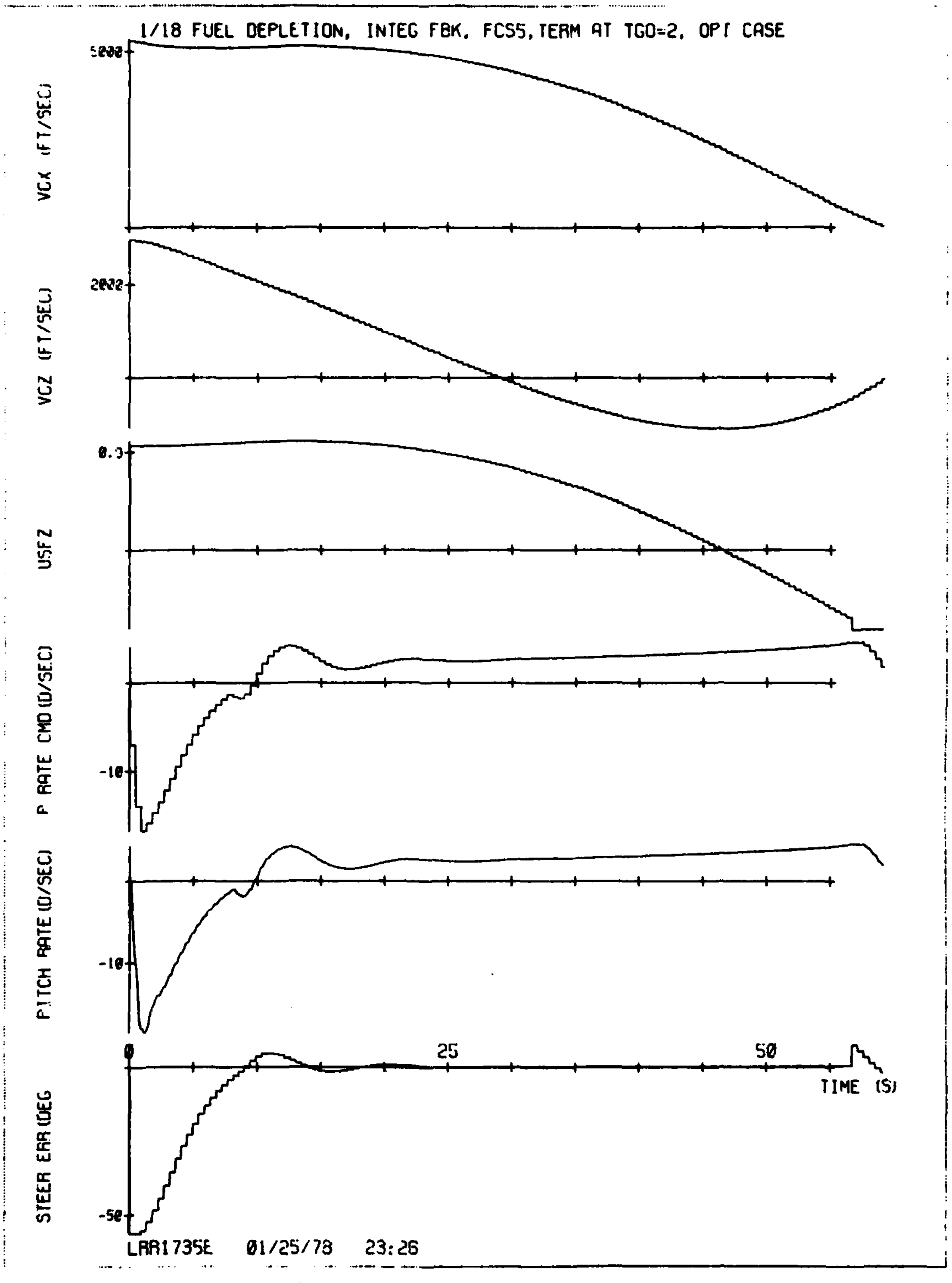

Figure 78-1. STEER, fuel depletion steering, optimized design, integral feedback, $T_{FR} = 2$.

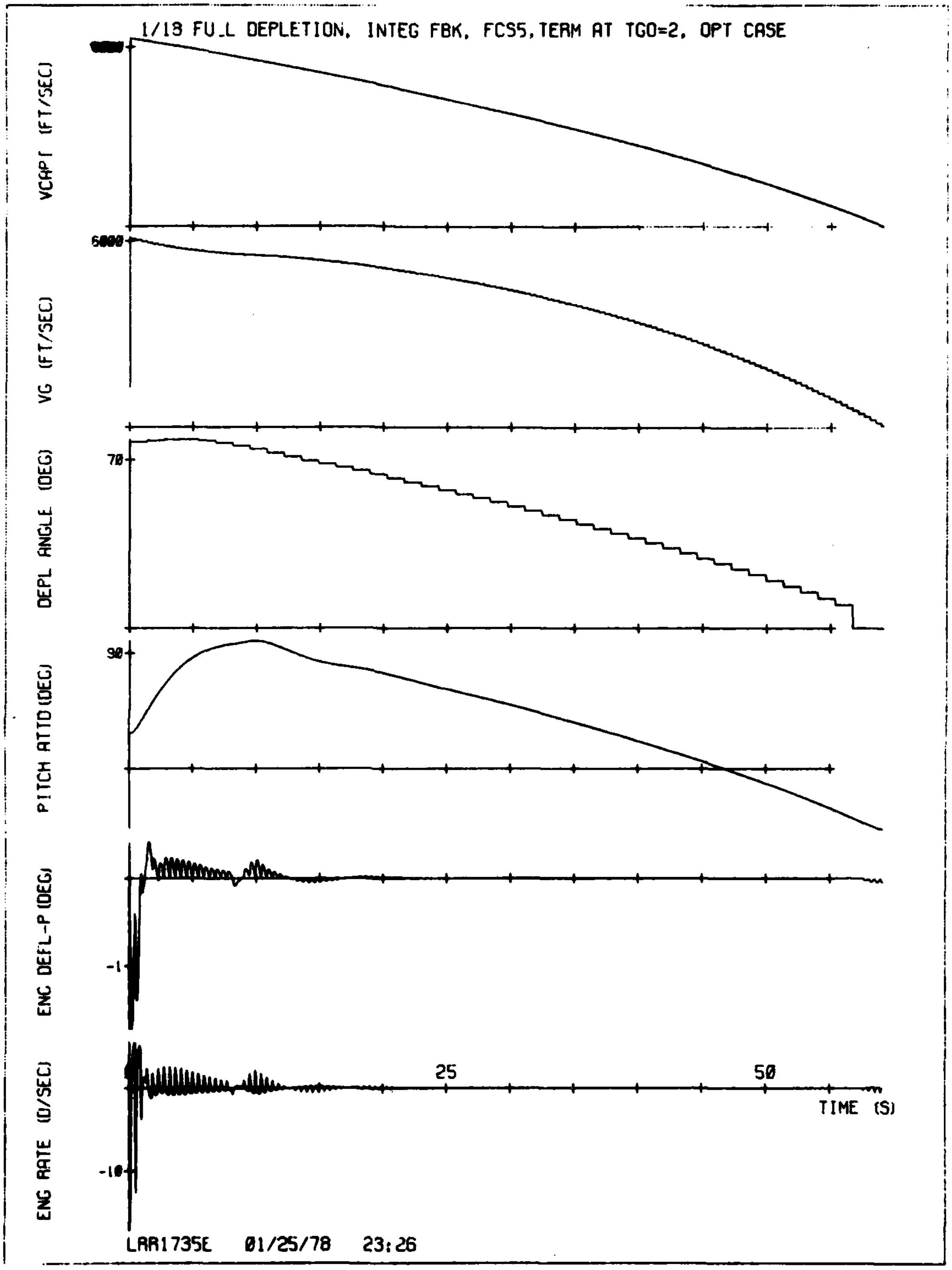

Figure 78-2. STEER, fuel depletion steering, optimized design, integral feedback, T_{FR} = 2.

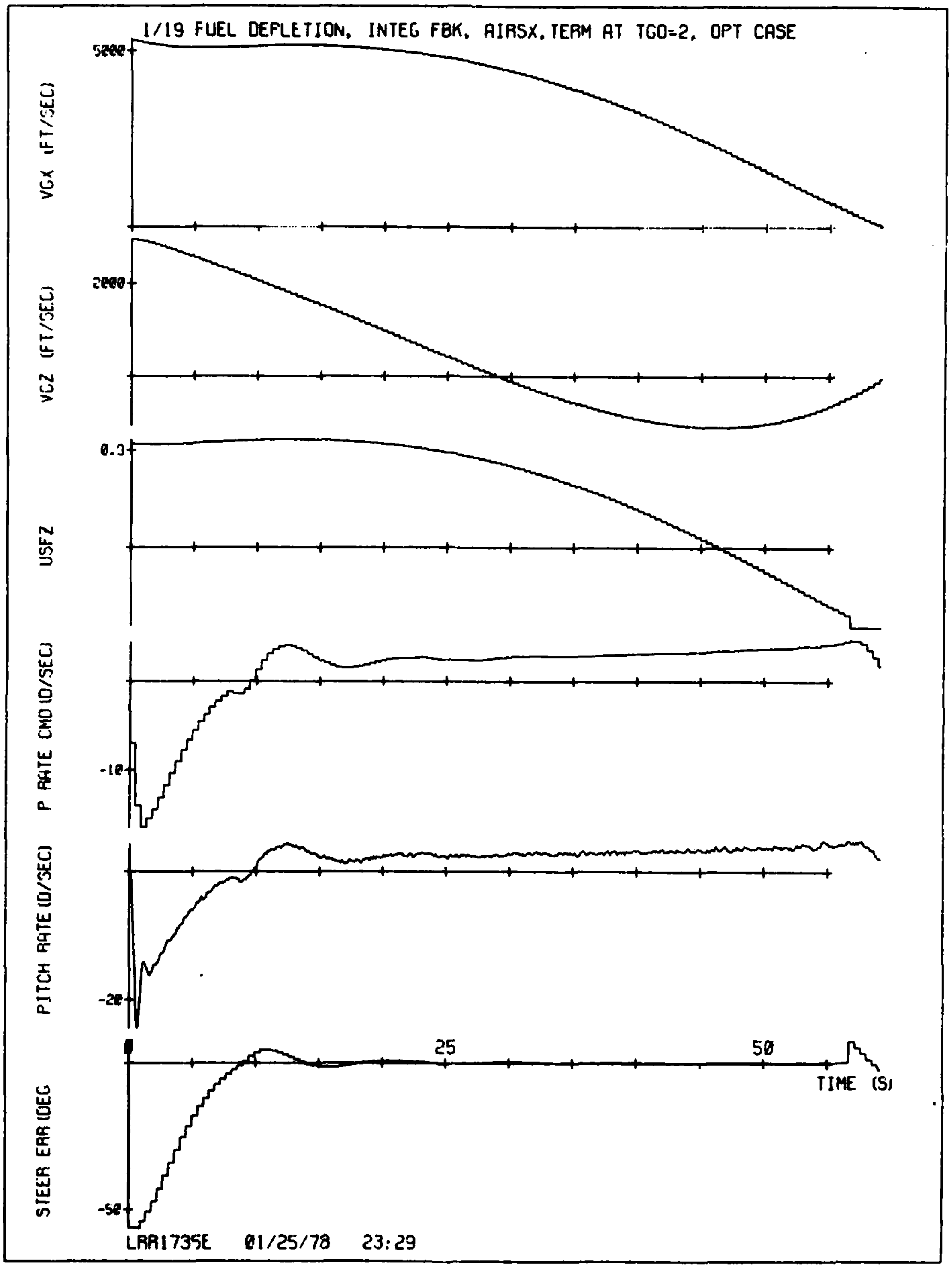

Figure 79-1. STEER, fuel depletion steering, optimized design, integral feedback, AIRSX, T_{FR} =2.

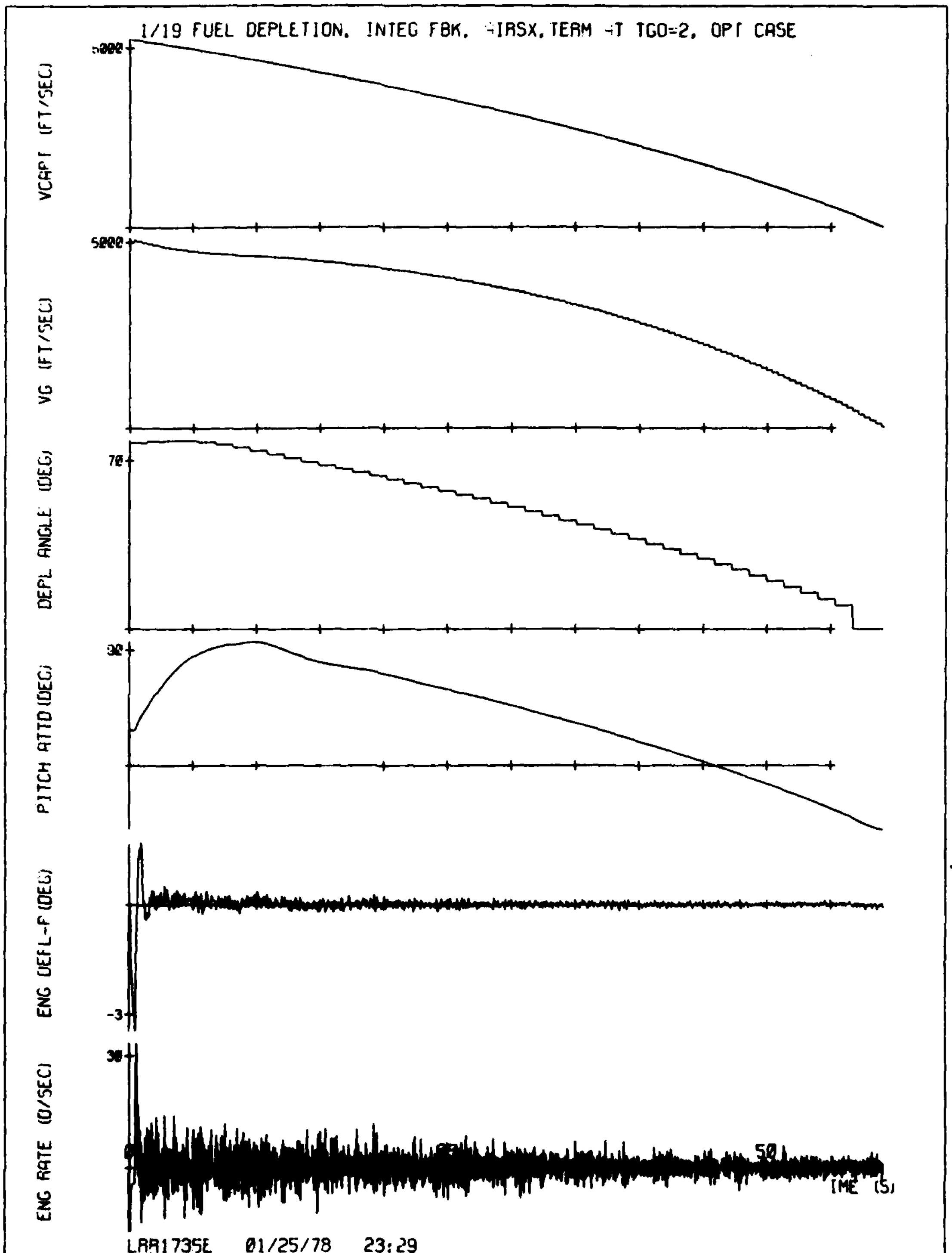

Figure 79-2. STEER, fuel depletion steering, optimized design, integral feedback, AIRSX, $T_{FR} = 2$.

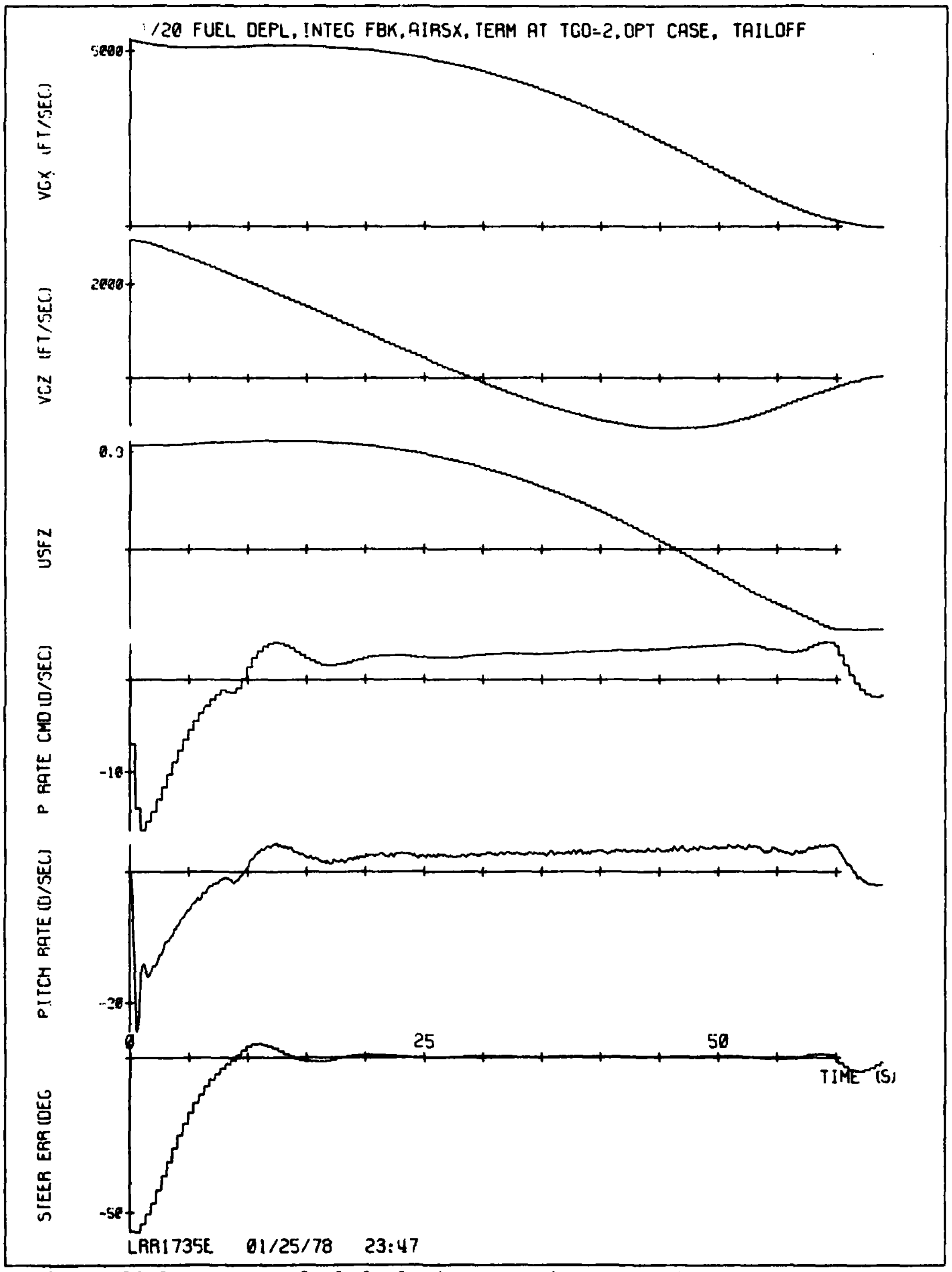

Figure 80-1. STEER, fuel depletion steering, optimized deisgn, integral feedback, AIRSX, thrust tailoff, T_{FR} = 2.

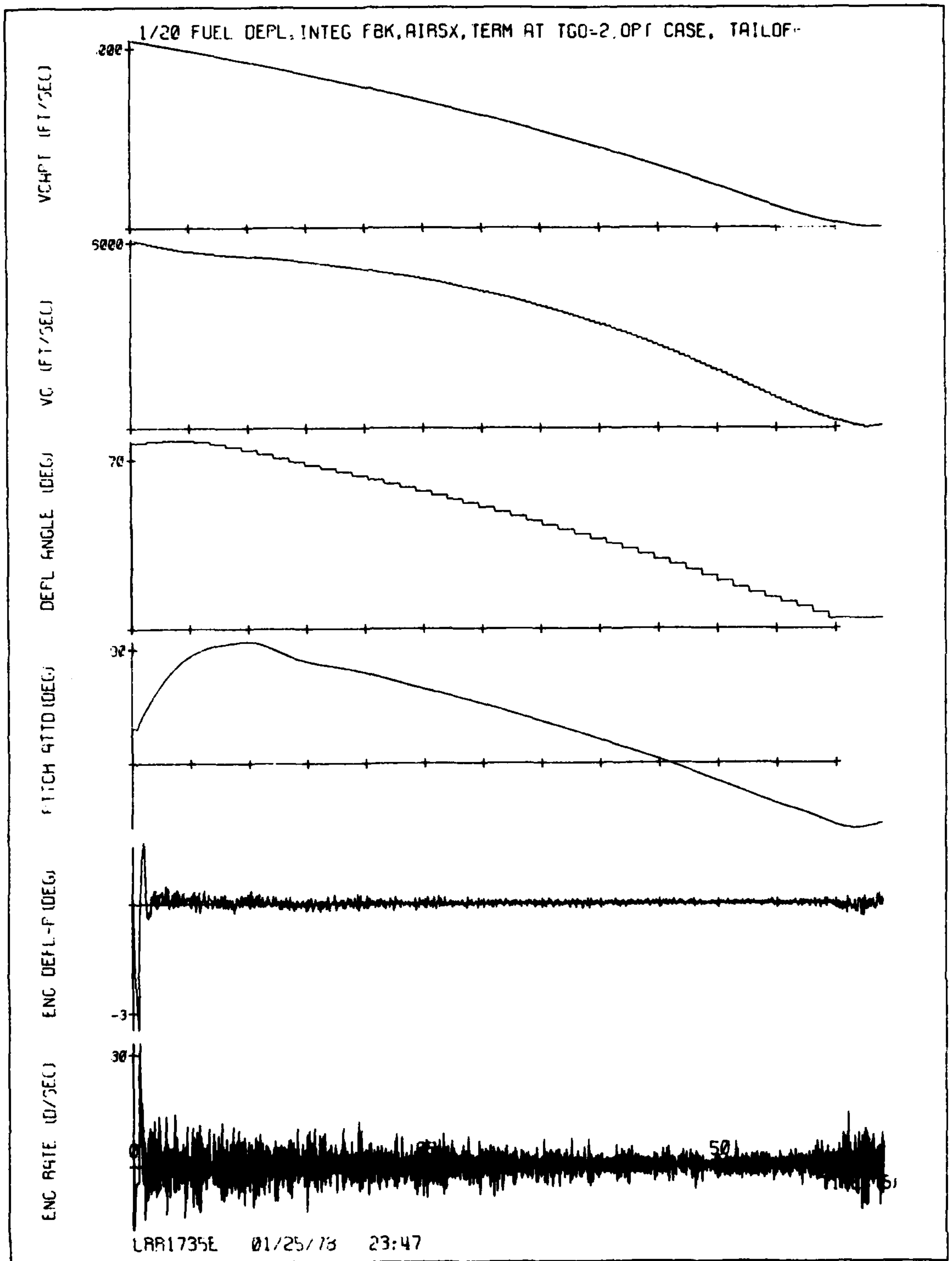

Figure 80-2. STEER, fuel depletion steering, optimized design, integral feedback, AIRSX, thrust tailoff, T_{FR} = 2.

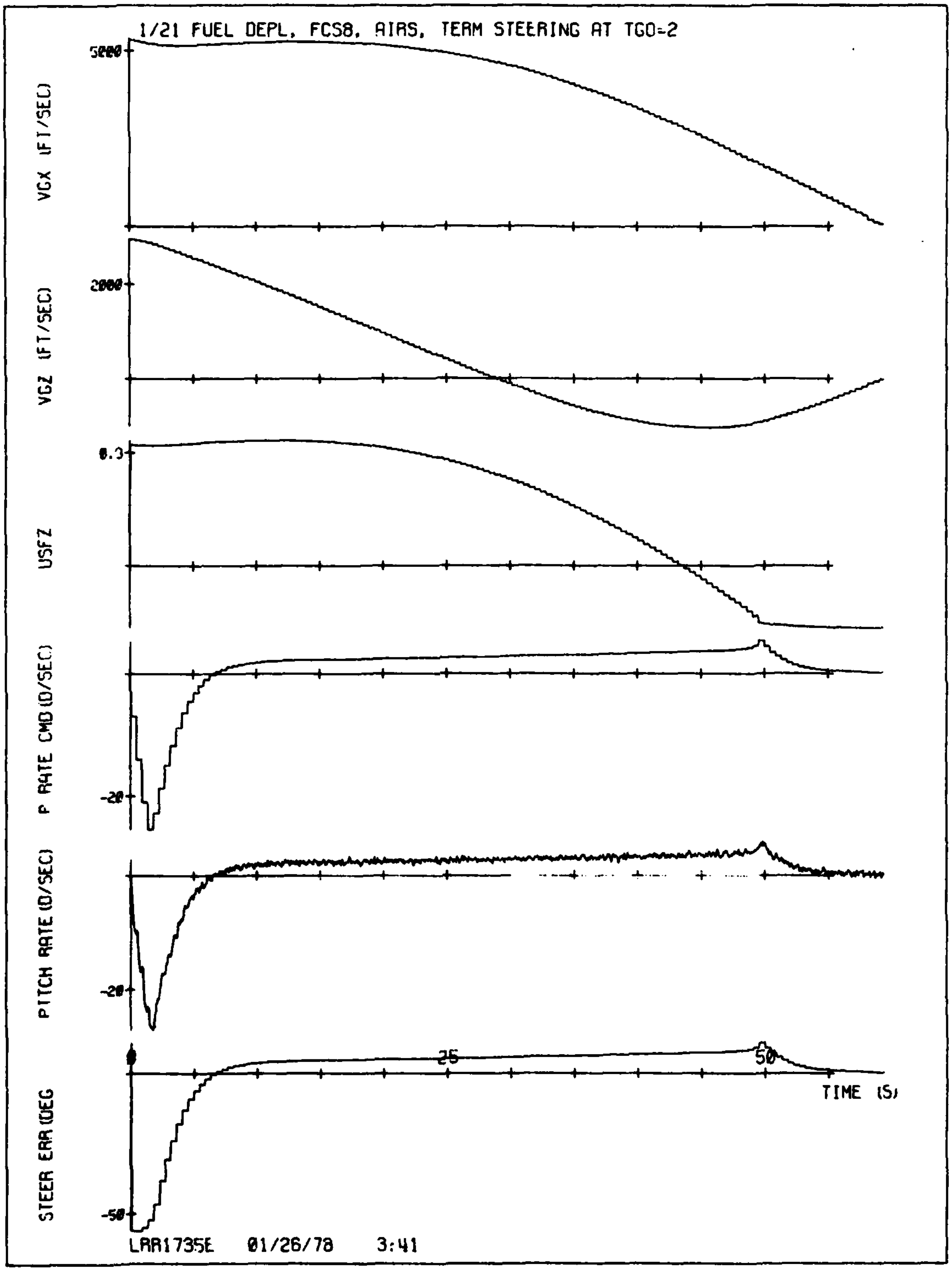

Figure 81-1. STEER, fuel depletion steering, 8 rad/sec autopilot, AIRS, $T_{FR} = 2$.

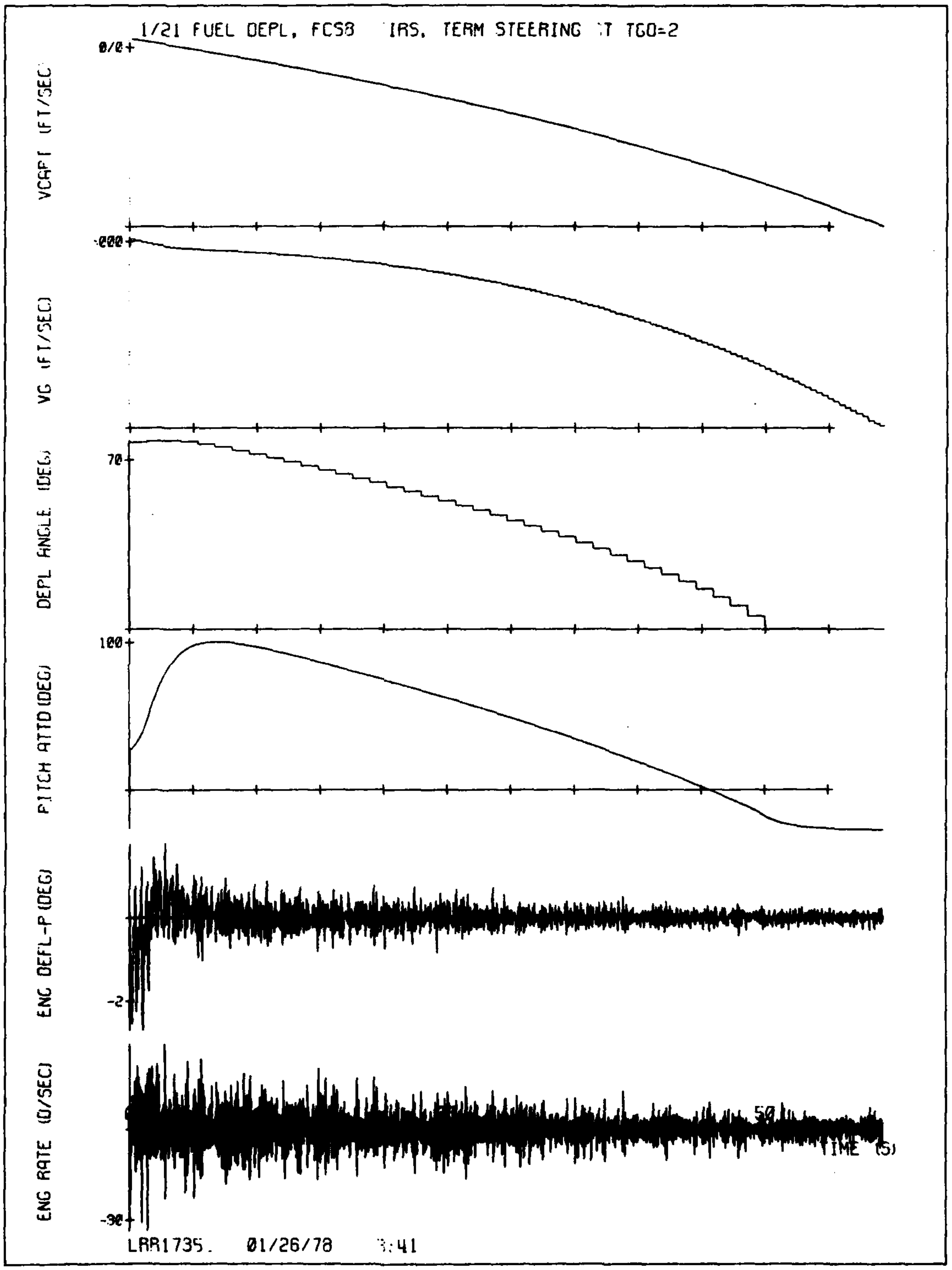

Figure 81-2. STEER, fuel depletion steering, 8 rad/sec autopilot, AIRS, T_{FR} = 2.

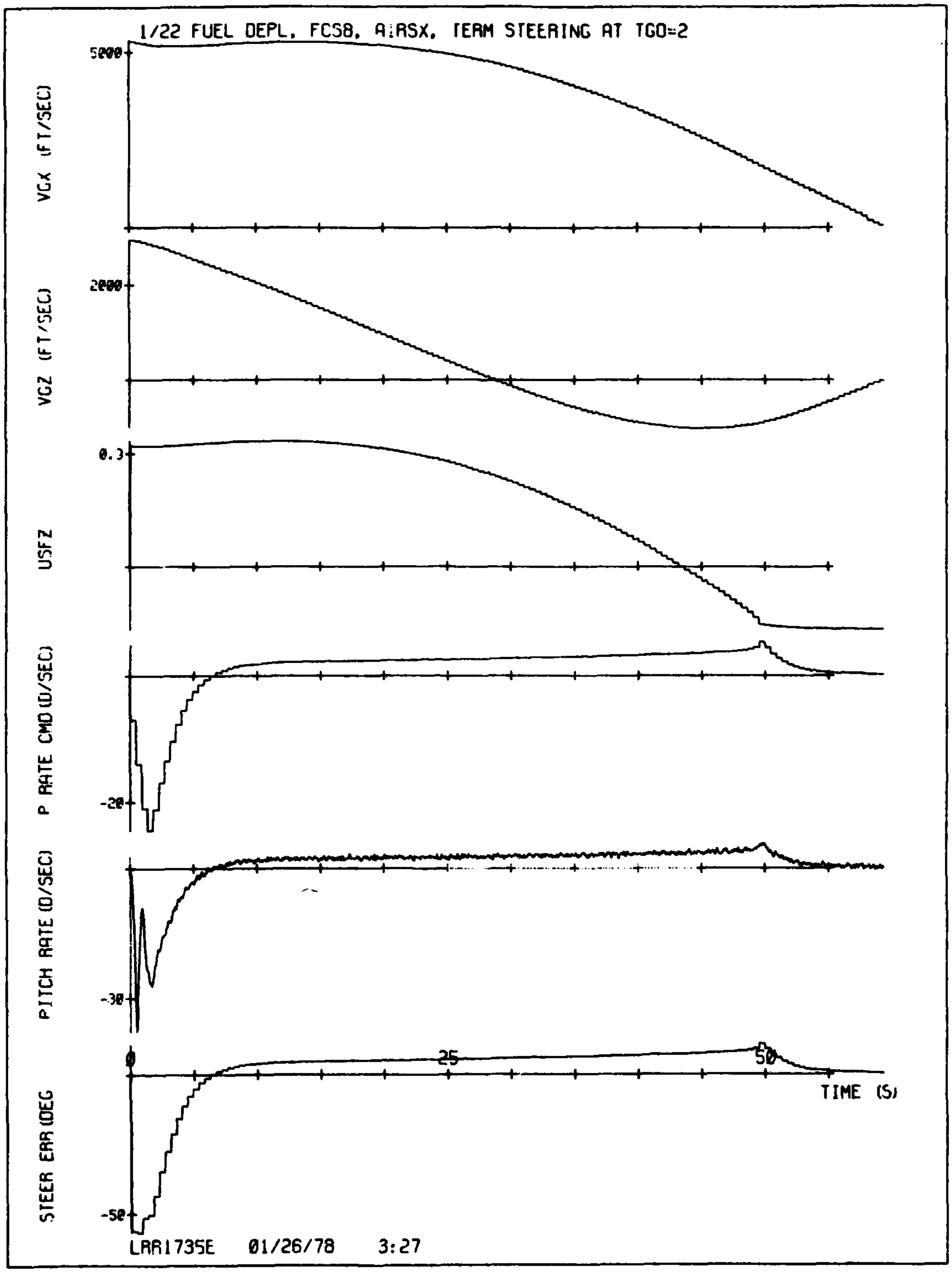

Figure 82-1. STEER, fuel depletion steering, 8 rad/sec autopilot, AIRSX, T_{FR} = 2.

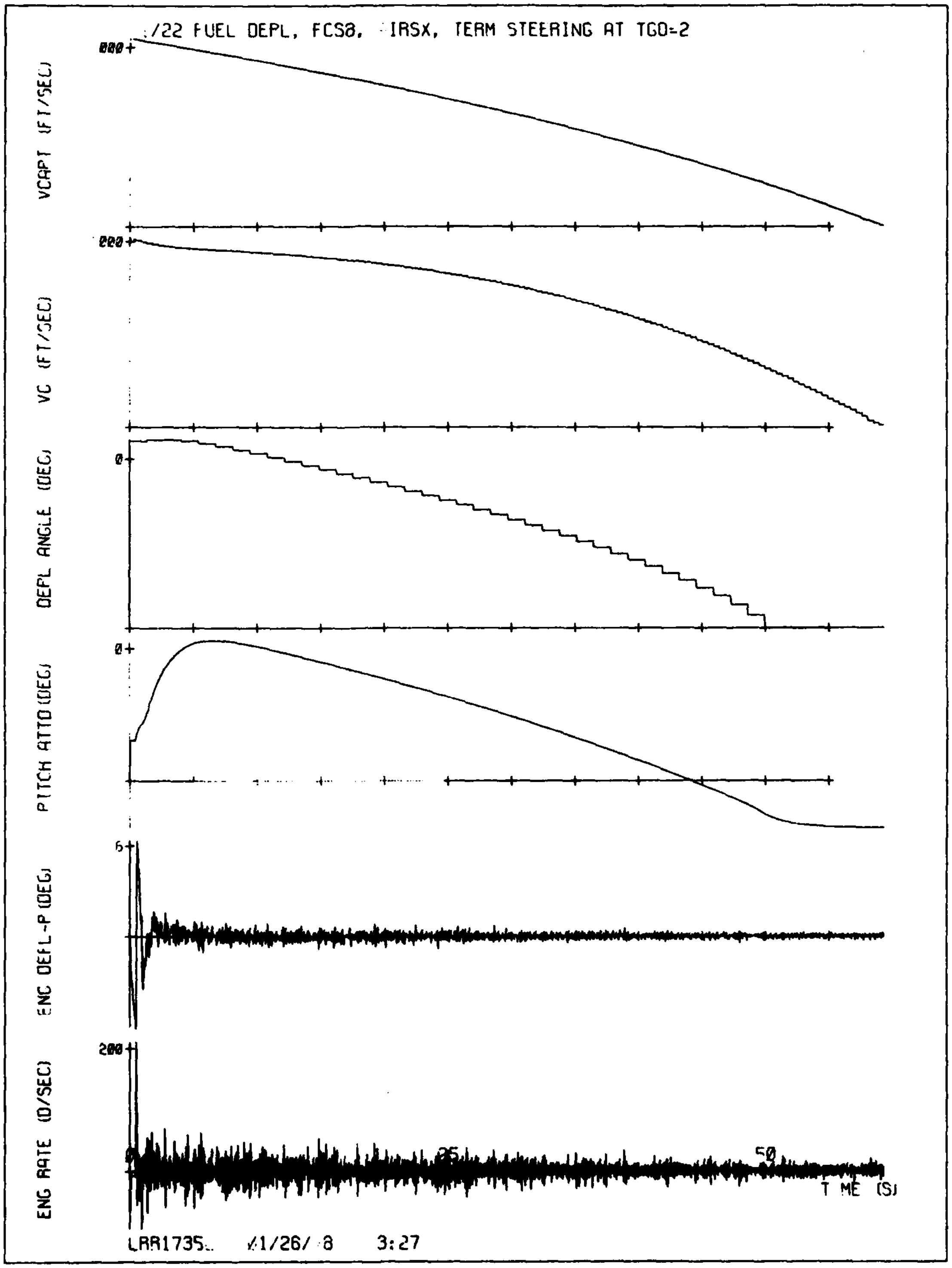

Figure 82-2. STEER, fuel depletion steering, 8 rad/sec autopilot, AIRSX, T_{FR} = 2.

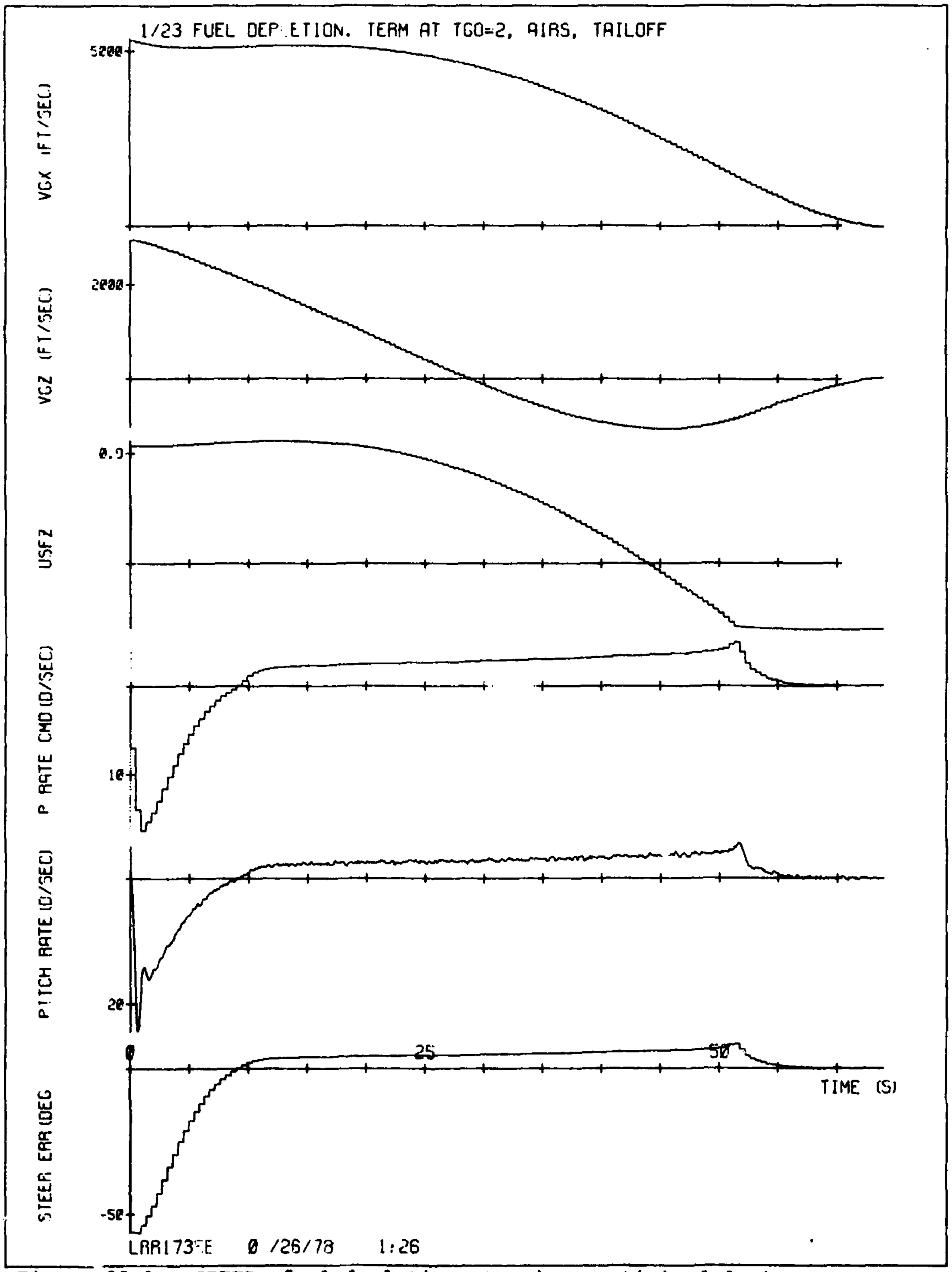

Figure 83-1. STEER, fuel depletion steering, optimized design, AIRSX, thrust tailoff, $T_{FR} = 2$.

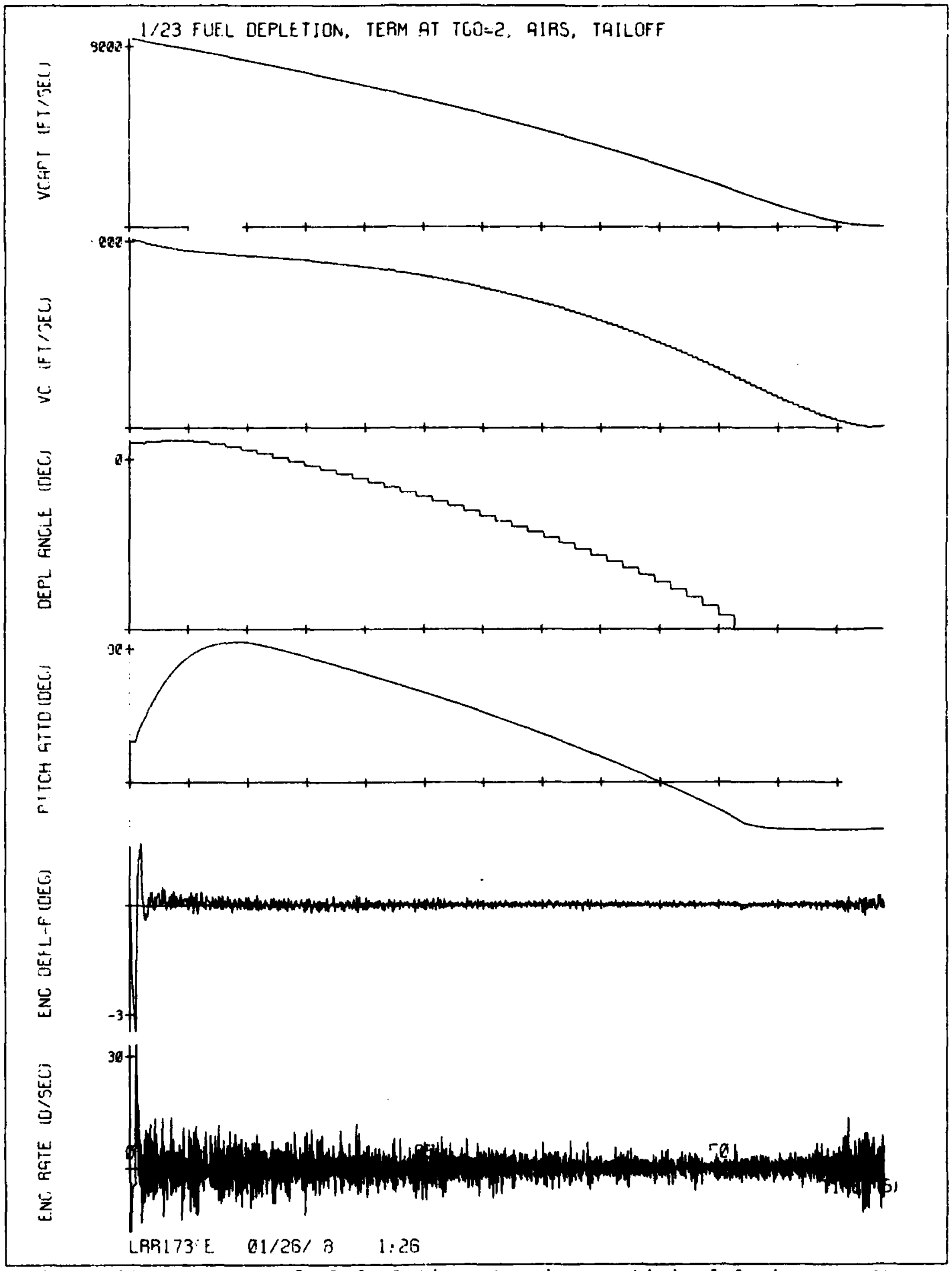

Figure 83-2. STEER, fuel depletion steering, optimized design, AIRSX, thrust tailoff, $T_{FR} = 2$.

Table 20. STEER simulation runs.

Figure	Run	Autopilot/ Steering	Mode	T_{FR}	AIRS	Tailoff	Comments
61	1/01	5/01	V_g	0	0	No	Normalized Design
62	1/02	5/01	V_g	0	2	No	Normalized Design
63	1/03	5/01	V_g	0	2	Yes	Normalized Design
64	1/04	5/01	V_g	5	2	Yes	Terminal Steering
65	1/05	5/01	FD	0	0	No	Normalized Design
66	1/06	5/02	FD	0	0	No	Integral Feedback
67	1/07	5/02	FD	2	0	No	Terminal Steering
68	1/08	5/02	FD	2	2	No	
69	1/09	5/01	FD	2	2	Yes	
70	1/10	5/01	FD	2	0	No	Simplified θ Computation
71	1/11	5/01	FD-Reentry Ctl.	2	0	No	Gamma/TOT
72	1/12	5/02	FD-Reentry Ctl.	2	0	No	Gamma/TOT
73	1/13	2/01	FD	2	0	No	FCS2
74	1/14	2/02	FD	2	0	No	FCS2
75	1/15	8/01	FD	2	0	No	FCS8
76	1/16	8/02	FD	2	0	No	FCS8
77	1/17	5*/01	FD	2	0	NO	Optimized Design
78	1/18	5*/02	FD	2	0	No	Optimized Design
79	1/19	5*/02	FD	2	2	No	Optimized Design
80	1/20	5*/02	FD	2	2	Yes	Optimized Design
81	1/21	5*/01	FD	2	2	Yes	Optimized Design
82	1/22	8/01	FD	2	1	No	FCS8 w/AIRS
83	1/23	8/01	FD	2	2	No	FCS8 w/AIRSX

The output parameters shown in Figures 61-83 and not previously explained (Section 5.1) are discussed below.

P RATE COMMAND	-	The pitch rate command to the autopilot from the steering loop
PITCH RATE	-	The vehicle pitch rate
STEERERR	-	The angular difference between the vectors $U\overline{SF}$ and $\overline{\Delta}V$
PITCH ATT	-	The vehicle pitch attitude measured from the local vertical
ENG DEFL-P	-	The pitch deflection of the engine actuator
ENG RATE	-	The pitch deflection rate of the engine actuator

Note that in these figures, a negative pitch rate command or response is actually nose-up due to the sign convention established in Section 1. A negative pitch response (up) corresponds to a negative rotation (up) of the engine nozzle. Pitch attitude, however, is defined in the opposite (and more logical) sense. Negative pitch rotation of the vehicle will result in a positive increase in the pitch attitude, which is measured from the local vertical. Note also, that the fuel depletion angle is measured from the $\overline{V}_g$ vector rather than the inertial axes.

SECTION 6

CONCLUSIONS

6.1 Overview

The purpose of this study was to examine the design of the autopilot and steering loops and the attitude processing requirements for the third stage of a ballistic missile. In accomplishing this, we have discussed the design of the steering loops and examined the stability of these loops as a function of the changing vehicle parameters. Then, we developed a simplified method for determining the parameters of the autopilot filter for any desired crossover frequency by normalizing the design to a convenient parameter.

We have examined the effect of the steering loop on the system response and then used the steering dynamics to "optimize" the closed-loop response in a simple manner.

The guidance equations for position offset guidance for velocity-to-be-gained and fuel depletion steering were then discussed, and a perturbation study was performed to determine analytically and empirically the sensitivity of these methods to steering errors, and evaluate the analytical expression so determined. Next, several attitude processing methods were developed and compared as to their effectiveness in reducing the computation load of the attitude system. Then, two of the methods were evaluated by using them in a simulation of the vehicle in maneuvers involving high timing rates.

Finally, the autopilot and steering loops and the "best" attitude data processing method were combined with the guidance methods and evaluated in a full system simulation of a ballistic missile flight. In this simulation, the effects of data measurement noise, thrust tailoff, and terminal steering were interjected to test the system response and performance compared to an ideal system. The conclusions arrived at through this process are presented in this section.

6.2 Attitude Measurement Studies

From the study done to compare the worst case errors for AIRS and AIRSX, we see that AIRSX (AIRSME4) has a distinct advantage over the other methods of processing the attitude data. The worst case errors for AIRSX were significantly lower than those for "standard" AIRS (AIRSBAE). It we also compare the computational requirements required for each method, we notice that, although, AIRSX requires slightly more computation time than AIRS, the difference in the computational requirements is negligible compared to the total time required. This is particularly true if the difference is compared to the other computational requirements of the guidance computer. When these two methods are compared in the STAR simulation, we see that, again, the AIRSX data is consistently more accurate than the AIRS data, particularly at the higher rotation rates.

6.3 STEER Simulation Studies

This section presents the conclusions drawn from the OFFSETT and STEER programs. We will discuss the results of simulation runs that were made with the autopilot designed using the normalized design process, and compare this system response with that of the system using the "optimized" autopilot and steering combination. Then these results will be compared to the ideal case, OFFSETT.

Normalized Design - The STEER simulation has verified that the normalized design process may be effectively used to determine the autopilot parameters for any desired crossover frequency. For each of the 3 designs (2, 5, and 8 rad/sec autopilot crossover/frequencies), the frequency response plots verify that the compensated system has the desired open and closed loop response, and the STEER simulations have indicated that these systems behave as they should. Specific conclusions that may be drawn from the simulation runs that involve the normalized design autopilots are described below:

I. Steering Model - For fuel depletion steering, the simplest steering model, i.e., the proportional steering mode, gave the lowest residual velocity-to-be-gained. Since this model is less accurate than it would be if integral feedback was added (as is shown by the magnitude of the steering errors for these cases), the excess ΔV capability is wasted early in the maneuver, the guidance system switches back to the V_g steering mode at an appreciable value of T_{go}. Hence, more

time is spent nulling the V_g errors with this steering model than there is with the integral feedback added.

II. Terminal Steering - Terminal steering is required during the last few seconds of the burn when fuel depletion steering is used. The instability is more noticeable when the switch back to V_g steering occurs in the last few seconds. Even with terminal steering in the last two seconds, the final pitch rates and residual V_g's are higher when the fuel depletion maneuver extends to the end of the burn.

III. Simplified θ Calculation - The use of the simplified expression for computing θ gave no noticeable degradation in response when used with the simple steering mode. Since this method always computes a smaller θ than the iterative method, particularly at the higher values of θ, when used with a more accurate steering method it could cause underwasting and the fuel depletion angle could suddenly increase at the end of the burn.

IV. Attitude Data Processing - The use of AIRSX or AIRS for attitude data processing interjects about 10 deg/sec of actuator rate noise with 5 rad/sec autopilot and about 40 deg/sec of noise with the 8 rad/sec autopilot. For the 8 rad/sec autopilot, this noise also causes significant residual V_g errors. Without AIRS or AIRSX, however, the 8 rad/sec autopilot gave the best performance in fuel depletion steering, particularly with the simple steering model.

V. Gamma/TOT Control - With the 5 rad/sec autopilot it was possible to control the reentry angle within the desired tolerance (10^{-6} radians) from the beginning of the burn until $t \cong 49$ seconds for the proportional steering model, and until $t \cong 59$ seconds for the proportional plus integral model. For the given initial conditions, however, an additional 1600 fps of ΔV capability was required to accomplish this.

IV. Specific Autopilot Capabilities - From examination of Figures 73 and 74, it should be clear that the 2 rad/sec autopilot is not capable of accurately following the pitch profile commanded by the guidance system during fuel depletion steering. The 5 rad/sec autopilot has adequate responsiveness to follow this probile, as well as the

desired noise attenuation characteristics at higher frequencies. The optimized 5 rad/sec autipilot has approximately the same response characteristics as the 8 rad/sec system, but, of course, has a narrower bandwidth. This is an important advantage, as was pointed out in IV.

Optimized Design

I. The optimized 5 rad/sec design gave much improved performance over the standard 5 rad/sec autopilot. The shape of the fuel depletion arc for this configuration is very much like that of the 8 rad/sec autopilot in that the switch to V_g steering occurs at about 50 seconds, rather than at 45 seconds. Delaying the switch back to V_g steering to about $T_{go} = 10$ seconds (or $t \cong 50$ seconds) lowers the required turning rate during the fuel depletion maneuver by stretching the maneuver over a longer period. This also seems to be about the optimal time to switch back to V_g steering in order to have the maximum time to null the $\overline{V}_g$ errors.

The numerical comparison of the terminal conditions for the OFFSETT and STEER simulation runs is given in Table 21. It should be noted that the residual $\overline{V}_g$ values shown in this table could in most cases be reduced by performing a fine countdown during the last few seconds of the burn. The V_g and V_{cap} values in the table are the results of shutting down the engine at the next autopilot cycle after either 1) the x-component of the $\overline{V}_g$ vector goes to zero (V_g steering) or 2) the magnitude of V_{cap} goes to zero (fuel depletion steering). Since the rate of change of V_{cap} is equal to the thrust acceleration and for the constant thrust case, the acceleration is about 300 ft/sec^2 at the end of the burn, we can see that V_{cap} changes by about 10 fps between autopilot cycles. Obviously, further refinements can be made. The lowest residual V_g error (1.24 fps) was achieved by the optimized 5 rad/sec autopilot (Run 1/23). This run also ended with the lowest terminal pitch rate (0.003 deg/sec).

Table 21. Comparison of STEER and OFFSETT terminal conditions.

Run #	V_g	V_{gx}	V_{gz}	V_{cap}	$\dot{\theta}$	Autopilot/ Steering/T_{FR}	Mode
1/01	5.13	-4.37	-2.68	-4.9	0.000	5/01/0	V_g
1/02	5.11	-4.35	-2.67	-4.9	0.161	5/01/0	V_g
1/03	1.60	-1.53	-0.46	2259.2	-0.250	5/01/0	V_g
1/04	1.60	-1.53	-0.46	2259.2	-0.225	5/01/5	V_g
1/05	7.67	-4.19	-6.42	-0.8	2.092	5/01/0	FD
1/06	19.46	-16.63	-10.11	-3.9	6.797	5/02/0	FD
1/07	24.58	-20.31	-13.84	-3.9	1.222	5/02/2	FD
1/08	24.60	-20.37	-13.80	-4.0	1.166	5/02/2	FD
1/09	26.81	-19.90	-17.96	0.2	-1.130	5/02/2	FD
1/10	11.61	-9.30	-6.94	-4.6	0.307	5/01/2	FD
1/11	15.09	-14.51	-4.15	-7.5	0.239	5/01/2	FD - γ
1/12	58.95	-57.82	-11.50	-2.5	-2.109	5/01/2	FD - γ
1/13	397.94	44.41	-395.46	365.8	4.177	2/01/2	FD
1/14	8.18	-6.06	5.50	-5.6	-1.903	2/02/2	FD
1/15	2.22	-1.84	-1.24	-1.0	0.082	8/01/2	FD
1/16	19.77	-17.00	-10.08	-3.8	1.921	8/02/2	FD
1/17	2.85	-2.83	0.29	-2.6	0.039	5*/01/2	FD
1/18	11.88	-11.22	-3.90	-4.2	1.787	5*/02/2	FD
1/19	12.07	-11.35	-4.10	-4.1	1.781	5*/02/2	FD
1/20	1.04	-0.69	-0.77	0.2	-1.958	5*/02/2	FD
1/21	72.12	59.55	-36.32	-5.2	0.141	8/01/2	FD
1/22	76.40	63.37	-38.47	-4.5	0.115	8/01/2	FD
1/23	1.24	0.91	-0.84	0.0	0.003	5*/01/2	FD
OFFSETT RUNS							
2/100	0.01	0.01	0.005	0.0	N/A	(Not applicable)	V_g
2/01	0.26	0.191	-0.171	0.2	N/A		FD
2/02	0.75	0.281	-0.692	0.7	N/A		FD - γ

APPENDIX A1

VEHICLE ROTATIONAL TRANSFER FUNCTION

Rotational Dynamics (Pitch or Yaw Axis)

Using Eulers' Equation

$$I\ddot{\theta} = \Sigma M = T\ell_{cg}\delta + M_e\ell_e\ell_{cg}\ddot{\delta} + I_e\ddot{\delta} \text{ (See Table 1)}$$

assuming

$$(\sin\delta = \delta)$$

The first term on the right-hand side is the torque about the vehicle cg caused by the defection of the thrust line; the second term is the inertial reaction torque due to lateral translation of the engine nozzle; and the third term is due to the angular acceleration of the engine. Taking the Laplace transform of both sides

$$Is^2\theta(s) = T\ell_{cg}\delta(s) + (M_e\ell_e\ell_{cg} + I_e)s^2\delta(s)$$

$$\frac{\theta(s)}{\delta(s)} = \frac{T\ell_{cg}}{I}\left\{\frac{\frac{s^2}{\omega_{TWD}^2} + 1}{s^2}\right\}$$

with

$$\omega^2_{TWD} = \frac{T\ell_{cg}}{M_e\ell_e\ell_{cg} + I_e}$$

If we substitute typical vehicle parameters into this expression, we find that $\omega_{TWD} \cong 80$ rad/sec. This frequency is much higher than the autopilot crossover frequency and for the purposes of this study, this effect will be neglected.

APPENDIX A2

ACTUATOR TRANSFER FUNCTION

The actuator open-loop transfer function consists of A DC gain factor, a first-order lag with time constant, τ, and an integrator, shown in Figure A2-1. With the unity feedback loop added, the closed-loop transfer function becomes

$$G_\delta(s) = \frac{K_s/\tau}{s^2 + \frac{s}{\tau} + \frac{K_s}{\tau}}$$

We choose $\tau = 1/K_s$ so that the damping ratio, ζ is equal to 0.5 and the natural frequency, ω_n, is equal to K_s. Then the closed loop transfer function can be written as

$$G_\delta(s) = \frac{K_s^{\,2}}{s^2 + K_s s + K_s^{\,2}}$$

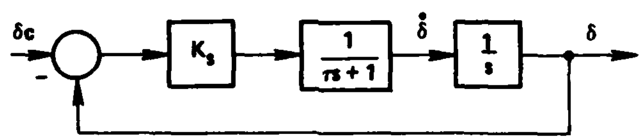

Figure A2-1. Actuator Model.

APPENDIX A3

DERIVATION OF $\lambda(s)/\theta(s)$

The autopilot and steering loop models described in Section 2.3 employ the variable λ to represent the angular position of the thrust acceleration in the pitch or yaw plane relative to the initial body x-axis that would be sensed by the zero-quantization accelerometers of an idealized IMU. If the vehicle rotates about its pitch (y) or yaw (z) axis with an angular velocity $\dot{\theta}$ the IMU-sensed acceleration will have an x-axis component

$$a_{X_{IMU}} = T \cos \delta_e / M + \ell_{IMU} \dot{\theta}^2 \qquad \text{(A-1)}$$

and a component perpendicular to the x-axis

$$a_{N_{IMU}} = - T \sin \delta_e / M + \ell_{IMU} \ddot{\theta} \qquad \text{(A-2)}$$

where δ_E is the angular displacement of the engine from the x-axis (defined positive in the direction that produces a positive $\ddot{\theta}$) and ℓ_{IMU} is the distance of the IMU forward of the vehicle center of mass.

We neglect the centripetal acceleration term, $\ell_{IMU}\dot{\theta}^2$, and assume that δ_e is small enough that

$$\cos \delta_e \simeq 1 \qquad \text{(A-3)}$$

$$\sin \delta_e \simeq \delta_e \qquad \text{(A-4)}$$

The body-axis components of the IMU-sensed acceleration are then approximated by

$$a_{X_{IMU}} \simeq T/M \qquad \text{(A-5)}$$

$$a_{N_{IMU}} \simeq - T/M \, \delta_e + \ell_{IMU} \ddot{\theta} \qquad \text{(A-6)}$$

Assuming that $a_{N_{IMU}} << a_{X_{IMU}}$, the angle of the IMU-sensed acceleration relative to the body x-axis is given by the ratio

$$\frac{a_{N_{IMU}}}{a_{X_{IMU}}} \simeq -\delta_E + \frac{\ell_{IMU}}{T/M}\ddot{\theta} \qquad \text{(A-7)}$$

The angle λ of this IMU-sensed acceleration, measured relative to the same inertially fixed coordinates in which θ is measured, must be given by the sum $\theta + a_{N_{IMU}}/a_{X_{IMU}}$, whence

$$\lambda \simeq \theta - \delta_E + \left[\ell_{IMU}/T/M)\ \ddot{\theta}\right] \qquad \text{(A-8)}$$

The transfer function $\lambda(s)/\theta(s)$ may therefore be expressed as

$$\frac{\lambda(s)}{\theta(s)} \simeq \left[1 + s^2\frac{\ell_{IMU}}{(T/M)}\right] - \frac{\delta_E(s)}{\theta(s)} \qquad \text{(A-9)}$$

But

$$I\ddot{\theta} \simeq T\ \ell_e\ \delta_e \qquad \text{(A-10)}$$

where

I = Moment of inertia about the axis of rotation for which θ is defined

ℓ_e = Moment arm between the engine hinge point and the vehicle center of mass

therefore

$$\frac{\delta_e(s)}{\theta(s)} \cong \frac{s^2 I}{T\ell_e} \qquad \text{(A-11)}$$

and

$$\frac{\lambda(s)}{\theta(s)} \simeq 1 + s^2\left[\frac{\ell_{IMU}}{(T/M)} - \frac{I}{T\ell_e}\right] \qquad \text{(A-12)}$$

APPENDIX A4

RELATIONSHIP BETWEEN λ, $\lambda_{\Delta V}$, AND λ_{V_g}

We suppose that Figure 5 in Section 2.3 represents transfer functions in a pitch plane whose inertially fixed x-axis is the reference for the previously defined θ and λ. If we further assume small engine deflections such that the thrust acceleration vector is approximately parallel to the vehicle x-axis we have from Figure A4-1.

$$\Delta V_z(mT_s) \cong \frac{T}{M} \int_{(m-1)T_s}^{mTs} \lambda dt$$

and

$$\Delta V_x(mT_s) = \frac{T}{M} T_s$$

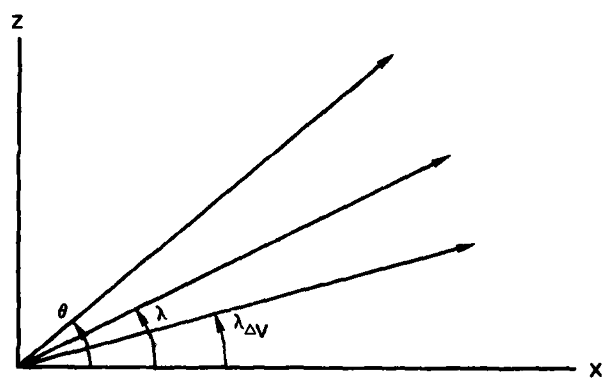

Figure A4-1. Definition of angles in inertial frame.

Therefore, using the fact that tan x ≅ x for small x

$$\lambda_{\Delta V}(mT_s) \cong \frac{\Delta V_z(mT_s)}{\Delta V_x(mT_s)} \cong \frac{1}{T_s} \int_{(m-1)T_s}^{mT_s} \lambda \, dt$$

The integral is equivalent to

$$\lambda_{\Delta V}(mT_s) \cong \frac{1}{T_s}\left[\int_o^{mT_s} \lambda dt - \int_o^{(m-1)T_s} \lambda dt\right]$$

which can be represented pictorially by Figure A4-2.

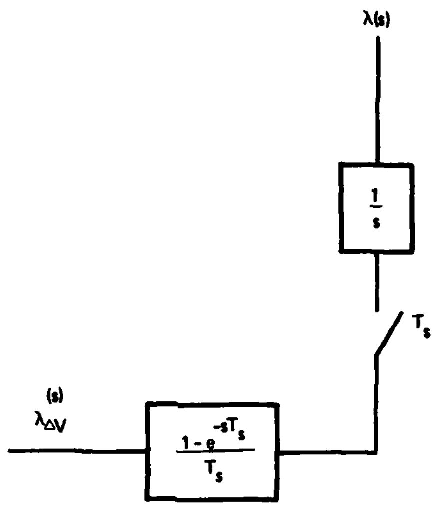

Figure A4-2. Relation between $\lambda(s)$ and $\lambda_{\Delta V}(s)$.

The representation of the effects of $\bar{V}_g$ in Figure 5 is based on the assumption that

$$\dot{\bar{V}}_g = -\dot{\bar{V}} = -\bar{A}_T$$

and the assumption that the initial direction of V_g points along the x-axis of the pitch (or yaw) plane. For the case of pitch plane motion, it is assumed in Figure 5 in Section 2.2 that

$$V_x \cong \frac{T}{M} t$$

$$V_z = \frac{T}{M}\int_o^t \lambda dt$$

and also that

$$V_{gx} \cong \frac{T}{M} t_{go}$$

$$V_{gz} \cong -V_z = -\frac{T}{M}\int_o^t \lambda dt$$

Finally, is is assumed that

$$\lambda_{V_g} \cong \frac{V_{gz}}{V_{gx}}$$

whence

$$\lambda_{V_g} = -\frac{1}{t_{go}} \int_o^t \lambda dt$$

Thus, the effect of sampling $\overline{V}_g$ to determine λ_{V_g} every T_s seconds can be represented by the following diagram.

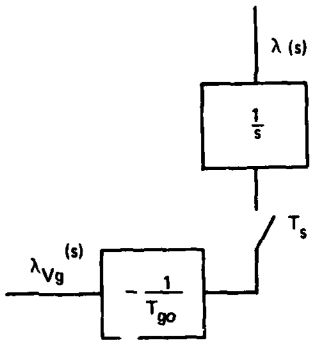

Figure A4-3. Relationship between λ_{V_g} (s) and λ(s).

In Figures 5 and 6, λ_{V_g} (s) has been replaced by the more general term λ_{USF}(s) and the term $-1/T_{go}$ has been changed to $-\gamma/T_{go}$ since the γ/T_{go} term represents the $1/T_{go}$ sensitivity for V_g steering and $4/T_{go}$ sensitivity of fuel depletion steering as discussed in Section 3.3.

APPENDIX A5

DERIVATIONS FOR FUEL DEPLETION STEERING

A5-1. Basic Relationship of Fuel Depletion Steering

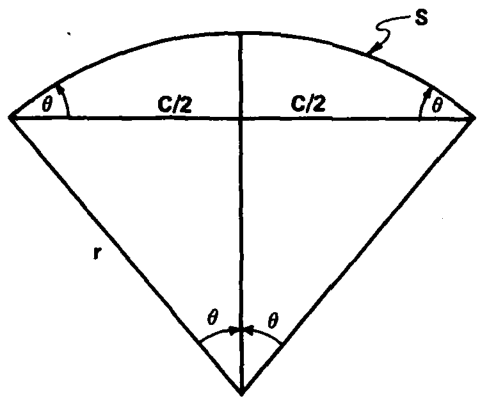

Figure A5-1. Geometry of the fuel depletion arc.

In this figure, θ represents the fuel depletion angle, the chord length c represents the magnitude of V_g and the arc length S represents V_{cap}.

Note that

$$\sin\theta = \frac{c/2}{r} = \frac{c}{2r}$$

and

$$S = 2\pi r\,\frac{2\theta}{2\pi} = 2\theta r$$

$$\therefore\ r = \frac{S}{2\theta}\ ;\ 2r = \frac{S}{\theta}$$

so

$$\sin\theta = \frac{c}{s/\theta} = \frac{\theta c}{S}$$

$$\frac{\sin\theta}{\theta} = \frac{c}{S}$$

and finally

$$\frac{\sin\theta}{\theta} = \frac{V_g}{V_{cap}}$$

APPENDIX A6

CALCULATION OF SPECIFIC FLIGHT CONTROL SYSTEM PARAMETERS

The relationship between the approximate autopilot crossover frequency and w' is

$$\omega_{xo} = \omega' \omega_2$$

and

$$\omega_2 = \omega_{xo}/\omega'$$

Once ω_2 is determined, w_2 is found from

$$w_2 = \frac{T}{2}\,\omega_2$$

Since we have selected $\omega_1/\omega_2 = 0.10$

$$\omega_1 = 0.10\,\omega_2$$

The w-plane pole of the compensator is given by

$$w_3 = \frac{T/2}{T_3}$$

and $T_3 = (\phi_o'/\omega_2) + T_{DAP}/2 + T_{ACT}$.

We have selected $\phi_o' = 0.25$ and

$$T_{DAP} = 0.03 \text{ and}$$
$$T_{ACT} = 1/\omega_{n_{act}} = 0.020833$$

Finally the compensator gain is

$$K_c = \frac{K_o' \omega_2^2}{Kv}$$

where

$$K_o' = 1.4$$

and

$$K_v = 20$$

Using these equations and values for the fixed parameters, we generate Table 7. With the substitution

$$w = \frac{z - 1}{z + 1}$$

for this simple compensator, we can determine the z-plane coefficients from the equations

$$D(z) = K_z \left[\frac{1 - A_2 z^{-1}}{1 - B_2 z^{-1}}\right]$$

with

$$K_z = \left[\left(\frac{w_3}{w_2}\right)\frac{1 + w_2}{1 + w_3}\right] K_w \ ; \ A_2 = \frac{1 - w_2}{1 + w_2} \ ; \ B_2 = \frac{1 - w_3}{1 + w_3}$$

The z-plane filter coefficients A_2 and B_2 used in the digital simulation are given in Table 8.

APPENDIX B

COORDINATE TRANSFORMATIONS

The coordinate transformations required for the simulation programs are presented herein. The relative orientation of the body frame and the inertial frame is shown in Figure B-1, and it assumes that the platform axes are initially aligned with the inertial axes. The platform-to-body transformation matrix, $\overset{*}{PB}$, and its inverse, the body-to-platform matrix, $\overset{*}{BP}$, are used to transform inertially-referred vectors into the body frame and body referenced vectors into the inertial (platform) frame. These transformation matrices are updated at the autopilot loop cycle time.

BODY FRAME TO INERTIAL FRAME TRANSFORMATION

FIRST ROTATION:

$$P\dot{B}' = \begin{bmatrix} \cos\psi & \sin\psi & 0 \\ -\sin\psi & \cos\psi & 0 \\ 0 & 0 & 1 \end{bmatrix}$$

SECOND ROTATION:

$$P\dot{B}'' = \begin{bmatrix} 1 & 0 & 0 \\ \cos\lambda & 0 & \sin\lambda \\ -\sin\lambda & 0 & \cos\lambda \end{bmatrix}$$

PRODUCT

$$P\dot{B} = P\dot{B}'\,P\dot{B}''$$

$$P\dot{B} = \begin{bmatrix} \cos\psi\cos\lambda & \sin\lambda & \cos\psi\sin\lambda \\ -\sin\psi\cos\lambda & \cos\psi & -\sin\psi\sin\lambda \\ -\sin\lambda & 0 & \cos\lambda \end{bmatrix}$$

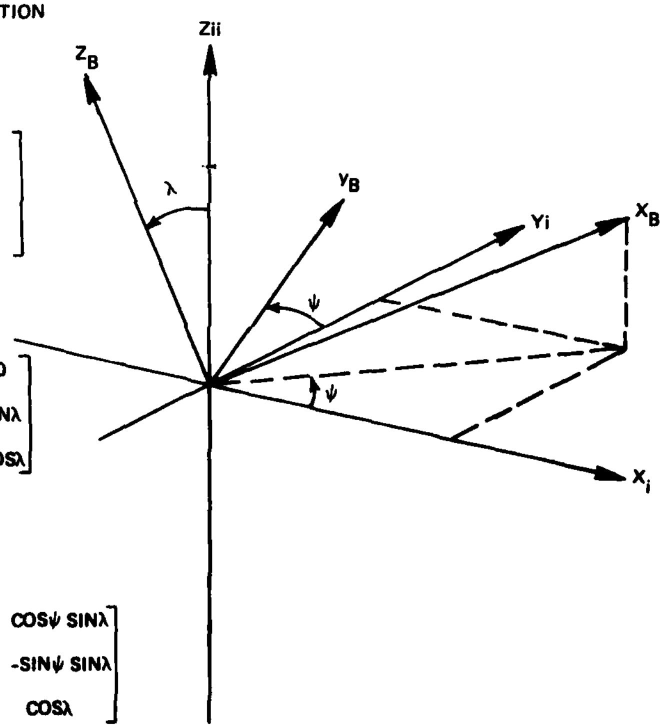

Figure B-1. Body frame to inertial frame transformation.

The engine frame-to-body frame transformation matrix is presented in Figure B-2. It is used to transform the engine orientation angles into a body referenced vector, $\overline{ENG}$, which is then transformed into the inertial frame by multiplying it by the body-to-platform transformation matrix, $\overset{*}{BP}$. This inertially referred vector, $ENG\overline{P}LAT$, represents the direction of the engine thrust vector.

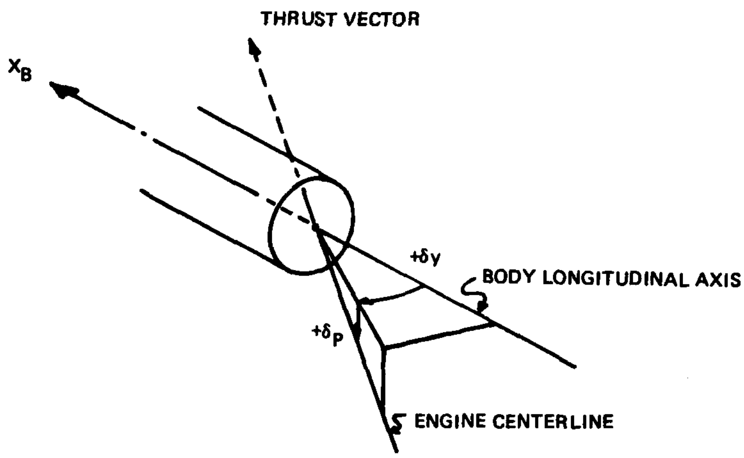

The direction of the thrust vector is referenced to the vehicle body axes using the $\overline{ENG}$ vector where

$$\overline{ENG} = \begin{bmatrix} \cos \delta y \cos \delta_p \\ -\sin \delta y \cos \delta_p \\ \sin \delta_p \end{bmatrix}$$

Figure B-2. Engine frame to body frame transformation.

APPENDIX C

SIMULATION DESCRIPTION

To evaluate the design of the guidance, steering, control and attitude measurement systems, digital computer programs were developed and run to simulate these systems independently, as well as in an integrated system. Three major programs (OFFSETT, STAR, and STEER), and five subroutines (PERT, AIRSBAE, AIRSME2, AIRSME4, and AIRSINC) were developed or used in this study.

OFFSETT is a simulation of the guidance system with simplified vehicle dynamics operating in orbit around a spherical, nonrotating earth. STAR simulates the steering and control loops and the vehicle and actuator dynamics, but has no guidance routine and operates in inertial space. These two major programs are merged into STEER, which is a complete simulation of the integrated guidance, steering, autopilot and actuator systems coupled with the complete vehicle dynamics in earth orbital flight. PERT is a subroutine to OFFSETT that is used to compute sensitivities to velocity errors. The AIRS programs are variations of the program that simulate the attitude data processing. A description of each of these programs is presented below.

OFFSETT

The OFFSETT program simulates the guidance system. The vehicle is represented by a point mass, with no steering or autopilot interactions or rotational dynamics. Normally, the thrust and the mass flow rate are constant, but the same thrust model (see Appendix D) used in STEER is available for use.

The program inputs are the initial and final radius vectors, the time of flight, the initial velocity, and the reentry angle control tolerance. The program begins by computing an impulsive velocity to be gained by solving the Lambert problem using the initial and final radius vectors and the time of flight. Then, at each guidance cycle, a position offset is calculated to account for the nonimpulsive

nature of the burn. The new velocity-to-be-gained is calculated from this offset position. The vehicle may be steered in either V_g steering or fuel depletion steering. If fuel depletion steering is used, the reentry angle may be controlled by modulating V_{cap} to change the fuel depletion angle and hence, change the pitch profile to control the reentry angle, while at the same time maintaining a fixed time of flight. The vehicle dynamics are simulated in a differential equation loop, and all measurements are considered ideal.

The OFFSETT program and its variations are used as an "ideal" case to show just the effects of the guidance computation without steering or vehicle lags.

OFFSETT1

This program is identical to OFFSETT, except that the thrust model explained in Appendix D is included to simulate the effects of thrust tailoff.

PERT

PERT is a subroutine to OFFSETT (and OFFSETT1) that computes the change in fuel depletion angle caused by a small variation in the velocity-to-be-gained. The PERT subroutine is called after the guidance calculations at a particular time have been made. A small variation in the vehicle velocity, and hence the velocity-to-be-gained, is made and the perturbed parameters are calculated at the same time as the unperturbed parameters. After these parameters are calculated, the unperturbed parameters are restored and the simulation continues.

Sample output for the OFFSETT program with the PERT feature activated is shown in Table C-1.

STAR

The STAR program simulates the steering loops, autopilot filter, engine actuator, attitude measurement and processing system (using the AIRS subroutines) without inputs from the guidance program. It was used to evaluate the response of the vehicle to test steering inputs to examine the steering concepts, autopilot filter parameters and two different methods of processing the attitude data. In the STAR program, the vehicle may be steered using V_g steering or a test steering input may be used. For the purpose of the AIRS study presented in Section 4,

Table C-1. Sample OFFSETT/PERT output.

```
          ###################################################
          GUIDANCE CALCULATION ++++++++++++++++++++++++++++++
          +++++++++++++++++++++++++++++++++++++++++++++++++++
TIME =    23.000 SEC          VG MAGNITUDE = 5192.43 FPS     VCAP =  6138.5 FPS          RATIO(VG/VCAPT) = 0.8458

DEPL ANGLE = 56.4534 DEG    DEPL ANGLE RATE =-2.211 D/S     CUTOFF TIME =  60.0 SEC        TIME ON TARGET = 2499.9

REENTRY ANGLE =-27.5479 DEG                                 REENTRY ANGLE ERROR = 0.12376 DEG

          AT = 122.17
          VG VECTOR = 5160.466     0.000   575.307
          ##### PERTURBATION PARAMETERS #######################
          TIME =  23.000 SEC     TIME TO GO =  37.035 SEC
          VGPERT=5196.6  FPS     THPERT - THREF =-2.8195- 3 RAD

          ANGL = 0.0005 RAD
          DTH/VERR =-5.639- 4 RAD/FT/SEC

          ERR1 = 0.00005  ERR3 = 0.00003  ERR4 = 0.00008  RADIANS

          VGPERT  = 5164.91    0.00   573.02 FPS
          USFPERT = 0.4593  0.0000  0.8882   RAD

          ###################################################
```

a combination of a parabolically increasing constant, and linearly decreasing rate input was used. In the STAR program, the mass, moments of inertia, and center of gravity location are linearly varying functions of time. The thrust is constant but the autopilot filter gain is changed as a function of thrust acceleration to maintain a constant value of open loop gain.

Sample output of the STAR program is given in Table C-2.

AIRS

The variations of the AIRS programs differ in the methods that are used to extrapolate and interpolate the AIRS band angles and compute the transformation matrices. In general, though, the AIRS programs receive the platform-to-body transformation matrix and the values of receiver and driver band noise from the main program and compute quantization and deterministic (table look-up) errors to determine the measured incremental attitude vector and the measured body-to-platform transformation matrix. The variations of the AIRS program are discussed further in Section 4.

STEER

The STEER program combines all aspects of the previously described programs into one complete simulation program, as shown in Figure C-1, the simplified STEER flowchart. Referring to Figure C-1, after initialization of the parameters, the program computes the guidance parameters under GUID. These parameters include, the predicted engine cut-off time, which is either the time when the velocity-to-be-gained should be zero or when the V_{cap} is exhausted, the position offset, the fuel depletion angle if fuel depletion guidance is used, the current velocity-to-be-gained, and the reentry angle. Within this loop, a solution convergence check recomputes the parameters until the position offset and guidance solution converges. After the guidance parameters are computed, the program enters the STEER routine where the velocity-to-be-gained, the steering error vector, and the rate command vector are computed. The rate vector is multiplied by T_{DAP} to compute the incremental attitude command vector. The program then enters CONTRL where this vector is compared to the incremental attitude feedback and an attitude error vector is computed. This error signal is used by the autopilot filter to generate actuator deflection commands. Under

Table C-2. Sample STAR output.

```
************************************
* STEERING INPUT TO CONTROL SYSTEM *
************************************
TIME =   4.949 SECONDS
VELOCITY TO BE GAINED =  1124.5  -  291.4  -   33.3 FPS


ALPHASTEER    =  0.000   25.722  -32.761 DEG
RATE COMMAND =  0.000   - 2.720   12.343 DEG/SEC
ALPHAINT      = 0.0000   $.$$$$   $.$$$$ DEG

W COMMAND =  0.0000  0.3403  0.3403                          THCMDINC  = 0.00000 0.01021 0.01021

        MEASURED PLATFORM TO BODY      -0.6331  0.5378  0.5566
        TRANSFORM                       0.7676  0.3436  0.5409
                                        0.0995  0.7698 -0.6304

        AIRS ANGLE INCREMENT = 0.5766  0.5842  0.5898
        TRUE ANGLE INCREMENT =-0.0000  0.5924  0.5847
        ***************************************************
        VEHICLE RESPONSE  ********************************
        TIME =   4.979 SECONDS

ATTITUDE =  28.051   25.860    25.896 DEG                    THETA INCREMENT = 0.5766    0.5842    0.5898 DEG

PITCH ENGINE DEFL= 0.474 DEG    YAW ENGINE DEFL= 0.438 DEG  MASS = 1008.0 SLUGS      ACTUATOR RATE =   0.114 D/S

ERRCR=-27.47444   0.69599   0.66604 DEG                      ERR1 =      0.00000   2.40188   2.29850 DEG
ERR2 =  0.00000   0.47210   0.43998 DEG                      TAUENG =     0.00   4481.76   4138.13 FT-LB

ROTATION RATE =   0.00000   19.59402   19.34950 DEG/SEC

W COMMAND =  C.0000  0.3455  0.3455                          THCMDINC  = 0.00000 0.01036 0.01036

        MEASURED PLATFORM TO BODY      -0.6261  0.5331  0.5688
        TRANSFORM                       0.7741  0.3381  0.5351
                                        0.0929  0.7754 -0.6244

        AIRS ANGLE INCREMENT = 0.5761  0.6006  0.5958
        TRUE ANGLE INCREMENT =-0.0000  0.6019  0.5935
        ***************************************************
```

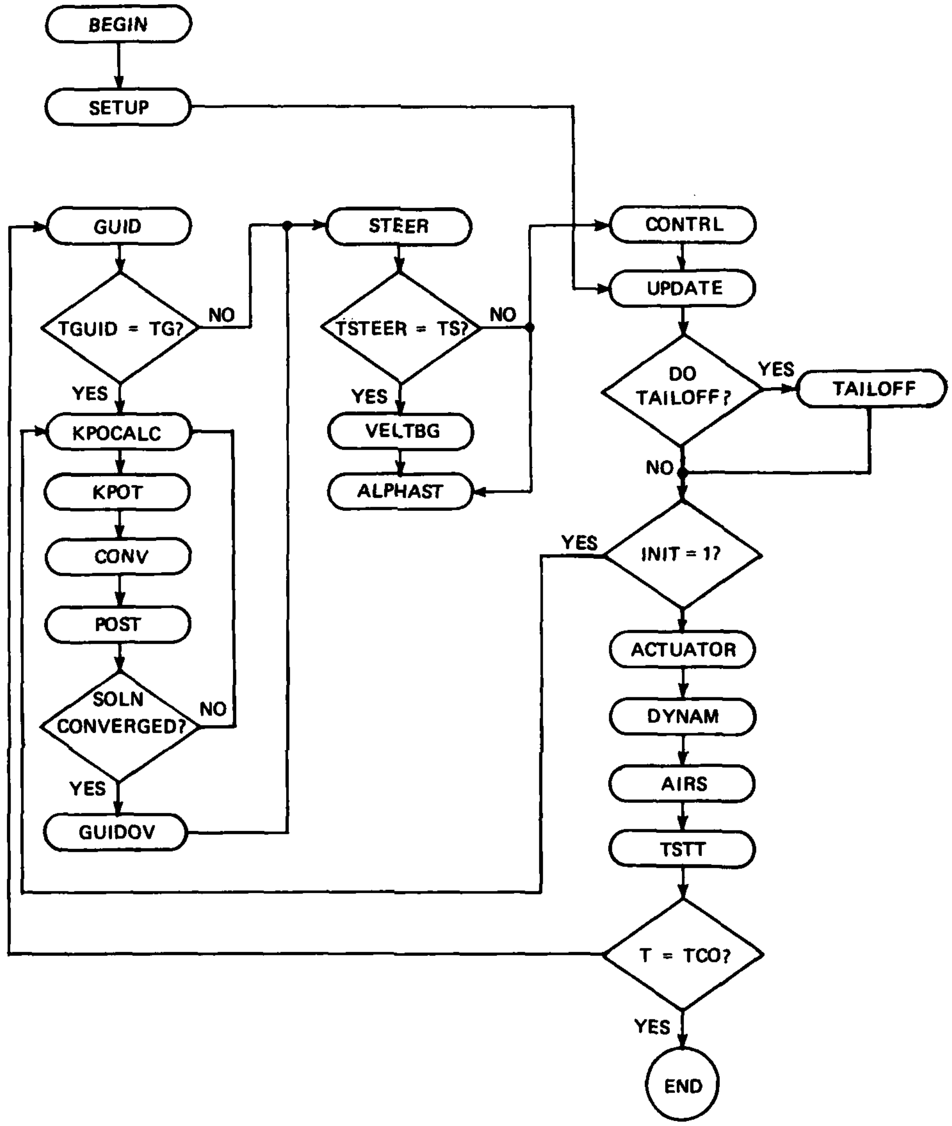

Figure C-1. Simplified flow chart-STEER program.

UPDATE, the vehicle mass, center of gravity, and moment of inertia data is updated and if the thrust tailoff option is selected, the thrust, mass flow rate, and exhaust velocity is modified. The vehicle acceleration is then calculated. The actuator commands previously computed are then used in the ACTUATOR subroutine which is the start of the differential equation routine to compute the actuator response. Under DYNAM, the actuator response and the rest of the vehicle parameters are used to compute the vehicle response. The program enters the AIRS subroutine where the actual and AIRS program computed attitude data is calculated. If the elapsed burn time is less than the cut off time, the program returns to GUID. However, since there are nominally 45 CONTROL cycles between GUID cycles, the program jumps to STEER. There are nominally 15 CONTRL cycles between STEER cycles, so the program then jumps to CONTRL and exercises that loop. This process continues for 15 CONTRL cycles and then the STEER routine is exercised. After a total of 45 CONTRL cycles (and 3 STEER cycles), the guidance parameters are recomputed. The program continues in this fashion until $T = T_{CO}$ at which time the program ends. Sample output for the STEER program is shown in Table C-3.

Table C-3. Sample STEER output.

```
        +++++++++++++++++++++++++++
        +  GUIDANCE COMPUTATION  +
        +++++++++++++++++++++++++++
        + TIME =  22.979 SECONDS    AT = 122.09       RATIO = 0.8387
        + VELOCITY  =          16096.4        0.0      10384.3 FPS +
        + REQUIRED VELOCITY =  21236.8        0.0      10612.4 FPS +
        + VEL TO BE GAINED  =   5140.4      0.0     228.0 FPS +

+ RADIUS VECTOR =  366320.4        0.0  21543519.9 FT       + POSITION OFFSET =-107118.7       0.0    33443.7 FT

+ FUEL DEPL ANGLE = 57.8 DEG     DEPL ANGLE RATE =-2.26 DEG/S REENTRY ANGLE =-27.539 DEG     VCAPT = 6134.47 +

+ V REQ = 23740.8 FPS            GAMMERR = 2.00- 3  RAD      DELTA VCAPT =    0.000 FPS       CUTOFF TIME =  60.00 SEC +

        ************************************
        * STEERING INPUT TO CONTROL SYSTEM *
        ************************************
        TIME =  22.979 SECONDS                RATIO  = 0.8387
        VG MAGNITUDE=  5145.4 FPS             VCAPT =  6134.4 FPS
        VELOCITY TO BE GAINED =  5140.4       0.0     228.0 FPS

        ALPHASTEER =      0.0000  0.1524  0.0000  RAD
        ALFHAINT =        0.0000  1.4744  0.0000  RAD
        RATE COMMAND  =     0.000    2.663   0.000 DEG/SEC

        VELOCITY INCREMENT = 19.533   0.000  51.194 FPS
        THRUST ATTD COMMAND = 0.494   0.000   0.869 RAD
                  WC STEER =  0.000   0.046   0.000 RAD/SEC
        ***************************************************
        VEHICLE RESPONSE **********************************
        TIME =  23.009 SECONDS

        ATTITUDE =     0.000   69.380     0.000 DEG
        THETA INCREMENT =  0.0000    0.0829  0.0000 DEG

ERROR=  0.00000    0.00253    0.00000 DEG                    ERR2  =      0.00000 - 0.01084   0.00000 DEG
ROTATION RATE =  0.000    2.768    0.000 DEG/SEC             PITCH ENGINE DEFL =-0.007 DEG  ENG DEFL RATE =- 0.20 D/SEC

THRUST = 100000 LBS    MASS =  818.7 SLUGS   AT = 122.1 FPSS    MDOT = 10.5 SLUGS/SEC     VCAPT =  6130 FT/SEC
```

APPENDIX D

THRUST TAILOFF MODEL

For the purposes of much of this study, the rocket thrust was assumed to be constant. The mass flow rate was also constant, and hence the mass decreased linearly with burn time. The magnitude of the thrust acceleration was given by

$$A_T = \frac{\text{Thrust}}{M_o - \dot{m}t} \tag{D1}$$

The ΔV capability of the vehicle is given by the integral of the thrust acceleration

$$V_{cap} = \int_o^t A_T dt = \int_o^t \frac{T}{M_o - \dot{m}t} dt \tag{D2}$$

With the assumptions stated above, this integral can be evaluated analytically as

$$V_{cap} = \frac{T}{\dot{m}} \ln(M_o/M_{burnout}) \tag{D3}$$

Recognizing $\frac{T}{\dot{m}}$ as the exhaust velocity, V_{ex}, the expression becomes

$$V_{cap} = V_{ex} \ln(M_o/M_{burnout}) \tag{D4}$$

While the assumption of constant thrust and linear mass change is a useful simplification in the design process, most real solid-fuel rocket engines exhibit thrust tailoff characteristics, marked by decreasing thrust, mass flow rate, and exhaust velocity in the latter part of the burn, as well as thrust variations throughout the burn, caused by unequal burning of the fuel.

As has been demonstrated in Section 2, the steering/autopilot/vehicle combination is stable only for a range of value of open-loop gains.

Since the gain contribution of the vehicle is $T\ell_{cg}/I$, as the thrust decreases rapidly at the end of the burn, the system tends toward instability. This effect may be compensated for by varying the steering and/or autopilot compensator gain as a function of sensed acceleration.

To correctly represent the effects of thrust tailoff, it is not adequate to simply decrease the thrust to zero in some fashion. The other engine and vehicle parameters ($\dot{m}$, V_{ex}, V_{cap}, M, A_T) must be simultaneously changed to make a consistent set. Since the ΔV_{cap} of the engine is assumed to be accurately known beforehand, the first requirement of consistency is to vary the acceleration such that the area under the curve (the vehicle ΔV capability) remains the same. Since the acceleration decreases with the thrust, in order to keep the same ΔV_{cap}, the burn time must be changed. This forces a change in the mass flow rate and hence the exhaust velocity changes. If the thrust and mass flow rate assumed constant up to a certain time into the burn the integral expression for ΔV may be expressed as

$$V_{cap} = \int_{o}^{tbo} A_T(t)dt = \int_{o}^{t1} \frac{T}{M_o - \dot{m}t} dt + \int_{t1}^{tbo} \frac{T(t)}{Mt1 - \dot{m}(t)t} dt \qquad (D5)$$

If we take $T(t) = T_{max} - K_1\tau^2$ and

$$\dot{m}(t) = \dot{m}_{max} - K_2\tau^2$$

where $\tau = (t - t1)$; from t1 to tbo,

$$M(t) = M_{t1} - (\dot{m} - K_2\tau^2)\tau$$

Then K_1 and K_2 can be computed from

$$K_1 = \frac{T_{max}}{\tau^2} \; ; \; K_2 = \frac{M_{bo} - M_{t1} + \dot{m}\tau}{\tau^3}$$

Where τ is selected to make V_{cap} equal the desired value. The variation of thrust, acceleration, mass, and mass flow rate are shown in Figures D1 through D4, Engine Tailoff Model.

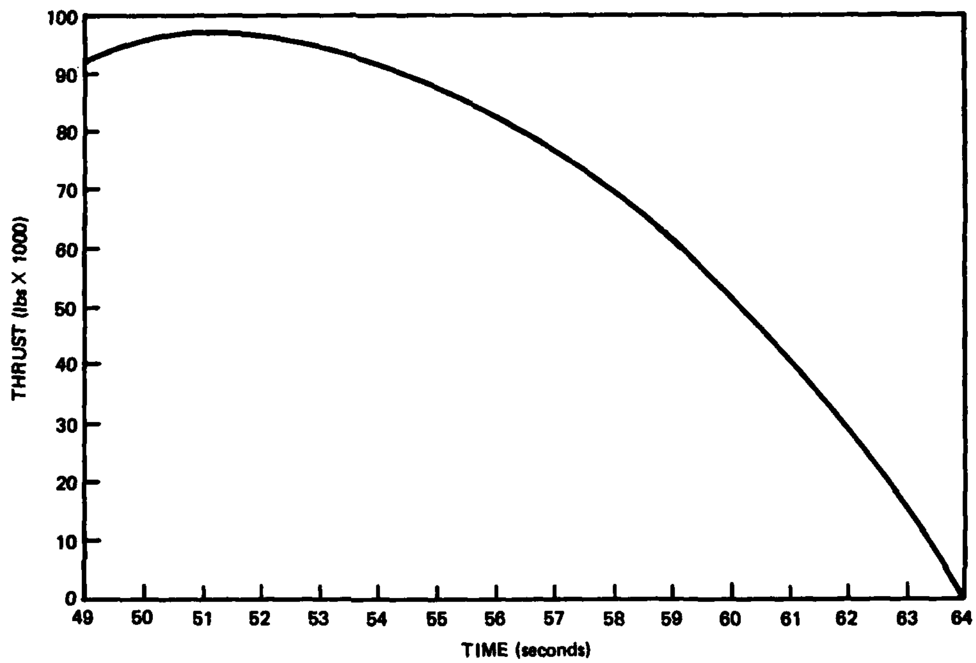

Figure D-1. Thrust vs time.

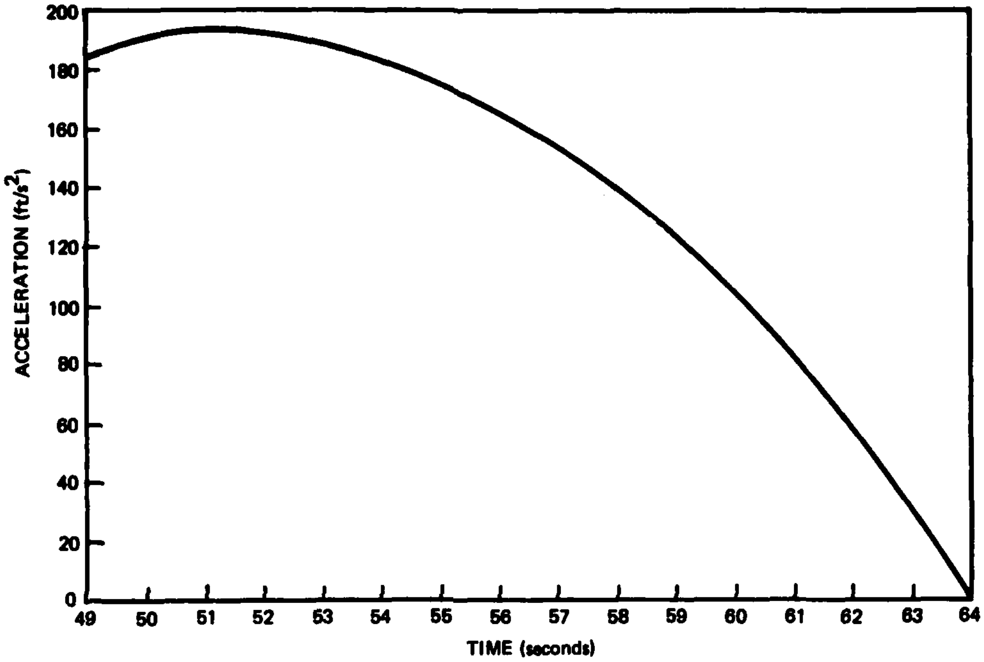

Figure D-2. Thrust acceleration vs time.

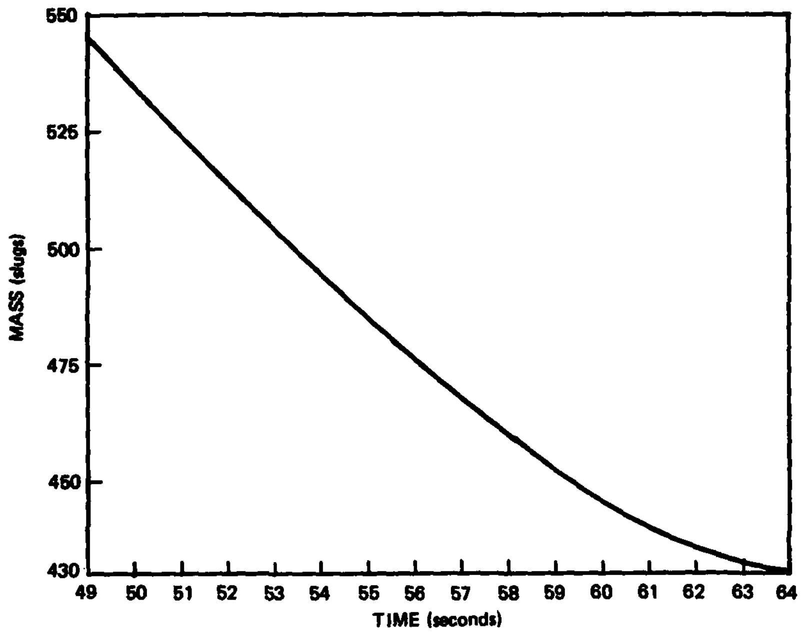

Figure D-3. Mass vs time.

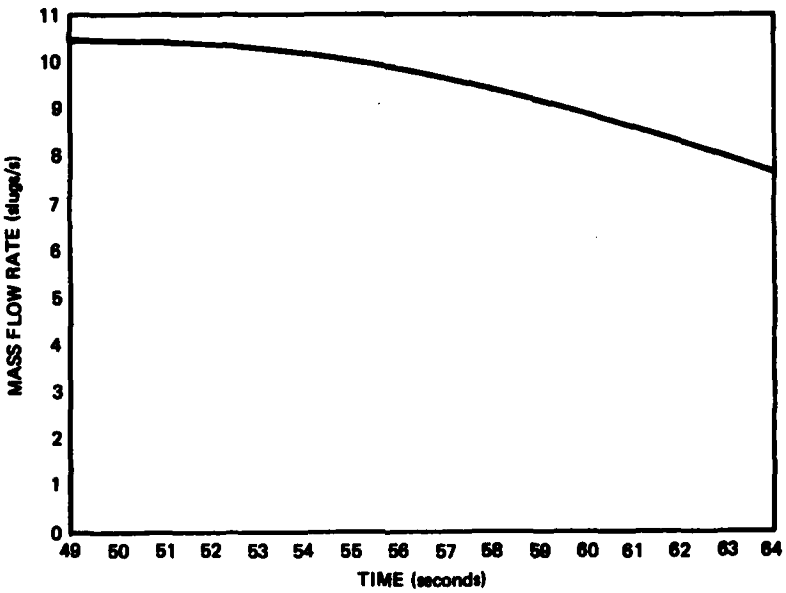

Figure D-4. Mass Flow rate vs time.

APPENDIX E1

EFFECT OF IMU POSITION
ON ACCELERATION AND RATE VECTORS SENSED

The Inertial Measurement Unit (IMU), which contains the accelerometer and rate gyros, is normally located in the post-boost vehicle or payload vehicle since this information is required after the powered flight portion of the trajectory is over. During the third stage burn, this results in a large moment arm between the center of gravity of the vehicle and the IMU location. The effect of this moment arm is to cause errors in the sensed rate and acceleration vectors when the vehicle is rotating. These errors are due to the centripetal and tangential components of acceleration caused by the rotation. Figure E1 shows this pictorially.

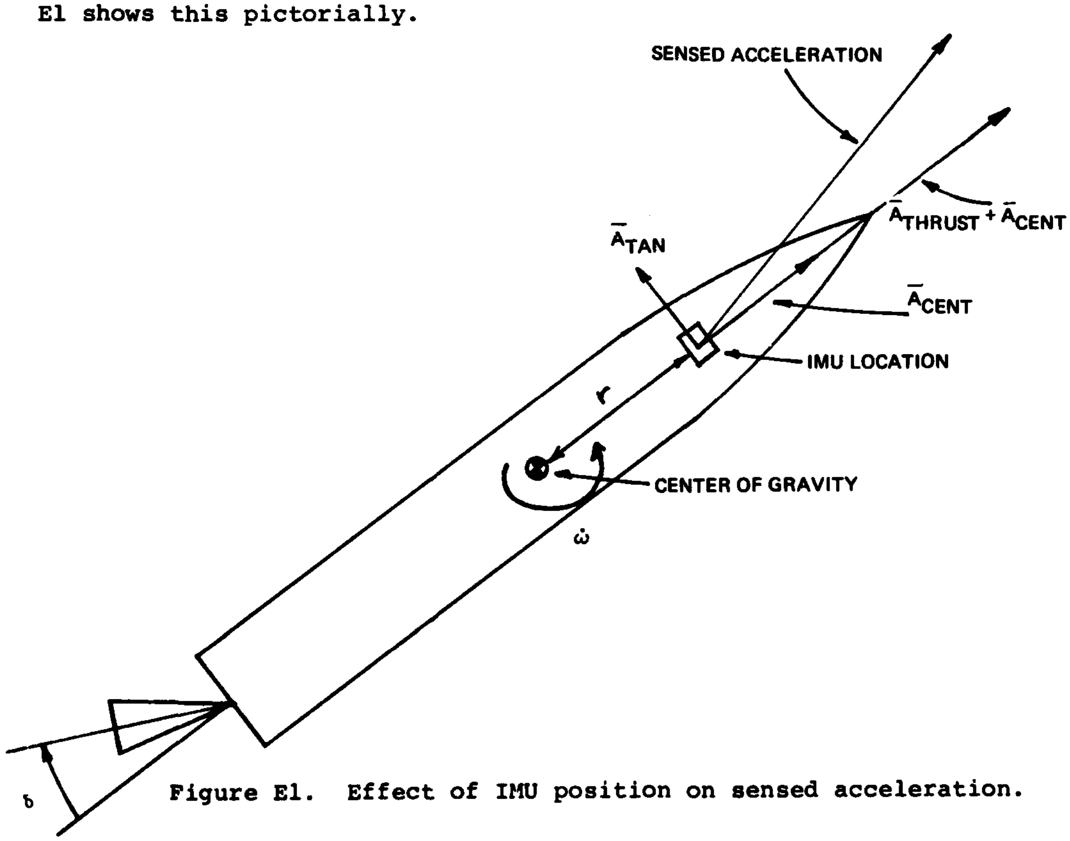

Figure E1. Effect of IMU position on sensed acceleration.

The maximum tangential acceleration, A_{TAN}, sensed by the IMU is the maximum angular acceleration, θ_{max} times the moment arm, r.

$$A_{TAN} = r\,\ddot{\theta}_{max} \qquad (E1)$$

Assuming $\theta_{max} = 20$ deg/sec^2, and r = 10 ft., this gives a maximum tangential acceleration of $A_{TAN} = 3.495$ ft/sec^2. The worst case condition occurs when the magnitude of the thrust acceleration A_T is at a minimum. The minimum (ignition) value of the thrust acceleration is $A_T = 94.3$ ft/sec^2. Adding these two accelerations vectorally gives a worst case false thrust direction indication of 2.12 degrees. Since this is a small value, and since the maximum value of $\ddot{\theta}$ occurs early in the burn (at the initiation of fuel depletion steering) and will be corrected by guidance, this effect will be neglected for the purposes of this study.

The maximum centripetal acceleration, A_{CENT}, sensed by the IMU is the square of the maximum angular rate, $\dot{\theta}^2$, times the moment arm, r.

$$A_{CENT} = r\dot{\theta}^2 \qquad (E2)$$

Assuming a maximum angular rotation rate, $\dot{\theta} = 25$ deg/sec, and again r = 10 ft., this gives a maximum centripetal acceleration of 1.904 ft/sec^2. Since this value is small compared to the magnitude of the thrust acceleration, it will be neglected for the purposes of this study.

78 08 31 006

LIST OF REFERENCES

CHARLES STARK DRAPER LABORATORY (CSDL) REPORTS

1. Brand, Timothy J., A New Approach to Lambert Guidance, R-694, June 1971.

2. D'Amario, Louis A., et al, Final Report, FY1974, Advanced Targeting and Software Design Studies, R-838, August 1974.

3. Phillips, Richard E., Final Report, Fuel Depletion Guidance, R-842, Sept. 1974.

4. D'Amario, Louis A., Stofko, David M., and Stubbs, Gilbert S., Final Report, FY1975, Advanced Targeting and Software Design Studies Post Boost Steering and Control, Volume 4, R-899 August 1975.

5. Downing, Glenn, Goss, Richard D., and Stubbs, Gilbert S., Advanced Software Design Studies, Volume 1, P-402, Nov. 1976.

6. Brand, Timothy J., and Phillips, Richard E., "Fuel Depletion Guidance for the IUS," 1 April 1976.

7. Collins, Sean, "A New Program for Implementation of the Position Offset Guidance Equations," 1 June 1977.

8. Phillips, Richard E., "Sensitivity of Trident Fuel Depletion Guidance to Velocity Application Errors," 9 April 1976.

9. Stubbs, Gilbert S., "Potential Problems in Thrust Vector Control Resulting from Application of Trident Fuel Depletion Guidance to IUS," 9 April 1976.

10. Stubbs, Gilbert S., "General Relationships for Computing Band Angles from Direction Cosines as Required for AIRS Simulation Studies," January 1972.

11. Battin, Richard H., Astronautical Guidance, McGraw-Hill Company, Inc. New York, 1964.

List of References (Cont.)

12. Bate, Roger R., Mueller, Donald D., and White, Jerry E., Fundamentals of Astrodynamics, Dover Publications, Inc., New York, 1971.

13. Thomson, William T., Introduction to Space Dynamics, John Wiley and Sons, New York, 1963.

78 08 31 006